Local and global interneuron function in the retina

Inauguraldissertation

zur

Erlangung der Würde eines Doktors der Philosophie
vorgelegt der
Philosophisch-Naturwissenschaftlichen Fakultät
der Universität Basel

von

Antonia Drinnenberg

aus Deutschland

Basel, 2018

Genehmigt von der Philosophisch-Naturwissenschaftlichen Fakultät auf Antrag von

Prof. Dr. Silvia Arber (Fakultätsverantwortliche)

Prof. Dr. Botond Roska (Dissertationsleiter)

Prof. Dr. Rava A. Da Silveira (Korreferent)

Basel, den 14. November 2017

Prof. Dr. Martin Spiess (Dekan)

"**Go big or go home**."

Olaf Obsommer, Whitewater Kayaker

Table of Contents

Preface

Animals evolved elaborated strategies to extract, process and utilize information about their environment. Since the era of Ramón y Cajal (~1900), neuroscientists have sought to identify the networks of connected neurons, or neuronal circuits, that constitute the basis for those strategies. To understand any given neuronal circuit it is essential to find out what the circuit computes and to elucidate how the architecture of the circuit—including the connectivity between the neurons and their functional properties—leads to the computation.

Dissection of neuronal circuits

Throughout the vertebrate brain, brain regions consist of intricate local neuronal circuits with diverse interneuron types. In order to gain mechanistic insights into brain function, it is essential to understand the computational purpose of the different types of interneurons. How does a single interneuron type shape the input-output transformation of a given neuronal circuit?

An intuitive strategy to address this question is to (1) control the inputs of the circuit, (2) perform a precise perturbation of a single interneuron type, and (3) monitor how the perturbation affects the outputs of the circuit. Recent advances in cell-type specific targeting and the invention of opto- and chemogenetic tools (Wiegert et al., 2017) allow for the precise perturbation of individual elements of neuronal circuits. However, as most brain regions transform the signals from multiple input channels into signals conveyed by multiple output channels, the complete control of the region's input channels, and a system-level read-out of the region's output channels still constitute a major technical challenge.

A model system where the systematic interrogation of interneuron function outlined above is feasible is the retina. Here, the input source—light—can be precisely controlled in both space and time, and the output—the spiking activity of the different ganglion cell types—can be recorded simultaneously in a large population of cells (Fiscella et al., 2012; Baden et al., 2016). Moreover, in the mouse retina, recent studies provided genetic access to individual interneuron types (Siegert et al., 2012). During my PhD, I investigated how different interneuron types contribute to retinal computations by performing targeted circuit perturbations and analyzing the perturbation-induced effects at the level of the retinal output.

Structure and function of retinal circuits

The retina is a thin, laminated sheet of nervous tissue lining the back of the eye. Despite its peripheral location, it is part of the central nervous system. Retinal circuits are assembled from ~100 different neuronal cell types, which fall into five main classes that are localized to different layers of the tissue (Figure 1). Photoreceptors detect the incoming light and send the signal via bipolar cells to ganglion cells. Horizontal cells and amacrine cells provide inhibitory input in the outer and inner retina, respectively. ~30 types of ganglion cells form the output channels of the retina (Sanes and Masland, 2015). Each ganglion cell type connects to a specific set of bipolar and amacrine cell types to form a retinal circuit module. The ~30 circuit modules extract specific visual features from the retinal image (Figure 2). Each circuit module is repeated in a regularly spaced arrangement, a 'mosaic', such that the receptive fields of each ganglion cell type cover the entire visual field (Azeredo da Silveira and Roska, 2011; Gollisch and Meister, 2010). Thus, retinal circuits create ~30 neural representations of the image that falls onto the photoreceptors (Figure 2), which are then simultaneously transmitted to the brain. The retina therefore does not simply convey a filtered pixel image to higher visual brain regions, but shapes the visual representation in a profound way.

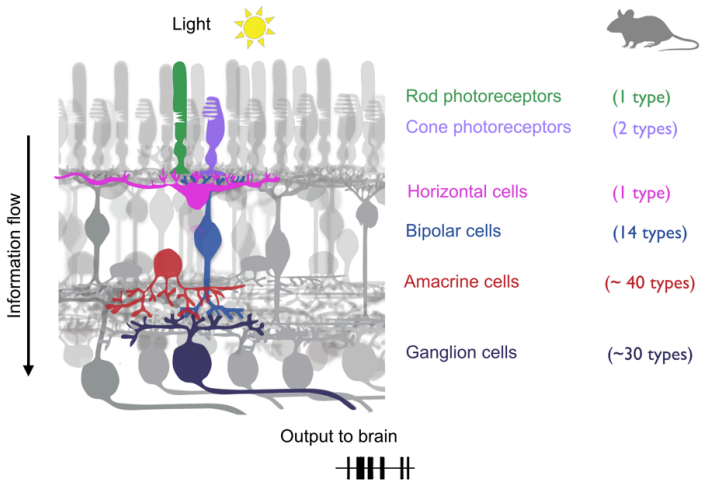

Figure 1. **Schematic of the cell types in the retina.** The drawing illustrates the five main classes of retinal cells: (1) Photoreceptors, which convert the incoming photons into neuronal activity. (2) Horizontal cells, which modulate the information flow between photoreceptors and bipolar cells. (3) Bipolar cells, which receive input from photoreceptors and convey information to amacrine cells and ganglion cells. (4) Amacrine cells, which provide inhibition in the inner retina. (5) Ganglion cells, whose axons convey the retina's output to the brain. Numbers in brackets refer to the numbers of cell types in the mouse retina.

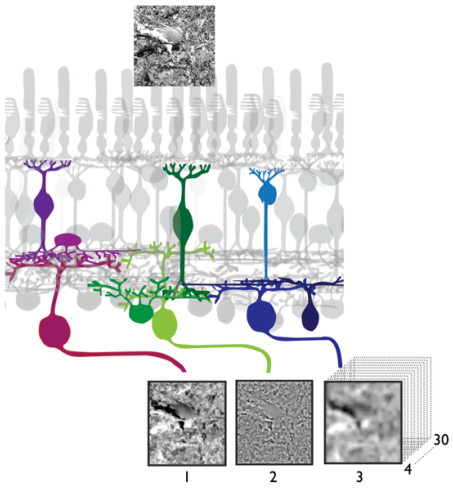

Figure 2. **Retinal circuits dissect the visual scene into distinct features.** Specific sets of bipolar, amacrine and ganglion cell types form retinal circuit modules that extract distinct features of the visual scene. The ~30 parallel circuit modules convey ~30 different dynamic activity patterns to the brain.

Local and global functions of retinal interneurons

In my PhD work, I studied how specific types of interneurons contribute to retinal computations. On a conceptual level, there are two kinds of retinal interneurons: Interneurons that act locally by influencing only few retinal output channels, or interneurons that act globally by shaping the activity of many retinal output channels. During my PhD, I studied the functional roles of a locally acting interneuron type, starburst amacrine cells, and of a globally acting type, horizontal cells.

Starburst amacrine cells are essential for the computations performed by a specific subset of ganglion cells—the ganglion cells coding for the direction of visual motion. In ***Chapter 1***, I show how a defined genetic perturbation in starburst amacrine cells, the mutation of the *FRMD7* gene, leads to specific effects in the direction-selective output channels of the retina. ***Chapter 2*** addresses how mutated *FRMD7* in starburst cells and the genetic ablation of starburst cells affect the computation of visual motion in the retina and in primary visual cortex.

Contrary to starburst amacrine cells, horizontal cells act globally on the retinal output, as they act at an early position in the retinal processing hierarchy—the first visual synapse between photoreceptors and bipolar cells (Figure 1). ***Chapter 3*** addresses how horizontal cells mediate rod depolarization under bright daylight conditions. In ***Chapter 4***, I investigate how horizontal cells shape the retinal outputs and show how their feedback at the first visual synapse gives rise to diverse retinal functions.

Contributions

Chapter 1 is based on a manuscript that I wrote in collaboration with Keisuke Yonehara, Michele Fiscella, and Botond Roska. In this work, we link a specific neuronal computation, retinal direction-selectivity, to a human disease—*FRDM7* based congenital nystagmus. The study has been published in *Neuron* (Yonehara et al., 2016). I contributed to this work as co-first author by revealing the retinal circuit mechanism that underlies the phenotype of *FRDM7* mutant mice.

Chapter 2 is based on a manuscript written by Daniel Hillier and Botond Roska. This study, which has been published in *Nature Neuroscience* (Hillier et al., 2017), addresses how the perturbation of direction-selectivity in the retina affects direction-selectivity in primary visual cortex. I contributed by investigating how genetically targeted direction-selective ganglion cells are affected by the two kinds of retinal perturbations used in this study—genetic ablation of starburst amacrine cells and mutation of *FRMD7*.

Chapter 3 is based on a manuscript written by Tamas Szikra, Rava A. da Silveira, and Botond Roska. This study, which has been published in *Nature Neuroscience* (Szikra et al., 2014), shows that rod photoreceptors relay cone-driven surround inhibition to the inner retina. I contributed to this study by establishing the viral targeting of horizontal cells, which was necessary to show that horizontal cells mediate the rod depolarization.

Chapter 4 is based on a manuscript that I wrote in collaboration with Felix Franke, Rava A. da Silveira, and Botond Roska. This study, which is currently under review in *Neuron*, investigates how a single interneuron type, horizontal cells, affects the dynamics of the retinal output channels. This work constitutes the main part of my PhD thesis. I performed all experiments (except the cone imaging) and analyses. Felix Franke performed the hierarchical clustering and developed the computational model in collaboration with Rava A. da Silveira. Rei Morikawa-Kanamori performed the cone imaging.

Chapter 1 - Congenital nystagmus gene *FRMD7* is necessary for establishing a neuronal circuit asymmetry for direction selectivity

Yonehara K, Fiscella M*, **Drinnenberg A***, Esposti F, Trenholm S, Krol J, Franke F, Scherf BG, Kusnyerik A, Müller J, Szabo A, Jüttner J, Cordoba F, Reddy AP, Németh J, Nagy ZZ, Munier F, Hierlemann A & Roska B*

**Co-first authors*

Summary

Neuronal circuit asymmetries are important components of brain circuits, but the molecular pathways leading to their establishment remain unknown. Here we found that the mutation of FRMD7, a gene which is defective in human congenital nystagmus, leads to the selective loss of the horizontal optokinetic reflex in mice, as it does in humans. This is accompanied by the selective loss of horizontal direction selectivity in retinal ganglion cells and the transition from asymmetric to symmetric inhibitory input to horizontal direction-selective ganglion cells. In wild type retinas, we found FRMD7 specifically expressed in starburst amacrine cells, the interneuron type that provides asymmetric inhibition to direction-selective retinal ganglion cells. This work identifies FRMD7 as a key regulator in establishing a neuronal circuit asymmetry and suggests the involvement of a specific inhibitory neuron type in the pathophysiology of a neurological disease.

Introduction

Neuronal circuit asymmetries are important building blocks of the nervous system. Sensory circuits rely on circuit asymmetries to detect external features, like the position of sound sources, the orientation of visual objects or the direction of visual motion. In both invertebrates and vertebrates, neurons have been identified that respond selectively to the direction of visual motion: vigorously to motion in a 'preferred' direction, but only weakly to motion in the opposite, 'null', direction (Borst and Euler, 2011). Direction-selective neurons are already present at the sensory periphery, in the lobula and lobular plate of flies and in the retina of vertebrates (Borst and Helmstaedter, 2015). Retinal direction-selective neurons have preferred directions and corresponding circuit asymmetries along the cardinal directions. Due to their accessibility for physiological recordings and genetic manipulation, these circuits

serve as model systems for understanding the formation of neuronal circuit asymmetries (Wei and Feller, 2011). However, the molecules establishing the asymmetry of direction-selective circuits along the cardinal axes remain unknown.

A potential source for identifying candidate molecules involved in the development of cardinal direction selectivity are monogenic diseases, which disrupt human visual behaviors that depend on the activity of direction-selective retinal cells. A visually guided behavior that relies on the activity of retinal direction-selective neurons is the optokinetic reflex (Osterhout et al., 2015; Oyster et al., 1972; Sun et al., 2015; Yoshida et al., 2001). The optokinetic reflex is initiated by a visual scene drifting on the retina, which triggers the eye to follow it, thus keeping the image stable on the retina. The optokinetic reflex works together with the vestibulo-ocular reflex, in which eye movement is initiated by head or body motion, to stabilize the gaze while the animal moves its head or entire body (Schweigart et al., 1997). These two reflexes, driven by visual and body motion, are complementary. The optokinetic reflex dominates gaze stabilization at lower speeds, and the vestibular reflex at higher speeds (Faulstich et al., 2004; Iwashita et al., 2001; Van Alphen et al., 2001). The optokinetic reflex can be separated from the vestibulo-ocular reflex if the head is fixed in place (Bryan and Angelaki, 2009).

A neurological disease in which the optokinetic reflex is disturbed is idiopathic congenital nystagmus. Individuals with idiopathic congenital nystagmus, which occurs in 1 in 1,500 humans, have impaired eye movements resulting in impaired vision (Gottlob and Proudlock, 2014; Maybodi, 2003). In 70% of the detected cases, mutations in the *FRMD7* gene on the X chromosome have been reported (Tarpey et al., 2006). Individuals without a functional *FRMD7* allele have involuntary horizontal eye oscillations (nystagmus) and lack the optokinetic reflex along the horizontal axis (Thomas et al., 2011, 2008). In contrast, along the vertical axis no nystagmus can be observed and the optokinetic reflex is unaffected. The symptoms begin in early childhood, at an age of 2-3 months. While *FRMD7* expression has been localized to the retina and the vestibular system (Tarpey et al., 2006; Thomas et al., 2011), the neuronal circuit dysfunction responsible for the symptoms of the disease is unknown.

In the retina of mammals, including mice, three classes of direction-selective ganglion cells (DS cells) have been described: ON-OFF DS cells, ON DS cells, and OFF DS cells (Sanes and Masland, 2015). ON-OFF cells respond to both light increments and decrements, while ON cells respond only to increments and OFF cells only to decrements. ON-OFF DS cells are comprised of four types with preferred directions corresponding to each of the four cardinal directions (inferior, superior, temporal, or nasal; note that throughout the text the direction of motion is defined based on the direction of motion on the retina). ON DS cells can be

classified into three types, with preferred motion directions being inferior, superior, or temporal. OFF DS cells prefer motion in the inferior direction. Most ON DS cells and a type of ON-OFF DS cells are tuned to slow motion, while most ON-OFF DS cells and a group of ON DS cells prefer faster motion (Dhande et al., 2013; Gauvain and Murphy, 2015; Sivyer et al., 2010). DS cell types in the mouse retina are genetically determined populations of neurons: they can be labeled by distinct molecular markers and they form retinal mosaics (Sanes and Masland, 2015).

It has been suggested that slow-motion-tuned DS cells are the main source of direction-selective input driving the optokinetic reflex in response to slow drifts of the visual scene (Oyster et al., 1972; Sugita et al., 2013). Indeed, the optokinetic reflex is lost when retinal direction selectivity is abolished by genetic ablation of starburst cells, which are a key circuit component of the retinal direction-selective circuit (Yoshida et al., 2001). Slow-motion-tuned ON and ON-OFF DS cells project their axons to the nuclei of the accessory optic system (Dhande et al., 2013; Yonehara et al., 2009), which consists of the medial and lateral terminal nucleus (MTN, LTN), and the nucleus of the optic tract (NOT)/dorsal terminal nucleus (DTN) complex (Giolli et al., 2006; Simpson, 1984) (Figure 1.9C). In mice, the MTN receives retinal inputs from superior and inferior motion preferring ON DS cells (Dhande et al., 2013; Yonehara et al., 2009) and inferior motion preferring ON-OFF DS cells (Kay et al., 2011); the NOT/DTN complex receives retinal inputs from temporal motion preferring ON and ON-OFF DS cells (Dhande et al., 2013). Direction- selective responses with preferred directions along the vertical axis have been recorded in the MTN and LTN, while responses with preferred directions along the horizontal axis have been recorded in the NOT/DTN complex (Schmidt et al., 1998; Soodak and Simpson, 1988; van der Togt et al., 1993). Activity in the NOT/DTN complex has been shown to be required selectively for the horizontal optokinetic reflex (Hoffmann and Fischer, 2001), while MTN activity is required for the vertical optokinetic reflex (Sun et al., 2015). The accessory optic system is conserved across species, as the MTN and NOT/DTN have been anatomically identified in a number of species including mouse, rabbit, cat, monkey, and human (Giolli et al., 2006; Simpson, 1984).

The retinal circuitry underlying the direction-selective responses of ON-OFF and ON DS cells has been investigated in detail. DS cells receive excitatory input from glutamatergic bipolar cells, as well as inhibitory and excitatory input from starburst amacrine cells. Starburst cells release both GABA and acetylcholine (Vaney et al., 2012). The glutamatergic excitatory input from bipolar cells and the cholinergic excitatory input, which likely arrives via paracrine secretion from starburst cells (Briggman et al., 2011), are not direction selective (Chen et al., 2014; Lee et al., 2010; Park et al., 2014; Yonehara et al., 2013). The GABAergic inhibitory input from starburst cells is spatially asymmetric: in response to motion in the null

direction, inhibitory input is maximal; in response to motion in the preferred direction, inhibitory input is minimal (Vaney et al., 2012). Furthermore, active integration mechanisms in the dendrites of DS cells sharpen the spiking output of DS cells (Oesch et al., 2005; Sivyer and Williams, 2013; Trenholm et al., 2014). With the exception of the responses of a single ON-OFF DS cell type to slow motion (Trenholm et al., 2011), and the responses of the OFF DS cell type (Kim et al., 2008), the inhibitory input from starburst cells is necessary for the direction-selective responses of DS cells (Fried et al., 2002; Yoshida et al., 2001).

The direction selectivity of the inhibitory input to DS cells relies on two features of the retinal circuit. The first feature is an asymmetric neurotransmitter release from starburst cells. Starburst cell processes radiate away from the soma; they act both as dendrites, receiving input from bipolar cells and other starburst cells, and as axons, providing input to DS cells and other starburst cells (Famiglietti, 1991; Kim et al., 2014). A starburst cell process preferentially releases GABA if motion occurs in a centrifugal direction along the process, from the soma to the tip (Euler et al., 2002). This asymmetric release could be due to inputs from different types of bipolar cells with different temporal characteristics along the starburst cell process (Kim et al., 2014) an excitability gradient (Gavrikov et al., 2006, 2003; Hausselt et al., 2007), or inhibitory interactions between starburst cells (Lee and Zhou, 2006). This asymmetry is radial, centered on each starburst soma, and likely has no information about the cardinal directions. Therefore, the disruption of its development would likely result in a decrease in direction selectivity along all four cardinal directions. The second circuit feature, which direction selectivity relies on, is the spatially asymmetric inhibitory connectivity between starburst cells and DS cell types (Briggman et al., 2011; Fried et al., 2002). The angle of a starburst cell process relative to the cardinal directions in the retina determines the connectivity between the starburst cell process and the DS cell type (Figures 1.1A-B). For instance, starburst processes that point nasally connect to DS cell types preferring temporal motion, and starburst processes that point superiorly connect to DS types preferring inferior motion (Briggman et al., 2011). This spatially asymmetric connectivity is believed to be necessary for defining cardinal direction selectivity. Developmental disruption could potentially result in the loss of direction selectivity in specific directions, or combinations of directions.

Spatially asymmetric inhibitory connectivity between starburst cells and DS cells forms independent of visual activity or spontaneous retinal waves (Elstrott et al., 2008), and occurs rapidly between postnatal day 6 (P6) and eye opening, from previously established symmetric inputs (Wei et al., 2011; Yonehara et al., 2011). Molecules responsible for positioning DS cell dendrites, for establishing bipolar cell input, and for defining the morphology and spacing of starburst cells have already been described (Duan et al., 2014; Sun et al., 2013), and

molecules responsible for creating centrifugal direction selectivity in starburst cell processes have been proposed (Gavrikov et al., 2003). While disruption of some of these molecules results in decreased tuning of direction-selective responses (Sun et al., 2013), no molecules have been identified that are necessary for motion detection in specific directions (Duan et al., 2014; Gavrikov et al., 2003; Sun et al., 2013). Therefore, the molecular pathway responsible for setting up the circuit asymmetry along the cardinal directions remained unidentified.

Recently, using a transcriptional map of adult retinal cell types in mice, we found that *FRMD7*, the gene in which mutations result in the lack of the horizontal optokinetic reflex in humans, is enriched in starburst cells (Siegert et al., 2012), suggesting that direction-selective circuits in the retina could be involved in the disease. The *FRMD7* gene encodes a member of the FERM domain family of proteins (Moleirinho et al., 2013) and has been implicated in the reorganization of the cytoskeleton (Pu et al., 2013). Here we investigate a potential link between the function of *FRMD7*, the development of retinal direction selectivity, and the lack of the horizontal optokinetic reflex in *FRMD7*-based congenital nystagmus.

Results

FRMD7 is required for the horizontal optokinetic reflex in mice

We compared the optokinetic reflex and spontaneous eye movements of wild type and *FRMD7* hypomorphic mutant (*FRMD7*^{tm}, Experimental Procedures Chapter 1, Figure 1.1) mice (Figures 1.2 and 1.3). Head-fixed mice were presented with drifting gratings while their eye movements were tracked with a camera. In wild type mice, a strong optokinetic reflex could be elicited in nasal, temporal, and inferior directions (Figures 1.2C-E). The reflex was weak in the superior direction, as has been reported previously (Yonehara et al., 2009). Similarly to human subjects with *FRMD7* mutation (Thomas et al., 2011) (Figures 1.2H-J and 1.3), *FRMD7*^{tm} mice lacked the horizontal optokinetic reflex, both in the nasal and temporal directions (Figures 1.2C and 1.2D) but the vertical inferior optokinetic reflex of F *FRMD7*^{tm} mice was similar to that of wild type mice (Figure 1.2E). The absence of the horizontal optokinetic reflex did not appear to arise from an inability of the mice to move their eyes horizontally, as we observed spontaneous horizontal eye movements in wild type and *FRMD7*^{tm} mice (Figures 1.2F and 1.2G). Similarly, human subjects with *FRMD7* mutation could perform voluntary horizontal eye movements (Figures 1.2K and 1.2L). We observed no spontaneous oscillatory eye movements (nystagmus) in *FRMD7*^{tm} mice. These results suggest that one of the symptoms, the lack of the horizontal optokinetic reflex, is shared between *FRMD7*^{tm} mice and human subjects with *FRMD7* mutation and that the motor circuits of both humans and mice remain capable of moving the eyes horizontally.

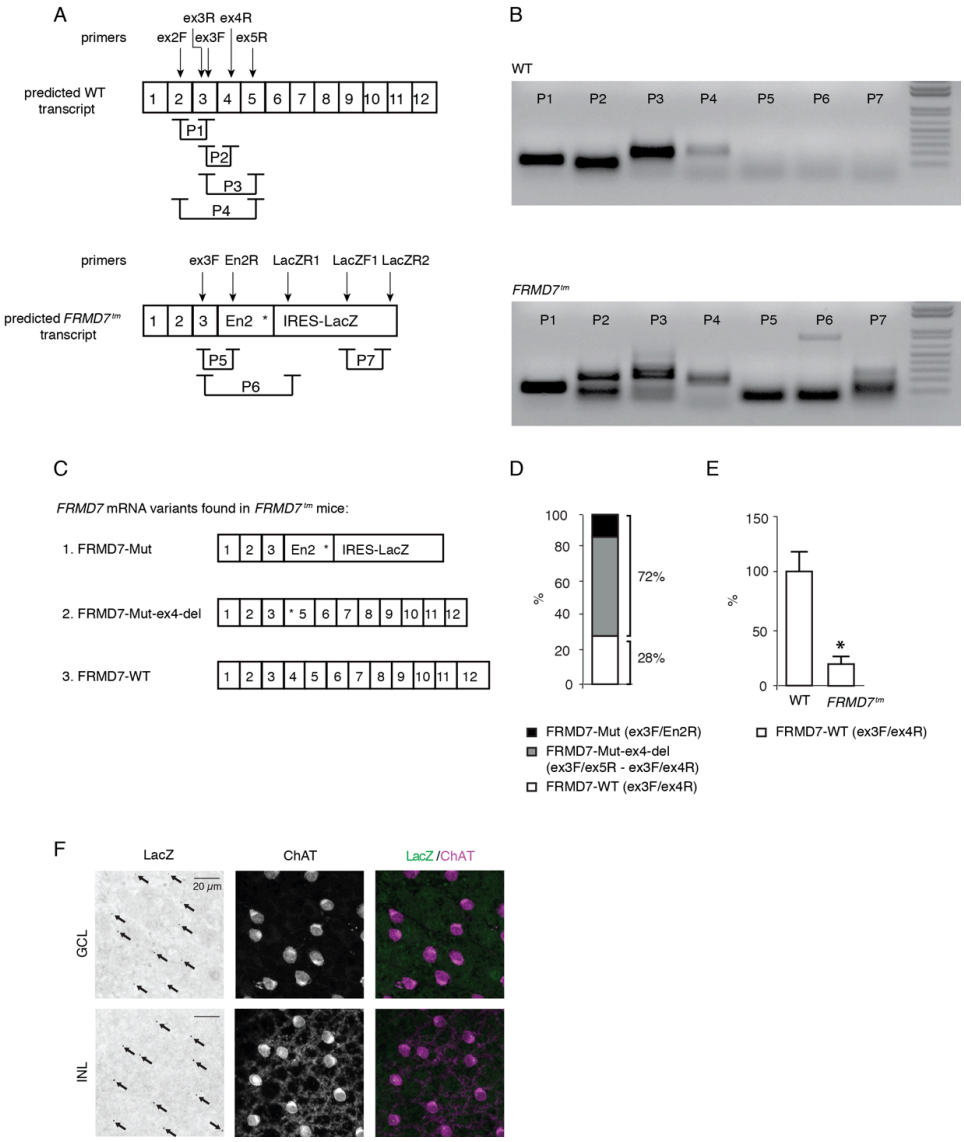

Figure 1.1 **Identification of *FRMD7* transcript variants in wild type and *FRMD7*^{tm} mice.** (**A**) Schematic representation of predicted mRNAs in wild type (WT) and *FRMD7*^{tm} mice together with the primer locations (sequences corresponding to the names are shown in Experimental Procedures) and predicted RT-PCR products (P1-P7). Numbers (1-12) refer to the corresponding exon. The En2 fragment and iRES-LacZ are part of the cassette used to generate *FRMD7*^{tm} knock-in mice. (**B**) Agarose gel electrophoresis of the RT-PCR products of *FRMD7* mRNA in wild type (WT) and *FRMD7*^{tm} mice. Names of specific lanes correspond to predicted PCR products indicated in A. (**C**) Schematic representation of different *FRMD7* transcript variants cloned and sequenced from *FRMD7*^{tm} mice. Asterisks indicate frame-shift-generated stop codons. (**D**) RT-qPCR quantified expression levels of *FRMD7* transcript variants in *FRMD7*^{tm} mice. Individual transcripts were amplified using the oligonucleotide primers indicated in brackets. Expression level of the FRMD7-Mut-ex4-del transcript variant was determined by subtracting the level of FRMD7-WT (ex3F/ex4R primer pair amplified) transcript from the level of ex3F/ex5R primer pair amplified transcripts. (**E**) Comparison of the expression of FRMD7-WT transcript in wild type and *FRMD7*^{tm} mice using RT-qPCR. (**F**) LacZ is specifically expressed in starburst cells in the retina of *FRMD7*^{tm} mice. Confocal images of the GCL

(top) and INL (bottom) of adult *FRMD7*^{tm} retina stained with antibodies for LacZ and ChAT. Black arrows indicate clustered LacZ signals.

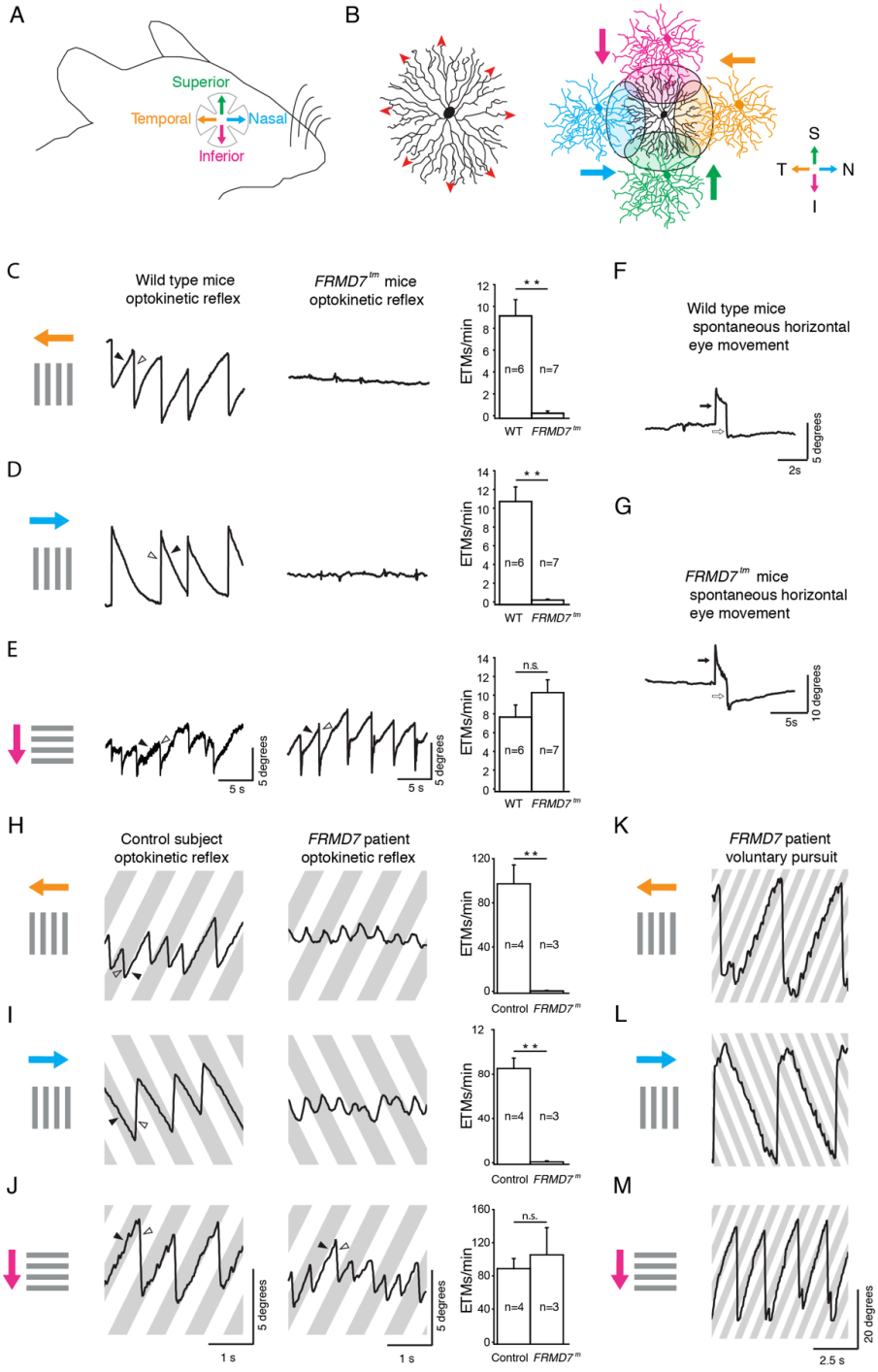

Figure 1.2 **Horizontal optokinetic reflex is absent in *FRMD7*^{tm} mice and in human subjects with *FRMD7* mutation.** (**A**) Retinal cardinal axes. (**B**) Left: a schematic of a starburst cell showing the direction of centrifugal motion (red arrowheads) that evokes transmitter release. Right: Spatial

organization of synaptic connectivity between a starburst cell (center, black) and four types of DS cells color-coded according to their preferred directions (colored arrows). (**C-E**) Optokinetic reflex eye movements produced by wild type (left) and *FRMD7*^{tm} (middle) mice in response to motion in the temporal (top), nasal (middle) and inferior (bottom) direction on the retina. Gray bars represent the motion stimulus and arrows colored according to the color code in A indicate the motion direction on the retina. The right column shows the quantification of optokinetic reflex eye-tracking movements per minute (ETMs) for wild type (WT) and *FRMD7*^{tm} mice, in the three directions. Filled and open arrowheads indicate the slow phase and fast phase of eye movements, respectively. **(F-G)** Spontaneous eye movements in wild type (F) and *FRMD7*^{tm} (G) mice along horizontal axes. For F and G, open and filled arrows indicate eye movements, to the left and right, respectively. **(H-J)** Optokinetic reflex in a control human subject (left) and a subject with *FRMD7* mutation (middle), in response to motion in the temporal (top), nasal (middle) and inferior (bottom) direction on the retina. Gray bars represent the motion stimulus and arrows colored according to the color code in A indicate the motion direction on the retina. The right column shows the quantification of optokinetic reflex ETMs for control human subjects and for subjects with *FRMD7* mutation in the three directions. Filled and open arrowheads indicate slow phase and fast phase of eye movements, respectively. **(K-M)** Voluntary pursuit movements in a human subject with *FRMD7* mutation in response to the motion protocols as in (H-J).

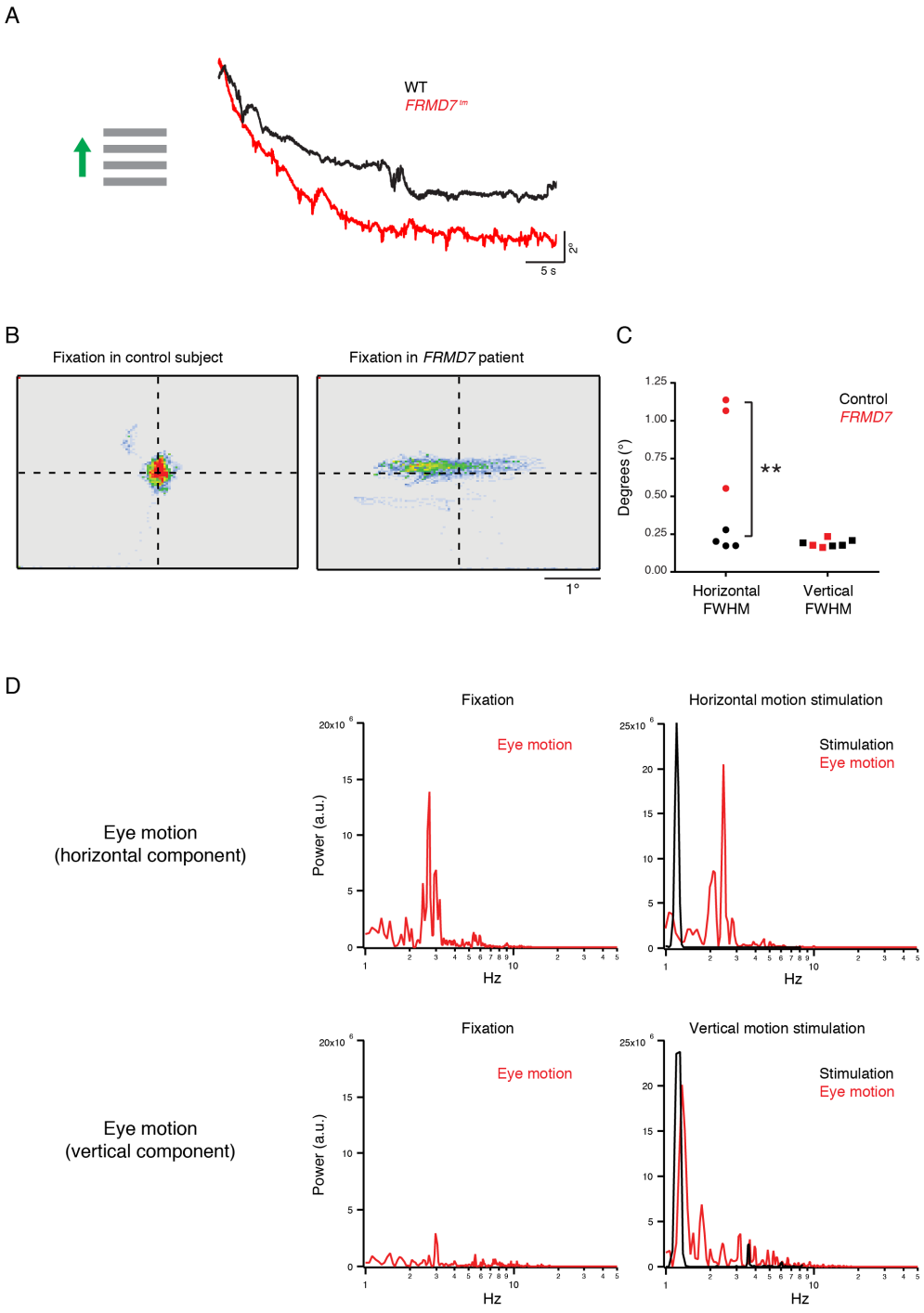

Figure 1.3 **Nystagmus and optokinetic reflex. (A)** Eye movements produced by wild type (black) and *FRMD7*^{tm} (red) mice in response to motion in the superior direction on the retina. **(B)** Distribution of fixation points during fixation in a control human subject (left) and a subject with *FRMD7* mutation (right). **(C)** Quantification of data in B using the full-width-at-half-maximum values (FWHM) of fitted 2D Gaussian curves. **(D)** Power spectra (red traces, arbitrary units) of the horizontal (top) and vertical eye movements (bottom) of a human subject with *FRMD7* mutation during fixation (left) and during visual stimulation with gratings moving at 15 degrees/second (right). The panels demonstrating eye

motion during motion stimulation also show the power spectrum of the visual stimulation (black traces). Note that the power spectra of stimulation and eye motion do not overlap when the human subject was stimulated with horizontal motion, but do overlap when stimulated with vertical motion.

Lack of horizontal direction selectivity in the retina of *FRMD7*^{tm} mice

We investigated whether the lack of the horizontal optokinetic reflex is accompanied by altered retinal activity in *FRMD7*^{tm} mice. We recorded the spiking activity of retinal ganglion cells in wild type and *FRMD7*^{tm} mice using microelectrode arrays. The retina was stimulated with light flashes and bars moving in different directions and at different velocities. Light flashes were used to segregate ON and ON-OFF cells, motion in different directions was used to determine direction selectivity, and different velocities were used to differentiate between slow and fast motion preferring DS cells. Retinas of *FRMD7*^{tm} mice responded well to both light flashes and slow and fast motion (Figure 1.4A-C). However, in *FRMD7*^{tm} mice the fraction of cells with direction-selective responses were significantly lower (by 52% and 44%) than in wild type mice when stimulated with fast and slow motion, respectively (Figure 1.4C).

In wild type retinas, we recorded direction-selective responses along both the horizontal and the vertical axes: we identified fast motion tuned DS cells preferring motion along the cardinal directions, and slow motion tuned DS cells types preferring superior, inferior, or temporal motion (Figure 1.5). Similarly we found ON-OFF DS cells preferring motion along the cardinal directions and ON DS cells preferring mainly superior, inferior, or temporal motion (Figure 1.6). Strikingly, in *FRMD7*^{tm} mice, the fraction of horizontal motion (temporal or nasal) preferring DS cells decreased by 95% (fast motion) and 93% (slow motion) compared to wild type mice (Figure 1.5). The nearly complete lack of direction selectivity along the horizontal axis was found in both ON and ON-OFF DS cells (Figure 1.6). Nevertheless, in *FRMD7*^{tm} mice, the number of vertical motion preferring direction-selective cells relative to all recorded ganglion cells remained similar to wild type (Figure 1.5F). Thus, the loss of *FRMD7* leads to the specific loss of horizontal direction-selective responses in the retina.

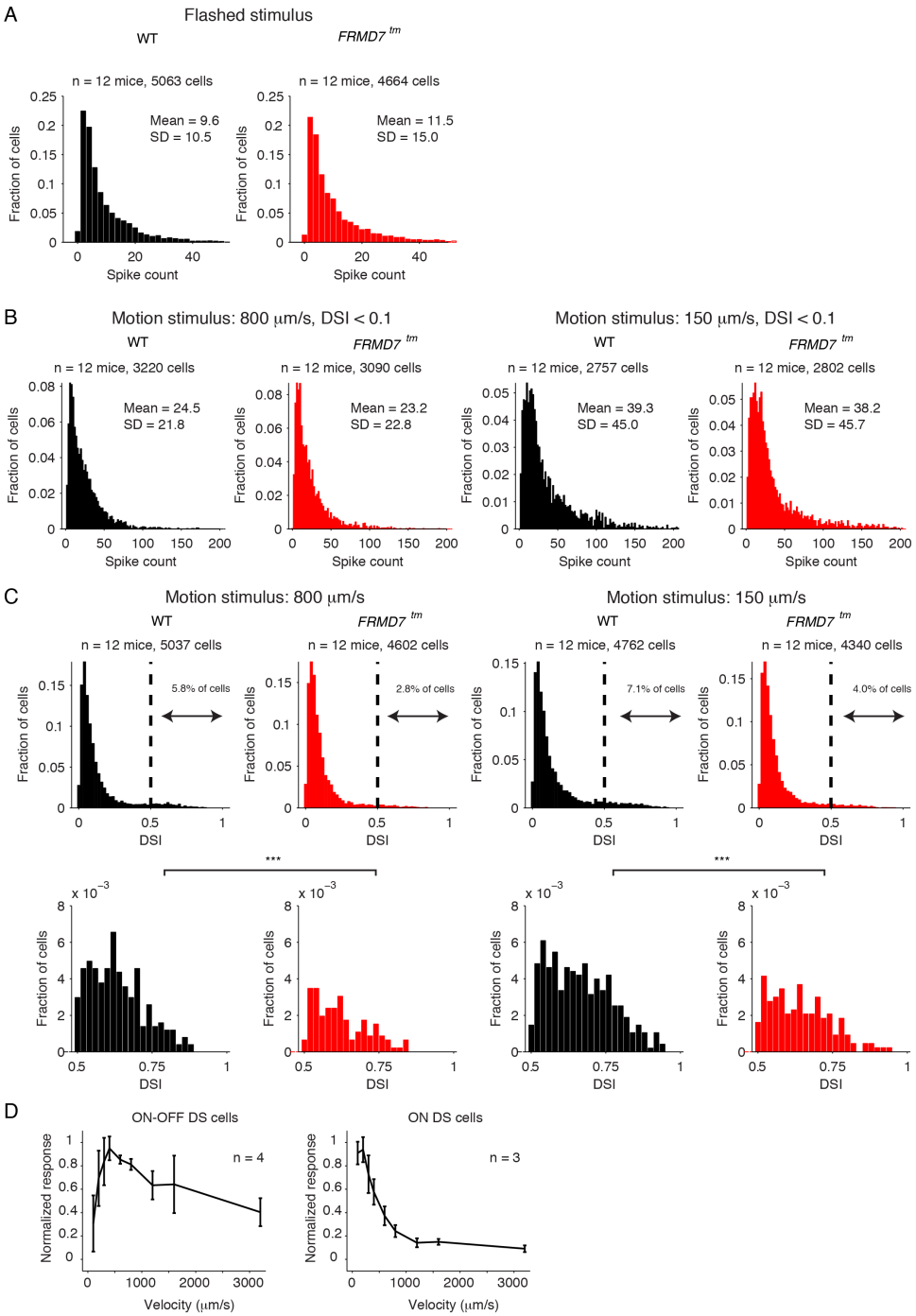

Figure 1.4 **Visual responses of retinal ganglion cells in wild type and *FRMD7*^{tm} mice.** The figure shows data obtained with microelectrode arrays. Black is wild type, red is *FRMD7*^{tm}. (**A**) Distributions of the number of spikes in response to flashed stimuli in all recorded ganglion cells. (**B**) Distributions of peak responses to fast (left) and slow (right) motion stimulation in non-DS (DSI < 0.1) ganglion cells. (**C**) Upper panels, distribution of DSI in response to fast (left) and slow (right) motion in all ganglion cells. Lower panels, same as shown in upper panels but only cells having a DSI of 0.5-1 are shown. (**D**) Velocity tuning of ON-OFF and ON cells. Number of spikes (normalized to the maximum) evoked by motion at different velocities in ON-OFF (left) and ON (right) cells. Error bars indicate SD.

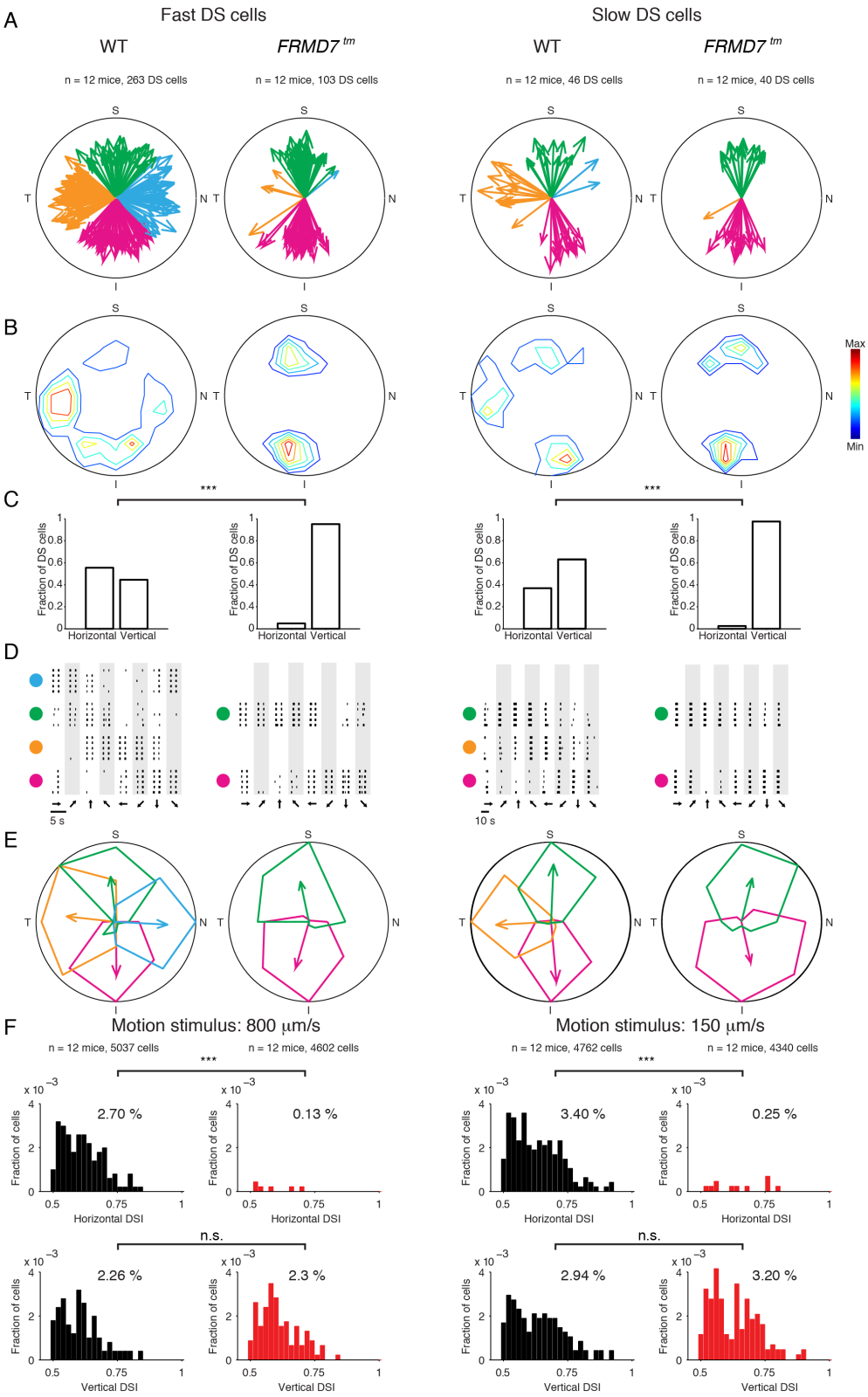
A
Fast DS cells
Slow DS cells
WT
FRMD7 tm
WT
FRMD7 tm
n = 12 mice, 263 DS cells
n = 12 mice, 103 DS cells
n = 12 mice, 46 DS cells
n = 12 mice, 40 DS cells
S
T
N
I
B
Max
Min
C
***
Fraction of DS cells
Horizontal Vertical
D
5 s
10 s
E
F
Motion stimulus: 800 μm/s
Motion stimulus: 150 μm/s
n = 12 mice, 5037 cells
n = 12 mice, 4602 cells
n = 12 mice, 4762 cells
n = 12 mice, 4340 cells
x 10 −3
Fraction of cells
2.70 %
0.13 %
3.40 %
0.25 %
Horizontal DSI
n.s.
2.26 %
2.3 %
2.94 %
3.20 %
Vertical DSI

Figure 1.5 **Lack of horizontal direction selectivity in the retina of FRMD7^{tm} mice**. The figure shows data obtained with microelectrode arrays. In A-E, the left two columns correspond to cells tuned to fast motion and the right two columns to cells tuned to slow motion (Experimental Procedures). The radius of each circle corresponds to DSI = 1. (**A**) Polar plots showing the preferred directions (direction of arrow) and direction selectivity index (DSI, length of an arrow) of individual DS cells (DSI > 0.5, each recorded DS cell is represented by an arrow) in wild type and FRMD7^{tm} retinas. The color code shows the different directions according to Figure 1.2A. (**B**) Contour plots showing the density of DS cells at different DSIs and preferred directions. Red indicates maximal density. (**C**) The proportion of horizontal (nasal and temporal) and vertical (superior and inferior) motion preferring DS cells in wild type and FRMD7^{tm} retinas. (**D**) Raster plots showing the spike responses (each black line is a spike) of example DS cells in wild type and FRMD7^{tm} retinas in response to motion in eight different directions, indicated by the arrows at the bottom of the plot. Responses to stimulus repetitions (n = 5) are shown in different rows. Large colored dots indicate the preferred directions of DS cells according to the color code in Figure 1.2A. (**E**) Polar plots of the mean spike numbers of cells shown in D. The preferred direction and DSI of each cell are shown by the direction and length of the corresponding (color-coded) arrow. (**F**) Distribution of the horizontal (top) and vertical (bottom) DSIs (Experimental Procedures) of DS cells in wild type (black) and *FRMD7*^{tm} (red) retinas for fast (left) and slow (right) stimulus speeds are shown.

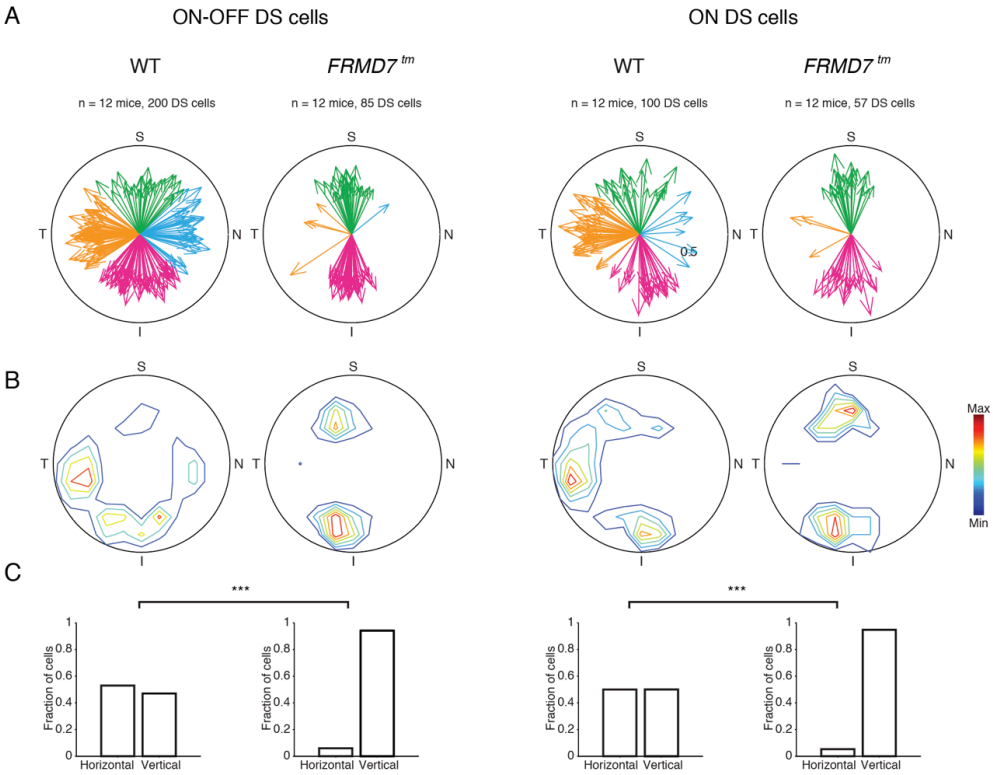

Figure 1.6 **Lack of horizontal direction selectivity in ON-OFF and ON cells in the retina of *FRMD7*^{tm} mice.** The figure shows data obtained with microelectrode arrays. In A-C, the left two columns show ON-OFF DS cells and the right two columns ON DS cells (Experimental Procedures). The radius of each circle corresponds to DSI=1. (**A**) Polar plots showing the preferred directions (direction of an arrow) and direction selectivity index (DSI, length of an arrow) of individual DS cells (DSI > 0.5, each recorded DS cell is represented by an arrow) in wild type and *FRMD7*^{tm} retinas. The color code designates the different directions according to Figure 1.2A. (**B**) Contour plots showing the density of DS cells with different DSIs and preferred directions. Red indicates maximal density. (**C**) The proportion of horizontal (nasal and temporal) and vertical (superior and inferior) motion preferring DS cells in wild type and *FRMD7*^{tm} retinas.

***FRMD7* is selectively expressed in starburst cells in the retina**

A transcriptional map of adult retinal cell types in mice suggested that *FRMD7* is enriched in adult starburst cells (Siegert et al., 2012). To test whether starburst cells specifically express *FRMD7* we performed double-label quantitative fluorescent in situ hybridization with antisense probes for *FRMD7* mRNA and *ChAT* mRNA at different developmental times (Figures 1.7A-B and 1.8A). *ChAT* is a specific marker for starburst cells. Both *FRMD7* and *ChAT* expression was first observed at P3. Once expressed, *FRMD7* and *ChAT* mRNAs were co-localized in the same cells, both in the ganglion cell layer and in the inner nuclear layer. We did not detect signals with control sense probe for *FRMD7* mRNA (Figures 1.7C and 1.8B).

We obtained further evidence that *FRMD7* expression is specific to starburst cells using immunohistochemistry: in *FRMD7*^{tm} mice, lacZ is inserted into the locus between exons 3 and 4. By performing antibody staining against LacZ and ChAT, we confirmed that the expression of LacZ is restricted to ChAT-positive cells in the retina (Figure 1.1F). Thus, in the developing and adult retina *FRMD7* is specifically expressed in starburst cells, the key cell type for establishing retinal direction selectivity.

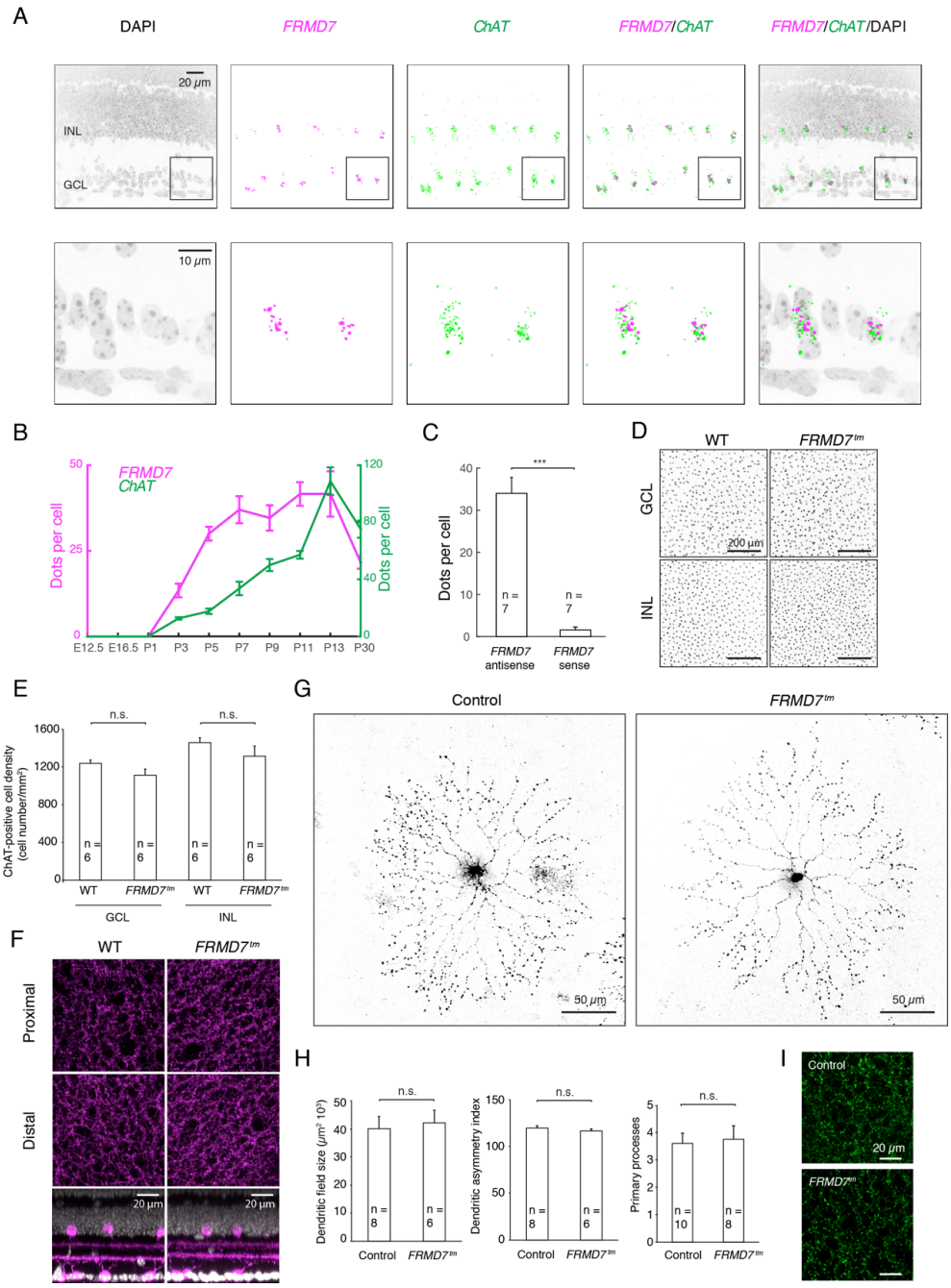

Figure 1.7 ***FRMD7* is specifically expressed in starburst cells in the mouse retina**. (**A**) Confocal images of a mouse retinal section stained by double-label quantitative fluorescence in situ hybridization using antisense probes for mouse *FRMD7* mRNA and mouse *ChAT* mRNA and DAPI. Bottom panels are magnifications of the insets in top panels. (**B**) Fluorescent dots per cell for *FRMD7* mRNA (magenta) and *ChAT* mRNA (green) at different developmental stages. (**C**) Quantification of hybridization signal for control sense probe. (**D**) Confocal images of the inner nuclear layer (INL) and ganglion cell layer (GCL) of wild type (WT, left) and *FRMD7*^{tm} (right) retinas stained with anti-ChAT antibody. (**E**) Quantification of the density of ChAT-positive cells from images as shown in C. (**F**) Top view of confocal images of wild type (left) and *FRMD7*^{tm} (right) retinas stained with anti-ChAT antibody at the proximal (top) and distal (middle) ChAT-positive strata in the inner plexiform layer.

Side view is shown at the bottom. (**G**) Confocal images of starburst cells sparsely labeled with GFP-expressing rabies virus in *ChAT-Cre* mice in control (left) and *FRMD7*^{tm} (right) background. (**H**) Dendritic field size (left), dendritic asymmetry index (middle) and the number of primary processes (right) of GFP-labeled starburst cells quantified from images as shown in G. Dendritic asymmetry index refers to the ratio of length of widest diameter to that of narrowest diameter of the dendritic arbor (%). (**I**) Confocal images of starburst cell processes at the proximal IPL sublayer labeled with synaptophysin-GFP expressing AAV in *ChAT-Cre* mice in control (top) and *FRMD7*^{tm} (bottom) background. Data are shown as mean ± SEM, n refers to the number of retinas in E and cells in C and H.

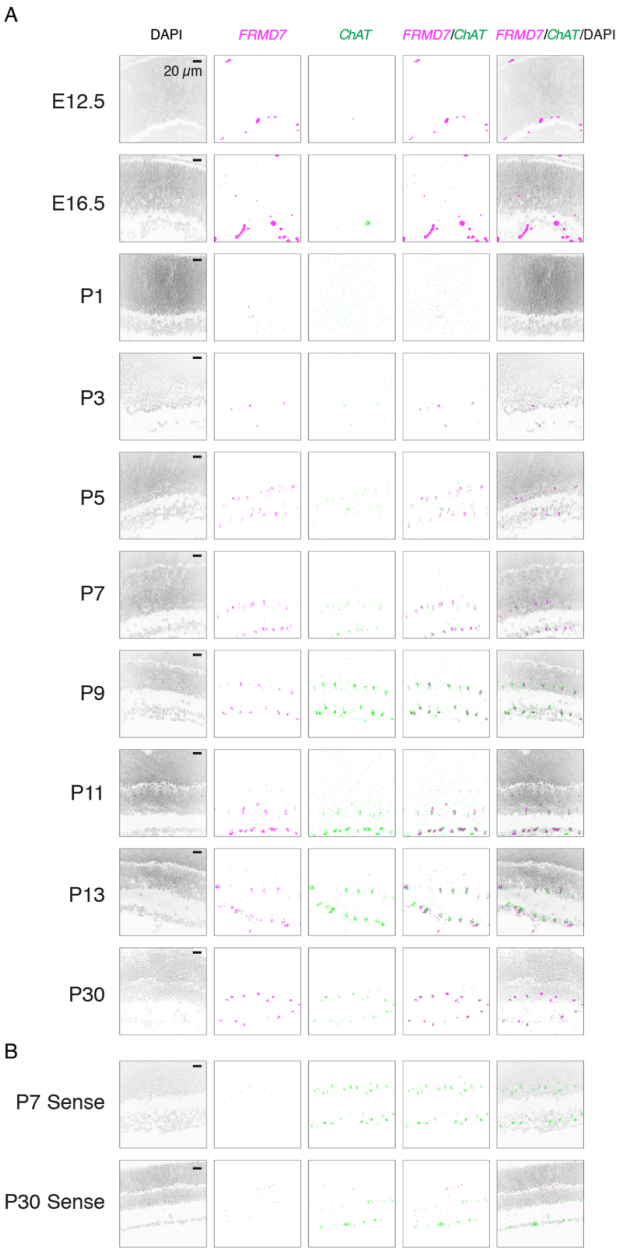

Figure 1.8 ***FRMD7* is specifically expressed in starburst cells in the mouse retina during development**. (**A**) Confocal images of mouse retinal sections stained by double-label fluorescence *in situ* hybridization using antisense probes for mouse *FRMD7* mRNA and mouse *ChAT* mRNA as well as DAPI at different developmental stages. Large dots at E12.5 and E16.5 are non-specific signals. (**B**) Confocal images of mouse retinal section stained using sense probe for mouse *FRMD7* mRNA and antisense probe for mouse *ChAT* mRNA as well as DAPI at P7 and P30.

Starburst cells in *FRMD7*^{tm} mice have normal morphology and stratification

We then tested whether the morphology of starburst cells is affected in *FRMD7*^{tm} mice. Starburst cell processes stratify into ON and OFF sublayers as early as P3, and bistratified ganglion cell dendrites follow these processes as early as P3-P4 (Stacy and Wong, 2003). ON-OFF DS cells receive inhibitory input from starburst cells already at P4 (Wei et al., 2011). The density of starburst cell somas, labeled with an antibody against ChAT, was similar in wild type and *FRMD7*^{tm} mice, both in the ganglion cell and in the inner plexiform layer (Figures 1.7D and 1.7E). Furthermore, starburst cells extended their processes to the same depths in the inner plexiform layer in wild type and *FRMD7*^{tm} mice (Figure 1.7F).

To examine the morphology of individual starburst cells, we sparsely labeled them in both control and *FRMD7*^{tm} mice. For this we used control Chat-Cre mice and *FRMD7*^{tm};Chat-Cre mice and infected the retina in vivo with conditional adeno-associated virus (AAV), expressing a mutant TVA receptor (TVA66T) (Miyamichi et al., 2013), and EnvA-coated SADΔG-GFP rabies virus. Confocal imaging of infected starburst cells revealed that the gross morphology of starburst cells, the size of the dendritic field, the symmetry of the processes, and the number of primary processes is similar in control and *FRMD7*^{tm} mice (Figures 1.7G and 1.7H).

To visualize the output synapses of starburst cells, we labeled starburst cells with a fluorescently tagged presynaptic marker in both control and *FRMD7*^{tm} mice. We infected the retinas of control Chat-Cre mice and *FRMD7*^{tm};Chat-Cre mice in vivo with AAV, expressing GFP-tagged synaptophysin in the presence of Cre recombinase. Confocal imaging of the infected starburst cells indicated no sign of abnormal density of output synapses in *FRMD7*^{tm} mice (Figure 1.7I).

Loss of the asymmetry of inhibitory inputs to horizontal DS cells

There could be several reasons for the lack of horizontal direction selectivity in the *FRMD7*^{tm} retinas. First, it is possible that horizontal DS cells are lost in *FRMD7*^{tm} mice. Alternatively, horizontal DS cells might remain present, but lose their horizontal direction-selective responses due to changes in the retinal circuit. To further examine the circuit mechanism underlying the lack of horizontal direction selectivity, we used Hoxd10-GFP mice, in which the three ON DS cell types and one temporal ON-OFF DS cell type, but no other retinal cell type, are genetically labeled (Dhande et al., 2013). All GFP-labeled ganglion cells in Hoxd10-GFP mice project to the nuclei of the accessory optic system and prefer slow motion. We crossed *FRMD7*^{tm} mice with Hoxd10-GFP mice and compared the labeled ganglion cell population with that of control Hoxd10-GFP mice. We found that the density of GFP-labeled cells was unchanged in *FRMD7*^{tm};Hoxd10-GFP mice compared to control mice (Figures 1.9B

and 1.9C), suggesting that cells with the genetic identity of wild type horizontal DS cells are not lost in the *FRMD7*^{tm} background.

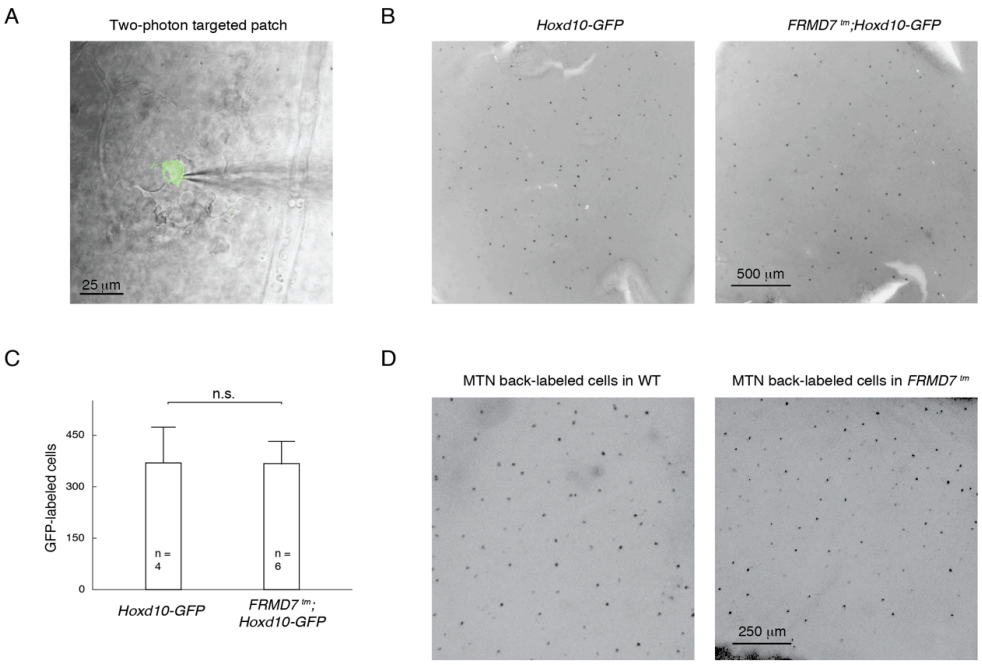

Figure 1.9 **Characterization of genetically labeled DS cells in the retina of FRMD7^{tm} mice.** (**A**) Overlay of infrared image (black-white) and two-photon microscope image (green) of the ganglion cell layer of Hoxd10-GFP mice during two-photon targeted patch-recording. GFP-labeled DS cell (green, center) is being recorded in cell-attached mode using a glass-pipette (dark shape on right side of green cell). (**B**) Epi-fluorescence microscope images of GFP-labeled cells (black) in fixed retinas after immunostaining in Hoxd10-GFP (left) and FRMD7^{tm};Hoxd10-GFP (right) mice. (**C**) Quantification of GFP-labeled cells counted in unstained, freshly dissected Hoxd10-GFP and FRMD7^{tm};Hoxd10-GFP retinas. Data points represent mean ± SEM, n refers to the number of retinas. (**D**) Epi-fluorescence microscope images of MTN back-labeled cells (black) in wild type (left) and FRMD7^{tm} (right), unstained, dissected retinas.

The lack of horizontal direction selectivity in *FRMD7*^{tm} retinas can be a sign either of no motion responses, or of responses which have similar magnitudes in all motion directions in ganglion cells that have the genetic identity of wild type horizontal DS cells. The third possibility, that horizontal motion preferring DS cells are converted to vertical motion preferring cells in *FRMD7*^{tm} retinas, is not likely since the number of vertical DS cells does not increase in *FRMD7*^{tm} retinas compared to wild type (Figure 1.5F). We performed two-photon targeted patch clamp recordings from GFP-labeled cells (Figure 1.9A) in isolated retinas of control Hoxd10- GFP mice and *FRMD7*^{tm};Hoxd10-GFP mice. We recorded spiking activity, as well as inhibitory and excitatory currents, while stimulating the retina with light spots, either flashed to the receptive field center, or moving across the retina in eight different directions (Figure 1.10).

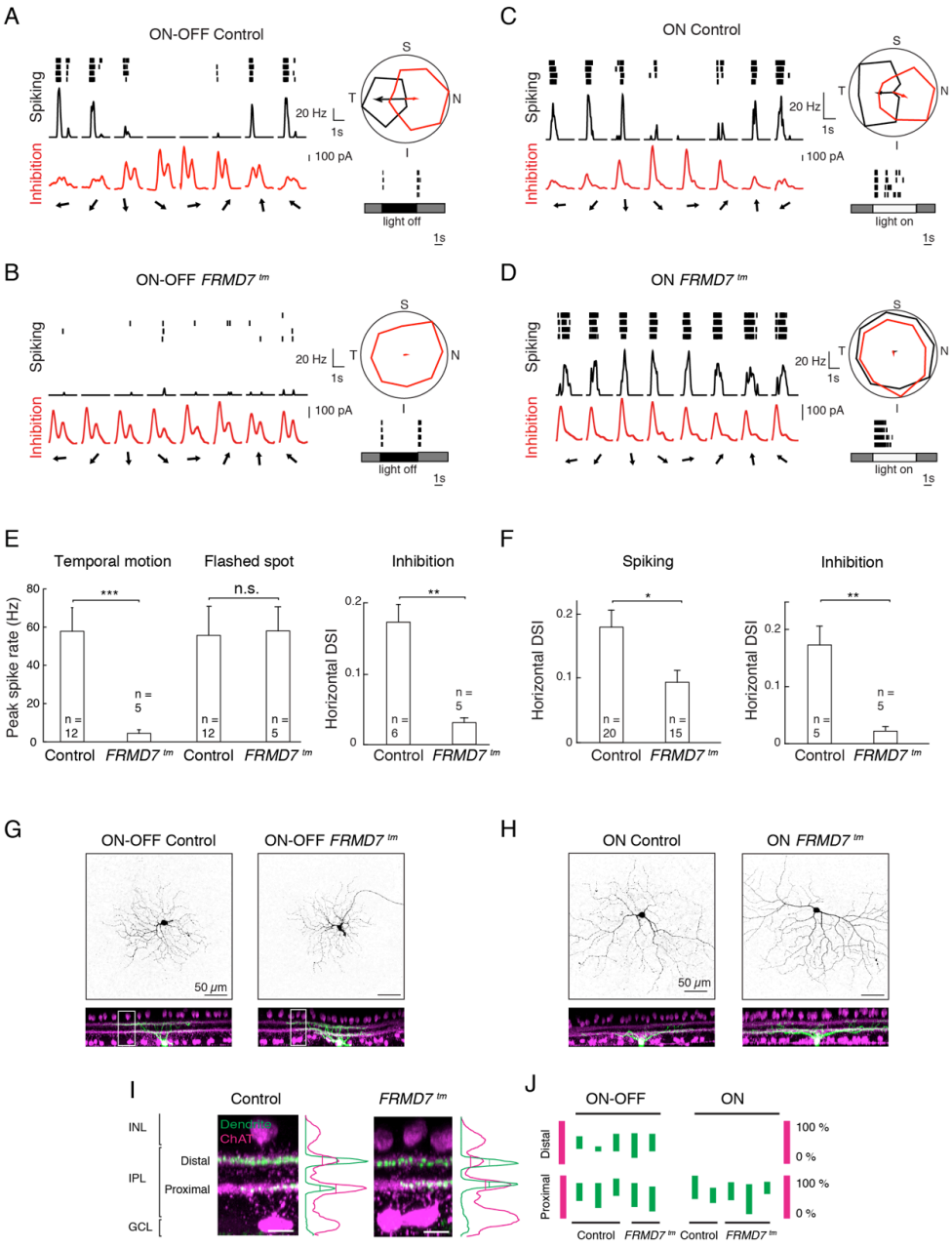

Figure 1.10 **Ganglion cells in FRMD7^{tm} retinas with genetic identity of horizontal motion preferring DS cells lack asymmetric inhibitory input**. (**A-D**) Examples of cell-attached and whole-cell voltage clamp recordings of GFP-labeled ON-OFF cells (A, B) and ON cells (C, D) in Hoxd10-GFP (Control; A, C) and FRMD7^{tm};Hoxd10-GFP (FRMD7^{tm}; B, D) retinas. On each panel A-D, left column, spike raster plot (black, top), spike rate (black, middle), and inhibition (red, bottom) in response to motion stimulus. Arrows indicate the direction of motion. Right column top, polar plot of normalized (to the maximum) spike number (black) and peak inhibition (red) during motion stimulation. The vector sum of spiking (black) and inhibitory (red) responses are shown by arrows. The vector sum for spikes was only plotted if the cell responded to stimulation (Experimental Procedures). Right column bottom, spike raster plot in response to a 300 µm flashed spot stimulus centered onto the cell body. Grey, white and dark areas indicate the stimulus contrast. Abbreviations: N, nasal; T, temporal; S, superior; I, inferior. (**E**) Quantification of spiking (left) and inhibitory (right) responses in

ON-OFF cells. (**F**) Quantification of spiking (left) and inhibitory (right) responses in ON cells. In E and F, data points represent mean ± SEM, n refers to the number of recorded cells. DSI, direction selectivity index (Experimental Procedures). (**G-H**) Confocal images of neurobiotin-filled, physiologically recorded ON-OFF (G) and ON (H) cells in top view (top) and side view (bottom). In side view, ChAT signals are shown (magenta) together with filled cells (green). (**I**) Magnification of insets in G. Fluorescence intensity profile for filled dendrite (green) and ChAT (magenta) along retinal depth is shown at the right of the images. Vertical lines in the profiles indicate the full-width at half maximum within the inner plexiform layer (IPL). INL, inner nuclear layer, GCL, ganglion cell layer. (**J**) Full-width at half maximum of filled dendrites is shown as bars (green) relative to that of ChAT-positive proximal and distal strata (magenta).

We first analyzed GFP-labeled ON-OFF cells since these cells belong to a single horizontal motion preferring DS cell type in control *Hoxd10-GFP* retinas. Targeting GFP-labeled ON-OFF cells in *FRMD7^{tm};Hoxd10-GFP* retinas, therefore, allows for identifying ganglion cells with the genetic identity of wild type horizontal DS cells in the *FRMD7^{tm}* background. In control mice, spike recordings performed in cell-attached mode confirmed that GFP-labeled ON-OFF cells respond to motion stimulation and preferred temporal motion (Figures 1.10A and 1.10E). In contrast, in *FRMD7^{tm};Hoxd10-GFP* mice, GFP-labeled ON-OFF cells lacked direction selectivity by not responding to motion stimulation in any direction (Figures 1.10B and 1.10E). However, the spike responses to flashed spots remained similar to those in control mice (Figure 1.10E). To understand the cause for the lack of direction selectivity, we recorded excitatory and inhibitory currents from GFP-labeled ON-OFF cells in whole-cell patch clamp mode after the spike recording from the same cells was finished. The excitatory inputs during motion stimulation remained similar to those in the control (Figure 1.11A). As far as inhibition, in control retinas, GFP-labeled ON-OFF cells received asymmetric inhibitory inputs: the inhibition was largest when the stimulus moved nasally, the null direction. In contrast, in *FRMD7^{tm};Hoxd10-GFP* mice, GFP-labeled non-DS ON-OFF cells received symmetric inhibitory inputs: the magnitude of inhibition was similar across all directions and its value ranged between the nasal and temporal values of the motion-evoked inhibition measured in control retinas (Figures 1.10A-1.10B, 1.10E, and 1.11E). These results suggest that the increased inhibition evoked by motion in the temporal direction abolishes motion-evoked spiking activity in GFP-labeled ON-OFF cells and, furthermore, that the decreased magnitude of inhibition in the nasal direction is enough to suppress spiking in this direction.

We then analyzed the spiking activity of GFP-labeled ON cells that were not vertically tuned. While these cells preferred horizontal motion in control mice (Figures 1.10C and 1.10F), they responded in all motion directions, indiscriminately, in *FRMD7^{tm};Hoxd10-GFP* mice (Figures 1.10D and 1.10F). Analysis of the inhibitory input to these cells revealed that the asymmetry of the inhibition was significantly reduced along the horizontal axis (Figure 1.10F). The magnitude of the inhibition lay between the nasal and temporal values of the motion-evoked

inhibition measured in control retinas, but closer to the temporal side (Figure 1.11E). The distribution of the motion-evoked inhibitory responses of ON cells was significantly different from that of ON-OFF cells in *FRMD7^{tm};Hoxd10-GFP retinas* (Figure 1.11F). Comparing the timing of spiking, inhibition and excitation evoked by motion stimulation in ON-OFF and ON cells revealed that, while inhibition and excitation temporally overlap in the non-spiking ON-OFF cells, the spiking in ON cells corresponded to the sustained phased of excitation, suggesting that the reduced inhibition is unable to block the effect of this part of the excitatory input (Figures 1.11A-C). Taken together, in both GFP-labeled ON-OFF and ON cells (which were not tuned vertically) of *FRMD7^{tm};Hoxd10-GFP* mice, the inhibitory input is symmetric. Depending on the magnitude and time course of excitation and inhibition, the symmetric inhibition either blocks spiking in all motion directions, as in ON-OFF cells, or leads to indiscriminate spiking in all motion directions, as found in ON cells.

To examine whether the dendrites of GFP-labeled non-DS ON-OFF and ON cells in *FRMD7^{tm};Hoxd10-GFP* mice were mistargeted, we filled the cells with neurobiotin during the recording and subsequently reconstructed their dendritic stratification. Similar to GFP-labeled cells in control Hoxd10-GFP mice, the dendrites of the recorded GFP-labeled non-DS ON-OFF and ON cells in retinas of *FRMD7^{tm} Hoxd10-GFP* mice co-stratified with either the proximal, or both the proximal and distal, ChAT-positive strata (Figures 1.10G-1.10J). This is consistent with a view that the symmetric inhibitory input to GFP-labeled non-DS cells is delivered by starburst cells in *FRMD7^{tm}* mice.

We encountered only a few GFP-labeled vertical motion preferring DS cells in *Hoxd10-GFP* retinas, both in the control and *FRMD7^{tm}* background. Therefore, we used a different approach to label vertical DS cells and compare their tuning in wild type and *FRMD7^{tm}* retinas. We injected a retrograde fluorescent tracer, cholera toxin subunit B Alexa 488 conjugate, into the MTN of wild type and *FRMD7^{tm}* mice. We performed two-photon targeted patch clamp recordings from Alexa 488-labeled cells in isolated retinas (Figures 1.12 and 1.9D). We recorded spiking activity in cell- attached mode and inhibitory currents in whole-cell mode. The MTN back-labeled ganglion cells in *FRMD7^{tm}* retinas had direction-selective spiking responses and inhibitory currents similar to the MTN back-labeled ganglion cells recorded in wild type retinas. The preferred direction of the spiking responses and inhibitory currents opposed each other and pointed either superior or inferior (Figure 1.12). Thus, in *FRMD7^{tm}* mice, vertical motion preferring ON DS cells are direction selective similar to wild type mice.

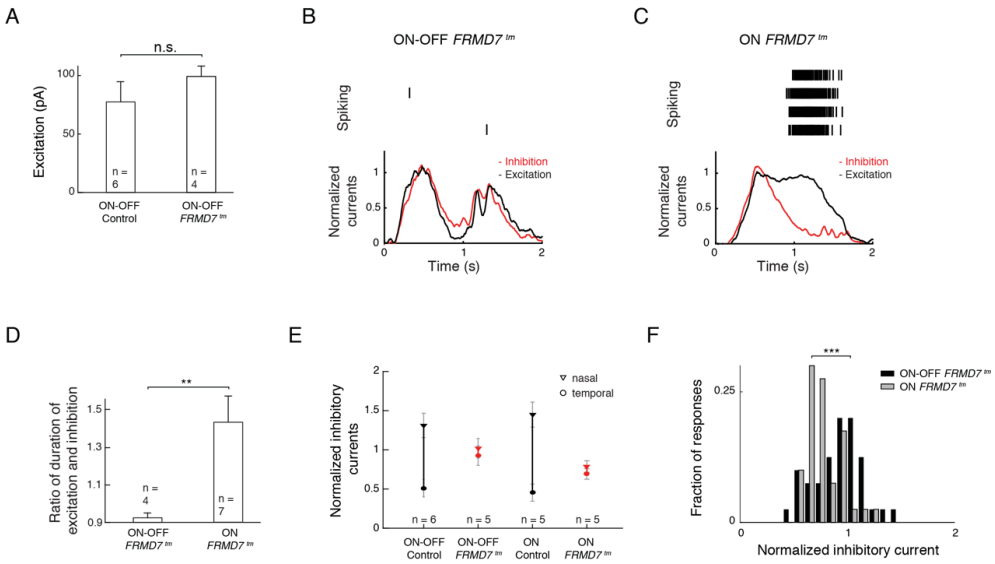

Figure 1.11 **Input currents to ganglion cells with genetic identity of horizontal motion preferring DS cells in FRMD7^{tm} retinas.** (**A**) Bar graph displaying amplitudes of excitatory input current to GFP-labeled ON-OFF cells in *Hoxd10*-GFP (Control) and FRMD7^{tm};*Hoxd10-GFP* (FRMD7^{tm}) retinas. Data points represent mean ± SEM, n refers to the number of cells. (**B, C**) Spike raster plot (top, black, four repetitions) and normalized excitation (bottom, black) and inhibition (bottom, red) recorded in ON-OFF (C) and ON (C) example cells of FRMD7^{tm};*Hoxd10-GFP* mice in response to motion. (**D**) Bar graph displaying the ratio of the duration of excitation and inhibition in ON-OFF cells and ON cells recorded in FRMD7^{tm};*Hoxd10-GFP* mice. Data from the eight motion directions were averaged. Data points represent mean ± SEM, n refers to the number of cells. (**E**) Magnitudes of inhibitory currents evoked by stimulation with temporal (circles) or nasal (triangles) motion recorded in ON-OFF cells and (non-vertically tuned) ON cells in *Hoxd10*-GFP (Control, black) and FRMD7^{tm};*Hoxd10-GFP* (FRMD7^{tm}, red) retinas. Values were normalized by the magnitude of inhibitory current evoked by a flashed-spot stimulus. Data points represent median values, temporal and nasal median values are connected with solid lines, ± SEM is shown by gray bars, n refers to the number of cells. (**F**) Histogram showing the distribution of inhibitory current magnitudes evoked by motion in eight directions recorded in ON-OFF cells (black, n=5) and (non-vertically tuned) ON cells (grey, n=5) in FRMD7^{tm};*Hoxd10-GFP* retinas. Values were normalized by the magnitude of inhibitory current evoked by a flashed spot stimulus.

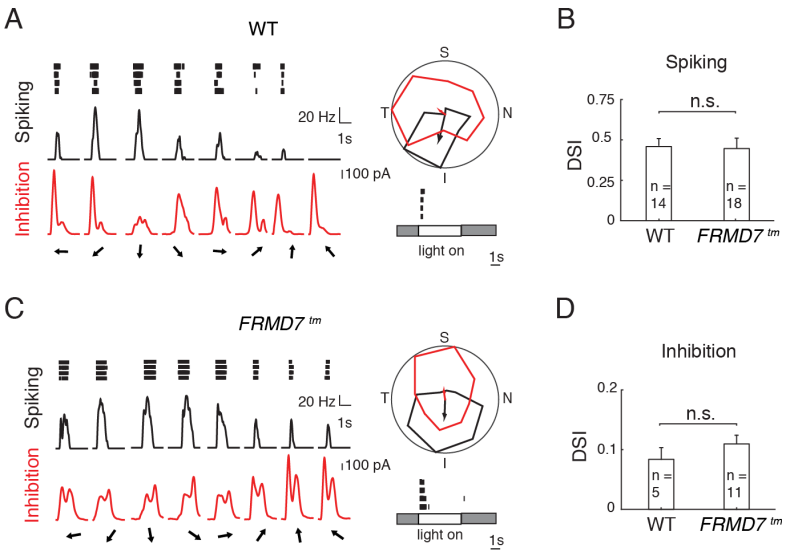

Figure 1.12 **Ganglion cells in *FRMD7*^{tm} retinas with genetic identity of horizontal motion-preferring DS cells lack asymmetric inhibitory input**. (**A–D**) Examples of cell-attached and whole-cell voltage-clamp recordings of GFP-labeled on-off cells (A and B) and on cells (C and D) in *Hoxd10-GFP* (Control; A and C) and *FRMD7*^{tm};*Hoxd10-GFP* (*FRMD7*^{tm}; B and D) retinas. (Left column) Spike raster plot (black, top), spike rate (black, middle), and inhibition (red, bottom) in response to motion stimulus are shown. Arrows indicate the direction of motion. (Right column top) Polar plot of normalized (to the maximum) spike number (black) and peak inhibition (red) during motion stimulation is shown. The vector sum of spiking (black) and inhibitory (red) responses are shown by arrows. The vector sum for spikes was only plotted if the cell responded to stimulation. (Right column bottom) Spike raster plot in response to a 300-mm flashed-spot stimulus centered onto the cell body is shown. Gray, white, and dark areas indicate the stimulus contrast. N, nasal; T, temporal; S, superior; I, inferior

Developmental time window in which *FRMD7* is required for establishing horizontal direction selectivity

We investigated whether *FRMD7* is required for the formation or for the maintenance of horizontal direction selectivity. The in situ hybridization experiments show that *FRMD7* expression is first detected at P3 (Figure 1.7B and 1.8). To narrow down the time window of *FRMD7* function, we tested whether the lack of horizontal direction selectivity in *FRMD7*^{tm} mice is already present at eye opening. We performed microelectrode array recordings from *FRMD7*^{tm} retinas just after eye opening, at P13-14. Whereas P13-14 wild type retinas had both vertical and horizontal direction-selective responses, P13-14 retinas of *FRMD7*^{tm} mice lacked horizontal direction-selective responses, suggesting that the mechanism leading to the loss of horizontal direction selectivity operates before eye opening (Figures 1.13). Thus, *FRMD7* is required for the formation of horizontal direction selectivity between birth and eye opening.

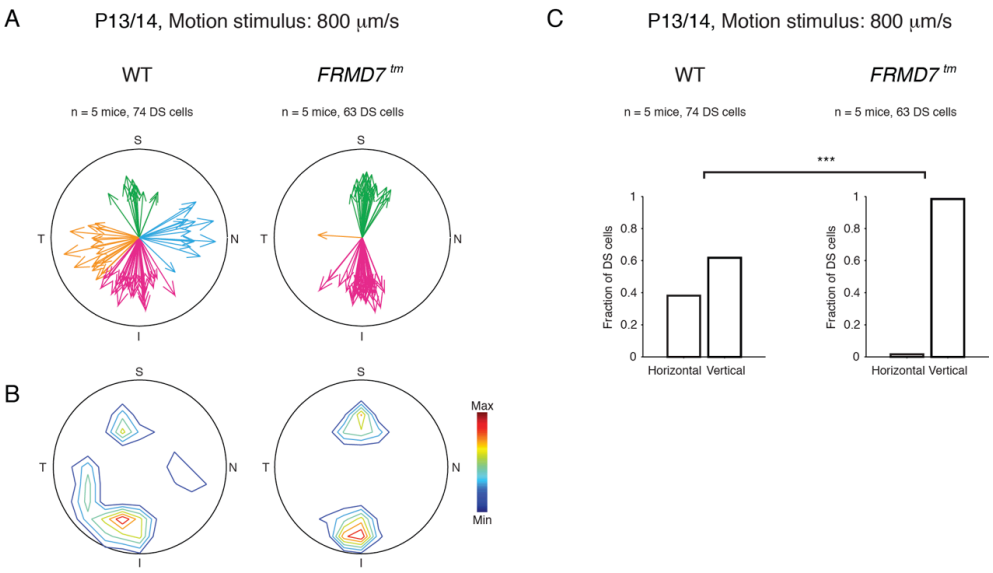

Figure 1.13 **Lack of horizontal direction selectivity in the retina of FRMD7^{tm} mice at P13/14.** (**A**) Polar plots showing the preferred directions (direction of arrow) and direction selectivity index (DSI, length of arrow) of individual DS cells (DSI > 0.5, each recorded DS cell is represented by an arrow) in wild type and FRMD7^{tm} retinas. The color code designates the different directions according to Figure 1A. (**B**) Contour plots showing the density of DS cells with different DSIs and preferred directions. Red indicates maximal density. (**C**) The proportion of horizontal (nasal and temporal) and vertical (superior and inferior) motion preferring DS cells in wild type and FRMD7^{tm} retinas.

The accessory optic system in *FRMD7*^{tm} mice

We asked whether those ON and ON-OFF DS cells in *FRMD7*^{tm} mice which lost their horizontal direction selectivity and which normally project their axons to the NOT/DTN nuclei of the accessory optic system keep their central target. We labeled the retino-recipient areas of *FRMD7*^{tm}*;Hoxd10-GFP* mice by injecting CTB conjugated to Alexa dye into one of the eyes. CTB is taken up by retinal ganglion cells and is transported to their axon terminals (Morin and Studholme, 2014). Subsequently, we examined the GFP-labeled axons in the retino-recipient brain areas labeled with CTB. We found that all nuclei of the accessory optic system, MTN and NOT/DTN, were innervated by GFP-positive axons, as in wild type mice (Figure 1.14).

Next, we mapped *FRMD7* and ChAT expression in the brain of P11 wild type mice using fluorescent in situ hybridization (Figure 1.15). The nuclei of the accessory optic system were labeled by injecting CTB conjugated to Alexa dye into both eyes at P8. ChAT probe was used as a landmark to identify motor nuclei. The nuclei of the accessory optic system, NOT/DTN and MTN, were negative for *FRMD7* mRNA expression. Furthermore, we did not detect *FRMD7* mRNA expression in other major visual areas, such as the lateral geniculate nucleus, primary visual cortex, and superior colliculus (data not shown). We found that *FRMD7* and

ChAT mRNAs were co-localized in the same cells in some motor nuclei: the abducens nucleus, which innervates the lateral rectus of extraocular muscles, and the oculomotor/trochlear nuclei, which innervate the other extraocular muscles (Figure 1.15). Expression of *FRMD7* mRNA was also observed in the vestibulo-ocular reflex pathway, in the vestibular nuclei (Thomas et al., 2011) (Figure 1.15). These results suggest that *FRMD7* is expressed in selected cell types in the brain.

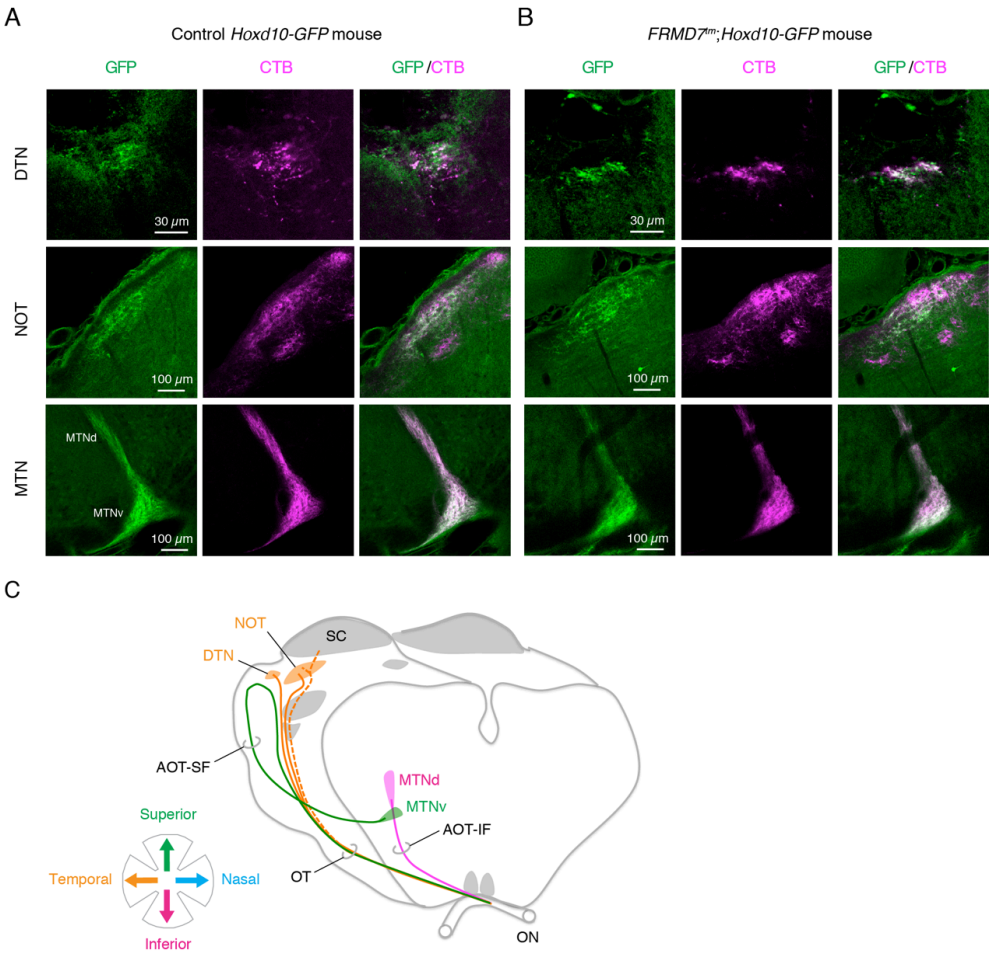

Figure 1.14 **Hoxd10-GFP labeled retinal ganglion cell axons innervate accessory optic nuclei in FRMD7^{tm} mice.** (A, B) Confocal images of DTN (top), NOT (middle), and MTN (bottom) innervated by GFP-labeled and cholera toxin subunit B-Alexa dye conjugate (CTB)-labeled retinal ganglion cell axons in control Hoxd10-GFP (A) and FRMD7^{tm};Hoxd10-GFP mice (B). (C) Schematic of central targets of Hox10-GFP labeled retinal ganglion cell axons. Axons and targets are color coded according to their directional tuning. Abbreviations: AOT-IF, inferior fasciculus of the accessory optic tract; AOT-SF, superior fasciculus of the accessory optic tract; MTNd, dorsal division of the MTN; MTNv, ventral division of the MTN; SC, superior colliculus; ON, optic nerve; OT, optic tract. Schematic adapted from (Dhande et al., 2013).

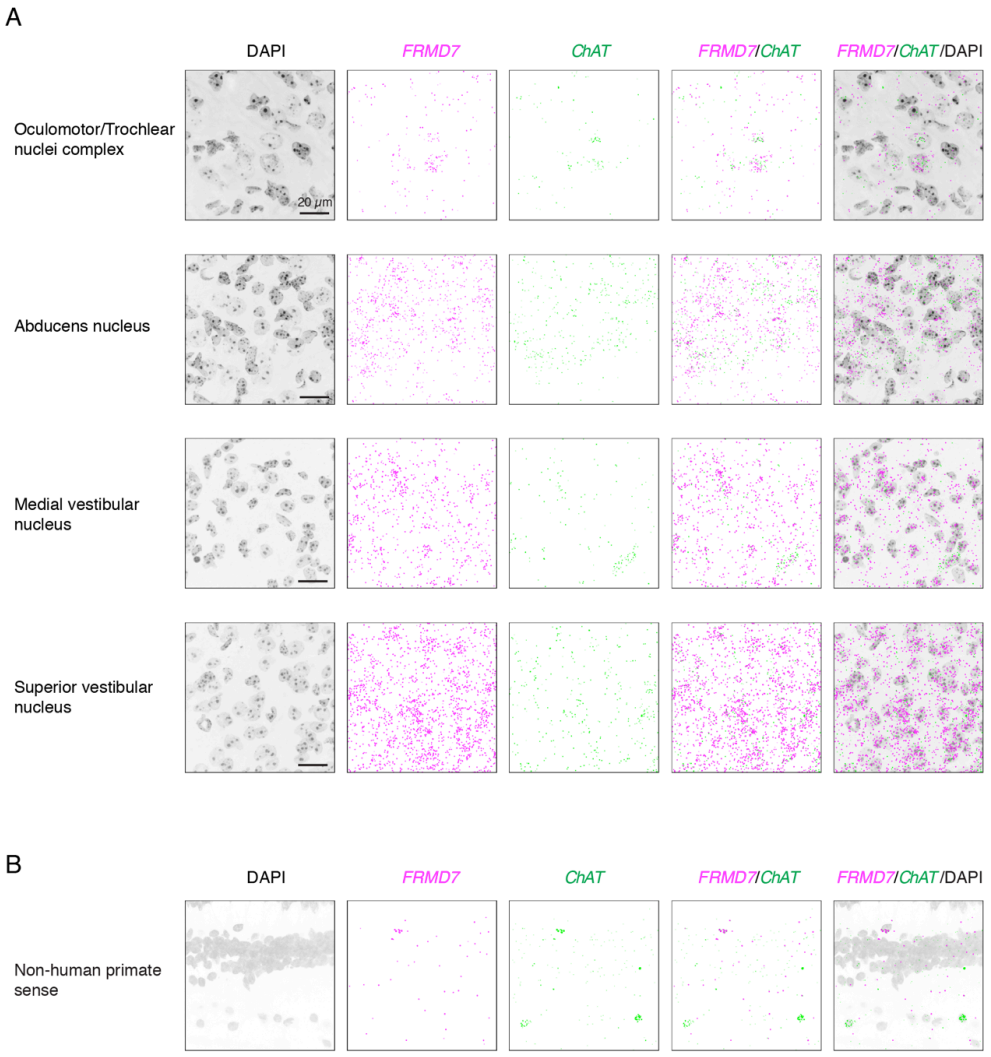

Figure 1.15 ***FRMD7* is expressed in motor nuclei, which innervate extraocular muscles, and vestibular nuclei.** (**A**) Confocal images of oculomotor/trochlear nuclei complex (top), abducens nucleus (second row), medial vestibular nucleus (third row) and superior vestibular nucleus (bottom) of P11 wild type mouse brain sections stained by double-label fluorescence *in situ* hybridization using antisense probes for *FRMD7* mRNA and *ChAT* mRNA as well as DAPI. (**B**) Confocal images of non-human primate retinal section stained using sense probe for non-human primate *FRMD7* mRNA and antisense probe for non-human primate *ChAT* mRNA as well as DAPI.

***FRMD7* is distributed symmetrically within starburst cell processes**

We examined where *FRMD7* is localized within starburst cells. We performed immunohistochemistry with anti-*FRMD7* and anti-ChAT antibodies on retinas at different developmental stages (P3, P5, and P7) and examined the stained retinas using confocal microscopy (Figure 1.16). In neonatal stages, *FRMD7* signals were present in the basal part of cell body and processes (Figures 1.16A and 1.16B). To quantify the degree of asymmetry in the distribution of the *FRMD7* signal within individual starburst cells, we determined the

angle of *FRMD7*- labeled primary processes at P5 in the wholemount retinas (Figure 1.16C). We found no sign of an asymmetric *FRMD7* localization, suggesting that the localization of *FRMD7* is not biased to specific starburst cell processes.

***FRMD7* is expressed in ChAT-expressing cells in the retina of non-human primates**

To determine whether *FRMD7* is expressed in ChAT-expressing cells in non-human primate retinas, we first performed immunohistochemistry with antibodies against ChAT in wholemount retinas (Figure 1.17A). Similar to the findings from mice, mosaics of ChAT-labeled cells were present in both the inner nuclear and ganglion cell layer of non-human primate retinas (Rodieck and Marshak, 1992). Moreover, as in mice, the ChAT antibody labeled two retinal strata in the inner plexiform layer (Figure 1.17A). We then performed fluorescent in situ hybridization with antisense and control sense probes for *FRMD7* mRNA and antisense probes for ChAT mRNA (Figures 1.17B and 1.15B). Almost all the ChAT-positive cells were also positive for *FRMD7*. Conversely, a substantial fraction (70%) of *FRMD7*-positive cells in both the ganglion cell layer and inner nuclear layer were ChAT-labeled (Figure 1.17C). We did not detect signals with control sense probe for *FRMD7* mRNA (Figure 1.15B). Thus, the mosaics of ChAT-labeled cells, and the ChAT-marked retinal strata, as well as the enrichment of *FRMD7* in ChAT-positive cells are conserved between mice and non-human primates.

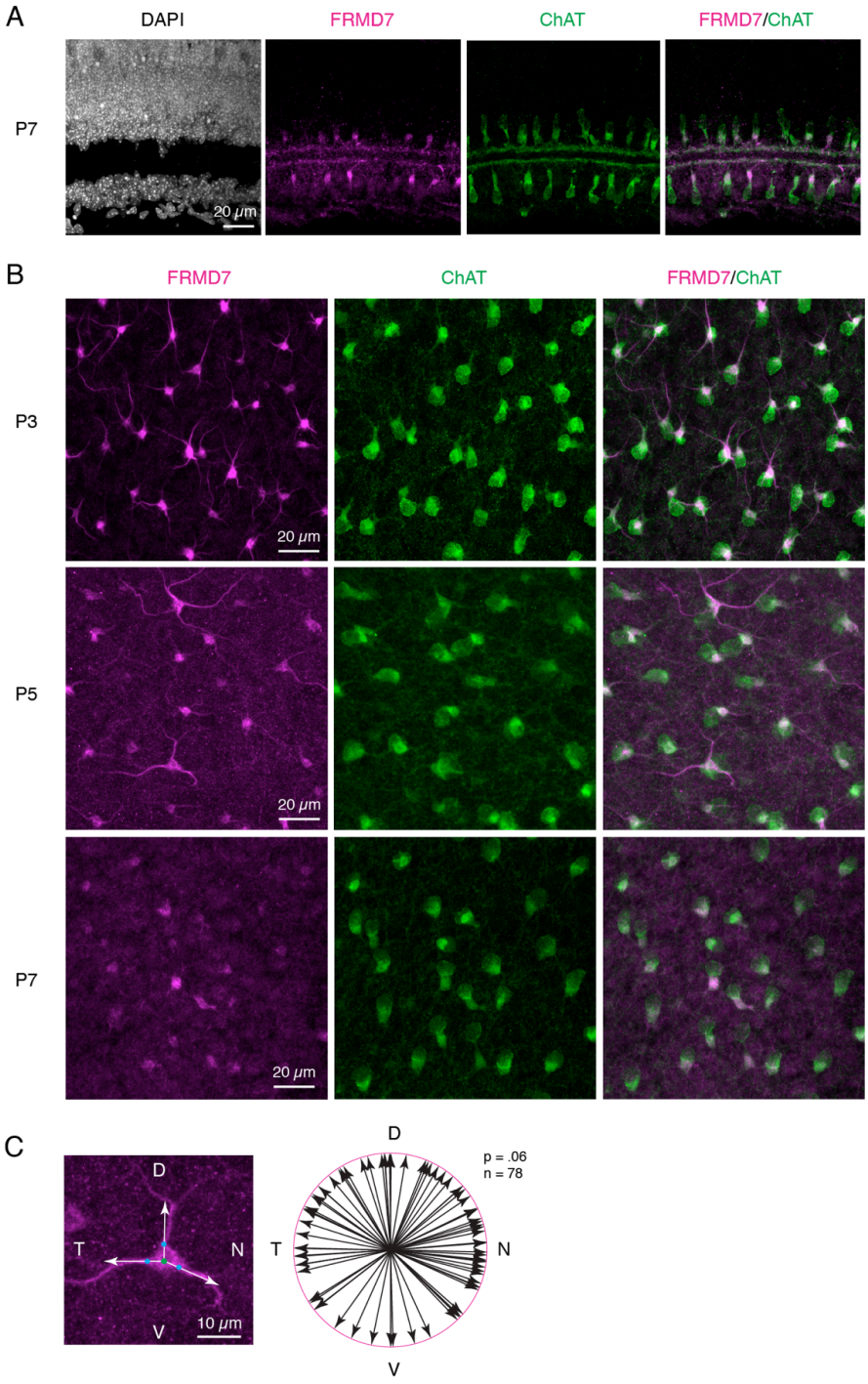

Figure 1.16 **FRMD7 is symmetrically localized within starburst amacrine cell processes.** (**A-B**) Confocal images of wild type retinas stained with antibody for ChAT (green) and FRMD7 (magenta) at different developmental time points (P3, P5, P7) in side view (A), and top view of z-stack of labeled cells in GCL (B). (**C**) Quantification of the subcellular distribution of FRMD7 within starburst cells. Left; The direction of FRMD7-labeled processes was defined by the angle of the vector, which points from the cell body center (green dot) to the exit point of the primary processes from cell body (cyan dots). Right; Distribution of the direction of FRMD7-labeled processes. Abbreviations: N, nasal; T, temporal; S, superior; I, inferior.

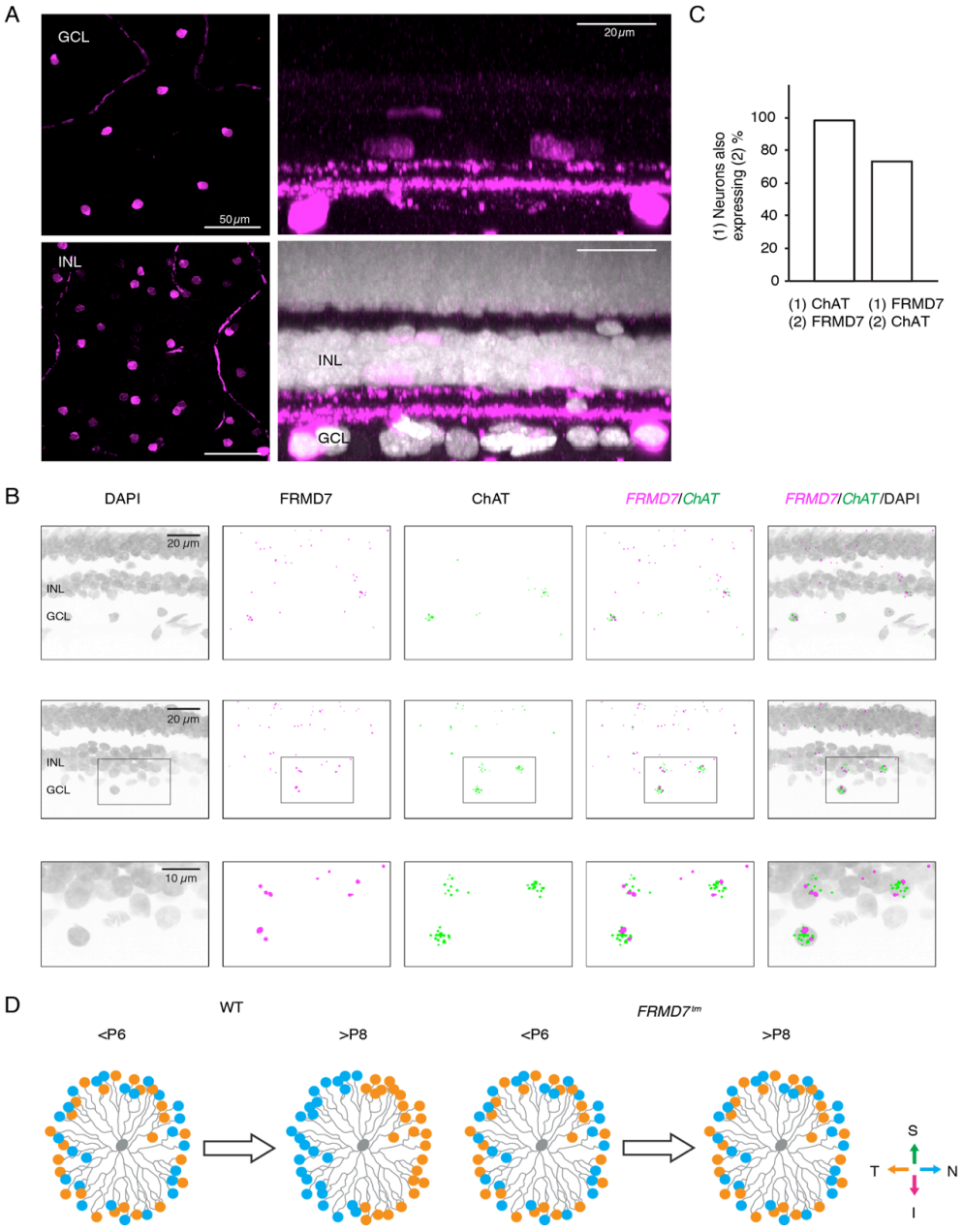

Figure 1.17 **FRMD7 is expressed in ChAT-labeled cells in the retina of non-human primates.** (**A**) Confocal images of wholemount non-human primate retinas stained with antibody for ChAT (magenta) and DAPI (white) in top view (left) and side view (right). (**B**) Confocal images of retinal sections stained by double-label fluorescence in situ hybridization using antisense probes for FRMD7 mRNA and ChAT mRNA as well as DAPI in non-human primate retinas. Two example regions (top and middle) and magnification of inset in middle panels (bottom) are shown. (**C**) Relationship between FRMD7 mRNA-expressing and ChAT mRNA-expressing cells. (**D**) Schematic of the development of horizontal asymmetric inhibitory outputs of a starburst cell (gray, center) in wild type (left) and FRMD7^{tm} mice (right) during the postnatal period before eye opening. Output inhibitory synapses are color-coded according to the preferred directions (colored arrows) of the postsynaptic DS cell partner. Symmetric inhibitory connectivity established during the first postnatal week is reorganized into asymmetric inhibitory connectivity during the second postnatal week in wild type mice (Wei et al., 2011; Yonehara et al., 2011) but not in FRMD7^{tm} mice.

Discussion

We found that *FRMD7*, a gene responsible for 70% of cases of idiopathic congenital nystagmus in humans, is required in the mouse retina to establish spatially asymmetric inhibitory inputs from starburst cells to DS cells along the horizontal axis, and is thus required for horizontal direction selectivity. The retinal expression of *FRMD7* is restricted to starburst cells in mice and enriched in ChAT-labeled cells in primates. Vertical direction selectivity was not dependent on *FRMD7*. Similarly to results in humans, the dysfunction of *FRMD7* in mice leads to the loss of the horizontal optokinetic reflex. These results establish *FRMD7* as a member of a previously unidentified molecular pathway that is necessary for the establishment of neuronal circuit asymmetries.

Circuit mechanism underlying the lack of horizontal direction selectivity in *FRMD7*^{tm} mouse retina

We suggest that the lack of horizontal direction selectivity in the retina of *FRMD7*^{tm} mice is due to the lack of asymmetric connectivity between starburst cells and ganglion cells with the genetic identity of wild type horizontal motion preferring DS cells. The following set of evidence supports this conclusion. First, *FRMD7* was only expressed in ChAT-labeled cells (Figures 1.7A, 1.7B, 1.8 and 1.17), and ChAT is a selective marker of starburst cells in mice (Ivanova et al., 2010). Second, we found symmetric inhibitory currents in GFP-labeled ON-OFF cells in the *FRMD7*^{tm} background in a mouse line in which, in the wild type background, all GFP-labeled ON-OFF cells are DS cells preferring horizontal motion (Figures 1.10). Third, vertical direction selectivity persists in *FRMD7*^{tm} retinas (Figures 1.5 and 1.12). The first and second points indicate that starburst cells are the defective circuit element. The third point favors the hypothesis that among the two key features determining asymmetric inhibition, namely the cardinal-direction- organized asymmetric connectivity between starburst cell and DS cell and the centrifugal- direction-organized asymmetric GABA release from starburst cell processes, it is the asymmetric connectivity between starburst cells and horizontal DS cells which is defective.

Potential role of *FRMD7* in establishing horizontal asymmetric connectivity

The results obtained are consistent with a role of *FRMD7* in the reorganization of the synaptic input from starburst cells to DS cells. During the development of wild type mice, by P6, in both ON-OFF and ON DS cells, first symmetric connections between starburst cells and DS cells are established. These symmetric connections are then reorganized to asymmetric connections before eye opening (Wei et al., 2011; Yonehara et al., 2011). Our findings

suggest that in *FRMD7*^{tm} mice this symmetric-to-asymmetric transition is defective along the horizontal axis (Figure 1.17D).

How could *FRMD7* contribute to the establishment of the selective connectivity between nasally or temporally pointing starburst cell processes and temporal or nasal motion preferring DS cells? To enable the correct matching of starburst cell process and DS cell type, it is likely that nasally and temporally pointing starburst cell processes are labeled by distinct molecules or combinations of molecules. This would require a sorting machinery in the soma which "knows" about the horizontal directions and sends different molecules to nasally and temporally pointing processes. Since it is widely documented that the retina has a number of molecules forming nasal-temporal gradients, such as ephrins and BMPs (McLaughlin et al., 2003; Sakuta et al., 2006; Shintani et al., 2004), it is likely that the "knowledge" of starburst cells about the opposing horizontal directions is learned from these gradients. Along the vertical axis a similar differential sorting mechanism may label superiorly and inferiorly pointing starburst cell processes. The findings that both nasal and temporal direction selectivity are abolished in *FRMD7*^{tm} mice (Figures 1.5 and 1.6), and that *FRMD7* protein was found symmetrically distributed in the processes of starburst cells (Figures 1.16B and 1.16C), suggest that *FRMD7* is not a marker for nasal or temporal processes. It is more likely that *FRMD7* is part of the molecular machinery that is either involved in sensing or sorting along the horizontal axis.

While it is an open question where and how *FRMD7* exerts its function in the starburst cell to establish asymmetric connectivity, the organization of the protein and the precise location of the mutations found in individuals with congenital nystagmus provide insights. The *FRMD7* gene encodes a member of the FERM domain family of proteins (Moleirinho et al., 2013). The FERM domain of *FRMD7* is located in the N-terminus and is thought to link *FRMD7* to the cell membrane. Next to the FERM domain is a 'FERM-adjacent domain', which in other FERM- containing proteins is thought to be subject to phosphorylation. Notably, the mutations causing congenital nystagmus in humans are concentrated in the FERM domain and a region around the FERM-adjacent domain (Thomas et al., 2011). The C-terminal part of *FRMD7* has no homology with other proteins. Other FERM-domain-containing proteins are involved in the signal transduction between the plasma membrane and the actin cytoskeleton (Moleirinho et al., 2013). Indeed, the *FRMD7* protein interacts with the Rho GDP-dissociation inhibitor alpha, the main regulator of Rho GDPases, which are key regulators of the reorganization of actin cytoskeleton (Pu et al., 2013). These findings raise the possibility that *FRMD7* also signals between the plasma membrane and the cytoskeleton.

Circuit mechanism underlying the lack of the horizontal optokinetic reflex in *FRMD7*^{tm} mice

We propose that the lack of horizontal direction selectivity in the retina contributes significantly to the lack of the horizontal optokinetic reflex in *FRMD7*^{tm} mice. The following evidence supports this conclusion. First, it has previously been shown that mice whose retinal direction selectivity has been abolished by the genetic ablation of starburst cells lose the optokinetic reflex (Yoshida et al., 2001). In that study, the genetic manipulation was done in the retina alone, without affecting any circuits in the brain. Second, it has been shown in cats that activity in the NOT/DTN complex, which processes horizontal direction selective input, is required selectively for the horizontal optokinetic reflex (Hoffmann and Fischer, 2001). Third, we found that the defective DS cells in *FRMD7*^{tm} mice project to their normal brain targets (Figure 1.14). Fourth, *FRMD7*^{tm} mice were able to produce spontaneous, large-amplitude horizontal eye motions (Figures 1.2F and 1.2G). Fifth, *FRMD7*^{tm} mice had normal vertical retinal direction selectivity (Figures 1.5 and 1.12) and showed a normal vertical optokinetic reflex (Figure 1.2E). Sixth, the optokinetic reflex was measured in head-fixed mice, limiting possible interactions with the vestibular system. Taken together, these results suggest that the lack of horizontal direction selectivity in the retina is sufficient to abolish the horizontal optokinetic reflex. However, as we detected *FRMD7* mRNA expression in the motor nuclei responsible for eye movements and in the vestibular nuclei (Figure 1.15), we cannot rule out contributions to the defective optokinetic response from motor and vestibular nuclei.

Circuit mechanism underlying the symptoms of *FRMD7* based idiopathic congenital nystagmus in humans

Can *FRMD7* dysfunction in starburst cells be a contributor to, or cause of, the lack of horizontal optokinetic reflex in *FRMD7*-based congenital nystagmus in humans? The following findings support this interpretation. First, the neuronal pathways controlling the optokinetic reflex are highly conserved across mammals. Although ON DS cells have not yet been recorded in primate retinas, ON direction-selective cells preferring the ipsiversive direction (i.e., left NOT/DTN is activated by the leftward motion and vice versa) have been recorded in primate NOT/DTN brain areas (Distler and Hoffmann, 2011; Hoffmann, 1989), which are the targets of horizontal ON DS cells in other animals (Dhande et al., 2013). Second, in adult non-human primate retinas, the same ChAT antibody, which in mice labels two mosaics of starburst cells and two retinal strata in the inner plexiform layer where the processes of starburst cells ramify, also labeled two mosaics of cells in the same nuclear layers and two retina strata in the inner plexiform layer (Rodieck and Marshak, 1992) (Figure 1.17A). Third, *FRMD7* was expressed in those non-human primate retinal cells which were

marked by ChAT (Figures 1.17B and 1.17C). Fourth, we show that human subjects with congenital nystagmus were able to produce voluntary, smooth-pursuit, horizontal eye movements (Figures 1.2K and 1.2L). Fifth, the vertical optokinetic reflex is still present in individuals with congenital nystagmus (Figure 1.2J). Taken together, this evidence indicates that in primates *FRMD7* is expressed in a retinal cell population that has the morphological and genetic attributes of starburst cells in mice, and that the motor system controlling horizontal eye movements in individuals with congenital nystagmus is functional. These findings are consistent with a hypothesis that the loss of the horizontal optokinetic reflex in humans is, at least partly, due to the loss of *FRMD7* function in starburst cells. Note that, in humans, *FRMD7* mRNA expression has also been observed in the brain regions involved in vestibulo-ocular reflex (Tarpey et al., 2006; Thomas et al., 2011). However, since the optokinetic reflex was assessed in head-fixed human subjects, a potential dysfunction in the vestibular system is unlikely to fully explain the loss of the horizontal optokinetic reflex. In contrast to individuals with *FRMD7*-based nystagmus, we did not observe spontaneous oscillatory eye movements (nystagmus) in *FRMD7*^{tm} mice. This lack can be explained in at least two different ways. First, it is possible that the presence of horizontal nystagmus is linked to the lack of the horizontal optokinetic reflex in humans. For example, an inhibitory interaction between the control circuits generating the optokinetic reflex and microsaccades in humans (Otero-Millan et al., 2011) may exist. When the horizontal optokinetic reflex is lost, inhibition decreases and horizontal microsaccades become larger and uncontrolled, appearing as horizontal nystagmus. As wild type mice are not confirmed to have microsaccades, the absence of this type of eye movement may explain why there is no nystagmus in *FRMD7*^{tm} mice. Alternatively, the two symptoms, nystagmus and the lack of the horizontal optokinetic reflex, could be caused by two independent circuit mechanisms. Indeed, the presence of horizontal nystagmus together with a normal optokinetic reflex in achromatopsia shows that the two symptoms can be independent of each other (Yee et al., 1981). It is possible that a defect in the connectivity between starburst cells and DS cells leads to the lack of the horizontal optokinetic reflex, and, independently, either a defect in the retinal fovea (Thomas et al., 2014), which is absent in mouse retinas, or a dysfunction of another brain circuit causes nystagmus.

Chapter 2 - Causal evidence for retina dependent and independent visual motion computations in mouse cortex

Hillier D, Fiscella M, ***Drinnenberg A****, Trenholm S, Rompani S, Raics Z, Katona G, Juettner J, Hierlemann A, Rozsa B & Roska B*

Summary

How neuronal computations in the sensory periphery contribute to computations in the cortex is not well understood. We examined this question in the context of visual-motion processing in the retina and primary visual cortex (V1) of mice. We disrupted retinal direction selectivity – either exclusively along the horizontal axis using FRMD7 mutants or along all directions by ablating starburst amacrine cells – and monitored neuronal activity in layer 2/3 of V1 during stimulation with visual motion. In control mice, we found an overrepresentation of cortical cells preferring posterior visual motion, the dominant motion direction an animal experiences when it moves forward. In mice with disrupted retinal direction selectivity, the overrepresentation of posterior-motion-preferring cortical cells disappeared, and their response at higher stimulus speeds was reduced. This work reveals the existence of two functionally distinct, sensory-periphery-dependent and -independent computations of visual motion in the cortex.

Introduction

Mammals process sensory stimuli in both the sensory periphery and the cortex. How computations in the sensory periphery contribute to computations in the cortex is not well understood. In the visual system, the primary visual cortex (V1) contains cells that respond preferentially to motion in a particular direction (Hubel and Wiesel, 1959). The neuronal circuits that are responsible for computing these direction-selective responses were thought to be within the cortex (Hubel and Wiesel, 1962; Priebe and Ferster, 2005) or in the thalamus (Stanley et al., 2012). However, direction-selective responses have been found in the retina of a number of species (Vaney et al., 2012; Wei and Feller, 2011), including mice. The majority of ON-OFF direction-selective retinal ganglion cells (ON-OFF DS cells) project to the lateral geniculate nucleus (LGN) (Huberman et al., 2009; Kay et al., 2011; Rivlin-Etzion et al., 2011), a part of the thalamus that receives input from the retina and relays it to V1. ON-OFF DS cells form 15% of retinal ganglion cells in mice (Kay et al., 2011). Four types of retinal

ON-OFF DS cells have been described, each providing the largest responses to motion in one of the four cardinal directions (Fiscella et al., 2012; Huberman et al., 2009; Kay et al., 2011; Rivlin-Etzion et al., 2011; Weng et al., 2005). Direction-selective responses have been measured in LGN cell bodies (Marshel et al., 2012; Piscopo et al., 2013) and axon terminals (Cruz-Martín et al., 2014; Sun et al., 2016), suggesting that ON-OFF DS cells could contribute to the computation of direction selectivity in the cortex. However, no causal link between retinal and cortical computations of direction selectivity has been established, leaving the questions unanswered whether and what form of cortical direction selectivity is linked to retinal direction selectivity.

To gain insight into these questions, we disrupted retinal direction selectivity *in vivo* using two independent genetic approaches, and recorded neuronal responses to visual motion in V1 (Figure 2.1A). In the first approach, we used *FRMD7* mutant mice (*FRMD7^{tm}* mice), in which horizontal direction selectivity in the retina is missing but vertical direction-selective responses persist (Yonehara et al., 2016), as a model system to study the contribution of retinal horizontal direction selectivity to cortical horizontal direction selectivity. In wild-type mice, *FRMD7* is specifically expressed in starburst amacrine cells, the interneuron type that provides asymmetric inhibition to direction-selective retinal ganglion cells. This asymmetric inhibition is necessary for direction selectivity. In *FRMD7^{tm}* mice, the loss of horizontal direction selectivity is caused by the transition from asymmetric to symmetric inhibitory input from starburst amacrine cells. *FRMD7* is not expressed in the LGN or V1 (Yonehara et al., 2016). In the second approach, we ablated starburst cells genetically. It has been shown before that ablating starburst amacrine cells in the retina leads to the loss of retinal direction selectivity (Yoshida et al., 2001).

In both *FRMD7^{tm}* and starburst-cell-ablated mice we found that a form of cortical direction selectivity is abolished when retinal direction selectivity is disrupted. This retina-dependent form of direction selectivity is tuned to higher stimulus speeds and is present along the horizontal cardinal axis in the posterior direction. The remaining cortical direction selectivity is distributed more evenly across different stimulus speeds and directions. Therefore, our results suggest the existence of two functionally distinct computations of visual motion in the cortex, one that originates in the retina and one that is computed in circuits downstream of the retina.

Results

In *FRMD7^{tm}* mice posterior-motion-preferring ON-OFF DS cells respond uniformly to motion in all directions

The lack of horizontal direction selectivity in the retina of *FRMD7^{tm}* mice could result from horizontal direction selective cells either spiking to all stimulus directions or not responding to motion in any direction (Yonehara et al., 2016). We determined which of these mechanisms acts in a type of ON-OFF DS cell that prefers a horizontal direction in wild type mice and projects to the LGN. We crossed *Drd4-GFP* mice, in which posterior-motion-preferring (motion direction refers to direction in the visual field) ON-OFF DS cells are labeled (Huberman et al., 2009), with *FRMD7^{tm}* mice. Using two-photon targeted patch clamp recordings in isolated retinas we recorded spiking activity from GFP-labeled cells in *Drd4-GFP* retinas (control) and from GFP-labeled cells in *Drd4-GFP* × *FRMD7^{tm}* retinas (Figures 2.1B-G and 2.2, *Drd4-GFP*, n = 12 cells from 3 mice, *Drd4-GFP* × *FRMD7^{tm}*, n = 16 cells from 3 mice).

GFP-labeled cells in control retinas showed direction-selective responses to visual stimuli moving in eight different directions at a speed of 40 visual degrees/s (°/s, Figures 2.1C and 2.2A). In contrast, GFP-labeled cells in *Drd4-GFP* × *FRMD7^{tm}* retinas were not direction selective (Figures 2.1D-F and 2.1B, Kolmogorov-Smirnov test, $p = 4.5 \times 10^{-6}$) and showed uniform responses to all directions of motion (Figures 2.1D, 2.1E and 2.2B, Hodges-Ajne test, $p = 0.44$). The uniform responses were mostly due to an increase in firing in non-preferred directions (Figures 2.1D, 2.1E and 2.2B). The distribution of firing rates across all stimulus directions was shifted to higher frequencies in *FRMD7^{tm}* mice (Figure 2.1G, Mann-Whitney U test, $p = 3.3 \times 10^{-9}$). Therefore, posterior-motion-preferring ON-OFF DS cells projecting to the LGN lose direction selectivity in *FRMD7^{tm}* retinas by responding uniformly to motion in all directions.

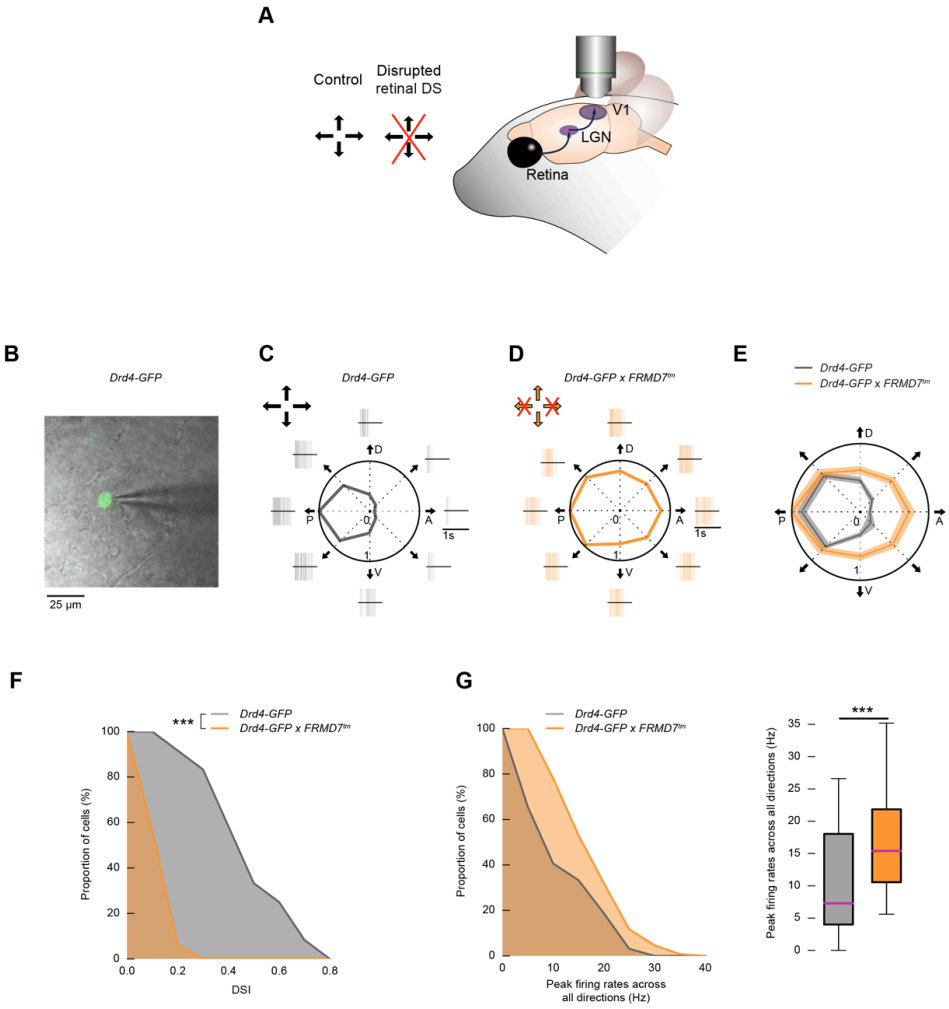

Figure 2.1 **FRMD7 mutation leads to spiking in all directions in posterior-direction-preferring retinal ON-OFF DS cells.** (**A**) Schematic of the experimental strategy throughout the paper. In the retina of control mice, ON-OFF DS cells prefer one of four cardinal directions (black arrows). The effect of disrupted retinal direction selectivity (red cross) is recorded in the retina, LGN, and V1. (B-G) Targeted patch clamp recordings in the retina. Control mice: Drd4-GFP, mutant mice: Drd4-GFP × FRMD7^{tm}. (**B**) A two-photon image of a GFP-labeled ganglion cell (green) in control retina is overlaid with the infrared image of the ganglion cell layer and a patch pipette (grey). (**C-D**) Example responses from GFP-labeled ganglion cells in control (C) and mutant (D) retinas to a stimulus moving in eight directions (black arrows). P denotes posterior, D dorsal, A anterior, V ventral motion direction in the visual field. Polar plots show the normalized peak firing rates (Experimental procedures) in each stimulus direction. Spike raster plots around polar plots show single trial responses. Arrows at the top left corner of C and D indicate the preferred directions of direction selective retinal ganglion cells. Crossed arrows: missing direction selectivity in that direction. (**E**) Polar plot of the normalized mean of the peak firing rates (Experimental procedures) in control and mutant retinas. The width of the grey and orange bands corresponds to 2 × s.e.m. (**F**) The proportion of GFP-labeled ganglion cells (indicated on the y-axis) with DSI larger than a specified value (indicated on the x-axis) in control and mutant retinas (complementary cumulative distribution of DSI values). (**G**) Left, complementary cumulative distribution of peak firing rates across all stimulus directions recorded from GFP-labeled ganglion cells in control and mutant retinas. Right, the boxplot representation of the distributions. Bottom and top whiskers: minimum and maximum; bottom and top of the rectangle: first and third quartiles; central line: median.

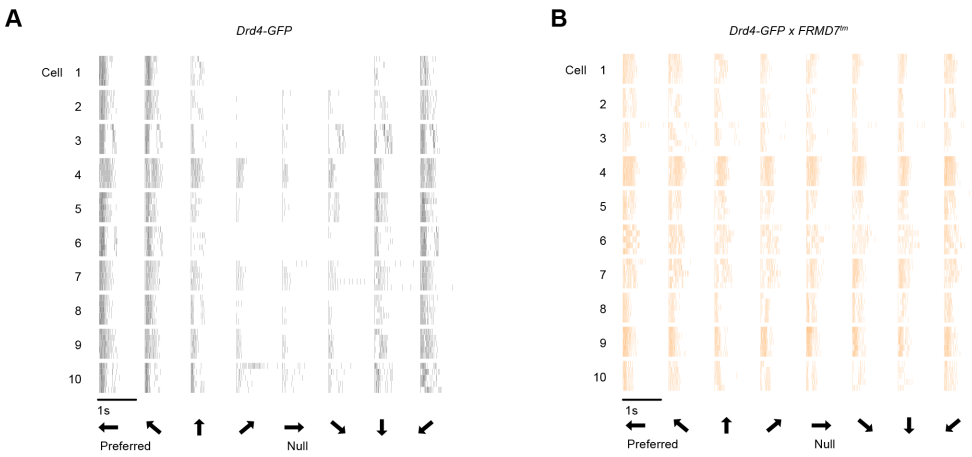

Figure 2.2 **FRMD7 mutation leads to spiking in all directions in posterior-motion-preferring retinal ON-OFF DS cells.** (**A-B**) Targeted patch clamp recordings in the retina. Control mice: Drd4-GFP, mutant mice: Drd4-GFP × FRMD7^{tm}. Example responses from GFP-labeled ganglion cells in control (A) and mutant (B) retinas to a stimulus moving in eight directions (black arrows at the bottom). Each block shows the response of a cell to motion in one of eight different directions. Each block has five rows representing five responses of the same cell to repeated stimulus presentations. Vertical lines mark spike occurrences.

In starburst-cell-ablated mice, ON-OFF DS cells respond uniformly to motion in all directions

We then abolished retinal direction selectivity acutely in adult mice. To selectively ablate starburst cells in adult mice, we crossed mice expressing Cre recombinase in starburst cells (*ChAT-Cre* (Ivanova et al., 2010)) with mice conditionally expressing the diphtheria toxin receptor (*LSL-DTR* (Buch et al., 2005)). Injecting diphtheria toxin (DT) into the eyes of *ChAT-Cre* × *LSL-DTR* mice led to the complete loss of starburst cells ('starburst-ablated mice'), seven days after injection, shown by immunohistochemistry using a ChAT antibody which selectively labels starburst cells (Figures 2.3 and 2.4). The number of retinal cells in other defined cell populations (that did not include starburst cells) did not change significantly (Figure 2.4). In all our experiments involving starburst ablation (in the retina, LGN, or cortex), we injected DT into both eyes and post-hoc stained both retinas with the ChAT antibody. We only considered those experiments for analysis in which we confirmed complete loss of starburst cells in both eyes.

We determined the effect of starburst ablation on the activity of a single, genetically defined type of ON-OFF DS cell by crossing *Hb9-GFP* mice, in which dorsal-motion-preferring ON-OFF DS cells are labeled (Trenholm et al., 2011), with *ChAT-Cre* and *LSL-DTR* mice. Using two-photon targeted patch clamp recordings in isolated retinas, we recorded spiking activity from GFP-labeled cells in DT-injected *Hb9-GFP* retinas (control) and from GFP-labeled cells in *Hb9-GFP* starburst-ablated retinas (Figures 2.5A-F, *Hb9-GFP*, n = 18 cells from 5 mice,

Hb9-GFP starburst-ablated, n = 19 cells from 5 mice). GFP-labeled cells in control retinas showed direction-selective responses to visual stimuli moving at 40 °/s (Figures 2.5B and 2.6A). In contrast, GFP-labeled cells in starburst-ablated retinas were not direction selective at this speed, where direction-selective responses in *Hb9-GFP* mice are known to depend on starburst inhibition (Trenholm et al., 2011) (Figures 2.5C-E and 2.6B, Kolmogorov-Smirnov test, $p = 2.2 \times 10^{-8}$). GFP-labeled cells in starburst-ablated retinas showed uniform responses to all directions of motion (Figures 2.5C, 2.5D and 2.6B, Hodges-Ajne test, $p = 0.94$). The uniform responses were mostly due to an increase in firing in non-preferred directions (Figures 2.5C, 2.5D and 2.6B). The distribution of firing rates across all stimulus directions was shifted to higher frequencies in starburst-ablated mice (Figure 2.5F, Mann-Whitney U test, $p = 1.8 \times 10^{-1}$).

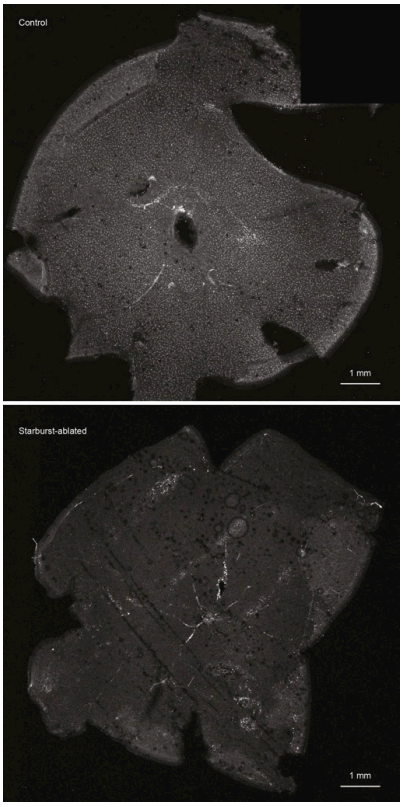

Figure 2.3 **ChAT staining labels starburst cells in control (top) and in starburst-ablated (bottom) whole-mount mouse retina**. The white dots in starburst-ablated retina are fluorescent aggregates and not cell bodies. No cell bodies are present in starburst-ablated retinas.

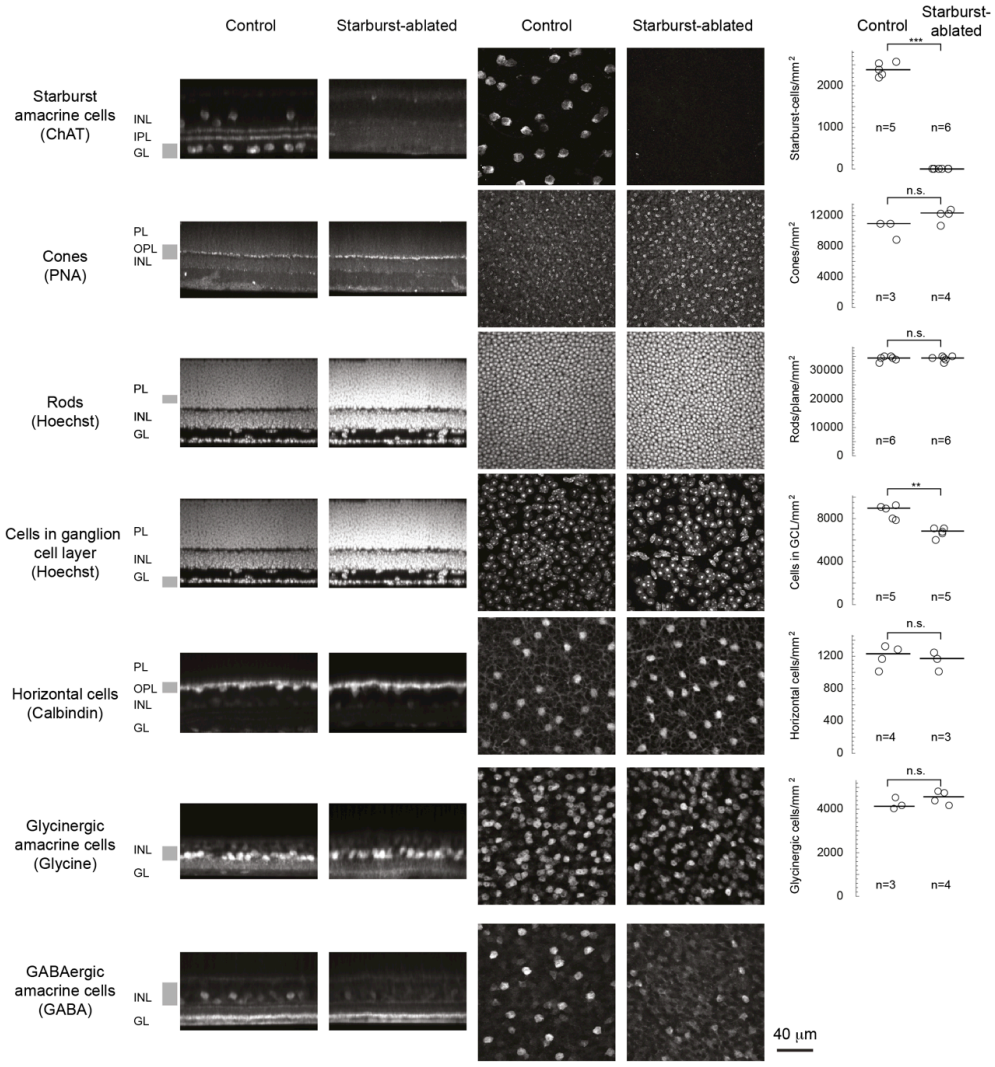

Figure 2.4**. DT injection to the eye selectively ablates starburst cells but leaves other cell populations intact.** The number of retinal cells of a given type or class in control and starburst-ablated retinas. Left, retinal section; middle, top view from confocal projection at the levels marked left to the retinal section by the grey bar; right, quantification. "n" refers to the number of retinas. Starburst cells are GABAergic cells; half of the starburst cells have cell bodies in the ganglion cell layer, which explains the reduction in the number of cell bodies in that layer. Due to the large number of faintly stained GABA cells, this population was not quantified. Note that a brightly labeled subset of GABAergic cells disappeared in the starburst-ablated retina. PL, photoreceptor layer; OPL, outer plexiform layer; INL, inner nuclear layer; GL, ganglion cell layer.

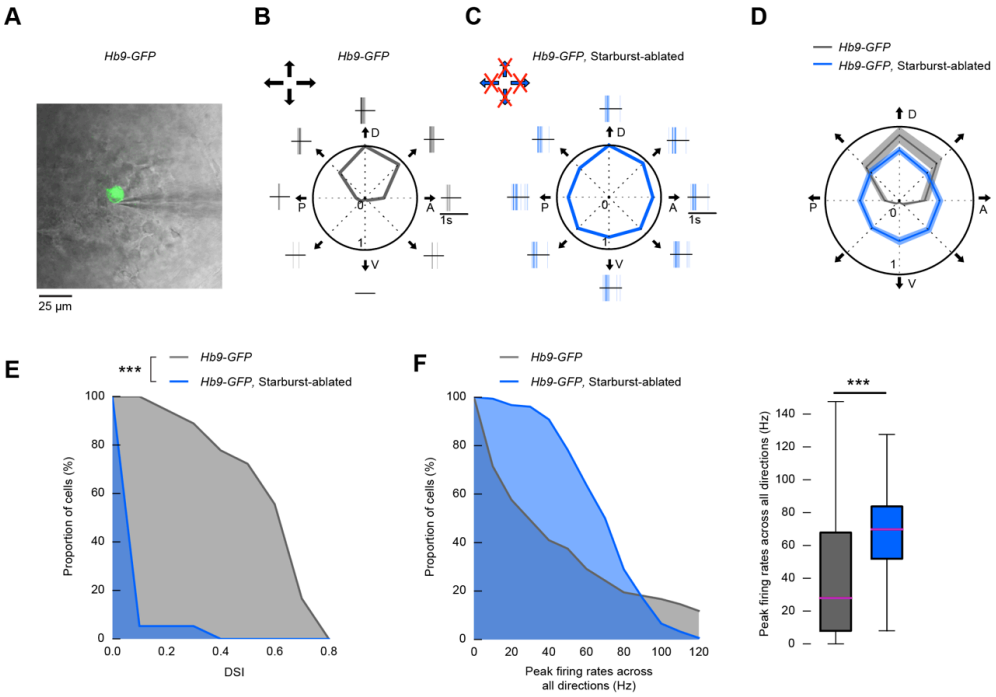

Figure 2.5 **Starburst cell ablation leads to spiking in all directions in dorsal-direction-preferring retinal ON-OFF DS cells**. (A-F) Control mice: Hb9-GFP injected with DT, starburst-ablated mice: Hb9-GFP × ChAT-Cre × LSL-DTR injected with DT. (**A**) A two-photon image of a GFP-labeled ganglion cell (green) in control retina is overlaid with the infrared image of the ganglion cell layer and a patch pipette (grey). (**B-C**) Example responses from GFP-labeled ganglion cells in control (B) and starburst-ablated (C) retinas to a stimulus moving in eight directions (black arrows). P denotes posterior, D dorsal, A anterior, V ventral motion direction in the visual field. Polar plots show the normalized peak firing rates in each stimulus direction. Spike raster plots around polar plots show single trial responses. Arrows at the top left corner of (B) and (C) indicate the preferred directions of direction selective retinal ganglion cells. Crossed arrows: missing direction selectivity in that direction. (**D**) Polar plot of the normalized mean of the peak firing rates of all the recorded cells in control and starburst-ablated retinas. The width of the grey and blue bands corresponds to 2 × s.e.m. (**E**) Complementary cumulative distributions of DSI values of recorded GFP-labeled ganglion cells in control and starburst-ablated retinas. (**F**) Left, complementary cumulative distributions of peak firing rates across all stimulus directions recorded from GFP-labeled ganglion cells in control and starburst-ablated retinas. Right, the boxplot representation of the distributions. Bottom and top whiskers: minimum and maximum; bottom and top of the rectangle: first and third quartiles; central line: median.

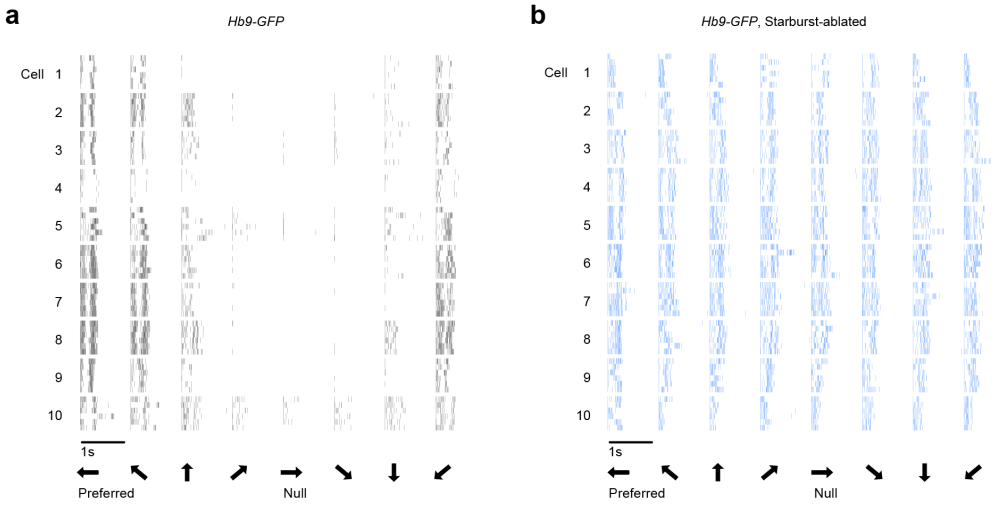

Figure 2.6 **Starburst cell ablation leads to spiking in all directions in dorsal-motion-preferring retinal ON-OFF DS cells**. (**A-B**) Targeted patch clamp recordings in the retina. Control mice: Hb9-GFP injected with DT, starburst-ablated mice: Hb9-GFP × ChAT-Cre × LSL-DTR injected with DT. Example responses from GFP-labeled ganglion cells in control (A) and starburst-ablated (B) retinas to the stimulus moving in eight directions (black arrows at the bottom). Each block shows the response of a cell to motion in one of eight different directions. Each block has five rows representing five responses of the same cell to repeated stimulus presentations. Vertical lines mark spike occurrences.

We then tested the effect of starburst cell ablation on the visual-motion-evoked spiking activity of retinal ganglion cells at the population level in isolated retinas using high-density microelectrode arrays (Müller et al., 2015a) (Figure 2.7, control, n = 1008 cells from 5 mice, starburst-ablated, n = 1199 cells from 5 mice). Wild type mice in which DT was injected into both eyes served as control here and in all subsequent experiments in retina and cortex involving starburst-ablation. Starburst cell ablation resulted in a 93% decrease in direction-selective spiking responses in the retina of *ChAT-Cre* × *LSL-DTR* mice (Figure 2.7E, Fisher's exact test, $p = 1.1 \times 10^{-12}$, control, 5.37%, starburst-ablated, 0.40% direction-selective responses at direction selectivity index (DSI) > 0.5). ON-OFF ganglion cells in starburst-ablated retinas responded to motion, but the responses were uniform in all directions (Figures 2.7C and 2.7D, Hodges-Ajne test, p = 0.16). The distribution of firing rates of the entire recorded ganglion cell population in response to motion across all eight directions in starburst-ablated retinas was shifted slightly, but significantly, to higher frequencies than in control retinas (Figure 2.7F, Mann-Whitney U test, $p = 8.0 \times 10^{-53}$). The firing rates in uninjected (n = 1074 cells from 5 mice) and DT-injected wild type mice were similar (Figure 2.7G, Mann-Whitney U test, p = 0.075). Starburst-ablation did not affect the proportion of ON-OFF cells (Fisher's exact test, p = 0.67, control, 33.0%, starburst-ablated, 33.7% of ON-OFF responses at ON-OFF index (OOI) < 0.3) or the proportion of orientation-selective cells

(Fisher's exact test, p = 0.89, control, 4.4%, starburst-ablated, 4.3% orientation-selective responses at orientation selectivity index (OSI) > 0.2 and DSI < 0.2).

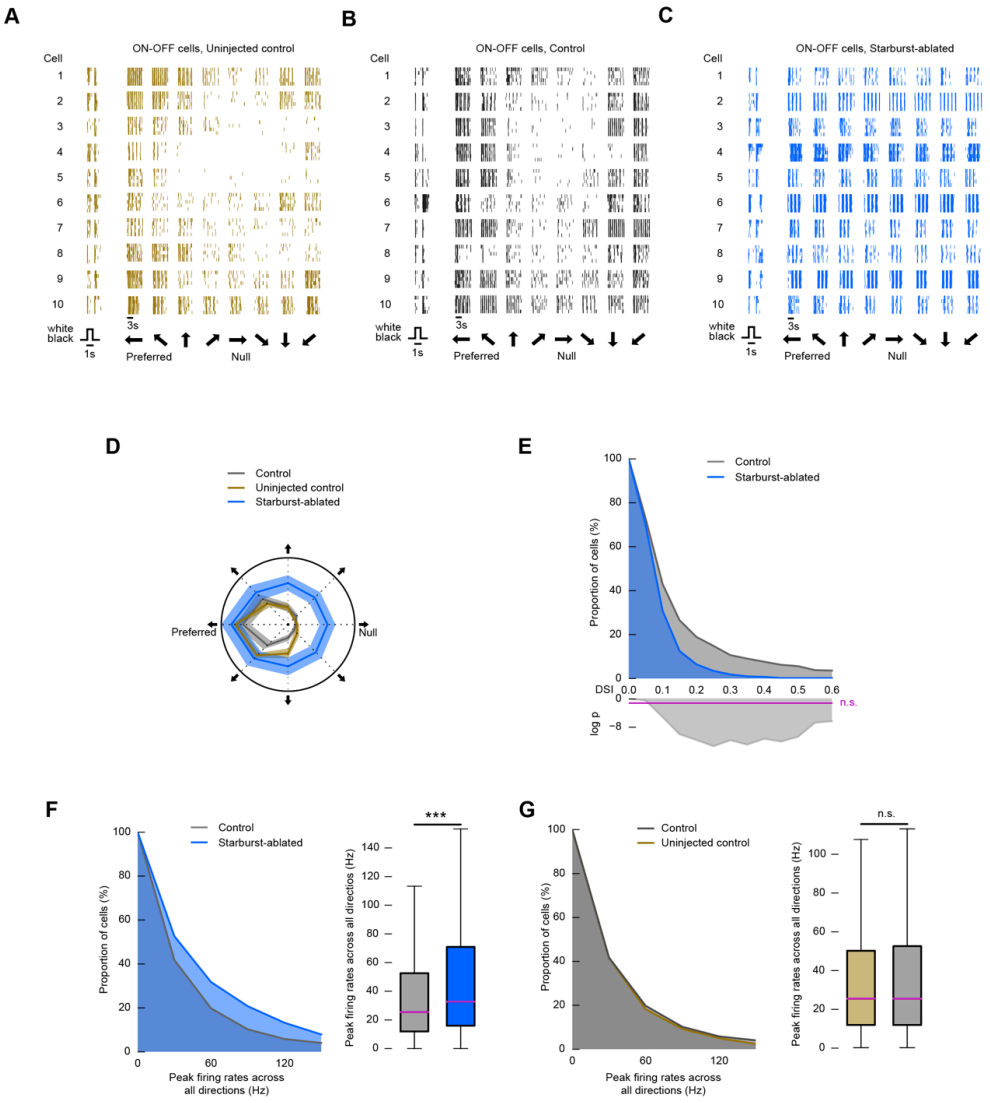

Figure 2.7 **Direction selectivity is largely reduced in starburst-ablated retinas.** (A-G) Microelectrode array recordings of the retina. Uninjected control mice: wild type, control mice: wild type injected with DT, starburst-ablated mice: ChAT-Cre × LSL-DTR injected with DT. (**A-C**) Example responses from ten ON-OFF ganglion cells in uninjected control (A), control (B), and mutant (C) retinas to a flashed positive-contrast stimulus (timing is shown at the bottom) and a stimulus moving in eight directions (black thick arrows at the bottom). During motion stimulation, each block shows the response of a cell to motion in one of eight different directions. Each block has five rows representing five responses of the same cell to repeated stimulus presentations. Vertical lines mark spike occurrences. (**D**) Polar plot of the normalized mean of the peak firing rates of the recorded cells (A-C) in uninjected control, control, and mutant retinas. The width of the grey, blue and brown bands corresponds to 2 × s.e.m. (**E**) Top, the complementary cumulative distribution of DSI values of recorded ganglion cells in control and starburst-ablated mice. Bottom, the logarithm of p values comparing the pairs of conditions using Fisher's exact test. Values above the magenta line are non-significant. (**F**) Left, complementary cumulative distributions of peak firing rates across all stimulus directions in control and starburst-ablated retinas. Right, the boxplot representation of the distributions.

Bottom and top whiskers: minimum and maximum; bottom and top of the rectangle: first and third quartiles; central line: median. (**G**) Left, complementary cumulative distributions of peak firing rates across all stimulus directions in uninjected control and control retinas. Right, the boxplot representation of the distributions.

The starburst ablation experiments described so far were performed *ex vivo* in isolated retinas. To assess how the activity of retinal ganglion cells is affected by starburst ablation *in vivo*, we injected an AAV expressing GCaMP6s into the eyes of control and starburst-ablated mice (*ChAT-Cre* × *LSL-DTR* + DT). We then imaged (Figures 2.8A and 2.8B) the axon terminals of GCaMP6s-expressing ganglion cells in the outer shell region of the LGN (control, n = 73 responding terminals from 2 mice, starburst-ablated, n = 132 responding terminals from 3 mice). In control mice, axon terminals fell into three groups with qualitatively different responses. The first group had direction-selective responses with direction tuning along the cardinal directions. The second group had orientation-selective responses, mostly vertically oriented. The third group had no direction or orientation preference. In starburst-ablated mice we found no direction-selective axon terminals (Figure 2.8C), and the distribution of DSIs shifted significantly to lower values (Figure 2.8D, Fisher's exact test, $p = 8.1 \times 10^{-8}$, control, 17.8%, starburst-ablated, 0.0% direction-selective axon terminals, at DSI > 0.5), indicating a decrease in direction selectivity. Similar to the *ex vivo* retinal recordings, the peak responses of ganglion cell axon terminals in starburst-ablated mice were slightly, but significantly, higher than those in control mice (Figure 2.8E, Mann-Whitney U test, $p = 1.0 \times 10^{-6}$). Consistent with the lack of change in the proportion of retinal orientation-selective responses *ex vivo*, the proportion of orientation-selective responses *in vivo* was also similar (Fisher's exact test, p = 0.31, control, 39.7%, starburst-ablated, 47.7% orientation-selective responses in axon terminals, at OSI > 0.2 and DSI < 0.2). The response amplitudes of vertical orientation-selective axon terminals were similar in control and starburst-ablated mice (Figure 2.8F, Mann-Whitney U test, p = 0.1), suggesting that the activity of this ganglion cell type (Nath and Schwartz, 2016; Venkataramani and Taylor, 2010) is unaffected by starburst ablation. We found an increase in the proportion of non-selective terminals (Fisher's exact test, p = 0.0016, control, 4.1%, starburst-ablated, 19.7%, at OSI < 0.2 and DSI < 0.2), which is consistent with ON-OFF DS cells being direction non-selective in starburst-ablated mice. The large increase in the proportion of non-selective terminals is likely due to the high density of ON-OFF DS cell axon terminals in the outer shell region (Cruz-Martín et al., 2014) of the LGN where we performed imaging. These results show that starburst cell ablation affected the activity of direction-selective retinal ganglion cells similarly *in vivo* and *ex vivo*.

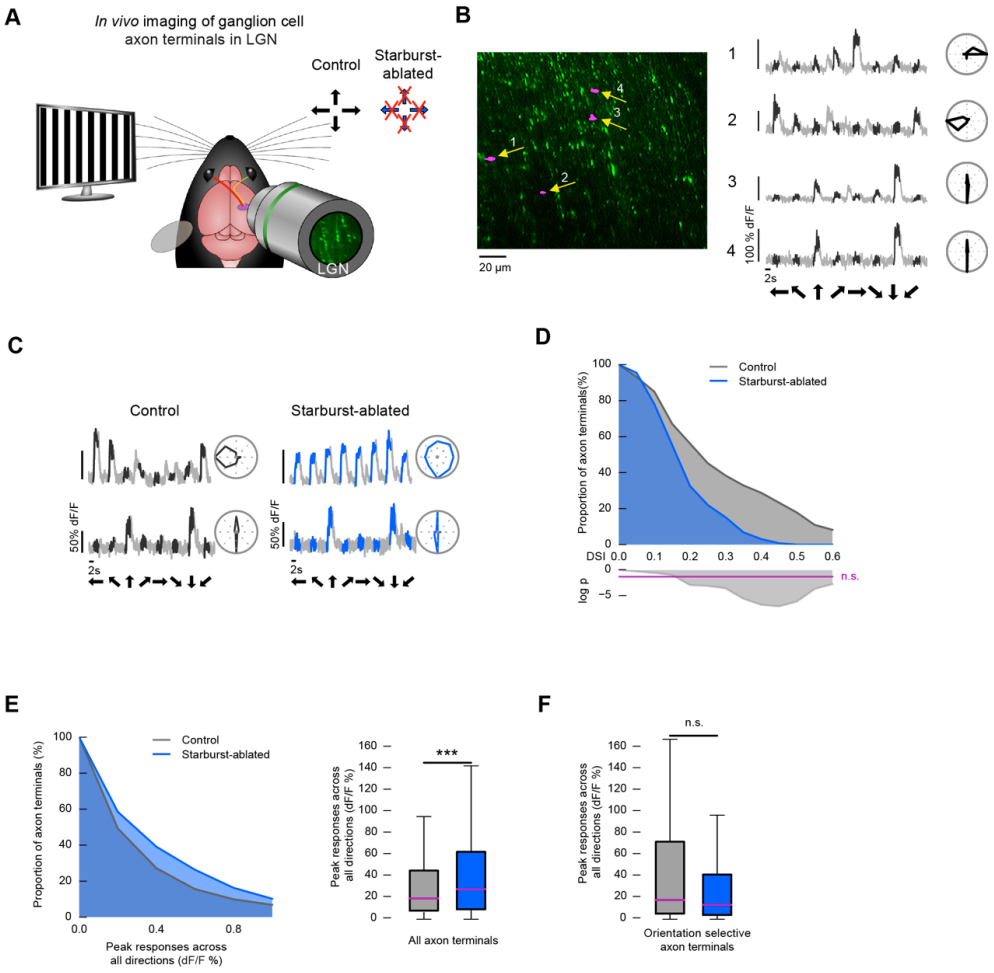

Figure 2.8 **Starburst ablation reduces direction selectivity in retinal ON-OFF DS cells in vivo.** (A-F) Two-photon imaging of ganglion cell axon terminals in the LGN. Control mice: wild type injected with DT, starburst-ablated mice: ChAT-Cre × LSL-DTR injected with DT. (**A**) Schematic of the experiment in the LGN. The stimulus was a grating drifting in eight directions. Responses of ganglion cell terminals in the LGN were measured in control and starburst-ablated mice. Arrows at the top right corner indicate the preferred directions of direction selective retinal ganglion cells. Crossed arrows: missing direction selectivity in that direction. (**B**) Left, two-photon image of GCaMP6s-labeled retinal ganglion cell axons in the LGN. Middle, examples of responses measured from control ganglion cell axon terminals corresponding to the labeled regions on the image (magenta regions indicated by yellow arrows). Here and in subsequent panels, the black part of a grey trace shows the response during image motion in control mice and black arrows below the traces show the stimulus direction. Right: polar plots of response magnitudes normalized to the response in the preferred direction. (**C**) Responses to motion, and polar plots of responses of two retinal ganglion cell axon terminals recorded in the LGN of control (left) and starburst-ablated (right) mice. Blue part of the grey trace shows the response during image motion in starburst-ablated mice. Right of each curve: polar plots of response magnitudes normalized to the response in the preferred direction. (**D**) Top, complementary cumulative distributions of DSI values of recorded ganglion cell axon terminals in control and starburst-ablated mice. Bottom, the logarithm of p values comparing the pairs of conditions using Fisher's exact test. Values above the magenta line are non-significant. (**E**) Left, complementary cumulative distributions of peak responses across all stimulus directions in ganglion cell axon terminals of control and starburst-ablated mice. Right, boxplot representation of the distributions. Bottom and top whiskers: minimum and maximum; bottom and top of the rectangle: first and third quartiles; central line: median. (**F**) Boxplot representation of the distributions of peak responses across all stimulus directions within vertically oriented orientation-selective responses in control (grey) and starburst-ablated (blue) mice.

Visual behavior in starburst-cell-ablated mice

We used two behavioral tests to determine the effect of starburst ablation on the activity of retinal ganglion cells. First we tested the pupil reflex, which depends predominantly on the activity of melanopsin-containing, direction non-selective ganglion cells (Güler et al., 2008). We found no difference in the pupil reflex between control and starburst-ablated mice (Figures 2.9A and 2.9B, Mann-Whitney U test, p = 0.886, control, n = 4 mice, starburst-ablated, n = 4 mice), indicating that starburst cell ablation left the melanopsin-containing ganglion cells and their retinal circuits intact. Second, we tested the optokinetic reflex, which relies on direction-selective ganglion cells and has previously been shown to become dysfunctional upon the loss of starburst cells(Yoshida et al., 2001). The optokinetic reflex was lost after DT injection in *ChAT-Cre* × *LSL-DTR* mice but remained intact when DT was injected into wild type mice (Figures 2.9C and 2.9D, Mann-Whitney U test, p = 0.002, control, n = 6 mice, starburst-ablated, n = 6 mice).

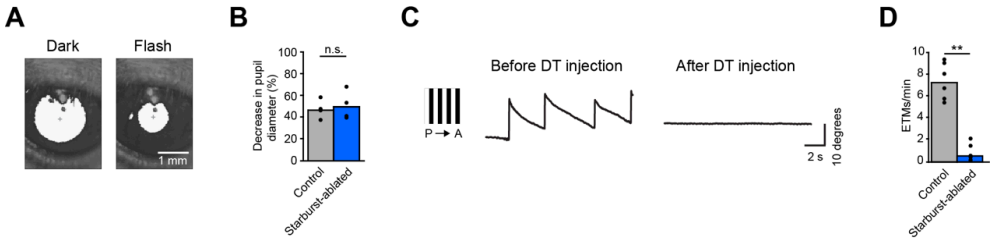

Figure 2.9**. Effect of starburst cell ablation on visual reflexes**. (A-B) Pupil reflex test. (**A**) The pupil of a starburst-ablated mouse is shown in the dark (left) and after a flash of light (right). The extent of the pupil is indicated in white. (**B**) Quantification of pupil reflex, the relative decrease in pupil diameter after a flash of light, is shown for control and starburst-ablated mice. (C-D) Optokinetic reflex test. Error bars represent ±s.d. (**C**) Mice were stimulated with gratings moving in a horizontal direction (left). Eye position in response to stimulation before (middle), and seven days after (right) DT injection in the same mouse. Negative deflections indicate eye movements in the anterior (A) direction, while positive deflections indicate eye movements in the posterior (P) direction. (**D**) Quantification of optokinetic reflex: eye-tracking movements (ETMs) per minute in control and starburst-ablated mice. Error bars represent ±s.d.

Diphtheria toxin acts locally in the eye

In *ChAT-Cre* mice, a population of cortical cells also expresses Cre recombinase (Figure 2.10). To determine if the injection of DT into the eye affects cortical circuits by DT leaking out from the eye and locally ablating Cre- and DTR-expressing cortical cells, we crossed *ChAT-Cre, LSL-DTR* and *LSL-tdTomato* mice and compared the density of tdTomato-expressing cells in V1 in DT-injected and uninjected (control) *ChAT-Cre* × *LSL-DTR* × *LSL-tdTomato* mice. We found no significant difference between the densities of tdTomato-expressing cells in V1 (Figure 2.10, Mann-Whitney U test, p = 0.40, control, 125 cells/mm^3 ± 4 s.e.m, n = 3 mice, starburst-ablated, 132 cells/mm^3 ± 10 s.e.m, n = 3 mice), despite the loss of starburst cells in the retina of DT-injected mice. Furthermore, *ChAT-Cre* × *LSL-DTR* mice

showed no apparent differences in motor behavior before and after DT injection, suggesting that the cholinergic motor neurons, which also express the DT receptor, were not affected by the DT injection into the eye. Together, these results indicate that DT does not spread out after being injected into the eye, but acts locally within the eye.

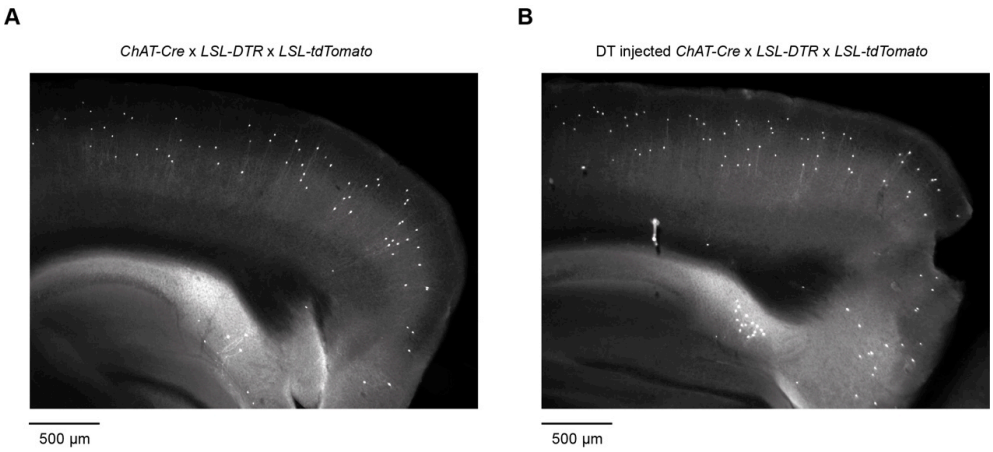

Figure 2.10 **DTR-expressing ChAT cells in V1 are not affected by DT injection to the eye**. tdTomato-labeled cells in V1 in uninjected (**A**) and DT-injected (**B**) *ChAT-Cre* × *LSL-DTR* × *LSL-tdTomato* mice.

One form of cortical direction selectivity relies on retinal direction selectivity

We then investigated how the disruption of retinal direction selectivity affects cortical direction selectivity in either *FRMD7^{tm}* (Figure 2.11, control of *FRMD7^{tm}*, n = 4961 cells from 9 mice, *FRMD7^{tm}*, n = 4379 cells from 9 mice) or starburst-ablated mice (Figure 2.12, control of starburst-ablated, n = 1669 cells from 4 mice, starburst-ablated, n = 1632 cells from 4 mice). We compared the distribution of direction-selective cells in layer 2/3 of V1 (cortical DS cells) in control mice and in mice with disrupted retinal direction selectivity by imaging neuronal activity using genetically-encoded calcium sensors: GCaMP6s in *FRMD7^{tm}* and its control mice; and GCaMP6f (Chen et al., 2013) in starburst-ablated and its control mice. We used AAV serotype 1 delivered by cortical injection or PHP.B serotype (Deverman et al., 2016) delivered by intravenous injection (the latter mentioned specifically for the corresponding experiments). The advantage of serotype PHP.B AAV is that it leads to widespread labeling of cortical cells and yields no nuclear expression of GCaMP6 for at least 10 weeks, the latest time we tested. We stimulated one eye with gratings moving in eight directions at 40 °/s, and recorded neuronal activity in the contralateral V1 (Figures 2.11A and 2.12A).

In control mice, the distribution of cortical DS cells across different preferred directions (Figures 2.11B and 2.12B) showed a significant bias to posterior motion (Hagihara et al., 2015) (Figures 2.11D, 2.11E, 2.12D and 2.12E; Hodges-Ajne test, control of *FRMD7^{tm}*, $p = 9.7 \times 10^{-47}$, control of starburst-ablated, $p = 5.5 \times 10^{-17}$, at DSI > 0.5): 27.0% (control of *FRMD7^{tm}*) and 26.8% (control of starburst-ablated) of cortical DScells preferred posterior motion (at DSI > 0.5). In contrast, cortical DS cells in mice with disrupted retinal direction selectivity (Figures 2.12C and 2.12D) were not biased to posterior motion: a significantly smaller fraction, only 10.3% (*FRMD7^{tm}*) and 6.2% (starburst-ablated), preferred posterior motion (Figures 2.11D, 2.11E, 2.12D and 2.12E, Fisher's exact test, *FRMD7^{tm}* $p = 1.9 \times 10^{-18}$, starburst-ablated $p = 3.7 \times 10^{-11}$, at DSI > 0.5). Together with the decrease in the proportion of posterior-motion-preferring cortical DS cells, we found a significant increase in the proportion of dorsal-motion-preferring cortical DS cells (Figures 2.11D and 2.12D, Fisher's exact test, *FRMD7^{tm}*, p = 0.0003, starburst-ablated, p = 0.01, at DSI > 0.5). Therefore, the balance between the representation of horizontal and vertical directions, quantified with a selectivity index (Experimental procedures), significantly changed between control mice and mice with disrupted retinal direction selectivity (Figures 2.11F and 2.12F, Fisher's exact test, *FRMD7^{tm}*, $p = 3.1 \times 10^{-12}$, starburst-ablated, $p = 1.2 \times 10^{-8}$, at DSI > 0.5) while the overall distribution of direction-selective cells remained similar (Mann-Whitney U test, Figure 2.11G, p = 0.81, control of *FRMD7^{tm}*, 46.25%, *FRMD7^{tm}*, 41.66%; Figure 2.12G, p = 0.39, control of starburst-ablated 26.6%, starburst-ablated, 28.4%, at DSI > 0.5). The proportion of direction-selective cells was different in the control of *FRMD7^{tm}* and in the control of starburst-ablated mice, which was likely due to the use of different promoters or sensors (control of *FRMD7^{tm}*, promoter: EF1a, sensor: GCaMP6s; control of starburst-ablated, promoter: hSyn, sensor: GCaMP6f).

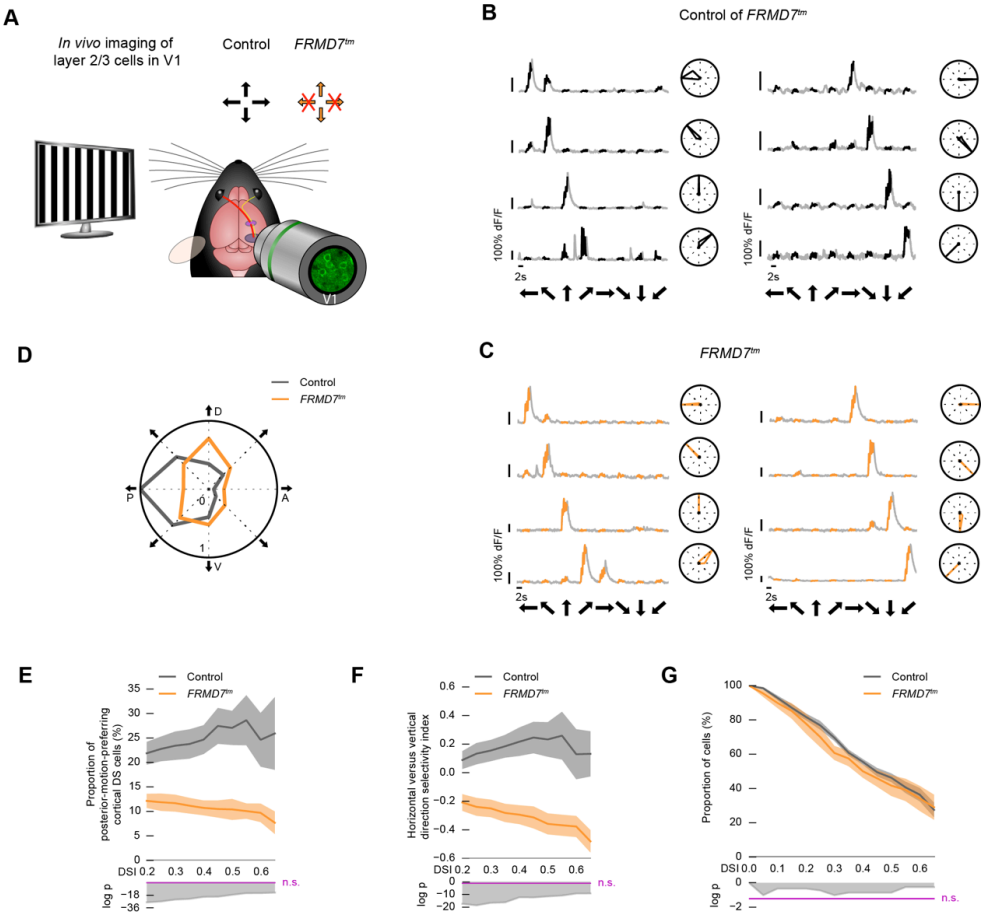

Figure 2.11 **Disrupting retinal direction selectivity decreases the proportion of posterior-motion-preferring cortical DS cells in FRMD7^{tm} mice**. (**A**) Schematic of the experiment in the cortex. Two-photon imaging cells in layer 2/3 of V1 in control mice and in FRMD7^{tm} mice with disrupted retinal direction selectivity along the horizontal axis. The stimulus was a grating drifting in eight directions. Arrows at the top right corner indicate the preferred directions of direction selective retinal ganglion cells. Crossed arrows: missing direction selectivity in that direction. (b-g) Control mice: wild type, mutant mice: FRMD7^{tm}. (**B-C**) Example responses from cortical DS cells recorded in control (B) and FRMD7^{tm} (C) mice. Black (B) or orange (C) part of a grey trace shows the response during image motion. Black arrows below the traces show the stimulus direction. Right: polar plots of response magnitudes normalized to the response in the preferred direction. (**D**) Polar plot showing the proportion of cortical DS cells preferring each of the stimulus directions in control and mutant mice. The proportions are normalized to the largest proportion across the two conditions. Cells with DSI > 0.5 are included in the plot. P denotes posterior, D dorsal, A anterior, V ventral motion direction in the visual field. (**E**) Top, proportion of posterior-motion-preferring cortical DS cells in control and mutant mice. Dark curves show mean values, shaded areas show ±s.e.m around the means. Bottom, the logarithm of p values comparing the conditions using Fisher's exact test. Values above the magenta line are non-significant. The DSI values shown along the horizontal axis denote the DSI thresholds defining cells as direction selective. (**F**) Top, horizontal versus vertical direction selectivity index in control and mutant mice (Experimental procedures). Bottom, the logarithm of p values comparing the conditions using Fisher's exact test. Values above the magenta line are non-significant. The DSI values shown along the horizontal axis denote the DSI thresholds defining cells as direction selective. (**G**) Top, complementary cumulative distributions of DSI values of recorded cells in control and mutant mice. Bottom, the logarithm of p values comparing the conditions using Fisher's exact test. Values above the magenta line are non-significant.

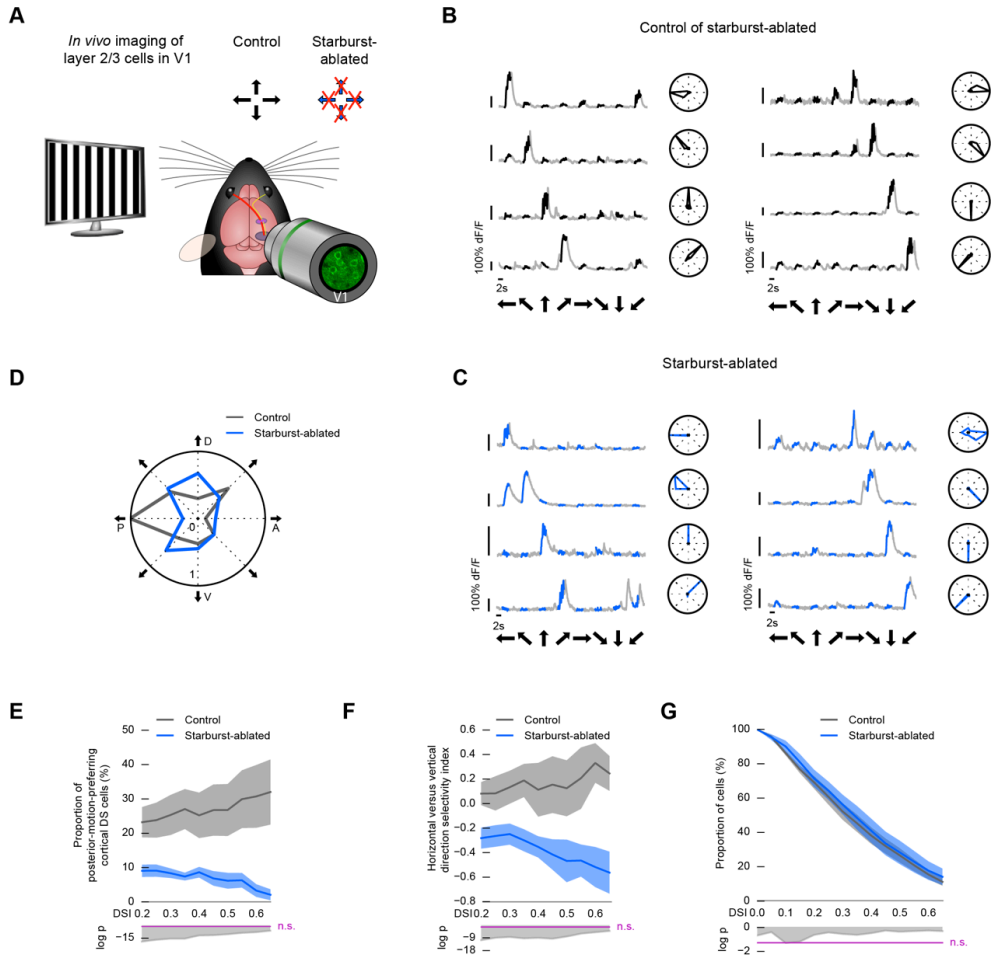

Figure 2.12 **Disrupting retinal direction selectivity decreases the proportion of posterior-motion-preferring cortical DS cells in starburst-ablated mice.** (**A**) Schematic of the experiment in the cortex. Two-photon imaging cells in layer 2/3 of V1 in control mice and in starburst-ablated mice with disrupted retinal direction selectivity along both the horizontal and the vertical axes. The stimulus was a grating drifting in eight directions. Arrows at the top right corner indicate the preferred directions of direction selective retinal ganglion cells. Crossed arrows: missing direction selectivity in that direction. (B-G) Control mice: wild type injected with DT, starburst-ablated mice: ChAT-Cre × LSL-DTR injected with DT. (**B-C**) Example responses from cortical DS cells recorded in control (B) and starburst-ablated (C) mice. Black (B) or blue (C) part of a grey trace shows the response during image motion. Black arrows below the traces show the stimulus direction. Right: polar plots of response magnitudes normalized to the response in the preferred direction. (**D**) Polar plot showing the proportion of cortical DS cells preferring each of the stimulus directions in control and starburst-ablated mice. The proportions are normalized to the largest proportion across the two conditions. Cells with DSI > 0.5 are included in the plot. P denotes posterior, D dorsal, A anterior, V ventral motion direction in the visual field. (**E**) Top, proportion of posterior-motion-preferring cortical DS cells in control and starburst-ablated mice. Dark curves show mean values, shaded areas show ±s.e.m around the means. Bottom, the logarithm of p values comparing the conditions using Fisher's exact test. Values above the magenta line are non-significant. The DSI values shown along the horizontal axis denote the DSI thresholds defining cells as direction selective. (**F**) Top, horizontal versus vertical direction selectivity index in control and starburst-ablated mice. Bottom, the logarithm of p values comparing the conditions using Fisher's exact test. Values above the magenta line are non-significant. The DSI values shown along the horizontal axis denote the DSI thresholds defining cells as direction selective. (**G**) Top, complementary cumulative distributions of DSI values of recorded cells in control

and mutant mice. Bottom, the logarithm of p values comparing the conditions using Fisher's exact test. Values above the magenta line are non-significant.

Similar to the distribution of cortical DS cells according to their preferred directions (Figure 2.11, Figure 2.12), the distribution of response amplitudes of cortical DS cells also showed a significant bias to posterior motion and this bias was not present in mice with disrupted retinal direction selectivity (Figure 2.13). Despite the slight increase in overall activity in the retina (Figure 2.7F), the average activity levels of responding cortical cells were similar between control mice and mice with disrupted retinal direction selectivity. This maintained activity level is consistent with previous reports that the amplitude distribution of cortical cells is under homeostatic control (Hengen et al., 2016; Keck et al., 2013).

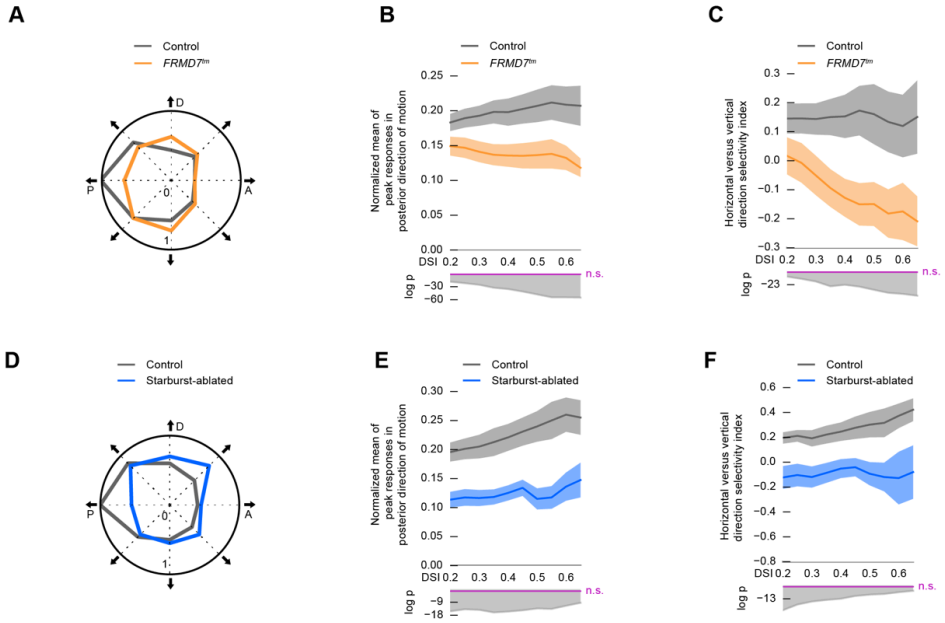

Figure 2.13 **Disrupting retinal direction selectivity decreases the mean response amplitudes of posterior-motion-preferring cortical DS cells in *FRMD7^{tm}* and starburst-ablated mice.** (**A, D**) Polar plots showing the normalized mean of the peak responses of cortical DS cells in each of the stimulus directions in *FRMD7^{tm}* and its control (A) and starburst-ablated and its control (D) mice. Cells with DSI > 0.5 are included in the plot. P denotes posterior, D dorsal, A anterior, V ventral motion direction in the visual field. (**B, E**) Top, normalized mean of the peak responses in posterior direction of motion in *FRMD7^{tm}* and its control (B) and starburst-ablated and its control (E) mice. Dark curves show mean values, shaded areas show ±s.e.m around the means. Bottom, the logarithm of p values comparing the conditions using Fisher's exact test. Values above the magenta line are non-significant. The DSI values shown along the horizontal axis denote the DSI thresholds defining cells as direction selective. (**C, F**) Top, horizontal versus vertical direction selectivity index computed from the normalized mean peak responses of cortical DS cells along horizontal and vertical directions in control and mutant mice. Bottom, the logarithm of p values comparing the conditions using Fisher's exact test. Values above the magenta line are non-significant. The DSI values shown along the horizontal axis denote the DSI thresholds defining cells as direction selective.

We examined the robustness of the finding that the proportion of posterior-motion-preferring cortical DS cells decreases in mice with disrupted retinal direction selectivity. First, we analyzed whether the decrease in the proportion of posterior-motion-preferring cortical DS cells depends on the choice of inclusion criteria for defining cells as 'responding'. So far, we have defined a cortical cell as 'responding' if its response to the stimulus moving in any of the directions was above the response threshold for a contiguous block of at least one second for at least two repetitions of the stimulus. When we relaxed this definition to include cells that responded to at least one stimulus presentation, the reduced cortical representation of posterior motion remained significant (Figure 2.14). Second, we tested whether the decrease in the proportion of posterior-motion-preferring cortical DS cells depends on the number of stimulus repetitions. We infected mice intravenously with AAV PHP.B serotype expressing GCaMP6s. We stimulated one eye with gratings moving in eight directions at 40 °/s, and recorded neuronal activity in the contralateral V1 in control and *FRMD7*^{tm} mice (control, n = 595 cells from 4 mice, *FRMD7*^{tm} n = 403 cells from 4 mice). We presented the stimulus six times in each imaging plane and analyzed the distribution of cortical DS cells as a function of stimulus repetitions. The decrease in the proportion of posterior-motion-preferring cortical DS cells was significant at each number of stimulus repetitions, from two to six (Figure 2.15). Therefore, the observed difference between the distributions of cortical DS cells in control mice and in mice with disrupted retinal direction selectivity does not depend on the stringency of response inclusion criteria or on the number of stimulus repetitions.

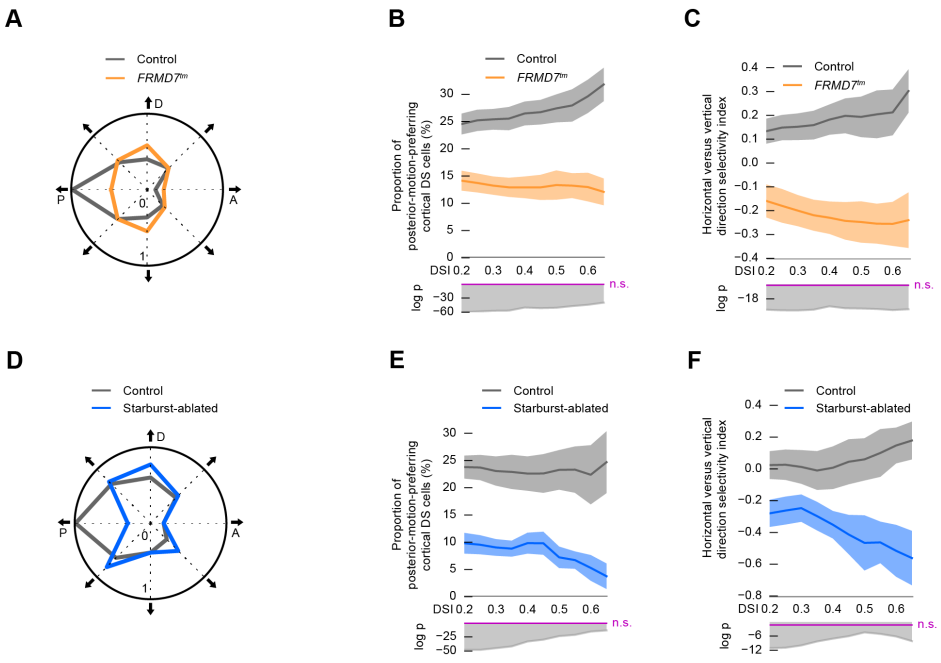

Figure 2.14 **Disrupting retinal direction selectivity decreases the proportion of posterior-motion-preferring cortical DS cells in *FRMD7^{tm}* mice when less reliably responding neurons are included.** Cell inclusion criteria were relaxed to include unreliable cells responding to only one stimulus repetition. (**A, D**) Polar plot showing the proportion of cortical DS cells preferring each of the stimulus directions in *FRMD7^{tm}* and its control (A) and starburst-ablated and its control (D) mice. The proportions are normalized to the largest proportion across the two conditions. Cells with DSI > 0.5 are included in the plot. P denotes posterior, D dorsal, A anterior, V ventral motion direction in the visual field. (**B, E**) Top, proportion of cortical DS cells preferring posterior motion in *FRMD7^{tm}* and its control (B) and starburst-ablated and its control (E) mice. Dark curves show mean values, shaded areas show ±s.e.m around the means. Bottom, the logarithm of p values comparing the conditions using Fisher's exact test. Values above the magenta line are non-significant. The DSI values shown along the horizontal axis denote the DSI thresholds defining cells as direction selective. (**C, F**) Top, horizontal versus vertical direction selectivity index in *FRMD7^{tm}* and its control (C) and starburst-ablated and its control (F) mice. Bottom, the logarithm of p values comparing the conditions using Fisher's exact test. Values above the magenta line are non-significant. The DSI values shown along the horizontal axis denote the DSI thresholds defining cells as direction selective.

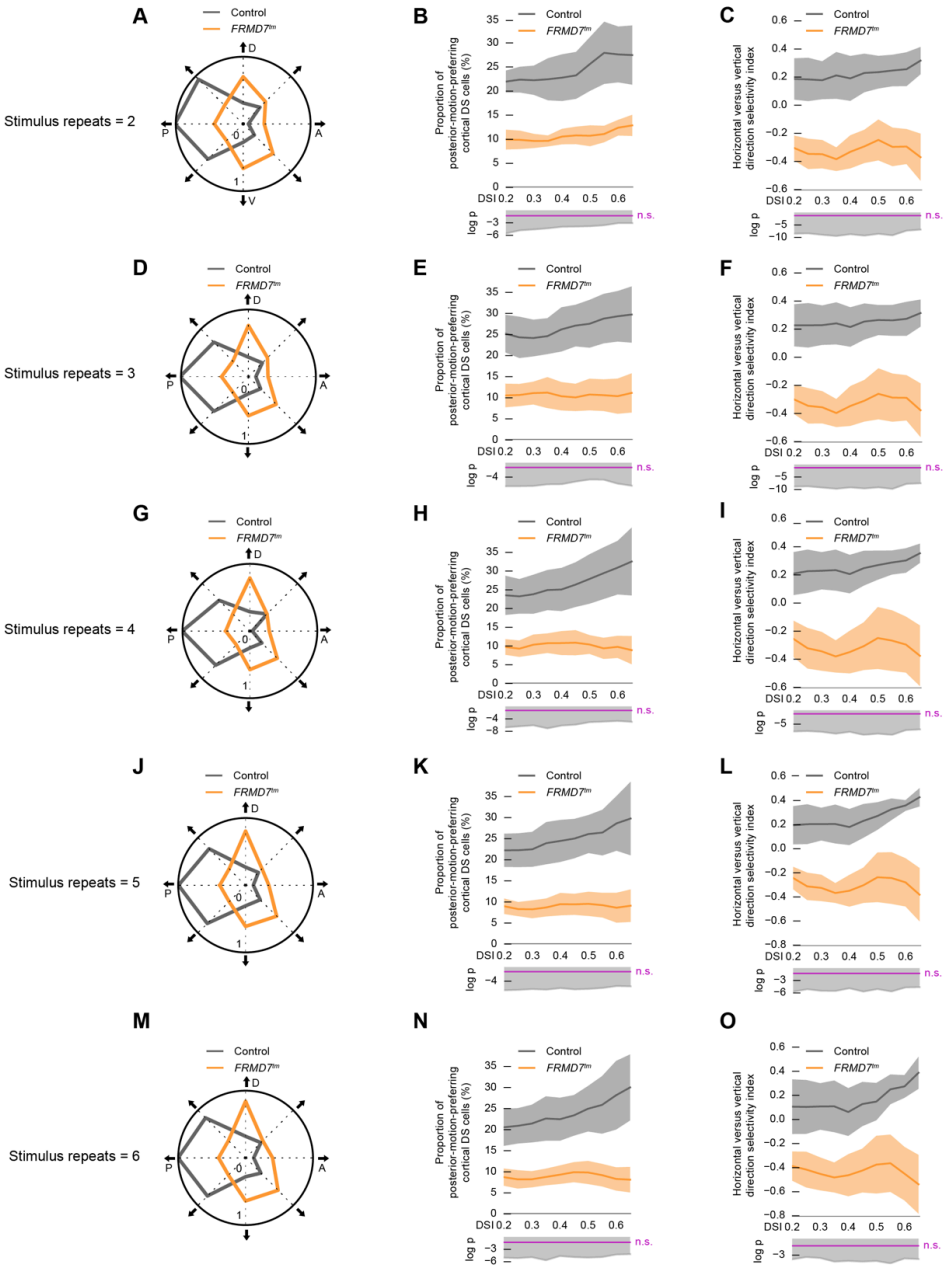

Figure 2.15 **Disrupting retinal direction selectivity decreases the proportion of posterior-motion-preferring cortical DS cells in *FRMD7^{tm}* mice.** The dependence on the number of stimulus repetitions. The stimulus was presented six times and each row shows response analysis using a subset (two (top row) to six (bottom row)) of stimulus repetitions. (A-O) Control mice: wild type, mutant mice: *FRMD7^{tm}*. (**A, D, G, J ,M**) Polar plots showing the proportion of cortical DS cells preferring each of the stimulus directions in control and mutant mice. The proportions are normalized to the largest proportion across the two conditions. Cells with DSI > 0.5 are included in the plot. P denotes posterior, D dorsal, A anterior, V ventral motion direction in the visual field. (**B, E, H, K, N**) Top, proportion of cortical DS cells preferring posterior motion in control and mutant mice. Dark curves show mean values, shaded areas show ±s.e.m around the means. Bottom, the logarithm of p values comparing the conditions using Fisher's exact test. Values above the magenta line are non-significant. The DSI values shown along the horizontal axis denote the DSI thresholds defining cells as direction

selective. (**C, F, I, L, O**) Top, horizontal versus vertical direction selectivity index in control and mutant mice. Bottom, the logarithm of p values comparing the conditions using Fisher's exact test. Values above the magenta line are non-significant. The DSI values shown along the horizontal axis denote the DSI thresholds defining cells as direction selective.

In the retina, the spike frequency of ON-OFF DS cells monotonically increases with stimulus speed up to around 40 °/s (Hoggarth et al., 2015; Weng et al., 2005). We therefore investigated whether the speed of the stimulus affected the responses of posterior-motion-preferring cortical DS cells in control and *FRMD7^{tm}* mice differently. We infected mice intravenously with AAV PHP.B serotype expressing GCaMP6s. We stimulated mice with visual motion in eight different directions moving at 10, 16.6, 26.6, and 40 °/s and quantified the posterior component of the responses of cortical DS cells as a function of stimulus speed. In control mice, the response monotonically increased with speed, while in *FRMD7^{tm}* mice the response did not increase with speed (Figure 2.16, Kruskal-Wallis H test, p = 0.71, control, n = 1574 cells from 4 mice, *FRMD7^{tm}*, n = 1342 cells from 4 mice, at DSI > 0.5).

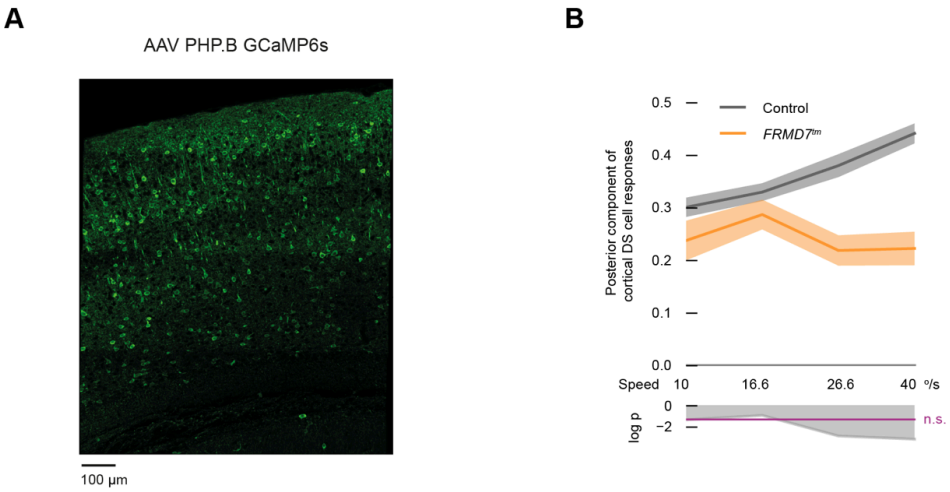

Figure 2.16 **Posterior component of cortical DS cell responses is reduced at high stimulus speeds in FRMD7tm mice.** (**A**) Intravenous injection of AAV serotype PHP.B yields widespread expression of GCaMP6s in the cortex. Cortical slice stained with anti-GFP antibody (representing GCaMP6s expression) is shown. (**B**) Control mice: wild type, mutant mice: FRMD7tm. Top, posterior component of the responses of cortical DS cells. Dark curves show mean values, shaded areas show ±s.e.m around the means. Bottom, the logarithm of p values comparing the conditions using the Mann-Whitney U test. Values above the magenta line are non-significant. The horizontal axis denotes the speed of the stimulus. Cells with DSI > 0.5 are included in the plot.

Discussion

Our results show the existence of two different forms of direction selectivity in mouse visual cortex, each with distinct functional properties. One form of cortical direction selectivity, which is tuned to higher stimulus speeds and is present along a cardinal direction, the posterior direction, relies on direction selectivity computed within the retina. A second form

of cortical direction selectivity, which is distributed more evenly across different stimulus speeds and directions, is computed by circuits downstream from the retina, possibly within the cortex or in the LGN. Therefore, cortical computations expand feature-selectivity computed in the periphery to a larger dynamic range in at least two stimulus dimensions: speed and direction.

In visual cortex, our analysis detected the influence of retinal direction selectivity only on posterior-motion-preferring cells in layer 2/3, despite the fact that our retinal manipulations disrupted retinal direction selectivity either along two (*FRMD7^{tm}* mice) or all four (starburst-ablated mice) cardinal directions. One explanation for this is a biased retinal direction representation combined with cortical plasticity following our manipulation of retinal direction selectivity. Posterior-motion-preferring ON-OFF DS cells labeled in *Drd4-GFP* mice outnumber dorsal-motion-preferring cells labeled in *Hb9-GFP* mice by 3.5 to 1 (Huberman et al., 2009; Trenholm et al., 2011), suggesting a dominance of posterior-motion-preferring cells in the retina (Rivlin-Etzion et al., 2011), which could lead to the overrepresentation of posterior-motion-preferring cortical DS cells. It is possible that the loss of the major direction-selective retinal input, tuned to the posterior direction, leads to a compensatory increase in direction selectivity computed locally in the cortex. Indeed, we detected such a significant increase in the dorsal direction. This compensatory increase in cortical direction selectivity could mask the loss of retinal direction-selective input from the three less-represented cardinal directions in the retina.

It is interesting to note that, in animal species with laterally positioned eyes (such as mice and rabbits), posterior image motion is the most prevalent motion direction when the animal moves forward, which is the dominant mode of whole-body locomotion. It is possible that in animals with laterally positioned eyes, the strong influence of retinal posterior direction selectivity on cortical direction selectivity is an adaptation of the retina to the statistics of image motion. In contrast, in animals with frontally positioned eyes, such as non-human primates and humans, forward locomotion is expected to elicit less asymmetry in the distribution of motion directions on the retina. Whether retinal ON-OFF DS cells exist in non-human primates and humans and, if they do exist, how they contribute to vision are intriguing and open questions in neuroscience.

Chapter 3 - Rods in daylight act as relay cells for cone-driven horizontal cell-mediated surround inhibition

Szikra T, Trenholm S, ***Drinnenberg A****, Jüttner J, Raics Z, Farrow K, Biel M, Awatramani G, Clark DA, Sahel JA, da Silveira R & Roska B*

Summary

Vertebrate vision relies on two types of photoreceptors, rods and cones, which signal increments in light intensity with graded hyperpolarizations. Rods operate in the lower range of light intensities while cones operate at brighter intensities. The receptive fields of both photoreceptors exhibit antagonistic center surround organization. Here we show that at bright light levels, mouse rods act as relay cells for cone-driven horizontal cell-mediated surround inhibition. In response to large, bright stimuli that activate their surrounds, rods depolarize. Rod depolarization increases with stimulus size, and its action spectrum matches that of cones. Rod responses at high light levels are abolished in mice with nonfunctional cones and when horizontal cells are reversibly inactivated. Rod depolarization is conveyed to the inner retina via postsynaptic circuit elements, the rod bipolar cells. Our results show that the retinal circuitry repurposes rods, when they are not directly sensing light, to relay cone-driven surround inhibition.

Introduction

Image forming vision is based on two types of photoreceptors: rods and cones (Yau and Hardie, 2009). Rods respond to light in the lower range of light intensities, characteristic of nighttime, while cones operate at higher light intensities, characteristic of daytime. These two photoreceptors interact with the third cell type of the outer retina, the horizontal cells, which provide feedback inhibition to both photoreceptors (Wässle, 2004). In most mammals there are two types of horizontal cells, one with a long axon and one without. In mouse there is only the axon bearing type of horizontal cell (Peichl and González-Soriano, 1994). It has been proposed that rods contact horizontal cell axon terminals while cones contact horizontal cell dendrites (Kolb, 1974, 1970), and that each of these horizontal cell compartments forms local negative feedback synapses with its corresponding photoreceptor class (Babai and Thoreson, 2009; Baylor et al., 1971; Davenport et al., 2008; Nelson et al., 1975; Pan and Massey, 2007; Thoreson et al., 2008; Trümpler et al., 2008). Furthermore, dendro-dendritic and axo-axonic

electrical synapses between horizontal cells have been shown to mediate lateral signal spread (Thoreson and Mangel, 2012). The neuronal circuit formed by rods, cones and horizontal cells results in antagonistic center surround receptive field organization in rods at low light levels and in cones and high light levels. Information from photoreceptors enters the inner retina by two primary pathways: from rods to rod bipolar cells and from cones to cone bipolar cells. Alternative pathways have also been described (Bloomfield and Volgyi, 2009; Wässle, 2004).

Rods and cones are also directly connected both to themselves and to one another with gap junctions (Asteriti et al., 2014; Bloomfield and Volgyi, 2009). Due to cone-rod coupling, it is expected that mammalian rods respond to light, indirectly, at high light levels, even when their photoresponses are at saturation. For this indirect rod response, cones would act as photoreceptors and drive changes in rod membrane potential via gap junctions, resulting in sign-conserving responses in rods (i.e. hyperpolarizing light responses). Alternatively, the bright light mediated cone signal could potentially arrive at rods via the inhibitory horizontal cells, leading to a change in response polarity, causing rods to exhibit a depolarizing response. This circuit involves feedforward inhibition via horizontal cells: cones drive horizontal cell dendrites, this signal spreads from horizontal cell dendrites to axon terminals, and then drives rod depolarization via sign-inverting synapses. However, it has been proposed that the long axons of horizontal cells do not conduct signals (Nelson et al., 1975), a notion which has recently been challenged (Trümpler et al., 2008). These two possible circuits for crosstalk between cones and rods are not mutually exclusive since they may act at different spatial or temporal scales or under different conditions, such as at different circadian times (Ribelayga et al., 2008).

The functional consequences of these two crosstalk pathways are different. In the first case, rods functionally copy cones and this sign-conserving pathway provides cones with a second "center-pathway" to the inner retina, as has been proposed before (Bloomfield and Volgyi, 2009). In the second case rods convey cone-driven, horizontal cell-mediated surround inhibition to downstream visual circuits. Similar to rods, cones may also display indirect (Asteriti et al., 2014) responses at low light levels at which they do not respond directly to light. Here the origin of the light response would be rods and the polarity of the response would be either sign-conserving or sign-inverting, depending on the pathway, via gap junctions or via horizontal cells. The presence and the relative magnitude of these crosstalk pathways, in different background light conditions, in intact mammalian retinas are not well understood.

Here we recorded light-evoked signals from single rods and cones in wholemount mouse retina. We show that, at high background light levels when stimulated with large spots, rods

respond with depolarization. Rod depolarization has the same action spectrum as cone photoresponses and is absent when cones are not functional or when horizontal cells are reversibly inactivated. Rod depolarization spreads to the inner retina via rod bipolar cells. When cones are stimulated with large spots at low background light levels, cones also respond with depolarization. These results suggest that mouse horizontal cell axons convey information in both directions, allowing cone hyperpolarization at high background light levels to cause rod depolarization and rod hyperpolarization at low background light levels to cause cone depolarization. As a consequence, outside of their photon sensing range of light intensities, mouse rods act as relay cells conveying cone-driven horizontal cell-mediated surround inhibition to downstream visual circuits.

Results

Rod depolarization at high light levels

We recorded voltage responses from single rod cell bodies in wholemount mouse retina, using the perforated patch clamp technique. We used perforated patch clamp to preclude the decrease of photoresponse over time due to the wash out of the phototransduction cascade components. We approached rods from the ganglion cell side, because from this side we could visualize individual rod cell bodies under infrared illumination. Since the recorded responses were small (Figure 3.1A), likely due to small seal-to-access resistance ratio, response amplitudes most likely did not represent real response amplitudes. Therefore, experiments with different rods were compared using their responses relative to their maximum hyperpolarizing response.

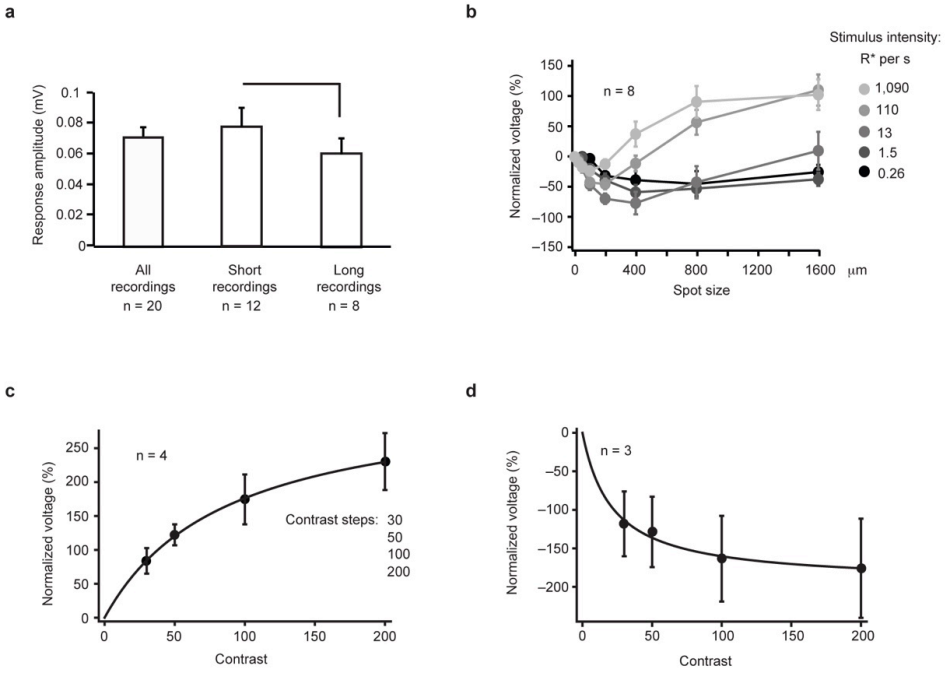

Figure 3.1 **Light responses of rod photoreceptors in mouse whole mount retina.** (**A**) First column shows the mean and standard error of rod depolarization evoked by a 800 μm spot at 1090 R*/s intensity. In the second and third column rod depolarization to 800 μm spot are compared in two different experimental conditions. Second column: rod depolarization was recorded immediately after getting electrical access to rods. Third column: rod depolarization was recorded at the end of the experimental series shown in Figure 3.2A. (**B**) Normalized response magnitudes in whole mount rods at five background intensities and different spot sizes. (**C**) Rod depolarization at high background light levels increased with increasing positive contrast. (**D**) Rods responded with hyperpolarization to negative contrast, and the hyperpolarization increased with increasing negative contrast.

We presented retinas with white spots of light of different sizes for two seconds, at a fixed contrast but at different background light intensities spanning six decades (Figure 3.2). As expected (Yau, 1994), the rod response to contrast increments was hyperpolarizing at low background light levels. The response was sustained, and its magnitude initially increased and then decreased with increasing spot size, displaying the classical center surround receptive field organization of rods. The initial increase in response was likely due to the electrical coupling between rods (Bloomfield and Volgyi, 2009; Li et al., 2012; Tsukamoto et al., 2001) and the decrease can be attributed to feedback inhibition from horizontal cells (Babai and Thoreson, 2009). At high light levels the response to small spots became smaller compared to low light levels, consistent with rod saturation. However, for spatially extended spots the surround response remained strong. Notably, stimulation with large spots caused a large depolarization (Figures 3.2A, 3.2B and 3.1B); the magnitude of the depolarizing response was at least as large as the maximum hyperpolarizing response (Figure 3.2C). Rod depolarization at high background light levels increased monotonically with the contrast of the stimulus, and

turned into hyperpolarization if the polarity of the contrast was reversed (Figures 3.1C and 3.1D). When rod responses were recorded in retinal slice preparations, we did not detect any depolarizing responses at any light level: the responses were exclusively hyperpolarizing (Figure 3.2D-I). All the measurements described henceforth were carried out in wholemount retinas unless otherwise noted.

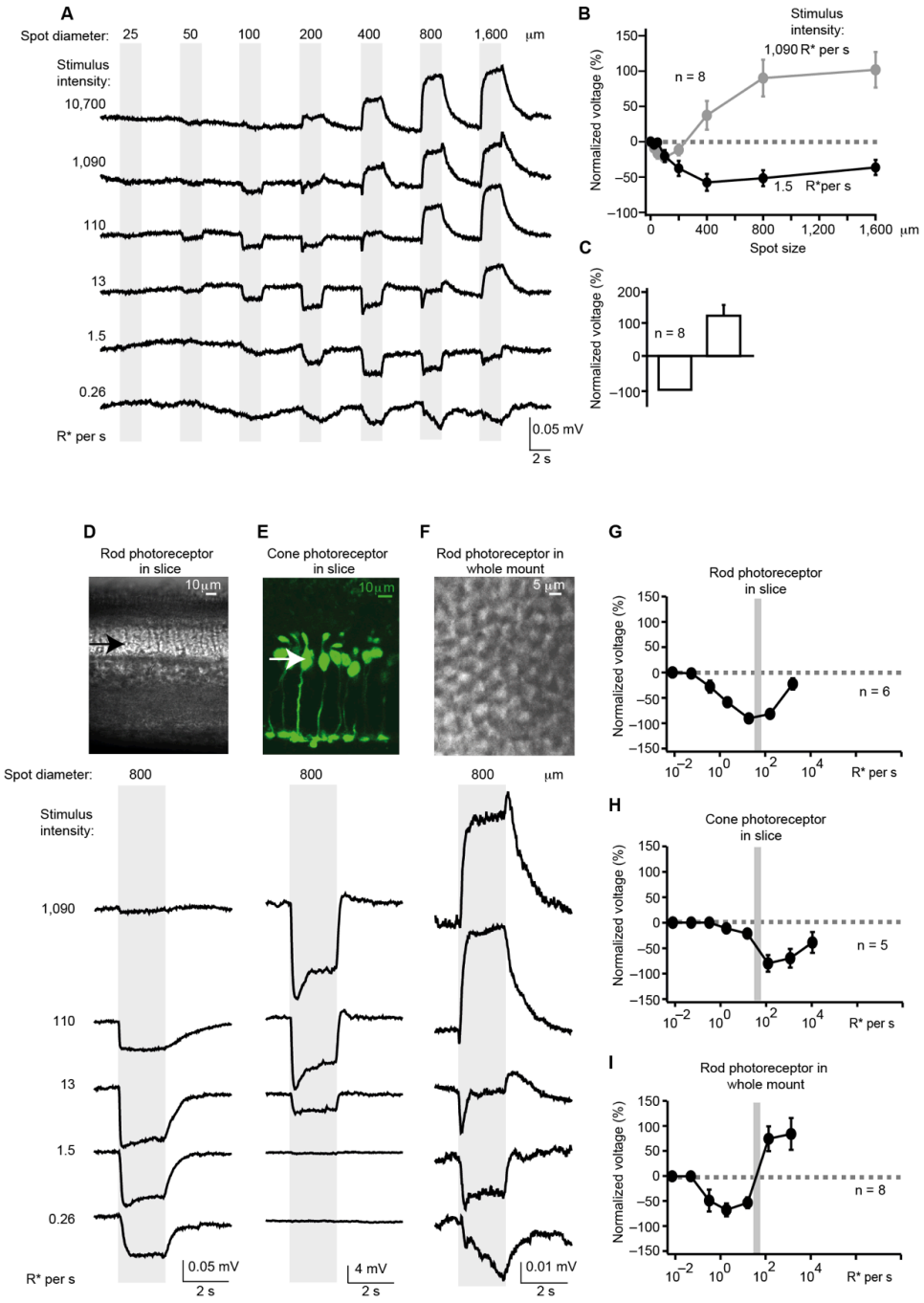

Figure 3.2 **Rods respond with depolarization to large spots at high light levels in wholemount retina.** (**A**) Light responses to contrast increments elicited by spots of different sizes were measured at different background/stimulus intensities from a rod in wholemount retina. The stimulus contrast was kept constant throughout different background intensities. Each row is ~1 log unit apart in intensity. Grey bars indicate the timing of the light stimulation. (**B**) Normalized response magnitudes in wholemount rods at two background intensities and with different spot sizes. Responses were normalized to the maximum average (n = 50 – 100) hyperpolarization across different light levels and spot sizes. Negative values represent hyperpolarizing responses while positive values represent depolarizing responses. (**C**) The largest depolarization in experimental series such as shown in (A)

normalized to the largest hyperpolarization. (**D-F**) Top, example images showing rods in slice (left), fluorescent cones in slice (middle) and rods in wholemount (right). Bottom, light responses of rod and cone photoreceptors to 800 μm spots at different light intensities in slice and in wholemount. The wholemount rod response was re-plotted from (A). (**G-I**) Normalized response magnitudes of rods and cones as a function of stimulus intensity. The stimulus was an 800 μm diameter spot. Normalization was performed as in (B).

Cone photoresponses are required for rod depolarization

Next, we investigated the mechanism driving the depolarizing surround response of rods. It is unlikely that this depolarization is mediated by rod feedback via horizontal cells since rods were close to saturation as shown by their small center response. Importantly, the light level at which the hyperpolarizing response of rods became more transient in wholemount retinas corresponded to the onset of cone response recorded in slice (Figure 3.2D-I). In order to examine whether the cone photoresponse is a prerequisite of the rod depolarizing response, we recorded from rods in both *Cnga*$^{-/-}$ (Biel et al., 1999) and *Gnat2*^{cpfl3} (Chang et al., 2006) mice, whose retinas lack functional cone photoresponses (Altimus et al., 2010). In both of these mouse lines, rods did not respond to light with depolarization at high background light levels even when stimulated with large spots (Figures 3.3A-C and 3.4A-B). This indicates that cone photoresponses are necessary for rod depolarization.

If rod depolarization is caused by cone activity, the action spectrum of rod depolarization should match the action spectrum of cone hyperpolarization. In the ventral part of the mouse retina, cones dominantly express ultraviolet photopigment with peak absorption at 355 nm (Lyubarsky et al., 1999). The absorption of rhodopsin, the photopigment of rods, peaks at 500 nm (Lyubarsky et al., 1999). We therefore recorded from genetically labeled cones using two-photon targeted perforated patch clamp and from unlabeled rods using infrared targeted perforated patch clamp in the ventral part of the retina at high background light levels, while we stimulated the retina with full-field monochromatic light with different wavelengths from 370 to 550 nm. At all stimulation wavelengths, cones responded with hyperpolarization and rods with depolarization, therefore with opposite polarity (Figure 3.3D-E). The action spectrum of cone hyperpolarization and rod depolarization matched closely, and both peaked at 370 nm, the shortest wavelength that we were able to use for stimulation (Figure 3.3F). At mesopic light levels, when both cones and rods respond to light directly, illumination with green and blue light caused responses with opposite polarity in rods: green light hyperpolarized rods while blue light depolarized them (Figure 3.3G). These experiments provide further support to the notion that cones are the photosensors that drive rod depolarization.

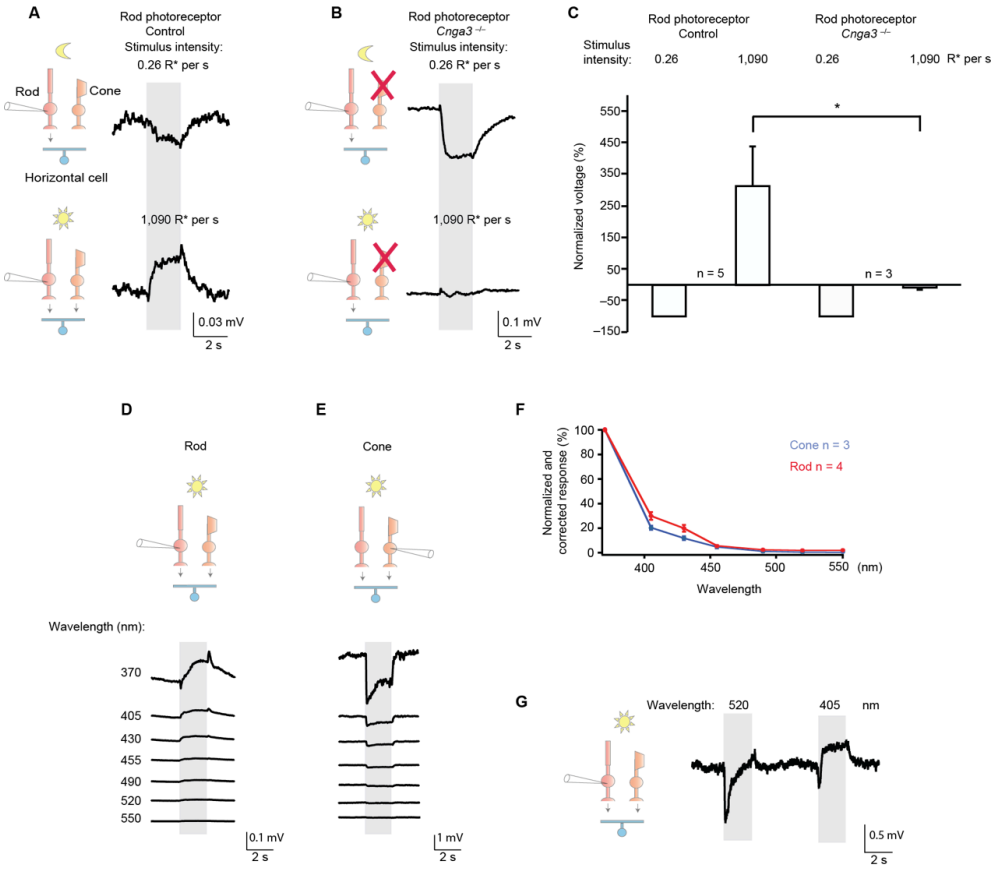

Figure 3.3 **Cone light responses are necessary for rod depolarization.** (**A-C**) Rod responses at two different background/stimulus intensities in wild type and in the Cnga3$^{-/-}$ mouse line. The stimulus was a positive contrast spot of 800 µm diameter. In (C) responses were normalized to the maximum hyperpolarization evoked by the 0.26 R*/s stimulus. Negative values indicate hyperpolarization, positive values depolarization ($p = 0.037$, $t(6) = 2.204$, Student's unpaired t-test). In this and subsequent figures, schematic diagrams showing the elements of the outer retinal circuit (rod, cone and horizontal cell), the recorded cell (pointed to with the electrode) and the blocked circuit element or synaptic connection (red crosses) are shown next to the recordings. (**D-E**) Light responses of a rod (D) and a cone (E) recorded in the ventral part of the retina, when stimulated with full-field light at different wavelengths. (**F**) Action spectrum of cone hyperpolarization and rod depolarization in the ventral retina. (**G**) Response of a rod in wholemount retina stimulated with 520 and 405 nm light.

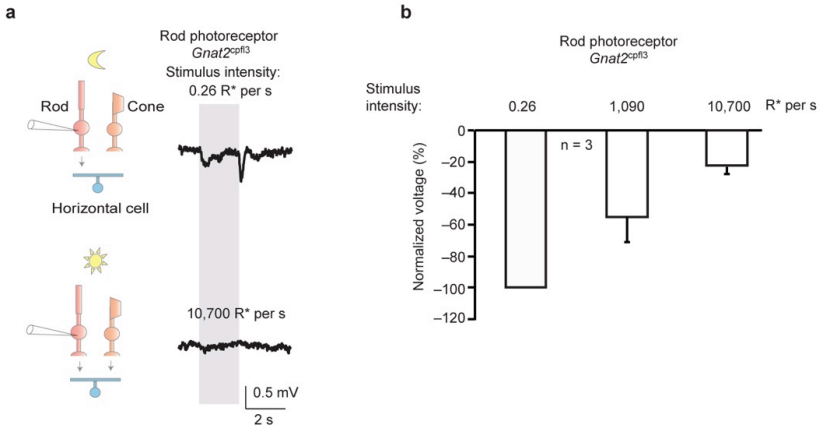

Figure 3.4 **Rod responses in Gnat2^{cpfl3} mouse.** (**A**) Rod responses at two different background intensities in Gnat2^{cpfl3} mice. The stimulus was a spot of 800 μm. (**B**) Quantification, responses were normalized to the maximum hyperpolarization evoked by the 0.26 R*/s stimulus

Horizontal cells mediate rod depolarization

If horizontal cells are acting as conduits of feedforward inhibition between cones and rods, we expect that silencing horizontal cells abolish rod depolarization. To test this, we developed a mouse line (*Gja10-Cre*) that expressed Cre recombinase (Siegert et al., 2012) and a red fluorescent marker, tdTomato, specifically in horizontal cells. We then used two-photon laser-targeted patch clamp to record from labeled horizontal cells. When we pharmacologically blocked photoreceptor inputs to horizontal cells, using the ionotropic glutamate receptor blocker NBQX, no depolarizing rod responses were detected (Figure 3.5A-D). Therefore, glutamatergic synaptic transmission is required for rod depolarization.

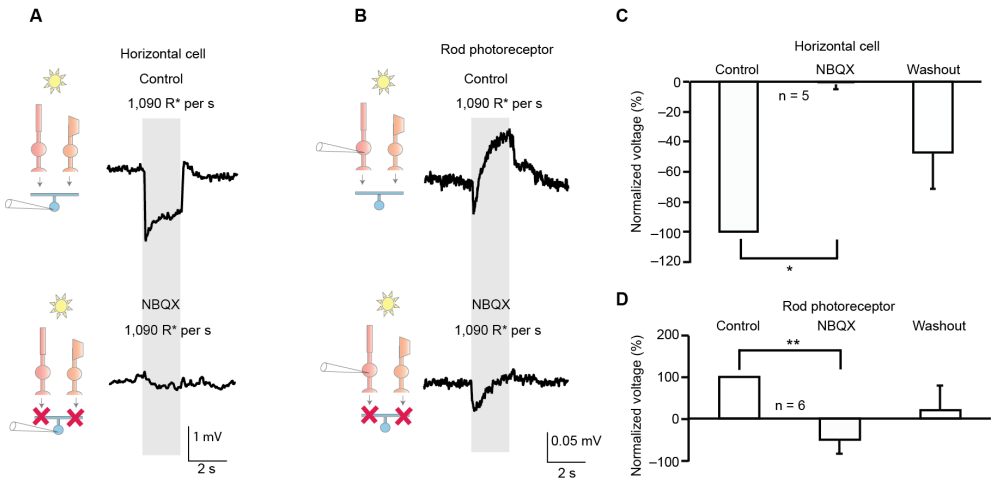

Figure 3.5 **Blocking photoreceptor input to horizontal cells abolishes rod depolarization.** The effect of NBQX on horizontal cell (**A, C**) and rod (**B, D**) responses. The stimulus was a positive contrast spot of 800 μm diameter at 1090 R*/s. In (C) and (D) responses were normalized to the maximum hyperpolarization and maximum depolarization, respectively. Negative values indicate hyperpolarization, positive values depolarization ($p = 0.012$ and $p = 0.005$ for (C) and (D) respectively, $U = 0$, Mann-Whitney U test).

In order to provide causal evidence that horizontal cells convey cone signals to rods and, consequently, drive rod depolarization, we reversibly inactivated horizontal cells while recording light responses from rods (Figure 3.8). We delivered a bi-stable channelrhodopsin (bi-ChR2) (Berndt et al., 2009) to horizontal cells using conditional adeno-associated viruses (Figure 3.8A); these viruses also labeled the horizontal cells with GFP (Experimental procedures, Figure 3.8B-D). Horizontal cell labeling was selective and efficient (Figures 3.8E-H and 3.6). We then recorded from horizontal cells and rods in retinas expressing bi-ChR2 in horizontal cells (Figure 3.8I).

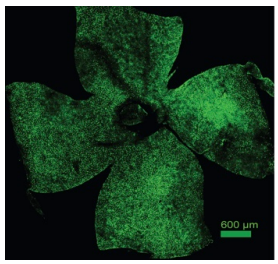

Figure 3.6 **Channelrhodopsin expression in horizontal cells.** We delivered a bi-stable channelrhodopsin (bi-ChR2) to horizontal cells using conditional adeno-associated viruses. A single subretinal injection led to the labeling of horizontal cells across the entire retina.

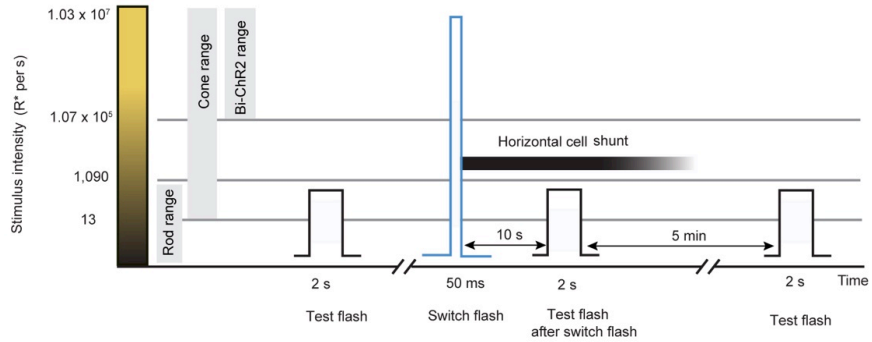

Figure 3.7 **Sequence of light stimulation in the experiments using reversible inactivation of horizontal cells**. First, the retina was stimulated with a test flash, a white spot of 800 µm in diameter shown for 2s. The test flash was not bright enough to activate bi-ChR2 (Figure 3.8J). Second, a switch flash was presented. The switch flash was a blue full-field light step that lasted 50 ms. The switch flash was brighter than the test flash and it activated bi-ChR2 (Figure 3.8J). Third, a test flash was presented again 10s after the switch flash. After waiting for 5 min we started a new "test flash-switch flash-test flash" cycle. The cycle was then repeated.

Our experiment making use of reversible horizontal cell inactivation was set up according to the following logic (Figure 3.7). A projector provided two kinds of light stimuli to the retina: a white flash that lasted for two seconds (the 'test flash') or a brief, high-intensity blue flash that lasted for 50 milliseconds (the 'switch flash'). The test flash was not intense enough to activate bi-ChR2, but was bright enough to evoke cone and horizontal cell hyperpolarization and rod depolarization. In contrast, the switch flash was bright enough to activate bi-ChR2 (Figure 3.8J). First, we recorded the voltage responses of rods and horizontal cells to the test flash. Next, we activated bi-ChR2 with the switch flash and, after several seconds, we measured the responses to the test flash again. Finally, we waited for a longer period of time, when horizontal cells had returned to their native state, and we measured the responses to the test flash again. We then repeated the flash series to ensure it was reproducible. We expected that the activation of bi-ChR2 by the switch flash would depolarize and shunt horizontal cells; this shunting, in turn, would suppress the effect of the cone input upon horizontal cells and, consequently, block the depolarization in rods.

We first applied this protocol while recording from horizontal cells. The test flash evoked a hyperpolarizing response in horizontal cells. In contrast, the switch flash depolarized horizontal cells for tens of seconds (Figure 3.8K-L); we observed a sustained depolarization following the switch flash, whether photoreceptor inputs to horizontal cells were intact or blocked by NBQX. Ten seconds after presentation of the switch flash, horizontal cells did not respond to a second test flash (Figure 3.8L-N). After five minutes, horizontal cells had returned to their native state and responded to the test flash once again (Figure 3.8L-N). We then measured from rods using the same protocol. Similarly to what we found in control

retinas, the first test flash evoked rod depolarization. However, following the presentation of the switch flash, the depolarizing response (to the test flash) disappeared and was replaced by a small hyperpolarizing response (Figure 3.8M-O). This small hyperpolarization likely reflected the direct light stimulation of the recorded rod and of the rods that were electrically coupled to it and that were not completely saturated. Alternatively, the hyperpolarization could reflect cone activity that reaches rods through cone-rod coupling. The rod hyperpolarization also served as a control, showing that the retina was not desensitized by the switch flash. From these experiments we conclude that cone-driven horizontal cell activity causes the inverted, depolarizing rod responses observed in the higher light intensity regime.

The molecular nature of the horizontal cell feedback to photoreceptors is not well understood (Thoreson and Mangel, 2012; Rozan Vroman et al., 2013) and may combine several pathways (Guo et al., 2010; Hirasawa and Kaneko, 2003; Kamermans et al., 2001; Vessey et al., 2005; Wang et al., 2014). It has been suggested that horizontal cells communicate with photoreceptors via a mechanism that does not use the inhibitory neurotransmitters GABA or glycine. However, this feedback is thought to be blocked by HEPES, a pH buffer (Thoreson and Mangel, 2012; Rozan Vroman et al., 2013). In agreement with this hypothesis, the amplitude of the depolarizing rod response was not suppressed when GABA and glycine receptors were blocked by picrotoxin and strychnine (Figure 3.9). GABA and glycine antagonists, however, did affect the rod response waveform, which suggests that these inhibitory transmitters influence some of the circuit elements (Liu et al., 2013). While HEPES decreased the mean rod depolarization significantly, a HEPES-independent rod depolarization persisted (Figure 3.10A-B).

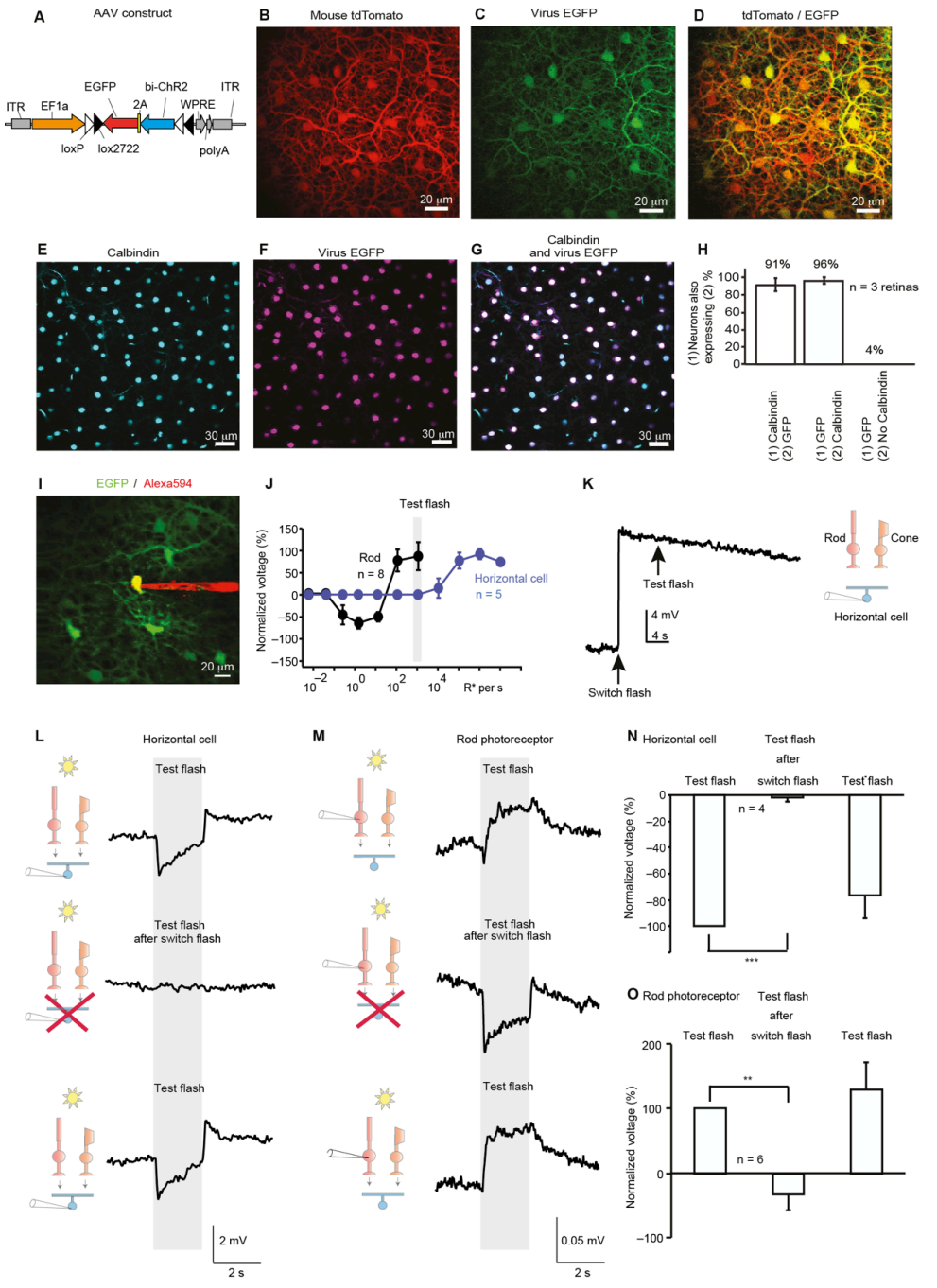

Figure 3.8 **Reversible inactivation of horizontal cells abolishes depolarizing light responses in rod photoreceptors.** (**A**) Conditional bi-ChR2- and EGFP-expressing adeno associated virus (AAV) construct. Mice expressing Cre and tdTomato in horizontal cells were injected with the conditional AAV. Horizontal cells expressing tdTomato (**B**) and EGFP (**C**) are co-labeled (**D**). (**E-H**) Quantification of horizontal cell transduction with AAV using the calbindin antibody that marks horizontal cells. (**I**) A patch pipette filled with Alexa594 recording from AAV-infected horizontal cells in wholemount retina is visualized by two-photon laser. (**J**) The blue trace shows normalized bi-ChR2-expressing horizontal cell responses to an 800 µm diameter light stimulus at different light levels (same positive contrast at each light level) in the presence of NBQX. These depolarizing light responses are

mediated by bi-ChR2. The black trace shows rod responses in control retinas, which were re-plotted from Figure 1k for comparison. The intensity of the test flash (gray bar) was chosen to evoke rod depolarization but not activate bi-ChR2 in horizontal cells. (**K**) Sustained depolarization recorded from bi-ChR2-expressing horizontal cells illuminated with high intensity blue light for 50 ms (switch flash, black arrow) in control solution. The response to the test flash (black arrow) is blocked 10 s after the switch flash. (**L-M**) Voltage responses of bi-ChR2-expressing horizontal cells (**L**) and rods (**M**) to test flash (top traces), test flash 10 s after switch flash (middle traces) and test flash at least five min after switch flash (bottom traces). (**N-O**) Quantification of the responses to the test flash before the switch flash, 10 s after the switch flash and five min after the switch flash. Responses were normalized to the magnitude of the response to the test flash before the switch flash. Negative values represent hyperpolarization, positive values depolarization (for N: $p < 0.001$, $t(3) = 131$, Student's paired t-test; for O: $p = 0.005$, $U = 0$, Mann-Whitney U test).

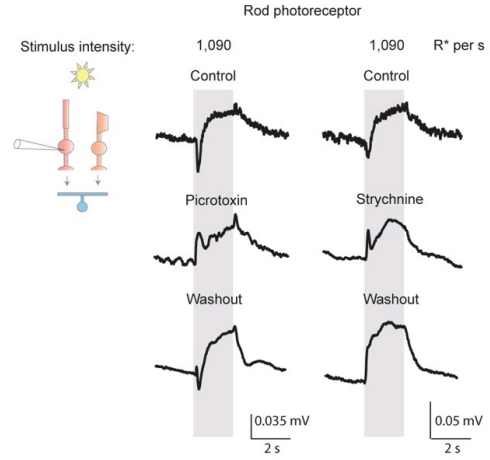

Figure 3.9. **The influence of picrotoxin and strychnine on the depolarizing rod response.** The effect of the GABA receptor blocker picrotoxin and the glycine receptor blocker strychnine on the depolarizing rod response evoked by an 800 µm diameter spot at 1090 R*/s intensity.

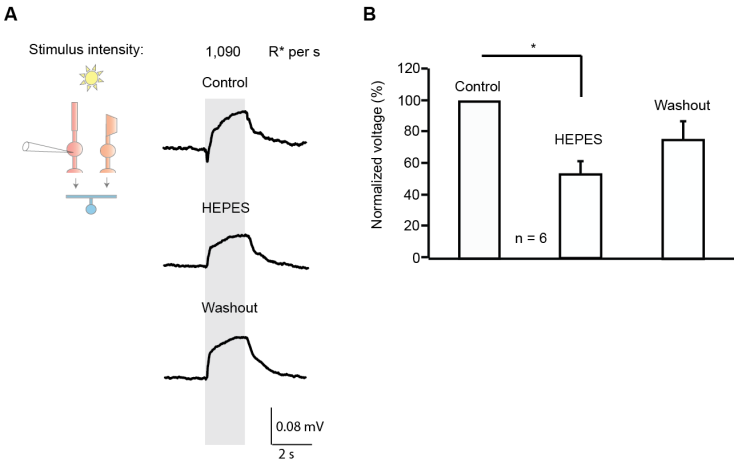

Figure 3.10 **The influence of HEPES on the depolarizing rod response.** (**A**) The effect of HEPES on the depolarizing rod responses. In (**B**) responses were normalized to the maximum depolarization evoked by the 800 µm spot at 1090 R*/s intensity ($p = 0.031$, Wilcoxon signed rank test).

Phenomenological model of rod depolarization

We constructed a phenomenological model of the cone-horizontal cell-rod circuit (Figure 3.11A). We used an earlier model of cone response (Clark et al., 2013) as a building block for our circuit model: the three 'blocks' in the model, for rod, cone, and horizontal cell, are described by simple equations with similar forms (Experimental procedures). Each of these three blocks represents an adaptive transfer in which the magnitude and the shape of the response depend on the stimulus history. Specifically, in each block the input is convolved with a filter, and the resulting quantity is then modulated in a non-linear way by another filtered version of the input (or two other filtered versions of the input, in the case of the rod block). Finally, the cone output serves as the input to the horizontal cell block, and the latter is coupled appropriately to the rod block (Experimental procedures).

The merit of this approach is not only the simplicity of the formulation and the low number of parameters, but also that the same model can be used to describe rod in slice and in wholemount retina. We first fitted parameters of the rod and cone equations; the fitting procedure is simplified by the fact that a subset of the parameters is fixed by the steady-state values of the responses (Figure 3.11B). The resulting blocks capture the behavior of rods and cones in slice (Figure 3.11C). Next, without re-fitting these rod and cone parameters, we coupled the two blocks through the horizontal cell block, for which parameters were fitted. In spite of its simplicity, the model captures both the magnitude and the dynamics of voltage responses across several decades of background light intensities (Figure 3.11C).

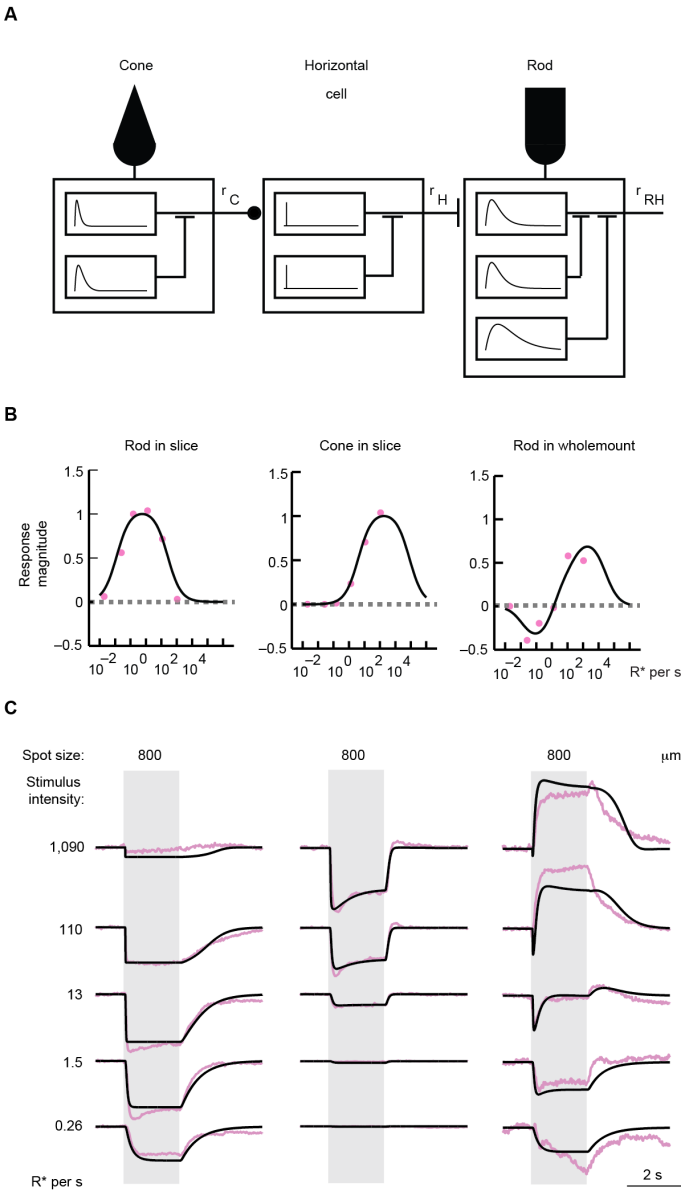

Figure 3.11 **Computational modeling of the cone-horizontal cell-rod circuit**. (**A**) Block model of the cone-horizontal cell-rod circuit. Each block consists of a non-linear combination of two filtered version of the input; in the case of the rod block, a third filter is necessary to describe the slower dynamics in rod response. Light intensity serves as the input to the rod block and the cone block, while cone output serves as the input to the horizontal cell block; the rod block also receives input from the horizontal cell block. See Experimental procedures for the equations schematized here. This quantitative model captures the response magnitude (**B**) and the dynamics (**C**) of rod and cone light responses across five decades of light intensities in slice (left and middle columns) and wholemount (right column). Model fit, black trace; recordings re-plotted from Figure 3.2D-F, magenta.

Cone depolarization at low light levels

Cones drive rod depolarization at high light levels when rods do not respond to light directly. Do rods, conversely, drive depolarization in cones at low light levels when cones do not respond to light directly?

To answer this question we recorded from cones at different background light intensities, spanning six decades, while stimulating the retina with large, positive-contrast spots. Cones in wholemount retina responded with a small and slow depolarization at those low light levels that evoked hyperpolarization in rods in wholemount and in slice (Figure 3.12A-C and 3.2D-I). The same stimulus evoked little or no response in cones in slice (Figure 3.2E-H). The depolarization turned to hyperpolarization at those light levels at which cones became responsive in slice preparation (Figure 3.2E-H). Therefore, while rods depolarize at high background light levels, cones depolarize, though to a smaller extent, at low light levels.

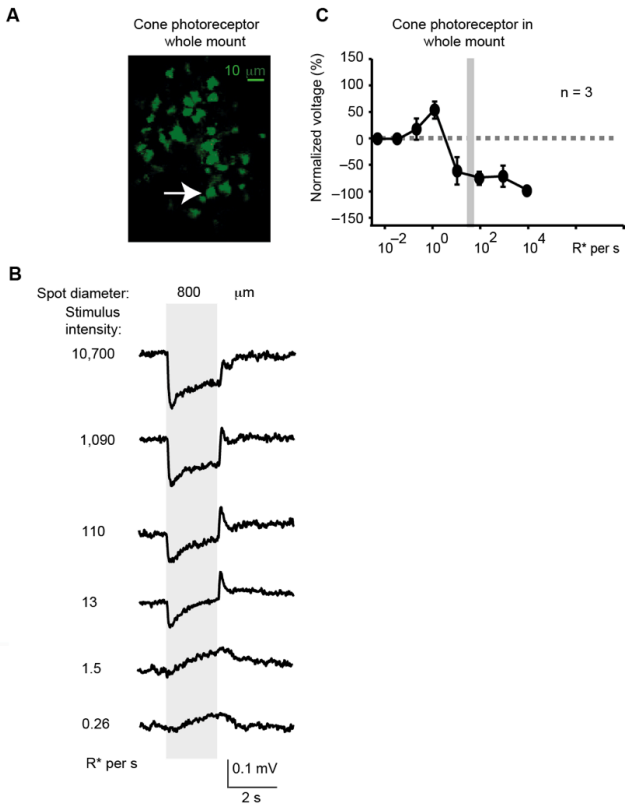

Figure 3.12 **Cone responses at different background intensities in wholemount retina**. (**A**) Cones were targeted in the Chrnb4-GFP mouse retina. The arrow indicates cell bodies on a two-photon image. (**B**) Responses of a cone to a positive contrast 800 µm diameter spot at different light intensities. Cones produced depolarization at low light levels and hyperpolarization at high light levels. (**C**) Normalized response magnitudes of cones as a function of stimulus intensity.

Rod depolarization propagates to the inner retina

Next we investigated if the depolarizing rod response at high background light levels affects the function of the inner retina. One way in which rod activity is transmitted to the inner retina is via rod bipolar cells (Wässle, 2004). Rod bipolar cells receive rod signals via sign-inverting synapses, which yield rod bipolar cell depolarization when rods hyperpolarize. To elucidate whether the depolarization of rods can influence the response of rod bipolar cells, we recorded from rod bipolar cells at different background intensities, in a mouse line in which these cells were GFP-labeled (Tomomura et al., 2001) (Figure 3.13A). At low light levels, bipolar cells responded to large spots of light with the usual depolarizing responses. However, their behavior changed at high light levels: when rods exhibited depolarizing responses to large spots, the rod bipolar cells displayed hyperpolarizing responses (Figure 3.13B). These hyperpolarizing responses were blocked by either APB, a drug which blocks communication between rods and rod bipolar cells, or NBQX, which blocks communication between photoreceptors and horizontal cells (Figure 3.13C). The rod bipolar cell hyperpolarizing response at high light levels cannot result from direct inhibition from horizontal cells to rod bipolar cells since APB blocked the response of rod bipolar cells. We conclude that the cone-driven horizontal cell-mediated surround inhibition leading to rod depolarization at high light levels is conveyed to the inner retina.

To test whether rod depolarization can affect the output cells in the retina, the ganglion cells, we developed an experimental approach that isolated signals induced by rods via rod bipolar cells and those induced by cones. We used a previously characterized inhibitory pathway in a genetically marked ganglion cell type, PV-5 cells (Münch et al., 2009), in mice which lacked the gap junction gene *Cx36* (Deans et al., 2002), as an indicator of rod bipolar-driven activity. Inhibitory input to PV-5 cells is received from AII cells, which are themselves stimulated by rod bipolar cells; in $Cx36^{-/-}$ background this pathway is decoupled from cone-driven bipolar cell activity (Münch et al., 2009). Similarly to rod bipolar cells, the inhibitory input in PV-5 ganglion cells, in response to stimulation with large spots, reversed polarity when the background light intensity was raised (Figure 3.13D-E). This experiment suggests that the influence of rod depolarization is relayed to the output cells of the retina.

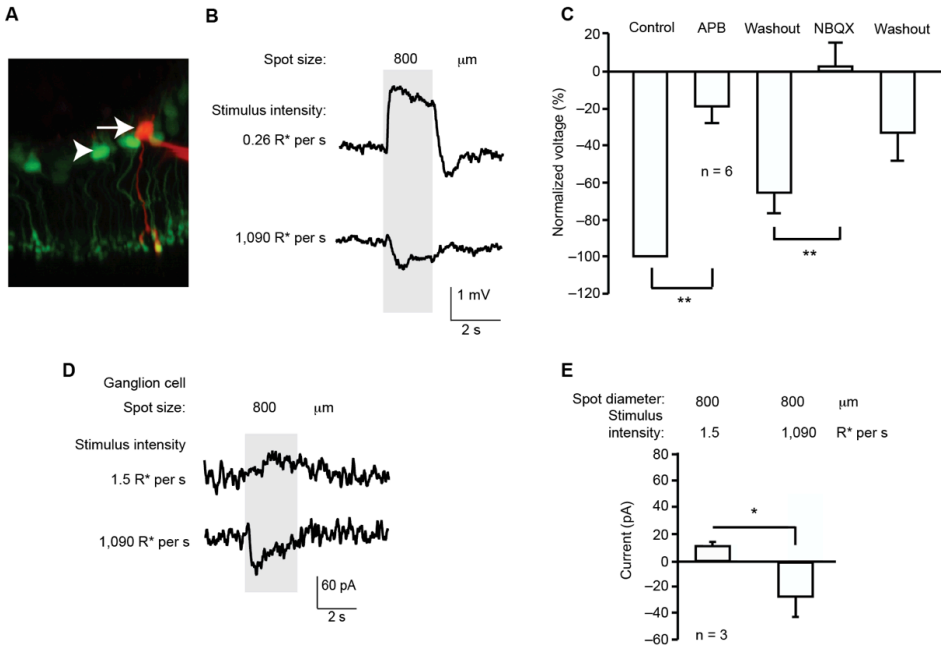

Figure 3.13 **Depolarizing rod responses are carried to rod bipolar cells and to the inner retina.** (**A**) The Pcp2-GFP transgenic mouse line was used to target GFP-labeled rod bipolar cells (arrowhead) in wholemount retina. The arrow indicates a rod bipolar cell targeted by a patch electrode filled with Alexa 594. (**B**) Voltage responses in a rod bipolar cell to an 800 μm diameter positive-contrast spot at two different light levels. (**C**) The effect of APB and NBQX on the hyperpolarizing responses at 1090 R*/s ($p = 0.005$, for both ABP and NBQX, $U = 0$, Mann-Whitney U test). Values were normalized to the magnitude of hyperpolarizing responses before drug application. (**D**) Inhibitory currents to a PV5 cell recorded during the presentation of an 800 μm diameter positive contrast spot at two different light levels. (**E**) Quantification of responses in D ($p=0.04$, $t(2) = 3.514$, Student's paired t-test).

Discussion

The key finding in this work is that in bright light conditions, rods relay cone-driven horizontal cell-mediated surround inhibition to the inner retina. The surround inhibition is measured as depolarization in rods and hyperpolarization in rod bipolar cells. Therefore in the light-adapted retina, the antagonistic surround of inner retinal cells is predicted to have two components: one that is mediated via the cone pathway and a second one, described here, that is mediated by the rod pathway. Our cone recordings suggest that cones carry rod surround at low light levels since they show depolarization by spatially extended stimulation at low intensities, when only rods are responding directly to light. This rod surround in the cone pathway could potentially also spread to the inner retina though we have not investigated this possibility in the present work.

Seesaw circuit

Our experiments suggest that the following sequence of events leads to cone-driven surround inhibition in the rod pathway: cones hyperpolarize in response to light; in turn, the dendrites of horizontal cells that contact cones hyperpolarize; dendritic hyperpolarization spreads to the axon terminals of horizontal cells via their long axons where horizontal cell hyperpolarization induces rod depolarization through a sign-inverting synapse. This is a feedforward inhibitory pathway. The circuit has a strong spatial component since both the axon terminals and the dendrites of horizontal cells are electrically coupled to the same compartments of neighboring horizontal cells. In addition, rods are also coupled to each other. This circuit acts like a 'seesaw' (Figure 3.14): under steady bright illumination that saturates rods, a light increment pushes the cone-end down (inducing a hyperpolarizing cone light response), and because of the sign-inverting horizontal cell, the rod-end swings up (depolarizes). Due to the extensive electric coupling of both rods and horizontal cells, the seesaw controlled by one cone can lift up many rods.

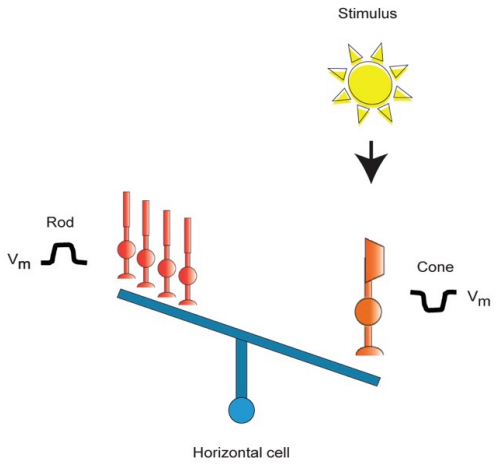

Figure 3.14 **The 'seesaw' model at daylight intensities**. Light stimulus leads to cone and, subsequently, horizontal cell hyperpolarization. Horizontal cell hyperpolarization, in turn, depolarizes rods via a sign-inverting synapse.

Rod depolarization carrying cone surround enters the inner retina via rod bipolar cells and likely gets back to the cone system at the terminals of cone ON and cone OFF bipolar cells, via the AII amacrine cells, which make sign-conserving electric synapses with ON cone bipolar cells and sign-inverting inhibitory chemical synapses with OFF cone bipolar cells (Wässle, 2004). At the axon terminals of bipolar cells, the portion of the cone surround that arrives via the rod pathway merges with the other portion that arrives via the cone-cone bipolar cell pathway. The cone surround relayed by the rod pathway and the cone pathway

likely have different functional properties: the surround via the rod pathway is broader since rods are coupled by gap junctions and likely more sustained.

Contribution of cone-rod coupling

Can rod depolarization be explained by an alternative circuit model, involving negative feedback between cones and horizontal cells (Thoreson and Mangel, 2012), together with electrical coupling between cones and rods (Bloomfield and Volgyi, 2009)? If negative feedback from horizontal cells is strong, a fullfield bright stimulus may evoke depolarization in cones, and this depolarization may spread to rods via electrical coupling, causing rods to depolarize. Our recordings argue against this model, since we recorded hyperpolarization in cones and depolarization in rods in response to fullfield stimulation in the same part of the retina.

Cone-rod coupling counteracts rod depolarization and therefore competes with the direct action of horizontal cells on rods. It has been suggested that cone-rod coupling is modulated by the circadian rhythm; it is stronger at night and weaker in daytime (Ribelayga et al., 2008). This could explain the relative weakness of this pathway in our experiments that were performed during daytime. A recent report has also emphasized the importance of the rod-rod bipolar pathway relative to cone-rod coupling in mice for transmitting rod activity to the inner retina (Ke et al., 2014). Nevertheless, cone-rod coupling could have contributed to the recorded voltage responses in our study in various ways. First, with small stimuli the suggested feedforward inhibitory pathway from cones to rods is weak: for these stimuli, cone-rod coupling would increase rod hyperpolarization recorded in light regimes at which cones are acting as photoreceptors. Similarly, cone-rod coupling would increase cone hyperpolarization when rods are acting as photoreceptors as shown in retinal slices (Asteriti et al., 2014). Second, using large stimuli, even at high light levels, we occasionally recorded a small hyperpolarizing transient in rods before the larger sustained depolarization. This fast hyperpolarization could be partially explained by cone-rod coupling. However, at the same light levels (1090 R*/s) we also recorded hyperpolarization in mice lacking cone responses (in *Gnat2*^{cpfl3} and *Cnga3*$^{-/-}$ mice). Therefore, it is likely that a part of the fast hyperpolarizing responses to large stimuli arises from rods responding directly to light (Naarendorp et al., 2010).

Rods have two distinct functional roles

Our findings indicate that rods fulfill at least two distinct functional roles, depending on the light conditions. First, in nightlight, rods capture photons and convey monochromatic visual information to the brain. Second, at high light levels at which only cones respond directly to

changes in light intensity, rods act as relay cells for horizontal cell surround inhibition. The retina is therefore efficient; the same retinal neurons are used for different purposes in different light conditions (Farrow et al., 2013; Grimes et al., 2014; Münch et al., 2009).

Interestingly, at light levels at which rods and cones both act as photosensors and where the absorption spectrum of the cones that drive horizontal cell inhibition to rods is substantially different from the absorption spectrum of rods, rods carry spectrally-opponent information. How the retina and higher visual centers use this spectrally opponent information remains to be understood.

Chapter 4 - How diverse retinal functions arise at the first visual synapse

Drinnenberg A*, *Franke F**, *Morikawa-Kanamori R, Juettner J, Hillier D, Hantz P, Hierlemann A, da Silveira R & Roska B*

**Co-first authors*

Summary

Many brain regions contain local interneurons of distinct types. How does an interneuron type contribute to the input-output transformations of a given brain region? We addressed this question in the mouse retina by chemogenetically perturbing horizontal cells, a single interneuron type acting at the first visual synapse, while monitoring the light-driven spiking activity in thousands of ganglion cells, the retinal output neurons. We uncovered six reversible perturbation-induced effects in the response dynamics and response range of ganglion cells. The effects were enhancing or suppressive, occurred in different response epochs, and depended on the ganglion cell type. A computational model of the retinal circuitry reproduced all perturbation-induced effects, and led us to assign specific functions to horizontal cells with respect to different ganglion cell types. Our combined experimental and theoretical work reveals how a single interneuron type can differentially shape the dynamical properties of distinct output channels of a brain region.

Introduction

Brain regions can be viewed as processing centers that transform the signals from several input channels into signals conveyed by several output channels. The circuits that compute these transformations often contain a diverse set of local interneuron types. How does an interneuron type contribute to the input-output transformations of a given brain region? A way to approach this question is to study how the activity of a given interneuron type affects the activity of the entire set of the region's output channels.

We employed this approach in the mouse retina, where the output channels consist of a diverse set of ganglion cell types (Sanes and Masland, 2015). Large populations of ganglion cells can be recorded simultaneously (Baden et al., 2016; Fiscella et al., 2012), and recent experimental progress provides genetic access to individual types of retinal interneurons (Siegert et al., 2012). Experimental knowledge on retinal physiology and circuitry is

advanced enough (Azeredo da Silveira and Roska, 2011; Masland, 2012) that it is possible to formulate computational models which are sufficiently precise to capture details in the data, but sufficiently general and simple to allow for a qualitative understanding of their mechanisms (Gollisch and Meister, 2010).

In this study we focus on retinal horizontal cells, which in mice constitute a single interneuron type (Peichl and González-Soriano, 1994). Horizontal cells reside at a strategic position within the visual system, since they act at the first visual synapse between photoreceptors and bipolar cells before the signal is split into parallel channels and, ultimately, gives rise to the responses of ~30 types of ganglion cells (Sanes and Masland, 2015). Horizontal cells receive glutamatergic input from photoreceptors; in turn, they deliver feedback inhibition to photoreceptors via a sign-inverting synapse (Baylor et al., 1971; Kamermans et al., 2001; Kramer and Davenport, 2015; Thoreson and Mangel, 2012; Vroman et al., 2013).

Previous work has suggested that horizontal cells contribute to the inhibitory surround of receptive fields (Chaya et al., 2017; Davenport et al., 2008; Ichinose and Lukasiewicz, 2005; Mangel, 1991; McMahon et al., 2004; Naka, 1971; VanLeeuwen et al., 2009; Vigh and Witkovsky, 1999), light adaptation (Chaya et al., 2017; Werblin, 1974; Wu, 1992), gain control (Klaassen et al., 2011; VanLeeuwen et al., 2009; Werblin, 1974), and color opponency (Joesch and Meister, 2016) in ganglion cells. These studies were based on pharmacological manipulations (Davenport et al., 2008; Ichinose and Lukasiewicz, 2005; McMahon et al., 2004; VanLeeuwen et al., 2009; Vigh and Witkovsky, 1999), current injections into horizontal cells (Mangel, 1991; Naka, 1971), or irreversible genetic perturbations, including horizontal cell ablation in adult mice (Chaya et al., 2017; Sonntag et al., 2012), and cell type-specific gene knock outs (Dedek et al., 2008; Klaassen et al., 2011; Pandarinath et al., 2010). However, these approaches provided only limited access to elucidate the roles of horizontal cells in shaping the responses of ganglion cells, as they either lacked cell-type specificity, were restricted to a limited retinal region, or did not allow for monitoring how the same ganglion cell responded in the presence and in the absence of horizontal cell feedback.

Here, we reversibly perturbed the activity of horizontal cells by targeting chemogenetic channels (Magnus et al., 2011) to horizontal cells across the entire retina. By performing two-photon calcium imaging of cones in whole-mount retinas, we show that the chemogenetic perturbation effectively and reversibly blocked horizontal cell feedback to cones. To monitor the perturbation-induced changes in the retinal output, we recorded the light-evoked spiking activity in thousands of ganglion cells before, during, and after the perturbation using high-density microelectrode arrays (Ballini et al., 2013; Müller et al., 2015b). We uncovered six reversible effects on the time course and the range of ganglion cell responses. By identifying

ganglion cell types on the microelectrode array and by performing targeted single-cell recordings, we investigated how the observed effects were distributed among different ganglion cell types. We then formulated a computational model to investigate how horizontal cell feedback can selectively influence different ganglion cells. The model captured the six experimentally observed effects, thus providing a unified picture of the diverse observations. Finally, based on our recordings and the model, we assigned specific functions to horizontal cells with respect to different ganglion cell types. Our combined experimental and theoretical work illustrates how a single site of feedback within a brain region can differentially influence the response dynamics of the region's output channels.

Results

Chemogenetic channel targeted to horizontal cells

To reversibly perturb the activity of horizontal cells, we targeted PSAM$^{L141F\ Y115F}$-GlyR (Magnus et al., 2011) (PSAM), a chloride-permeable ligand-gated ion channel, to horizontal cells. We injected AAVs that conditionally express PSAM into mice that express Cre recombinase in horizontal cells (*Gja10-Cre*) (Siegert et al., 2012; Szikra et al., 2014). We tested eight different AAVs with distinct serotypes, promoters and coding sequences to optimize expression in horizontal cells. Efficient and cell-type specific expression of PSAM was achieved by the systemic administration of AAV Ef1a-DIO-PSAM coated with the PHP.B capsid (Deverman et al., 2016) (Figures 4.1A-F and 4.2). A single intravenous injection led to retina-wide expression of PSAM in horizontal cells of both eyes. 89 ± 3% of horizontal cells expressed PSAM, and 99 ± 1% of PSAM-positive cells were horizontal cells (mean ± s.e.m; n = 6 mice, n = 352 horizontal cells, n = 316 PSAM-positive cells).

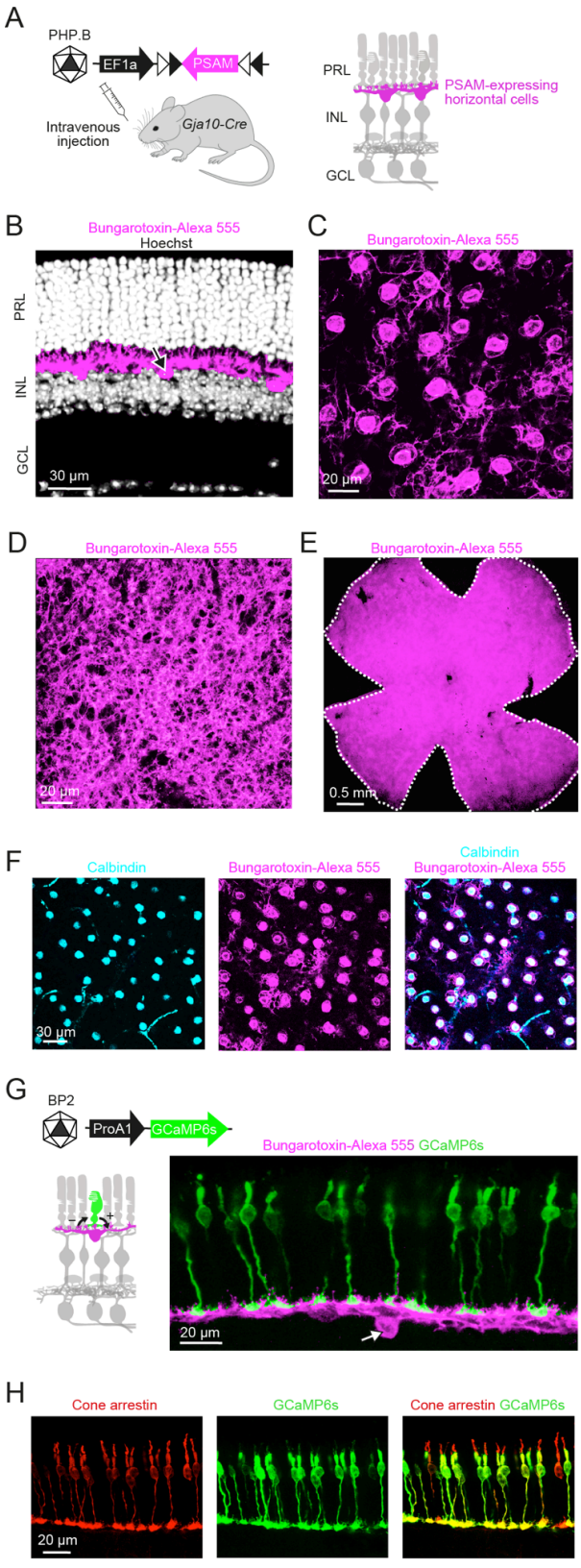

Figure 4.1 **Chemogenetic channel PSAM targeted to horizontal cells.** (**A**) Left, schematic of experimental strategy to target PSAM$^{L141F\ Y115F}$-GlyR (Magnus et al., 2011) (PSAM) to horizontal cells. Mice that expressed Cre recombinase specifically in horizontal cells (Gja10-Cre) were injected intravenously with AAV Ef1a-DIO-PSAM coated with the PHP.B capsid. Right, retinal circuit diagram with horizontal cells marked in magenta. PRL: photoreceptor layer; INL: inner nuclear layer; GCL: ganglion cell layer. (**B-E**) Confocal images of retinas of Gja10-Cre mice systemically injected with AAV Ef1a-DIO-PSAM. PSAM was labeled with bungarotoxin-Alexa 555 (magenta). Images show a retinal section (B), top view of the inner nuclear layer (C), top view of the outer plexiform layer (D), top view of the entire retina (E). In panel (B), cell bodies were stained with Hoechst (grey); arrow points at a cell body labeled with bungarotoxin-Alexa 555. The white dashed line in (E) indicates the outline of the retina. (**F**) Top view of the inner nuclear layer. Horizontal cells were labeled with calbindin antibody (cyan); PSAM was labeled with bungarotoxin-Alexa 555 (magenta). (**G**) Left, targeting cones by injecting serotype-BP2 AAV ProA1-GCaMP6s (schematic on top). ProA1 is a cone-specific promoter. The retinal circuit diagram (bottom) shows the sign-conserving synapse (+) from cones (green) to horizontal cells (magenta), and the sign-inverting synapse (−) from horizontal cells back to cones. Right, confocal image of a retinal section of a Gja10-Cre mouse systemically injected with AAV Ef1a-DIO-PSAM and subretinally injected with AAV ProA1-GCaMP6s. PSAM was labeled with bungarotoxin-Alexa 555 (magenta); GCAMP6s expression is shown in green. Arrow points at a cell body labeled with bungarotoxin-Alexa 555. (**H**) Confocal images of a retinal section of a Gja10-Cre mouse injected with AAV ProA1-GCaMP6s. Cones were labeled with cone arrestin antibody (red); GCAMP6s expression is shown in green.

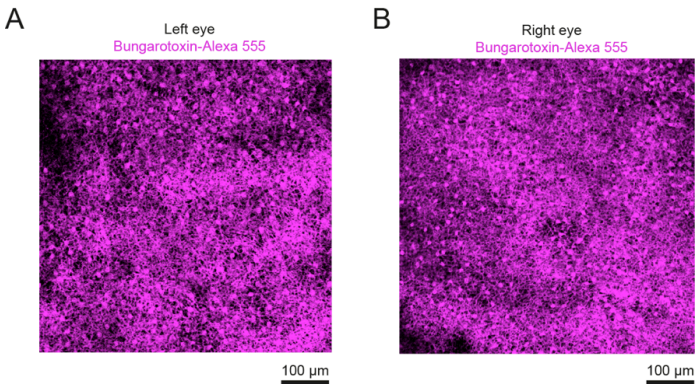

Figure 4.2 **Both eyes are infected after systemic AAV injection**. (**A-B**) Confocal images of the inner nuclear layer and outer plexiform layer (top view) of left (A) and right (B) retinas of a Gja10-Cre mouse that was injected intravenously with PHP.B AAV Ef1a-DIO-PSAM. PSAM was labeled with bungarotoxin-Alexa 555 (magenta).

We then imaged light-evoked calcium signals of individual cone axon terminals under photopic light conditions in whole-mount retinas of *Gja10-Cre* mice (Figure 4.3), either injected with the GCaMP6s-expressing AAV but not the PSAM-expressing AAV ('control retina', $n = 3$ mice, $n = 228$ cone terminals), or injected with both the PSAM-expressing AAV and the GCaMP6s-expressing AAV ('PSAM retina', $n = 3$ mice, $n = 256$ cone terminals). We imaged the same cone terminals before, during, and after PSEM application (bath-applied at a concentration of 3 µM (Basu et al., 2013)), and during the subsequent application of the AMPA receptor antagonist NBQX. NBQX blocks the glutamatergic input from cones to horizontal cells and, therefore, prevents horizontal cells from providing lateral inhibition to cones.

We quantified lateral inhibition in individual cone terminals, based on their responses to small and large flashed light spots, by computing a lateral inhibition index ('LII', the LII ranges from −1 to 1; it equals 1 when the response to the large spot is completely suppressed by lateral inhibition and it equals 0 when the response to the large spot is not affected by lateral inhibition). In control retinas (Figure 4.3A-F), lateral inhibition was not statistically different between 'non-PSEM' (mean of before PSEM application and after PSEM washout) and PSEM conditions (sign test, $P = 0.21$; non-PSEM, LII = 0.28 ± 0.02; PSEM, LII = 0.30 ± 0.03, mean ± s.e.m). Subsequent NBQX application strongly decreased lateral inhibition in the same cones (sign test, $P = 9.0\times10^{-43}$; before NBQX (same as washout of PSEM), LII = 0.28 ± 0.03; NBQX, LII = −0.020 ± 0.003, mean ± s.e.m). In contrast, in PSAM retinas (Figure 4.3G-L) PSEM strongly decreased lateral inhibition (sign test, P = 9.2×10-54; non-PSEM, LII = 0.25 ± 0.01; PSEM, LII = −0.00090 ± 0.003, mean ± s.e.m). Lateral inhibition before PSEM application and after washout of PSEM was not statistically different (sign test, P = 0.29; before PSEM, LII = 0.24 ± 0.01; after washout of PSEM, LII = 0.26 ± 0.01, mean ±

s.e.m). To assess the efficiency of the chemogenetic perturbation, we compared PSEM-induced and NBQX-induced effects in PSAM retinas. The NBQX-induced decrease was only slightly stronger than the PSEM-induced decrease (Figure 4.3L; sign test, P = 5.3×10-11; PSEM, LII = −0.00090 ± 0.003; NBQX, LII = −0.032 ± 0.008, mean ± s.e.m). The fraction of cones with decreased lateral inhibition was not statistically different between PSEM and NBQX conditions (Figure 4.3M; Fisher's exact test, P = 0.69; PSEM, 98%; NBQX, 99%), and the cones in which lateral inhibition was decreased by NBQX also showed a PSEM-induced decrease of lateral inhibition (Figure 4.3N; Spearman correlation coefficient R = 0.76). Together, these results show that the activation of PSAM in horizontal cells with 3 µM PSEM leads to specific, reversible, and efficient perturbation of horizontal cell feedback to cones.

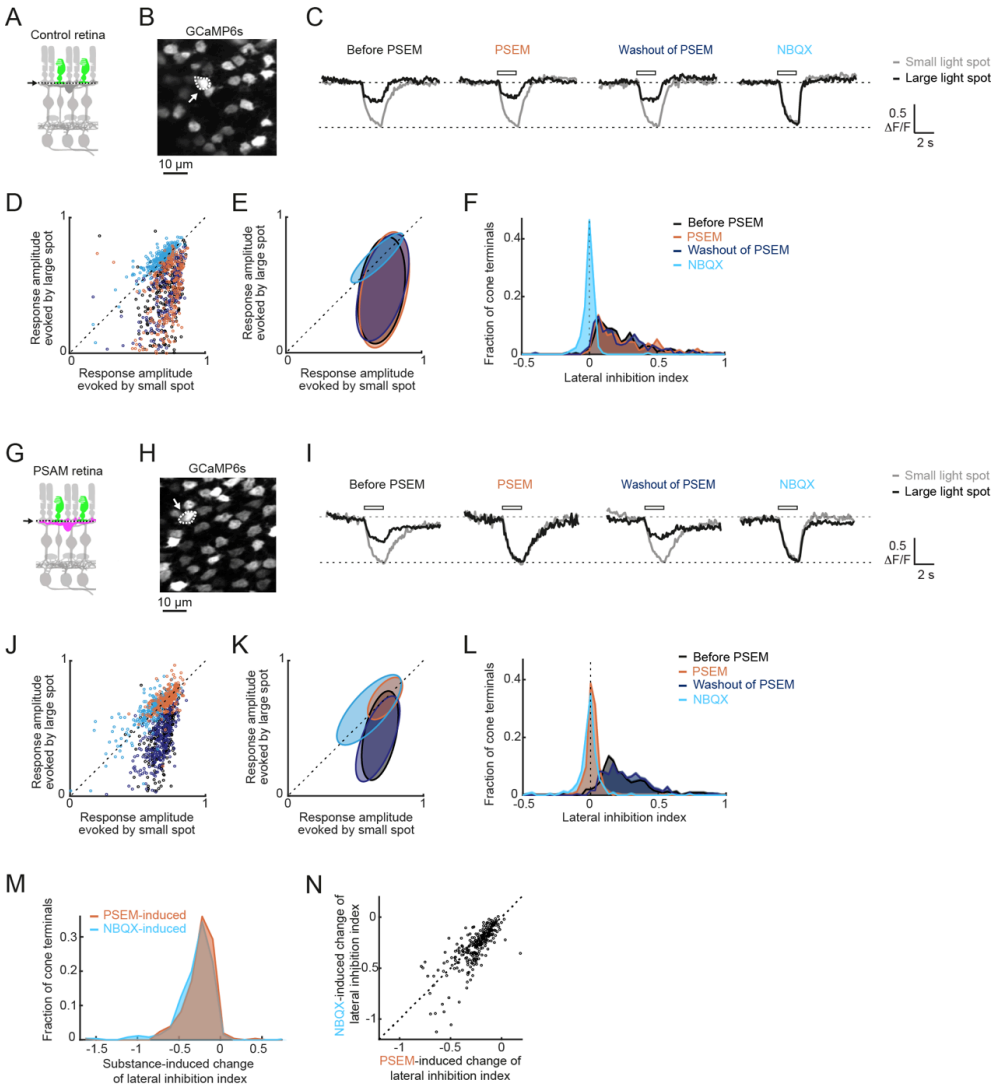

Figure 4.3 **Efficient and reversible perturbation of horizontal cell feedback revealed by imaging of cone axon terminals**. (**A**) Circuit diagram of the retina of a Gja10-Cre mouse injected with AAV ProA1- GCaMP6s ('control retina'). Cones expressed GCaMP6s (green). Dashed lines and arrow indicate the imaging plane. (**B**) Top view of a two-photon image of GCaMP6s-expressing cone axon terminals in a whole-mount preparation of a control retina. Dashed line and arrow indicate the terminal whose responses are shown in (C). (**C**) Example responses of a cone to 120 µm ('small', grey) and 3900 µm ('large', black) flashed light spots recorded in a control retina. Curves show the mean ΔF/F values of three stimulus repetitions. The white rectangles indicate the duration of the stimulus. Example responses of the same terminal are shown before, during, and after the application of the chemogenetic ligand PSEM, and during application of the AMPA receptor antagonist NBQX. (**D**) Scatter plots of response amplitudes evoked by small spots (x-axis) and large spots (y-axis) recorded in control retinas. Data points represent individual terminals. Responses of the same terminals are shown before, during, and after the application of the chemogenetic ligand PSEM, and during application of the AMPA receptor antagonist NBQX. Four data points were outside axis limits and are not shown. Dashed line indicates the unity line. (**E**) 2D Gaussian fits of data shown in (D). Ellipses show the two sigma equiprobability line. (**F**) Distributions of the lateral inhibition index ('LII') in control retinas for the four conditions. (**G**) Circuit diagram of the retina of a Gja10-Cre mouse injected with AAV ProA1-GCaMP6s and AAV Ef1a-DIO-PSAM ('PSAM retina'). Cones expressed GCaMP6s (green), and horizontal cells expressed PSAM (magenta). Dashed lines and arrow indicate the imaging plane. (**H-L**) As in (B-F), but for PSAM retinas. Two data points in (J) were outside axis limits and are not shown. (**M**) Distributions of the PSEM and NBQX induced changes in LII value in PSAM retinas. (**N**) Scatter plot of the PSEM-induced (x-axis) and the NBQX- induced (y-axis) changes in LII values of cones in PSAM retinas. Data points represent individual terminals. Four data points were outside axis limits and are not shown. Dashed line indicates the unity line.

Six distinct effects on the dynamics of ganglion cell responses

How does the perturbation of horizontal cells affect the retinal output? We recorded the light-evoked spiking activity of ganglion cells using high-density microelectrode arrays with >3,000 electrodes/mm2 (Ballini et al., 2013; Müller et al., 2015b) (Figure 4.4A-B). We selected blue (short-wavelength-sensitive) cones as the dominant image forming input by recording from the ventral retina under photopic light conditions. Green (medium-wavelength-sensitive) cones are largely restricted to the dorsal retina (Applebury et al., 2000; Baden et al., 2013), and light-sensing in rods is saturated in the light conditions we used. We monitored the activity of the same ganglion cells before, during, and after PSEM application in retinas of Gja10-Cre mice injected with the PSAM-expressing AAV ('PSAM retina', n = 29 mice) and in retinas of non-injected Gja10-Cre mice ('control retina', n = 5 mice), while probing the retina with a sequence of spatially uniform light stimuli of different contrasts (Figure 4.4C).

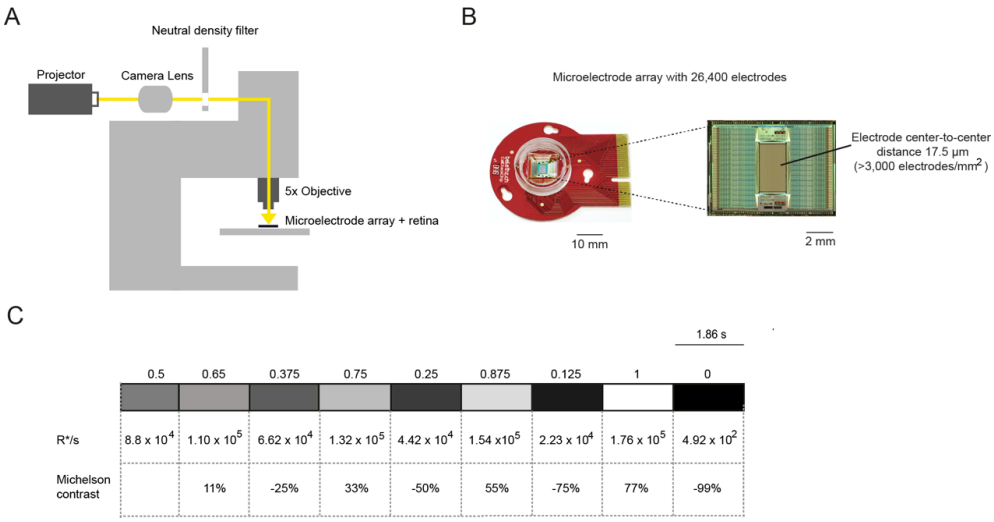

Figure 4.4 **System-level readout of retinal output.** (**A**) Schematic of experimental setup used for microelectrode array recordings. The light path for retinal stimulation is shown in yellow. The light was generated by a custom-built projector with two LEDs (395 and 505 nm) and focused on the microelectrode array by a camera lens and a 5× objective lens, after passing a neutral density filter (ND20). (**B**) Photos of a packaged CMOS-based high-density microelectrode array used in this study. Left, overview of a packaged chip. Right, zoom-in to the electrode area. (**C**) Sequence of spatially uniform light steps of increasing and decreasing contrasts used for retinal stimulation. The sequence starts with grey background light and consists of eight light steps. Top, grey values ranging from 0 (black) to 1 (white). Center, light intensity given in photoisomerizations per rod per second (R*/s, measured and computed as described previously (Farrow et al., 2013)). Bottom, Michelson contrast values.

We analyzed the responses of 6,591 ganglion cells and quantified PSEM-induced effects as the relative change (%) in the spike rate for PSEM versus non-PSEM conditions. We separately examined the responses to light increments ('on-responses') and to light decrements ('off-responses'). We defined ganglion cells that preferentially responded to light increments and light decrements as 'ON cells' and 'OFF cells', respectively. Moreover, for each light step we divided the responses into an early time window ('transient part of the response', first 0.5 seconds) and a late time window ('sustained part of the response', last 0.5 seconds of the 1.86 seconds duration of the light step). We then categorized ganglion cells based on their responses during the late time window: cells with <5 Hz activity were -classified as 'transient', while cells with >5 Hz activity were classified as 'sustained'. Finally, in OFF cells we analyzed rebound spiking responses to light increments ('rebound on-response', spike rate during 0.5-1.5 seconds time window after light increments), which are delayed on-responses that frequently occur in OFF cells under photopic light conditions (Tikidji-Hamburyan et al., 2015). In control retinas, we did not detect any significant off-target effects on the overall light-evoked spiking activity of ON cells and OFF cells using 3 µM PSEM (Figure 4.5). In the subsequent analysis, we compare PSEM-induced effects between PSAM retinas and control retinas.

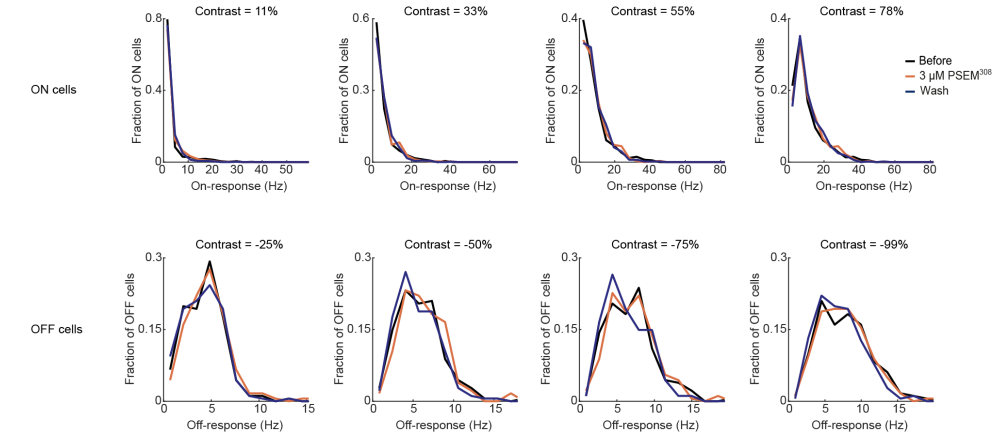

Figure 4.5 **No significant off-target effects of 3 μM PSEM on ganglion cells**. Spiking activity of ganglion cells recorded with microelectrode arrays from retinas of non-injected Gja10-Cre mice ('control retinas', n = 5 mice) in response to spatially uniform light steps of different contrasts before, during and after application of 3 μM PSEM. Responses were quantified as the mean spike rate during the entire duration (1.86 s) of the light step. Top row: the distributions of on-responses in ON cells were not statistically different between PSEM and non-PSEM conditions, for all four contrast steps tested (KS test, P-values at each contrast: 0.40, 0.57, 0.44, 0.44). Bottom row: the distributions of off-responses in OFF cells were not statistically different between PSEM and non-PSEM conditions, for all four contrast steps tested (KS test, P-values at each contrast: 0.21, 0.32, 0.32, 0.72).

We observed six strong and reversible PSEM-induced effects (numbered (*i*)-(*vi),* Figures 4.6, 4.7 and Table 4.1), which we describe hereafter. ON cells displayed three different effects (effects *i-iii,* Figures 4.6A-B and 4.7A-C). (*i*) First, in transient ON cells, PSEM suppressed the transient part of the on-response ('transient-on suppression'; Mann-Whitney U test, $P = 1.9\times10^{-30}$; PSAM retina, −14 ± 0.7%, n = 2,718 cells; control, 0.75 ± 0.9%, n = 484 cells, median ± s.e.m PSEM-induced change). 25% of transient ON cells showed transient-on suppression in PSAM retinas, whereas in control retinas, this fraction was significantly smaller, 1% (Fisher's exact test, $P = 2.9\times10^{-45}$). (*ii*) Second, both in transient and sustained ON cells, PSEM enhanced the sustained part of the on-response ('sustained-on enhancement'; Mann-Whitney U test, $P = 1.9\times10^{-7}$; PSAM retina, 37 ± 3%, n = 1,125 cells; control, 7.2 ± 5%, n = 129 cells, median ± s.e.m PSEM-induced change). 13% of transient ON cells and 24% of sustained ON cells showed sustained-on enhancement in PSAM retinas, whereas these fractions were significantly smaller in control retinas: 3.1% and 2.9% (Fisher's exact test, $P = 9.3\times10^{-13}$, transient cells; $P = 6.0\times10^{-6}$, sustained cells). Interestingly, we observed cases where transient-on suppression and sustained-on enhancement occurred in the same cell (Figures 4.6A and S3A-B; 19% of the transient ON cells showing sustained-on enhancement also showed transient-on suppression). (*iii*) Third, in sustained ON cells, PSEM enhanced the on-response over the entire duration of the light increment ('all-on enhancement'; Mann-Whitney U test, $P = 9.7\times10^{-4}$; PSAM retina, 19 ± 2%, n = 729 cells; control, 1.9 ± 2%, n = 70

cells, median ± s.e.m PSEM-induced change). 24% of sustained ON cells showed all-on enhancement in PSAM retinas, whereas in control retinas this fraction was significantly smaller, 4.3% (Fisher's exact test, $P = 3.3\times10^{-5}$).

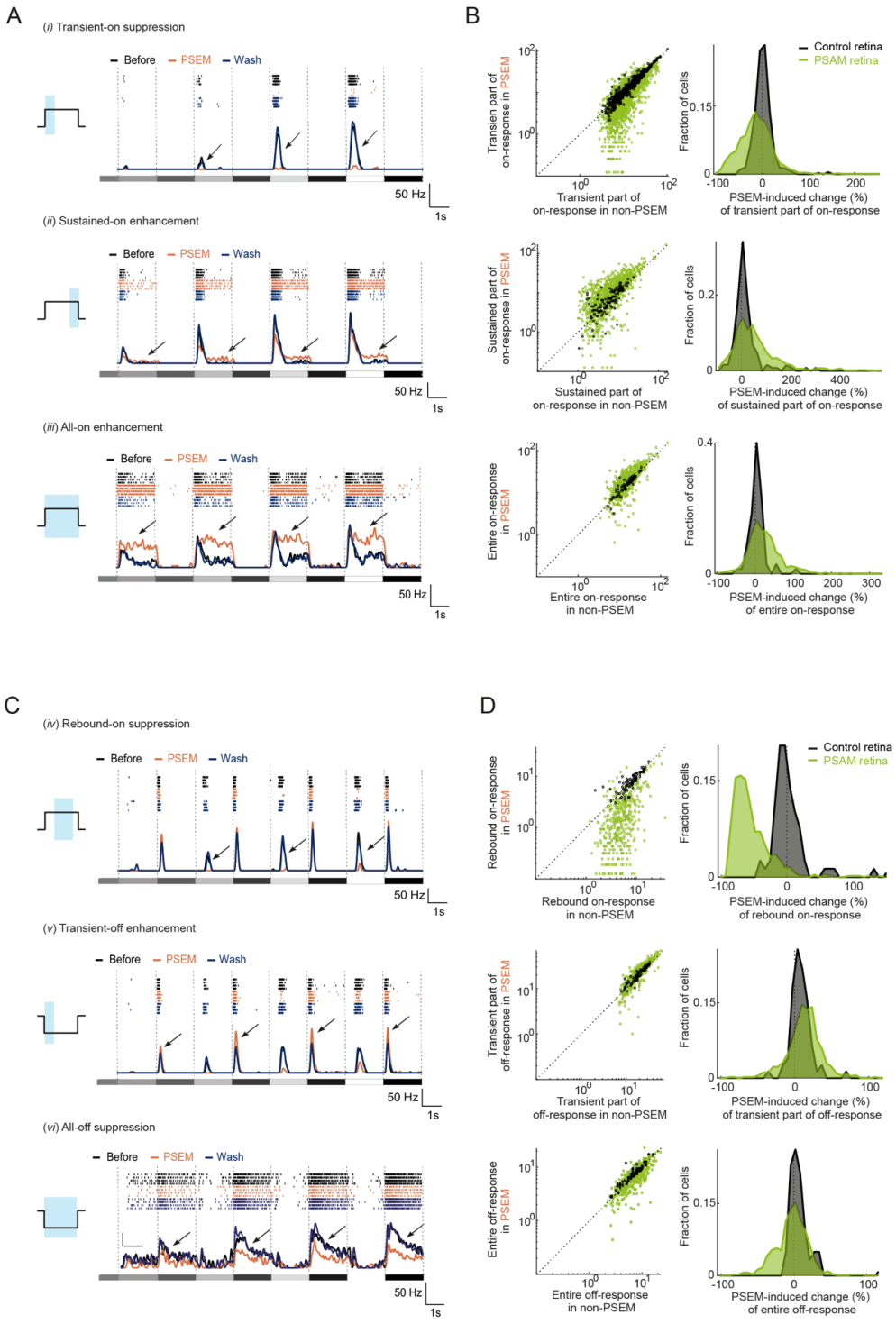

Figure 4.6 **Six distinct effects on the dynamics of ganglion cell responses.** (**A**) Spiking activity (top, raster plot, four repetitions per condition; bottom, spike rate, mean values of four repetitions) of three examples of ganglion cells that preferentially responded to light increments ('ON cells'), recorded with microelectrode arrays. The recordings were made in retinas of Gja10-Cre mice injected with AAV Ef1a-DIO-PSAM ('PSAM retina'). The stimuli consisted of spatially uniform light steps of different contrasts (grey shaded rectangles below response trace). Each cell exemplifies one PSEM-induced effect; arrows indicate the PSEM-induced effect. The schematic on the left illustrates the time window (blue area) with respect to a light step (black line) that was used for the quantification in (B). (**B**) Left, scatter plots of responses in 'non-PSEM' (refers to the mean value of 'before' and 'wash') conditions (x-axis) and 'PSEM' conditions (y-axis) recorded in retinas of non-injected Gja10-Cre mice ('control', black) or PSAM retinas (green). Responses were quantified as the mean spike rate during the respective time windows, averaged over the four positive contrast steps. Data points represent individual ON cells. Dashed line indicates the unity line. Right, distributions of PSEM-induced change values (in %) of the responses for the data shown in the left panel. (**C**) As in (A), but for three examples of ganglion cells that preferentially responded to light decrements ('OFF cells'). (**D**) As in (B), but responses were averaged over the four positive contrast steps (effect iv, top row of panels) or over the four negative contrast steps (effect v and vi, bottom two rows of panels).

In OFF cells, we also observed three reversible PSEM-induced effects (effects *iv*-*vi,* Figures 4.6C-D and 4.7D-F). (*iv*) First, in transient OFF cells that displayed rebound on-responses (47% of all transient OFF cells), PSEM suppressed the rebound on-responses ('rebound-on suppression'; Mann-Whitney U test, $P = 8.1\times10^{-37}$; PSAM retina, −63 ± 1%, n = 537 cells; control, −3.0 ± 3%, n = 78 cells, median ± s.e.m PSEM-induced change). This effect was very prevalent: 59% of transient OFF cells with rebound on-responses showed rebound-on suppression in PSAM retinas. In control retinas, this fraction was significantly smaller, 0% (Fisher's exact test, $P = 5.3\times10^{-28}$). (*v*) Second, in the same cells, PSEM enhanced the transient part of the off-response ('transient-off enhancement'; Mann-Whitney U test, $P = 5.3\times10^{-4}$; PSAM retina, 14 ± 1%; control, 5.9 ± 2%, median ± s.e.m PSEM-induced change). (*vi*) Third, in sustained OFF cells, PSEM suppressed the off-response over the entire duration of the light step in PSAM retinas compared to control retinas ('all-off suppression'; Mann-Whitney U test, $P = 0.00083$; PSAM retina, −1.0 ± 1%, n = 495 cells; control, 5.1 ± 2%, n = 61 cells, median ± s.e.m PSEM-induced change). 13% of sustained OFF cells showed all-off suppression in PSAM retinas, whereas in control retinas this fraction was significantly smaller, 0% (Fisher's exact test, $P = 5.0\times10^{-4}$).

Thus, the reversible perturbation of horizontal cells leads to an array of diverse and strong effects on the response dynamics of ganglion cells. Within a small area of the retina and at the same time, we found ganglion cells displaying different effects and ganglion cells that were not affected by PSEM (Figure 4.8), suggesting that the diversity of effects and the lack of effect in some ganglion cells, are not due to variations of PSAM expression or the adaptation state of the retina.

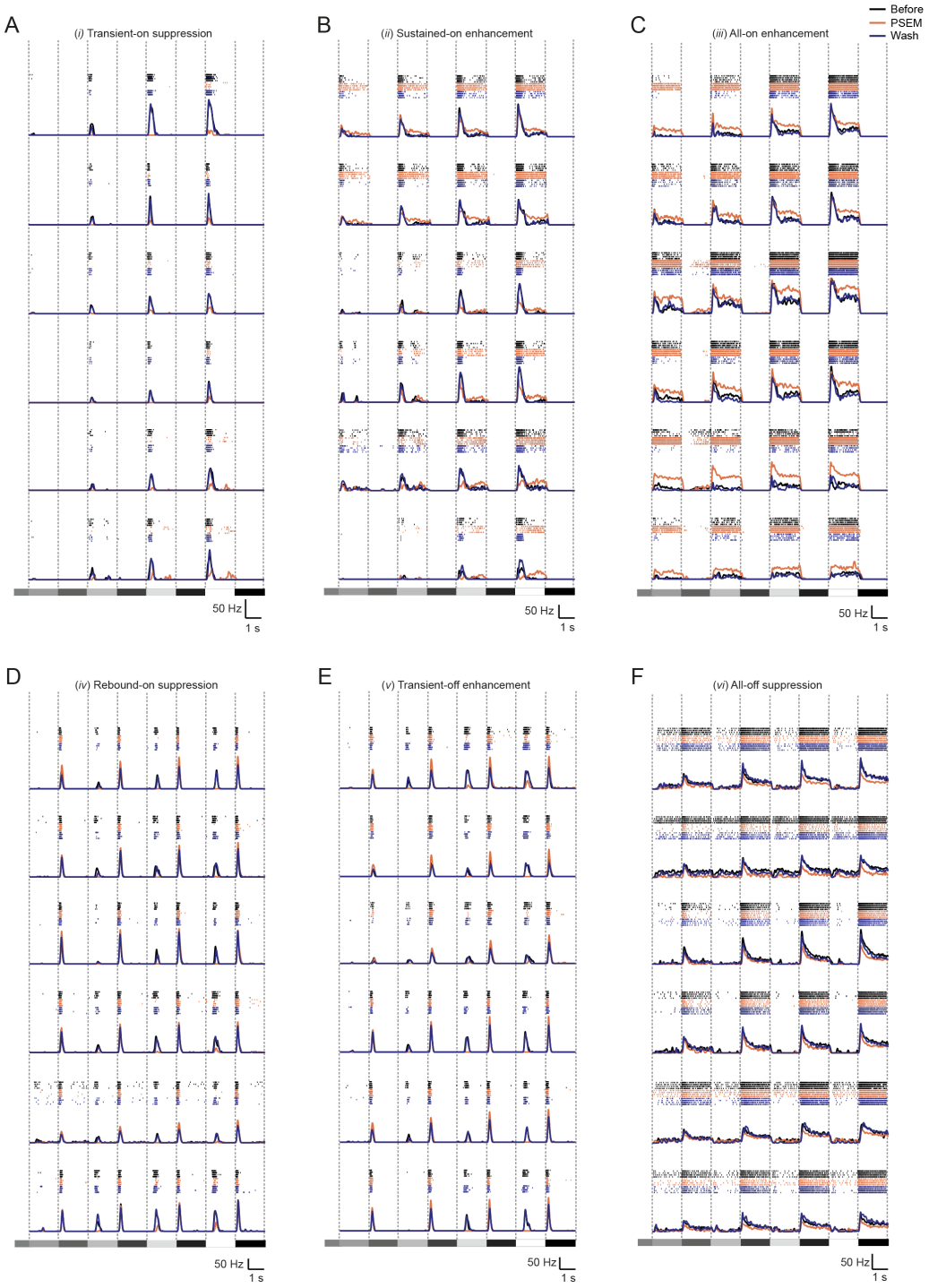

Figure 4.7 **Examples to illustrate the six effects of horizontal cells on the response dynamics of ganglion cells.** (**A-F**) Spiking activity (top, raster plot, four repetitions per condition; bottom, spike rate, mean values of four repetitions) of ganglion cells recorded with microelectrode arrays in retinas of Gja10-Cre mice that were injected systemically with AAV Ef1a-DIO-PSAM. Six example cells are shown for each PSEM-induced effect (Figure 4.6, effects i-vi). The grey shaded rectangles below the response trace indicate the stimulus contrast.

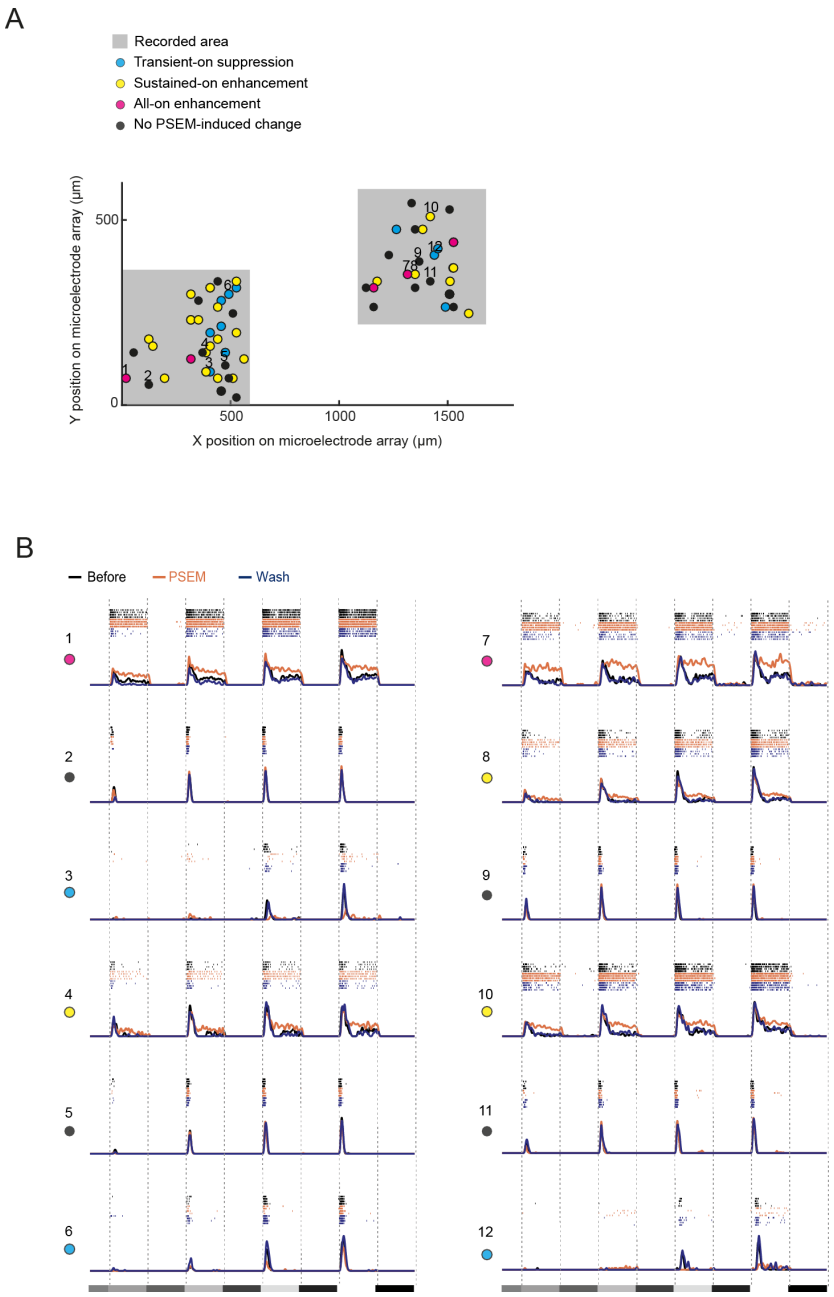

Figure 4.8 **Distinct effects can occur within a small retinal area and at the same time**. (**A**) The plot shows the spatial locations of ganglion cells exhibiting different PSEM-induced effects (blue, yellow, magenta), or no PSEM-induced response change (black), on a microelectrode array in an example PSAM retina. The cells were recorded simultaneously. The grey rectangles indicate areas with active electrodes. (**B**) Spiking activity (top, raster plot, four repetitions per condition; bottom, spike rate, mean values of four repetitions) of the twelve example cells whose locations are shown in (A). The grey shaded rectangles below the response traces indicate the stimulus contrast. The numbering and color-code of the spots below the numbers correspond to the numbering and color-code of (A).

Horizontal cells control the response range of ganglion cells

Next, we investigated how the six effects on the ganglion cell responses varied with stimulus contrast. We compared the response range of ganglion cells in PSEM and non-PSEM conditions (Figure 4.9). The response range is the difference between the maximal and minimal spiking response to different contrast steps, and quantifies the cell's ability to encode a range of different contrasts. We found that PSEM significantly compressed the response range of cells that exhibited suppressive PSEM-induced effects, i.e., (*i*) transient-on suppression (sign test, $P = 6.5\times10^{-118}$; non-PSEM 0.92 ± 0.007; PSEM 0.45 ± 0.009, median ± s.e.m response range; n = 675 cells), (*iv*) rebound-on suppression (sign test, $P = 4.1\times10^{-68}$; non-PSEM 0.96 ± 0.02; PSEM 0.10 ± 0.008, median ± s.e.m response range; n = 318 cells) and (v*i*) all-off suppression (sign test, $P = 2.0\times10^{-8}$; non-PSEM 0.46 ± 0.02; PSEM 0.30 ± 0.02, median ± s.e.m response range, n = 64 cells). In contrast, PSEM significantly extended the response range of cells that exhibited two of the enhancing PSEM-induced effects, i.e., (*ii*) sustained-on enhancement (sign test, $P = 4.7\times10^{-19}$; non-PSEM 1.2 ± 0.02; PSEM 1.8 ± 0.1, median ± s.e.m response range, n = 180 cells) and (*v*) transient-off enhancement (sign test, $P = 1.4\times10^{-4}$; non-PSEM 0.57 ± 0.02; PSEM 0.69 ± 0.04, median ± s.e.m response range, n = 73 cells). The response range of cells exhibiting (*iii*) all-on enhancement was not significantly changed (sign test, P = 0.13; non-PSEM 0.79 ± 0.02; PSEM 0.78 ± 0.03, median ± s.e.m response range, n = 177 cells), corresponding to a purely additive effect. These results indicate that horizontal cells can compress or extend the response range of ganglion cells, depending on the polarity and the time window of the response.

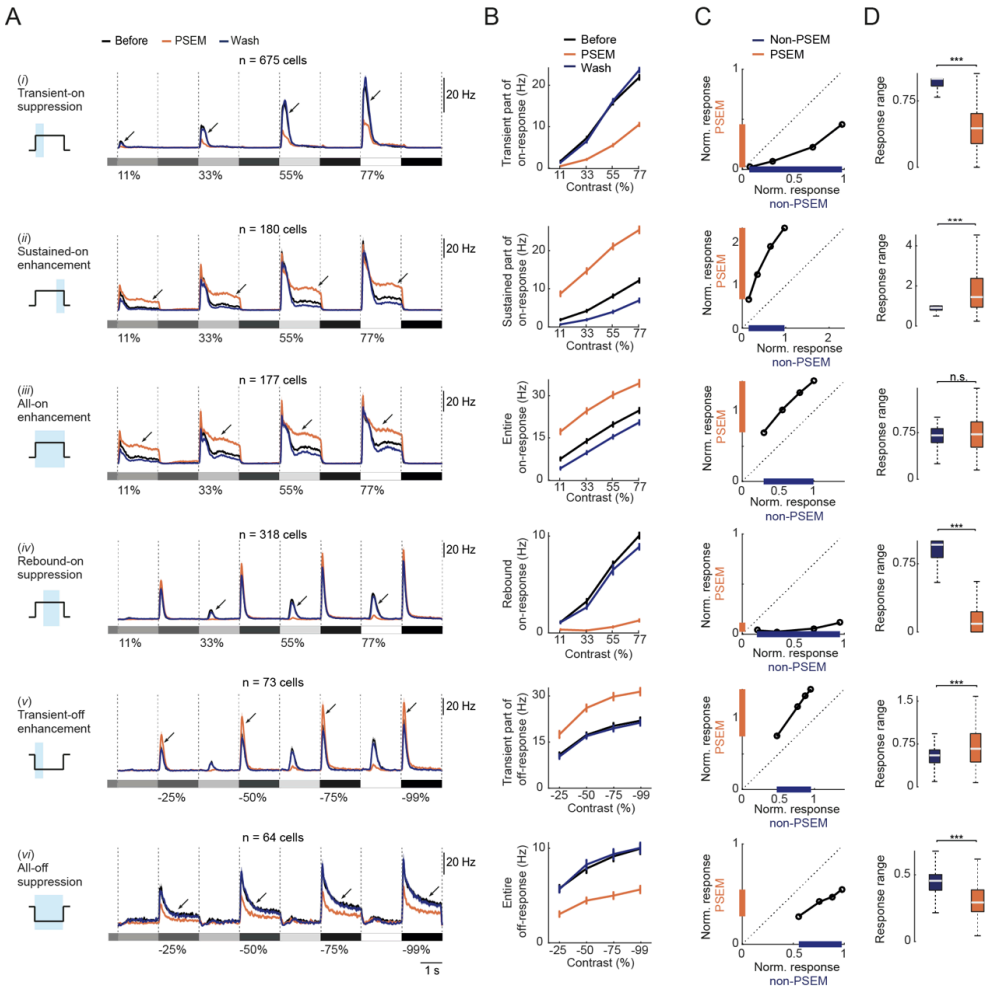

Figure 4.9 **Horizontal cells control the response range of ganglion cells.** (**A**) Each panel shows the spike rates of PSEM-affected cells in PSAM retinas for each of the six PSEM-induced effects (numbered i-vi, see Figure 4.6, PSEM-affected cells defined based on the distribution of responses in control retinas, see Methods). Curves show mean values across cells, shaded areas represent ± s.e.m. The grey shaded rectangles and the numbers (%) below the response traces indicate the stimulus contrast. Arrows indicate the PSEM-induced effects. The schematic on the left illustrates the time window (blue area) of the light step (black line) used for the quantification in (B, C). **(B)** Spiking responses (mean spike rate during the respective time window) of the cells shown in (A) plotted against the positive contrast steps of the stimulus (top four panels) or the negative contrast steps of the stimulus (bottom two panels), for each of the six PSEM-induced effects. Curves show mean values, error bars indicate s.e.m. (**C**) Scatter plots of normalized responses of cells shown in (A) in non-PSEM (x-axis) and PSEM (y-axis) conditions. Data points represent the responses to each of the four contrast steps, averaged across cells. The response of each cell was normalized to its maximal response in the non-PSEM condition. The colored intervals on the axes indicate the difference between the maximum and minimum of the normalized response ('response range') in PSEM (orange) and non-PSEM (blue) condition. Dashed line indicates the unity line. (**D**) Box-plot representation of the distributions of response ranges of PSEM-affected cells. Bottom and top whiskers indicate minima and maxima; bottom and top of the rectangle indicate first and third quartiles; the central line indicates the median. Outliers are not shown. n.s.: P >= 0.05, ***: P < 0.001.

	Effect name	Cell category	Polarity of response	Part of response	Direction of Effect	Effect on response range
(i)	transient-on suppression	transient ON cells	on-response	transient part	suppressive	compressed
(ii)	sustained-on enhancement	transient and sustained ON cells	on-response	sustained part	enhancing	expanded
(iii)	all-on enhancement	sustained ON cells	on-response	entire response	enhancing	-
(iv)	rebound-on suppression	transient OFF cells with rebound response	on-response	rebound response	suppressive	compressed
(v)	transient-off enhancement	transient OFF cells with rebound response	off-response	transient part	enhancing	expanded
(vi)	all-off suppression	sustained OFF cells	off-response	entire response	suppressive	compressed

Table 4.1 **Overview of the six effects (i-vi) of horizontal cell perturbation.**

Cell-type identification of ganglion cells on microelectrode arrays

So far, we have described how the perturbation of horizontal cells affects the response dynamics of the retinal output by classifying ganglion cells into broad functional categories (i.e., ON, OFF, sustained, transient). How are individual ganglion cell types affected? We designed a visual stimulus that allowed us to functionally classify ganglion cells into different types before monitoring how their responses were affected by horizontal cell perturbation. The stimulus was designed to meet three criteria: First, it should be short so that it can be used to classify cells before performing horizontal cell perturbation experiments. Second, cells positioned at different retinal locations should be exposed to the same light pattern, without the need of centering the stimulus on individual cells. Third, the stimulus should be naturalistic and rich in visual features. The resulting stimulus includes a series of vertical stripes of varying contrast, drifting across the retina at a constant speed along the horizontal axis ('barcode stimulus', Figures 4.10 and 4.11A). The stimulus is short (70 seconds for six repetitions) and exposes each cell to the same light pattern at different points in time so that the responses of individual cells can later be aligned to each other. Moreover, the stimulus is naturalistic, since the amplitude spectrum of the light intensity along the axis of drift was designed to follow a 1/f distribution (f: spatial frequency), which is typical for natural images (Burton and Moorhead, 1987; Field, 1987).

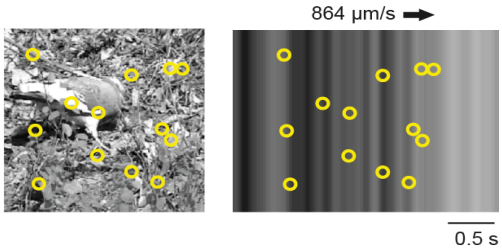

Figure 4.10 **Adapting natural stimuli for high-throughput recordings.** Left, schematic of a population of ganglion cells (yellow circles) exposed to a frame of natural movie (background image). Stimulation with natural movies poses the challenge that each cell of the population samples from a different movie patch, depending on its retinal location. Right, scheme of the same cell population exposed to a frame of the barcode stimulus (background image). Cells distributed vertically along the bars are exposed to the same stimulus. Since the stimulus is drifting across the retina at a constant speed (indicated by black arrow), horizontally distributed cells are also exposed to the same stimulus, just shifted in time.

We recorded the spiking responses of ganglion cells to the barcode stimulus using microelectrode arrays (n = 33 mice, n = 12,055 cells). The cells fired bursts of spikes that reliably occurred at distinct time points of the stimulus, which generated a characteristic response pattern in individual ganglion cells (Figure 4.11A). We performed hierarchical clustering to classify ganglion cells based on their responses to the barcode stimulus and assembled 30 clusters (Figures 4.11B-C). Within the clusters, the responses of the cells aligned, creating a pattern that resembled a barcode for a given cluster.

We compared how the functional clusters obtained using the barcode stimulus relate to previously characterized ganglion cell types. We developed a method to reveal the genetic identity of ganglion cells during microelectrode array recordings (Figure 4.11D-G). We targeted PSAM to a subset of previously characterized ganglion cells (Farrow et al., 2013; Viney, 2010) by injecting the eyes of *PV-Cre* mice with AAVs conditionally expressing PSAM. We identified PSAM-expressing PV ganglion cells by selecting the cells whose light-evoked spiking activity was reversibly suppressed by PSEM. Among PV ganglion cells, we focused on PV1, PV5, and PV6 cells by selecting PSEM-silenced cells with strong and reliable responses to large spatially uniform stimuli (Farrow et al., 2013; Viney, 2010) (Figure 4.12). We further categorized the cells into PV1 (ON cell, n = 18 cells), PV5 (OFF cell, n = 27 cells), and PV6 (OFF cell, n = 15 cells) cells based on the polarity and the time course of their responses (Figure 4.12). The responses of the PSEM-identified PV1, PV5 and PV6 cells to the barcode stimulus were similar across cells of the same type, but different across cells of different types (Figure 4.11H; one-way multivariate analysis of variance (MANOVA), $P = 1.4\times10^{-7}$). 94% of PSEM-identified PV1 cells were classified to cluster 1, while 80% of PSEM-identified PV6 cells were classified to cluster 14 (Figure 4.11I). Most PSEM-identified PV5 cells were found in cluster 13 (44%) and cluster 15 (48%). These results

indicate that ganglion cells of a given, previously characterized cell type accumulate in the same clusters.

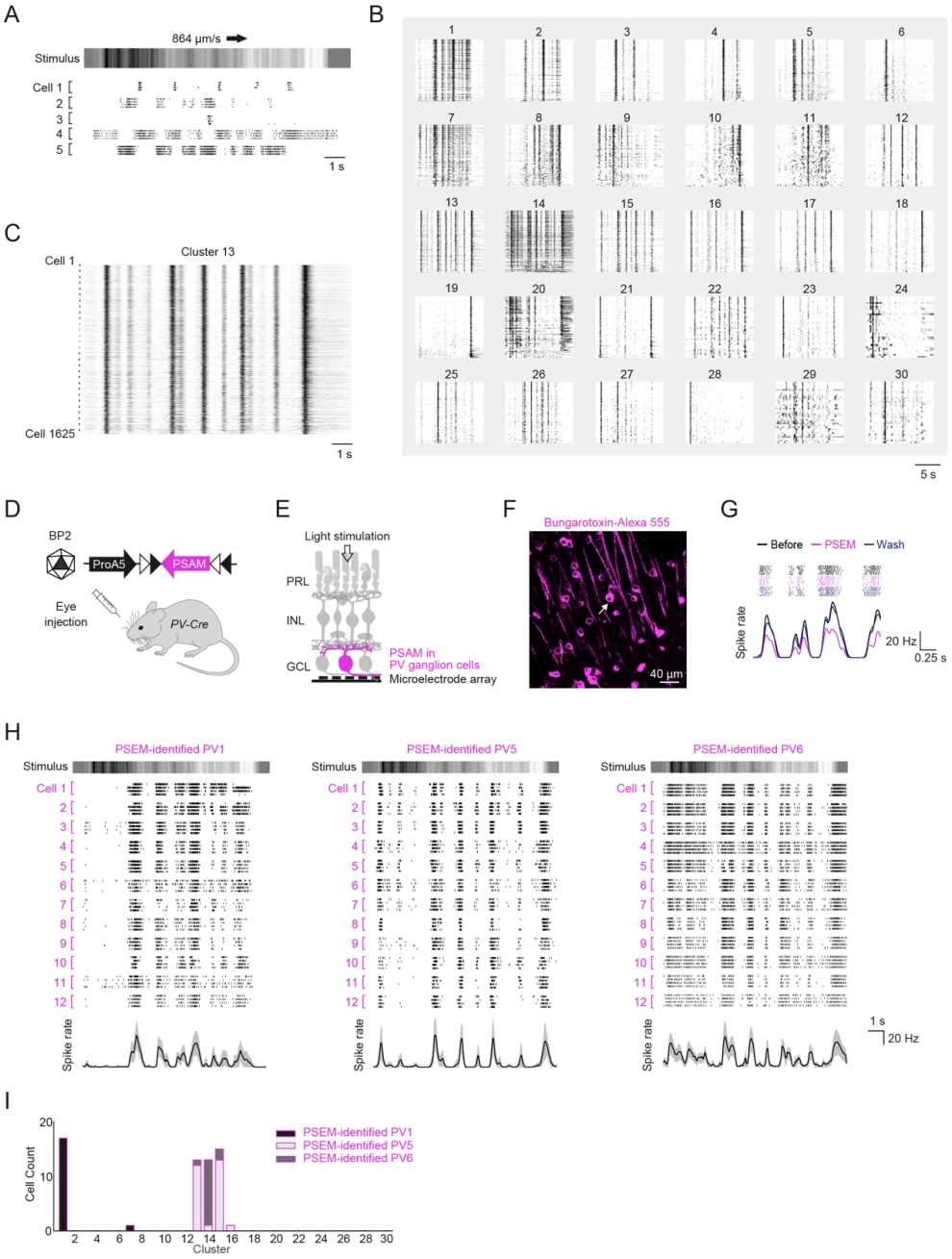

Figure 4.11 **Cell-type identification of ganglion cells on microelectrode arrays.** (**A**) Top, schematic of naturalistic stimulus ('barcode stimulus') designed for functional classification of ganglion cells on microelectrode arrays. Arrow indicates the motion of the stimulus across the retina at 864 µm/s. Bottom, raster plot of spiking activity of five example ganglion cells recorded with microelectrode arrays in response to the barcode stimulus. Four stimulus repetitions are shown for each cell. (**B**) Raster plots of the spiking activity of ganglion cells in response to the barcode stimulus. Each panel (1-30) shows the responses of all cells in one of the 30 clusters which were obtained by hierarchical

clustering. (**C**) Close-up of the responses of all cells classified to cluster 13. (**D**) Schematic of the experimental strategy to genetically identify ganglion cell types during microelectrode array recordings. The eyes of PV-Cre mice, which expressed Cre recombinase in a set of previously characterized ganglion cell types (Farrow et al., 2013; Viney, 2010), were injected with AAV ProA5-DIO-PSAM coated with the BP2 serotype. ProA5 drives expression in ganglion cells. (**E**) Retinal circuit diagram to illustrate chemogenetic labeling of PV ganglion cells (magenta) during microelectrode array recordings. (**F**) Confocal image (top view) of ganglion cell layer of the retina of a PV-Cre mouse injected with AAV ProA5-DIO-PSAM ('PV-PSAM retina'). PSAM was labeled with bungarotoxin-Alexa 555 (magenta). Arrow points to a labeled cell body. (**G**) Spiking activity (top, raster plot, seven repetitions per condition; bottom, spike rate, mean values of seven repetitions) of an example ganglion cell recorded with a microelectrode array from a PV-PSAM retina before, during, and after PSEM application. The stimulus was a short natural movie. (**H**) Top, schematic of the barcode stimulus. Middle, raster plots of responses of twelve example cells recorded in PV-PSAM retinas. The cells were reversibly silenced by PSEM, and further categorized as PV1 (left column of panels), PV5 (center), or PV6 (right) cells based on their responses to light steps of different contrast (Figure 4.12**,** Experimental procedures). Bottom, spike rate (black: mean values, grey areas: ± s.d.). (**I**) Distributions of PSEM-identified PV1, PV5 and PV6 cells over the clusters obtained using the barcode stimulus.

A

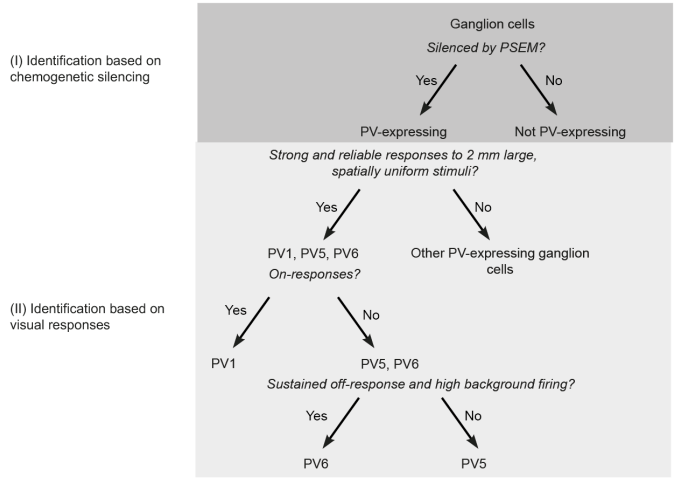

B

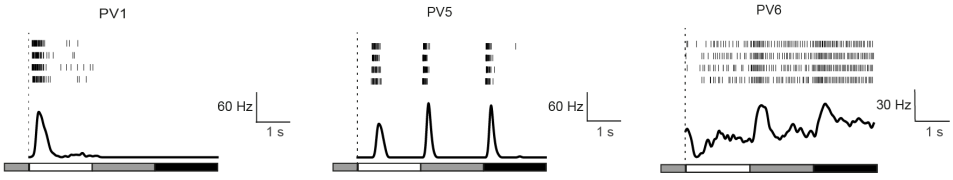

Figure 4.12 **Identification of PV-expressing ganglion cells on microelectrode arrays.** (**A**) Schematic of the decision tree to identify PV1, PV5, and PV6 cells on microelectrode arrays in retinas of PV-Cre mice injected with AAV ProA5-DIO-PSAM. Identification was performed in two steps: In a first step, PV ganglion cells were identified by determining those cells whose spiking activity was reversibly silenced by PSEM application. In a second step, PV1, PV5 and PV6 cells were selected by choosing cells with strong and reliable responses to large stimuli and the cells were further categorized into PV1, PV5, and PV6 cells based on their responses to light steps of different contrasts. (**B**) Spiking activity of three examples of PSEM-silenced cells in response to spatially uniform light steps of different contrasts (grey shaded areas below response traces). Based on the previously characterized responses of PV

ganglion cells (Farrow et al., 2013; Viney, 2010), these three PSEM-silenced cells were identified as PV1, PV5 and PV6 cells.

Horizontal cells differentially affect individual ganglion cell types

We used the identification of ganglion cell types on the microelectrode array ('on-array' cell type identification) to investigate how horizontal cells shape the response dynamics of PV1, PV5, and PV6 cells (Figure 4.13). We further confirmed our findings by performing targeted single-cell recordings of PV1, PV5, and PV6 cells using patch electrodes in retinas of triple transgenic mice (*Gja10Cre* × *PV-Flp* × *Flp-GFP*-reporter), injected with AAVs conditionally expressing PSAM (Figure 4.13A-C). On-array identified ganglion cells of cluster 1 (the cluster to which most PV1 cells were assigned), as well as single-cell recorded, GFP-identified PV1 cells (n = 11 mice, n = 16 cells) displayed sustained-on enhancement (Figure 4.13D-E; Mann-Whitney U test, $P = 5.7\times10^{-4}$; PSAM retina, 41 %, n = 638 cells; control, 1%, n = 28 cells; median PSEM-induced change). On-array identified ganglion cells of clusters 13 and 15 (the two clusters to which PV5 cells were assigned) and single-cell recorded, GFP-identified PV5 cells (n = 9 mice, n = 17 cells) showed rebound-on suppression (Figure 4.13F-G; Mann-Whitney U test, $P = 3.2\times10^{-22}$ PSAM retina, −62%, n = 444 cells; control, 3%, n = 42 cells; median PSEM-induced change), combined with transient-off enhancement (Figure 4.13F, H; Mann-Whitney U test, P = 0.0033; PSAM retina, 12 %, n = 675 cells; control, 3%, n = 55 cells; median PSEM-induced change). In on-array identified ganglion cells of cluster 14 (the cluster to which most PV6 cells were assigned) and in single-cell recorded, GFP-identified PV6 cells (n = 9 mice, n = 10 cells) the rebound-on suppression was present, but less pronounced than in cluster 13/15 (Figures 4.13I-J and 4.14; Mann-Whitney U test, $P = 4.3\times10^{-10}$; cluster 13/15, −62%, n = 422 cells; cluster 14, −29%, n = 375 cells; median PSEM-induced change) and the transient part of the off-response was suppressed rather than enhanced (Figures 4.13I, K and 4,14; Mann-Whitney U test, $P = 3.1\times10^{-4}$; cluster 13/15, 12%, n = 675 cells; cluster 14, −4%, n = 454 cells; median PSEM-induced change). These results indicate that horizontal cell perturbation differentially affects individual ganglion cell types.

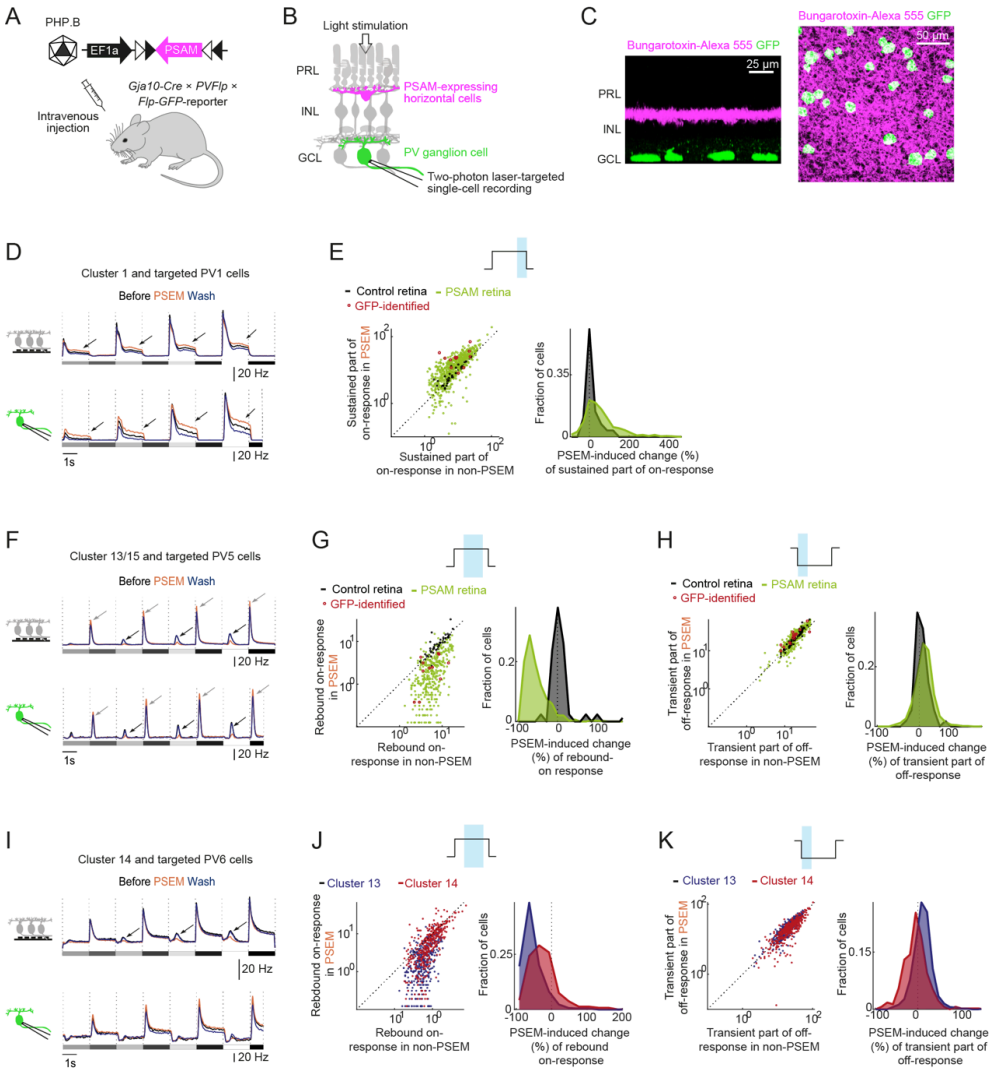

Figure 4.13 **Horizontal cells differentially affect individual ganglion cell types.** (**A**) Schematic of the experimental strategy allowing for targeted single-cell recordings of PV ganglion cells and chemogenetic perturbation of horizontal cells in the same mice. Gja10Cre × PV-Flp × Flp-GFP-reporter mice, which express Cre recombinase in horizontal cells and GFP in a set of previously characterized ganglion cell types (Farrow et al., 2013; Viney, 2010), are injected systemically with AAV Ef1a-DIO-PSAM coated with the PHP.B capsid. (**B**) Schematic to illustrate two-photon laser-targeted single-cell recording in retinas in which PV ganglion cells were GFP-labeled (green) and horizontal cells expressed PSAM (magenta). (**C**) Confocal images of retinas of Gja10Cre × PV-Flp × Flp-GFP-reporter mice injected with AAV Ef1a-DIO-PSAM ('PV-labeled PSAM retinas'). PSAM was labeled with bungarotoxin-Alexa 555 (magenta); GFP expression is shown in green. Left, side view of the confocal projection. Right, top view of the confocal projection. (**D**) Top, spike rates of cells that were classified to cluster 1 recorded in PSAM retinas using microelectrode arrays (schematic on left). Bottom, targeted single-cell spike recordings (schematic on left) of PV1 cells in PV-labeled PSAM retinas. Curves show mean values, shaded areas represent ± s.e.m. Arrows indicate the PSEM-induced effects. The grey shaded rectangles below the response indicate the stimulus contrast (same stimulus as in Figure 4.6). (**E**) Left, scatter plot of responses in non-PSEM (x-axis) and PSEM (y-axis) conditions. Data points represent individual cells of cluster 1, recorded in control retinas (black) or PSAM retinas (green), and targeted single-cell recordings of PV1 in PV-labeled PSAM retinas (red). Responses were quantified as the mean spike rate during the respective time window (blue area on top), averaged over the four positive contrast steps. Dashed line indicates the unity line. Right, distributions of PSEM-

induced relative changes (%) of the responses for the data recorded with microelectrode arrays shown in the left panel. (**F**) As in (D), but for cells classified to cluster 13/15 and targeted PV5 cells. (**G-H**) As in (E), but for cells classified to cluster 13/15 and targeted PV5 cells. In (H) responses were averaged over the four negative contrast steps. (**I**) As in (D), but for cells classified to cluster 14 and targeted PV6 cells. (**J-K**) As in (G-H), but for cells of cluster 13/15 (blue) and cluster 14 (red).

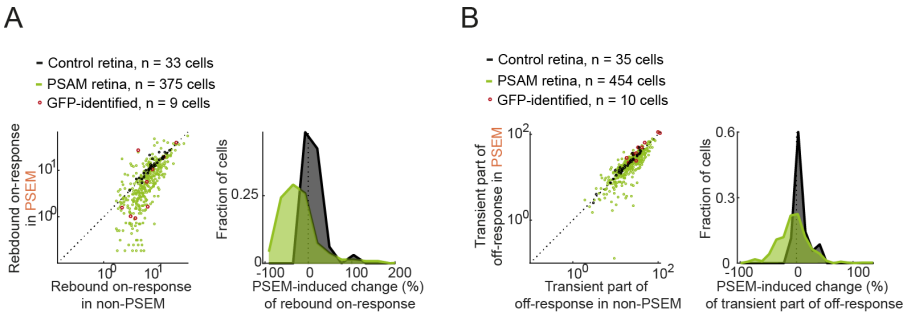

Figure 4.14 **Horizontal cell perturbation effects in Cluster 14 and PV6 cells.** (**A-B**) Left, scatter plots of spiking responses in PSEM versus non-PSEM conditions. Black and green indicate cells of cluster 14 recorded with microelectrode arrays in retinas of non-injected Gja10-Cre mice ('control retinas', black) and in retinas of Gja10-Cre mice injected with AAV Ef1a-DIO-PSAM ('PSAM retinas', green); red indicates cells recorded by two-photon laser-targeted patch-clamp recordings in retinas of Gja10Cre × PV-Flp × Flp-GFP-reporter mice that were systemically injected with AAV Ef1a-DIO-PSAM. Data points represent individual cells. Dashed line indicates the unity line. PSEM suppresses the rebound-on response (panel A; Mann-Whitney U test, $P = 4.3\times10^{-10}$ PSAM retina, −29%, n = 375 cells; control, 8%, n = 33 cells; median PSEM-induced change) and the transient-off response (panel B; Mann-Whitney U test, P = 0.00031; PSAM retina, −4 %, n = 454 cells; control, 5%, n = 35 cells; median PSEM-induced change). Right, distributions of PSEM-induced relative changes (%) of responses for the data shown in the left panel.

Computational model of retinal pathways

The reversible perturbation of horizontal cells led to a catalogue of distinct response changes in the retinal output, at different epochs in the response and in different ganglion cell types. Can our knowledge of the retinal circuitry account for the observed effects? In particular, how can the same interneuron type mediate both response suppression and enhancement in ganglion cells of a given polarity, or even in a single ganglion cell at different time points in its response?

To answer these questions, we constructed a computational circuit model, which related spatially uniform light input to ganglion cell output (Figure 4.15A). The model consisted of an outer retina component, describing the cone response together with horizontal cell feedback inhibition; an inner retina component, describing the parallel, feedforward processing of the signal; and a ganglion cell component, which received input from the inner retina component and transformed it to spiking activity. For the outer retina component we extended earlier models of the cone response (Clark et al., 2013; Szikra et al., 2014), which were supported by data, to include delayed feedback inhibition from horizontal cells. The

inner retina component consisted of six parallel, feedforward pathways (Figure 4.15A), three sign-conserving (OFF) pathways and three sign-inverting (ON) pathways. Each pathway consisted of a temporal filter and a thresholding unit. The temporal filters were identical for ON and OFF pathways and extracted different temporal properties of the cone response ('fast pathway': narrow biphasic temporal filter, computing an approximate derivative of the cone response; 'intermediate pathway': biphasic filter with narrow positive lobe and shallow negative lobe, removing the DC component of the cone output; 'slow pathway': monophasic (exponential) filter, smoothing the cone potential and retaining the DC component of the cone output). A model ganglion cell then linearly combined at most two inner retina pathways. An additive contribution corresponded to excitatory input from bipolar cells, while a subtractive contribution corresponded to inhibitory input from bipolar cells through amacrine cells. Finally, the spike rate of a ganglion cell was a function of its combined inputs ('S' in Figure 4.15A-B), in which a single parameter, α, controlled how strongly the cell's spike rate is driven directly by the cell's inputs (α close to 0) or by the derivative of the cell's inputs (α close to 1).

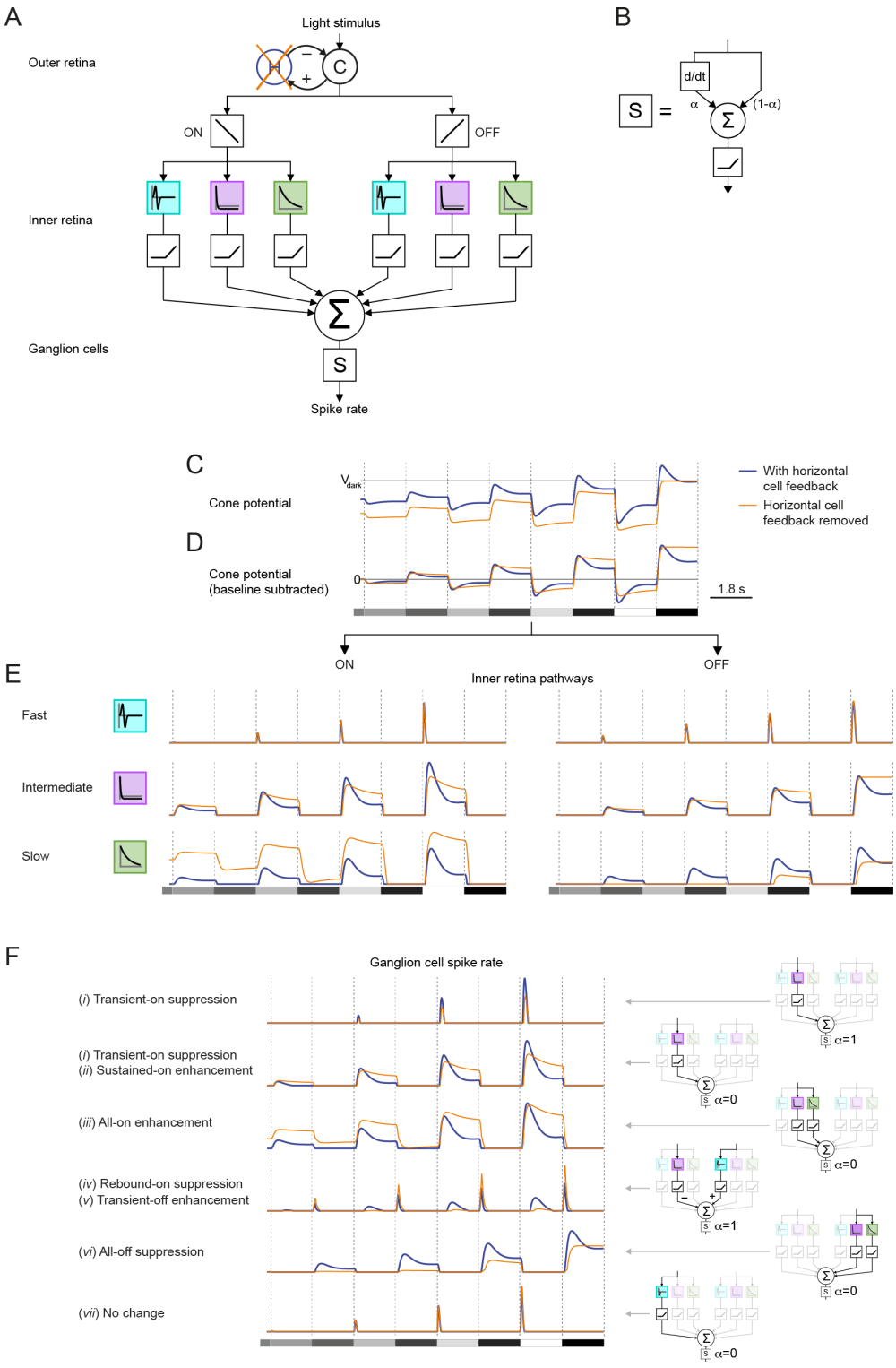

Figure 4.15 **Computational model of the retinal circuitry explains all perturbation-induced effects. (A)** Schematic of the retinal circuit model. From top to bottom: Circuit diagram of the cone-horizontal cell negative feedback circuit (horizontal cell 'H', cone 'C'), the subsequent split into 'ON'

pathways (left) and 'OFF' pathways (right), followed by the filtering operations (colored boxes) and threshold non-linearities (black boxes) of the inner retina pathways. Removal of horizontal cell feedback is illustrated by the orange cross. For each model ganglion cell, the inner retina pathways were linearly combined ('S') and subsequently converted to a spike rate by the function 'S'. (**B**) The function 'S' was the thresholded weighted average ('Σ', weighted by parameter α) of a ganglion cell's previously combined inputs (right) and the temporal derivative thereof (left, box 'd/dt' indicates derivative-taking unit). (**C**) Model cone potential in the presence (blue) and absence (orange) of horizontal cell feedback in response to the stimulus used in Figure 4.6 (grey shaded rectangles below response in panel (D)). V_{dark} refers to the cone potential in darkness. (**D**) To illustrate the effects of horizontal cell feedback on the dynamics of the cone response, the cone potentials were replotted with the baseline subtracted. (**E**) Responses of the six inner retina pathways after the thresholding non-linearity to the same stimulus as in (D). (**F**) Left, spike rates of six model ganglion cells reproducing the effects observed in the data (Figure 4.6 **(**i)-(vi) and cell not affected by PSEM). Right, diagrams depicting the combination of inner retina pathways and the parameter α used for each model ganglion cell. '+' or no marker indicates an excitatory contribution of a pathway; '−' indicates inhibition.

Selective effects on model inner retina pathways upon removal of horizontal cell feedback

We analyzed the model responses of the cone and the inner retina pathways in the presence and absence of horizontal cell feedback (Figure 4.15C-E), when the model was stimulated with the spatially uniform light steps of different contrasts that we used in our experiments.

At background light level, a model cone (Figure 4.15C) was light adapted at a given membrane potential, its 'baseline potential'. When stimulated with a contrast step, the model cone hyperpolarized in response to light increments and depolarized in response to light decrements. In both cases, the cone response had a transient part, in which the potential reached a peak, followed by a sustained part, in which the potential plateaued at a value different from its baseline. The removal of horizontal cell feedback had several effects on the cone. First, the cone baseline potential was shifted (i.e., hyperpolarized), which shifted the entire response (Figure 4.15C). Moreover, when deviations from the baseline potential were considered (for illustration purposes the cone response with subtracted baseline is shown in Figure 4.15D), two additional effects of the removal of horizontal cell feedback could be identified: the transient part of the cone response was suppressed, and the sustained part was enhanced with respect to the baseline potential. The suppression of the transient part was stronger for responses to light increments with respect to responses to light decrements. This asymmetry was not due to a specific choice of parameters, but originated from the asymmetry of the cone gain adaptation with respect to light increments and decrements, which has been measured experimentally (Burkhardt, 1994; Clark et al., 2013; Szikra et al., 2014) and which was captured by the model.

Downstream to the cone, the removal of horizontal cell feedback affected the individual inner retina pathways in distinct ways (Figure 4.15E). The fast pathways (both ON and OFF) were largely unaffected by the removal of the inhibitory feedback of horizontal cells, as the latter modulated the cone potential only in a delayed manner. The intermediate pathways (both ON

and OFF) showed a suppression of the transient part and an enhancement of the sustained part of their response upon removal of horizontal cell feedback. This effect occurred because these pathways behaved similarly to the baseline-subtracted, thresholded cone potential, and, therefore, inherited all effects of the cone except for the baseline shift. The effect was larger in the ON pathway than in the OFF pathway because of the asymmetry in the cone response. The slow pathways displayed an overall enhancement (ON pathway) or suppression (OFF pathway) of the response, because their responses amounted to the smoothed, thresholded cone response, and, therefore, retained information about the baseline shift of the cone potential. Thus, depending on the temporal filter and threshold non-linearities of the inner retina pathways, distinct effects of the feedback removal in the outer retina are selectively passed on to the ganglion cells.

The model captures all six perturbation-induced effects

We examined the ways in which the output of model ganglion cells is affected by the removal of the horizontal cell feedback. We constructed a set of model ganglion cells (Figure 4.15F) by combining different inner retina pathways and by varying parameter α. The model ganglion cells reproduced qualitatively the measured ganglion cell responses, and, remarkably, all six effects that we had observed experimentally during the reversible perturbation of horizontal cells (effects *i*-*vi*, compare Figure 4.6 with Figure 4.15F). Hereafter, we explain how the six effects emerge in different model ganglion cells.

(*i*) Transient-on suppression and (*ii*) sustained-on enhancement was shown by model ganglion cells driven by the intermediate ON pathway, which displayed these effects. The two effects could occur in the same model ganglion cell or occurred in separate cells, depending on parameter α: A model ganglion cell whose spike rate strongly depended on the derivative of its inputs (α close to 1) would not have any sustained response in the presence or absence of horizontal cell feedback (effect *i*), whereas a model ganglion cell with α close to 0 would exhibit a sustained response, which was enhanced upon the removal of horizontal cell feedback (effect *ii*). (*iii*) All-on enhancement was displayed by model ganglion cells that received input from a combination of pathways that included the slow ON pathway, as these cells inherited the overall response enhancement that the slow ON pathway displayed upon feedback removal. (*iv, v*) Rebound-on suppression and transient-off enhancement were displayed by model ganglion cells that were excited by the fast OFF pathway, inhibited by the intermediate ON pathway, and whose spike rate strongly depended on the derivative of their inputs (α close to 1). In the presence of horizontal cell feedback, the rebound on-response was elicited by the fast decay of the inhibitory input from the intermediate ON pathway. The transient off-response was elicited by two factors: the excitatory input from the fast OFF

pathway, as well as the removal of inhibition from the intermediate ON pathway at light decrements. In the absence of horizontal cell feedback, rebound-on suppression (effect *iv*) and transient-off enhancement (effect *v*) were caused by the changes of the intermediate ON pathway: As the transient response of the intermediate ON pathway was suppressed while its sustained response was enhanced, the decay of the inhibitory input was slowed down, and, therefore, no rebound on-response was elicited (effect *iv*). Moreover, since the sustained response of the intermediate ON pathway was enhanced, a larger inhibitory input from the ON pathway was removed at a light decrement, yielding a larger transient off-response (effect *v*), although the excitatory input from the fast OFF pathway remained unchanged. The model therefore suggested that effect *iv* and *v* share the same mechanism in the inner retina, which can explain why we observed effect *iv* and effect *v* in the same cells (Figure 4.6C). (*vi*) All-off suppression was exhibited in model ganglion cells that received input from a combination of pathways that included the slow OFF pathway, as these cells inherited the overall response suppression that the slow OFF pathway displayed upon feedback removal. (*vii*) Finally, model ganglion cells that mainly received input from the fast pathways were not affected by the removal of horizontal cell feedback.

Thus, the model provided insights into how horizontal cell feedback can differentially shape the response dynamics in distinct retinal output channels. Depending on their temporal properties and non-linearities, the inner retina pathways extracted different temporal components of the cone response, which ultimately shaped the time course of the ganglion cell responses, namely: the derivative of the cone response (maximum at 30-90 ms after the light step, depending on contrast), the cone response itself (220-310 ms), the decay of the transient cone response, which caused the rebound on-response in OFF cells (430-500 ms), the plateau of the cone response (>1 second) and, finally, the baseline shift of the cone response.

Beyond the first-order effects (*i*-*vi*), how does the change in the ganglion cell response upon the removal of horizontal cell feedback itself vary with stimulus strength? Answering this question revealed how the response range of a ganglion cell depends on the horizontal cell feedback. We found that the model captured, qualitatively and in some cases quantitatively, all effects of PSEM on the response range of ganglion cells that we had observed experimentally (Figure 4.16A-B). Specifically, the response range was compressed in the model whenever it was compressed in the data, and it was expanded whenever it was expanded in the data.

New model predictions and their experimental validation

The model led to predictions on the effect of the horizontal cell perturbation on the retinal output, four of which we tested in subsequent experiments and analyses (Figure 4.16C-G).

First, the most prevalent effect of perturbing horizontal cells experimentally was the suppression of the rebound on-response in transient OFF cells. The model explained this effect by a slower decay of the inhibitory input from the intermediate ON pathway upon removal of horizontal cell feedback. We tested this prediction by performing whole-cell patch-clamp recordings of PV5 cells in *Gja10Cre* × *PV-Flp* × *Flp-GFP*-reporter mice, injected with AAVs conditionally expressing PSAM (Figure 4.16C-D; $n = 3$ mice, $n = 3$ cells). Spiking responses of PV5 cells displayed strong rebound on-responses, which were suppressed by PSEM (−85 ± 8 %, median ± s.e.m PSEM-induced change). The same cells received transient inhibition with fast decay in response to light increments, which decayed slower in PSEM (Figure 4.16D; paired ***t***-test, $P = 0.012$; PSEM, 1.1 ± 0.01; non-PSEM, 0.99 ± 0.001, mean ± s.e.m normalized inhibition during 0.5-0.8 seconds after light increment). Together with the previously reported lack of excitation in response to light increments in PV5 cells (Münch et al., 2009; Viney, 2010), these findings were consistent with the model prediction.

Second, in the model, removal of horizontal cell feedback suppressed the transient part of the response in the intermediate ON pathway, but not in the fast ON pathway. Consistent with the model, in our experiments we found that ON cells that rapidly reached the peak of their response with respect to the stimulus onset displayed a weaker suppression of the transient part of the response compared to ON cells that responded slower (Figures 8E; Mann-Whitney U test, $P = 9.7\times10^{-54}$; fast-responding transient ON cells, −0.2 ± 1%, $n = 830$ cells; slow-responding transient ON cells, −21 ± 0.8%, $n = 1{,}888$ cells, median ± s.e.m PSEM-induced change). The fraction of cells in which PSEM suppressed the transient part of the on-response was 32% for slow-responding cells, while this fraction was significantly lower for fast-responding cells: 9.2% (Fisher's exact test, $P = 1.5\times10^{-42}$). Thus, horizontal cells influenced ganglion cells that carry fast signals to a lesser extent than those that carry slow signals.

Third, due to the asymmetry of the gain adaptation in the model cone response, model ganglion cells that received input from the intermediate ON pathway exhibited stronger suppression of their transient responses as compared to model cells that received input from the intermediate OFF pathway. Therefore, the model predicted that, among ganglion cells that are dominated by inputs from the intermediate pathways, ON cells would display a stronger suppression of the transient part of the response than OFF cells. To test this prediction, we focused on slow-responding transient ganglion cells in our recordings, because these cells

were neither dominated by the slow pathways (those would be sustained) nor by the fast pathways (those would be fast-responding). Consistent with the prediction, in our experiments we found that PSEM suppressed the transient part of the response more strongly in slow-responding transient ON cells than in slow-responding transient OFF cells (Figure 4.16F; Mann-Whitney U test, $P = 3.9\times10^{-27}$; transient part of the on-response in ON cells, −21 ± 0.8%, n = 1,888 cells; transient part of the off-response in OFF cells, 2.5 ± %, n = 333 cells, median ± s.e.m PSEM-induced change).

Fourth, model ganglion cells that displayed all-on enhancement or all-off suppression received input from the slow pathways, which were sensitive to the baseline shift in the cone potential due to the removal of horizontal cell feedback. Therefore, the model predicted that ganglion cells that exhibited either of these two effects would display changes in their spontaneous spiking activity during background light stimulation ('baseline spiking activity'). In our experiments (Figure 4.16G), we found that PSEM increased the baseline spike rate in ON cells displaying all-on enhancement (sign test, $P = 9.1\times10^{-16}$; non-PSEM, baseline spike rate = 2.4 ± 0.5 Hz; PSEM, baseline spike rate = 7.1 ± 0.8 Hz, mean ± s.e.m, n = 177 cells), while PSEM decreased the baseline spike rate in OFF cells displaying all-off suppression (sign test, $P = 1.1\times10^{-8}$; non-PSEM, baseline spike rate = 12 ± 1 Hz; PSEM, baseline spike rate = 6.5 ± 0.8 Hz, mean ± s.e.m, n = 64 cells), which was consistent with the model prediction.

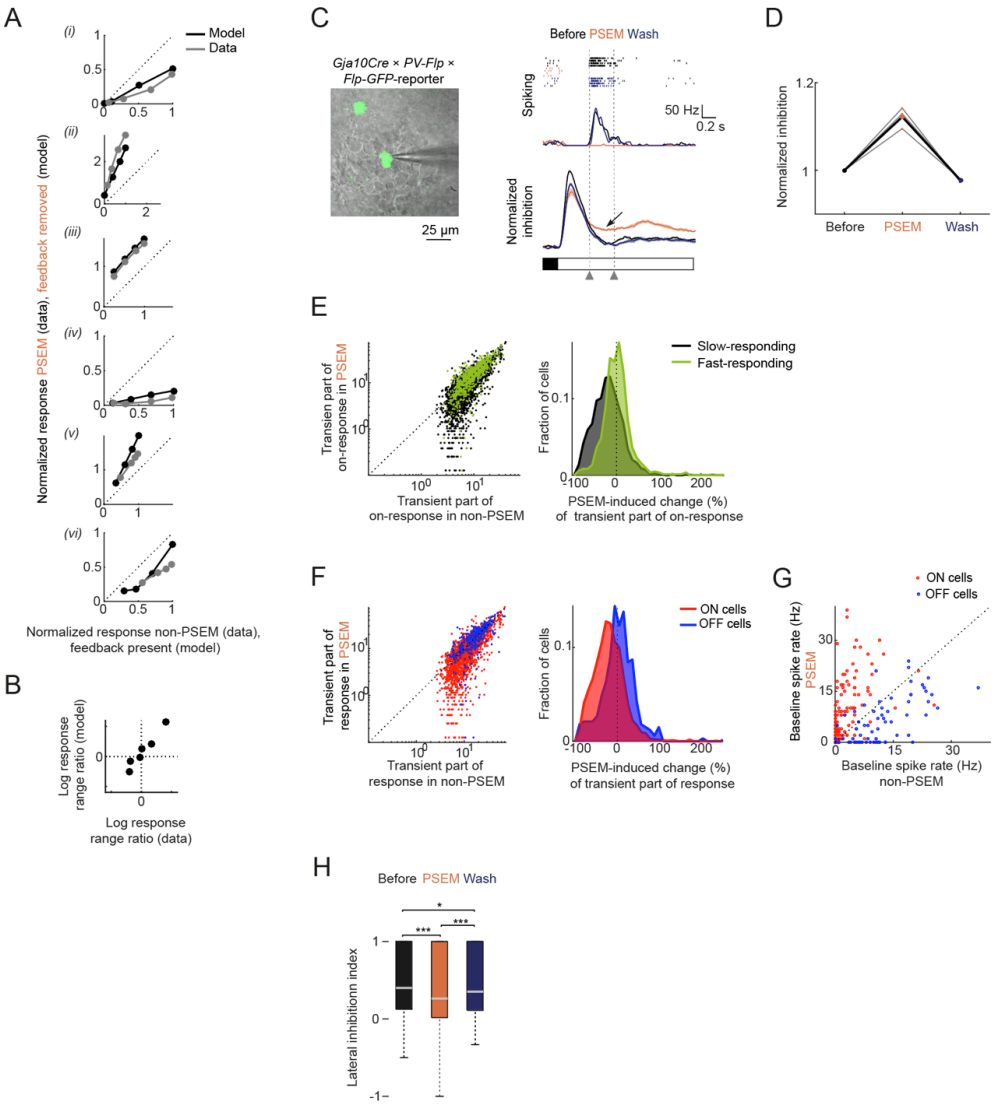

Figure 4.16 **Experimental validation of model predictions and effects of horizontal cells on spatial processing.** (**A**) Each panel shows a scatter plot of the responses of PSEM-affected cells in non-PSEM (x-axis) and PSEM (y-axis) conditions ('data', grey, replotted from Figure 4.9C) and of the responses of the corresponding model ganglion cell from Figure 4.15F in the presence (x-axis) and absence (y-axis) of horizontal cell feedback ('model', black) for the six PSEM-induced effects i-vi. Data points represent the response to each of the four contrast steps. The response of each cell was normalized to the maximal response in non-PSEM conditions (data), or to the maximal response in the presence of horizontal cell feedback (model). Dashed line indicates the unity line. (**B**) Scatter plot of the logarithm of the ratio of the recorded response ranges in non-PSEM and PSEM conditions ('data', x-axis) and the logarithm of the ratio of the model response ranges in the presence and absence of horizontal cell feedback ('model', y-axis). Each point represents one of the six effects i-vi. (**C**) Two-photon laser-targeted patch-clamp recordings of PV5 cells in PV-labeled PSAM retinas. Left, overlay of a two-photon image of a GFP-labeled cell (green) and an infrared image of the ganglion cell layer and the recording pipette (grey). Right, spiking activity (raster plot, four repetitions per condition, and spike rate, mean values of four repetitions) and inhibitory input current (bottom) of an example PV5 cell. Curves represent mean values across stimulus repetitions; shaded areas represent ± s.e.m. Inhibition was normalized relative to pre-stimulus levels. Shaded rectangles (bottom) indicate the stimulus contrast. Arrow points at the slowly decaying inhibitory input during PSEM application. Arrowheads

and dashed lines mark the time window that was used for the quantification in (D). (**D**) Normalized inhibitory input to PV5 cells recorded in PV-labeled PSAM retinas. Data were normalized to the 'before' condition. Grey lines represent data from individual cells; black lines represent the mean. (**E**) Left, scatter plots of the transient on-responses of transient ON cells in non-PSEM (x-axis) and PSEM (y-axis) conditions recorded in PSAM retinas. Data points represent the responses of individual fast-responding cells (green) and slow-responding cells (black). Dashed line indicates the unity line. Right, distributions of the PSEM-induced relative changes (%) of the transient part of the on-response for the data shown in the left panel. (**F**) Same as for (E), but for slow-responding transient ON cells (red, quantification of the transient part of the on-response) and slow-responding transient OFF cells (blue, quantification of the transient part of the off-response). (**G**) Scatter plot of the spontaneous spike rate during background light stimulation ('baseline spike rate') in ON cells displaying all-on enhancement (red) and in OFF cells displaying all-off suppression (blue). One data point from an ON cell is outside axis limits and is not shown. Dashed line indicates the unity line. (**H**) Box-plot representation of the distributions of LII values measured in ganglion cells. LII values were computed from the responses to small and large light spots of positive and negative contrasts. Bottom and top whiskers indicate minima and maxima; bottom and top of the rectangle indicate first and third quartiles; central line indicates median. ***: $P < 0.001$, n.s.: $P >= 0.05$.

Contribution of horizontal cells on the spatial processing of ganglion cells

So far we investigated how horizontal cells influence the time course of ganglion cell responses. Since spatial processing is one of the main suggested functions of horizontal cells (Chaya et al., 2017; Davenport et al., 2008; Ichinose and Lukasiewicz, 2005; Mangel, 1991; McMahon et al., 2004; Naka, 1971; VanLeeuwen et al., 2009; Vigh and Witkovsky, 1999), we tested if their reversible perturbation affects the inhibitory surround of ganglion cell receptive fields (Figure 4.16H). We quantified lateral inhibition in ganglion cells in PSAM retinas (n = 3 mice, n = 447 cells) based on their spiking responses to small and large flashed light spots. PSEM led to a LII decrease of 0.08, which corresponds to a 15% decrease in lateral inhibition (sign test, $P = 5.8\times10^{-13}$; non-PSEM, LII = 0.53 ± 0.02; PSEM, LII = 0.45 ± 0.02, mean ± s.e.m). This finding indicates that, at photopic light levels, lateral inhibition from horizontal cells contributes on average to less than a sixth of the strength of the inhibitory surrounds of ganglion cell receptive fields.

Discussion

This study investigates how a single interneuron type, horizontal cells, affects the dynamics of the output channels of a brain region, the retina. By combining experimental and theoretical approaches, we show how feedback at the first visual synapse can influence the retinal output in distinct ways by enhancing or suppressing ganglion cell activity during different epochs of the response and in different subsets of ganglion cells. Below we discuss the methodology to perturb horizontal cells, followed by a discussion of the observed effects on the retinal output, their functional significance, and how the diversity of effects can arise from dynamical processing in non-linear circuits.

Specific and reversible perturbation of feedback at the first visual synapse

We reversibly perturbed horizontal cell activity using chemogenetics. Compared to previous methods of perturbation, chemogenetic tools have several benefits for investigating the functions of horizontal cells. First, in contrast to optogenetic tools (Szikra et al., 2014), activation by light is not required, which is advantageous since the retina is light sensitive. Second, in contrast to genetic ablation of cells (Chaya et al., 2017; Sonntag et al., 2012), or cell type-specific gene knockouts (Dedek et al., 2008; Klaassen et al., 2011; Pandarinath et al., 2010; Ströh et al., 2013), chemogenetic perturbation allows for monitoring the responses before, during, and after the perturbation in the same ganglion cells. This helped us to uncover effects that silenced ganglion cell responses and allowed for observing multiple effects occurring in the same ganglion cell. The function of some retinal interneuron types has been successfully investigated using genetic cell ablation (Hillier et al., 2017; Yoshida et al., 2001). However ablation of horizontal cells leads to the degeneration of the outer retina (Sonntag et al., 2012), although restricting the observation time after ablation can extenuate these changes (Chaya et al., 2017) and allows inference about horizontal cell function. Third, compared to the reversible perturbation of activity through current injection into single horizontal cells (Mangel, 1991; Naka, 1971), chemogenetic tools allow for retina-wide, spatially uniform perturbation, provided the channel is expressed uniformly throughout the retina. We obtained uniform expression by administering the virus systemically, using the recently described PHP.B serotype (Deverman et al., 2016), which has the additional benefit that the eye is not injected and the retina remains untouched *in vivo*. The expression of PSAM in horizontal cells was high, especially in their processes (Figure 1D), allowing for efficient perturbation at low concentration (3 μM) of PSEM.

A prominent role of horizontal cells in shaping the dynamics of the retinal outputs

Previous studies, using irreversible perturbations or single-cell manipulations, have investigated how horizontal cells influence the responses of ganglion cells, but only limited contributions of horizontal cells to shaping the dynamics of ganglion cell responses have been reported. A study that analyzed retinas after genetic ablation of horizontal cells showed an increase in the sustained spiking activity of ganglion cells (Chaya et al., 2017). Consistent with this finding, we found that some ON cells increased their sustained spiking activity (effect *ii*) during chemogenetic perturbation of horizontal cells. However, by analyzing the responses of the same ganglion cells before, during, and after the perturbation, we revealed five other effects of horizontal cell perturbation on the response dynamics of ganglion cells (Figure 4.6 and Table 4.1). Furthermore, using current injection into single horizontal cells while recording the responses of nearby ganglion cells, it was previously shown that the sign

of the response modulation was opposite for ganglion cells of different polarities (Mangel, 1991) (i.e., hyperpolarizing current injections to horizontal cells led to a decrease in spiking in ON cells, but an increase in spiking in OFF cells). However, by perturbing horizontal cells uniformly across the retina and reading out the effects in a large population of ganglion cells, we find that, depending on the epoch of the response and on the ganglion cell type, horizontal cells can suppress or enhance the responses of ganglion cells of the same polarity, as well as modulate the responses of ganglion cells of different polarity with the same sign. Even in the same ganglion cell, horizontal cells can enhance and suppress the response at different epochs in the response. Together, our findings indicate that horizontal cells play a prominent role in shaping the response dynamics of the retinal output channels.

How diverse retinal functions arise at the first visual synapse

What is the functional relevance of the observed effects? Below we propose three functional roles of horizontal cells, which apply to different subsets of ganglion cells. We then discuss the contribution of horizontal cells to spatial processing.

First, horizontal cells can induce temporal sharpening of the response of ganglion cells, which resulted from two different effects occurring in the same ganglion cells (effect *i* and effect *ii* occurring in the same ON cells, Figures 4.6A and 4.7A-B). In these cells, horizontal cells sharpened the temporal profile of the response by enhancing the transient part and suppressing the sustained part of the response. Our computational model provided insights into how both effects can arise from a single site of negative feedback. The suppression of the sustained response is a simple consequence of the delayed feedback inhibition from horizontal cells. The enhancement of the transient response, however, is more interesting: generally, temporal sharpening is accompanied by gain suppression—a phenomenon referred to as the 'gain-bandwidth trade-off' (Seung, 2002). By contrast, we found that the temporal sharpening was accompanied by a larger (transient) gain. According to the model, this phenomenon is a direct outcome of non-linear processing in the retina: horizontal cell feedback modulates both the cone baseline potential and its dynamics, and downstream non-linearities couple the two to yield an enhanced transient response. As such, the model illustrates how negative feedback in the outer retina can enhance responses at the retinal output level without invoking a positive feedback mechanism of horizontal cells in the outer retina (Jackman et al., 2011; Kemmler et al., 2014; VanLeeuwen et al., 2009).

Second, horizontal cells influence the response range of the retinal output, as their activity can lead to a compression (effects *ii, v*) or an expansion (effects *i, iv, vi*) of the response range of ganglion cells, at different epochs of the response (Figure 4.9C-D). We observed response range compression only in a minority of the cases (253/1487 of cells showing one of the

effects *i-vi*, Figure 4.9C-D), even though compression of the response range is the effect expected from feedback inhibition. In the majority of cases (1057/1487 of cells showing one of the effects *i-vi*, Figure 4.9C-D), we found that horizontal cell activity led to an expansion of the response range, which was unexpected. The expansion was large for effect *i* (response range expanded by a factor of two) and effect *iv* (response range expanded by a factor of ten). The model captured the observed effects on the response range (Figure 4.16A-B) and offered insights on the underlying mechanisms. The expansion results from the non-linear coupling of the influence of horizontal cells on the cone baseline potential and the cone response dynamics (effect *i*); the rebound response that horizontal cells enable by shaping the time course of the inhibitory input to ganglion cells (effect *iv)*; and the influence of horizontal cells on the cone baseline potential which translates into response enhancement in the slow OFF pathway (effect *vi*).

Third, horizontal cells endow the retina with a 'memory' of light increments by enabling delayed rebound spiking responses to light increments in a large fraction of transient OFF cells (Figure 4.6, effect *iv*). Compared to the activity of sustained ON cells, which simply follow the light input (i.e., after a light increment, they rapidly stop spiking in response to a subsequent light decrement), the rebound-on response occurs after the light increment with a latency of ~0.5 seconds, independent of the momentary light input. As such, the rebound spiking enables the cell to 'memorize' that a light increment occurred ~0.5 seconds ago. Interesting phenomena can arise if a light decrement occurs shortly after the light increment, and, consequently, the rebound-on response starts to overlap, or even coincides with the transient off-response. The interaction of the two responses results in a temporal tuning of transient OFF cells with a peak at a frequency of ~2 Hz. Furthermore, when a bright object is moved across the receptive field of the cell, the rebound on-response to the leading edge can coincide with the transient OFF response to the trailing edge. This mechanism yields response tuning to a fixed ratio between size and velocity of the moving object.

Finally, regarding spatial processing, horizontal cells were proposed to contribute to the receptive field surrounds of retinal cells, including ganglion cells (Thoreson and Mangel, 2012; Wu, 1992). This suggested function has been derived in studies using pharmacological manipulations (Davenport et al., 2008; Ichinose and Lukasiewicz, 2005; McMahon et al., 2004; VanLeeuwen et al., 2009; Vigh and Witkovsky, 1999), current injections into horizontal cells (Mangel, 1991; Naka, 1971), and genetic ablation of horizontal cells (Chaya et al., 2017). At the same time, other studies have indicated that amacrine cells are the major contributors to the receptive field surrounds of ganglion cells (Cook and McReynolds, 1998; Dedek et al., 2008). By perturbing horizontal cells chemogenetically, we found that horizontal cells indeed contribute to the receptive field surrounds of ganglion cells (Figure 4.16H).

However, the contribution was modest (15%), which suggests that, under the conditions of our experiments, lateral inhibition from amacrine cells is the primary source of receptive field surrounds in ganglion cells.

In this work, we studied the influence of horizontal cells onto the retinal output while restricting the input to a single source, the blue cones. Additional functional roles of horizontal cells are likely to be uncovered, if the retina is probed at different wavelengths (Joesch and Meister, 2016; Szikra et al., 2014), using different sets of stimuli, and at different light levels. Horizontal cells are electrically coupled via gap junctions (Bloomfield and Volgyi, 2009; Shelley et al., 2006), whose coupling strength depends on the light-level (Weiler et al., 2000), suggesting that the horizontal cell network can fulfill different functions across light levels.

How a single site of feedback can shape the circuit's outputs in diverse ways

In our circuit model, the horizontal cell's ability to differentially shape the responses of individual retinal output channels results from the dynamical, non-linear processing of the signal through parallel channels. While, in linear systems, the response to an input consisting of components with different time scales is the sum of the responses to each of the individual components, this does not apply to non-linear systems: non-linearities can couple different time scales that are present in the signal. For example, in the presence of thresholding non-linearities, a baseline shift can affect the dynamics by rendering the response more or less sustained. Thus, simple non-linearities, combined with the presence of parallel pathways acting on different time scales, can give rise to a rich set of behaviors.

Our work illustrates the unexpected ways in which a neuron in a non-linear circuit can influence the circuit's outputs. First, consistent with our whole-cell patch data (Figure 4.16C-D), the model explains the horizontal-cell-driven suppression of the transient response in OFF cells (Figure 4.6, effect *v*) as resulting from the horizontal-cell-driven suppression of the sustained response in the intermediate ON pathway, which in turn is inherited from the modulation of the sustained cone response. Thus, even as simple a circuit as the one formulated in our model allows for a sustained modulation in the outer retina to be reflected in a transient modulation of a retinal output. A second interesting example relates to the asymmetry in response properties between intermediate ON and OFF pathways (Figure 4.15B). This asymmetry originates in the asymmetry of the cone response to light increments and decrements, which in turns relates to the adaptive nature of the cone response (Burkhardt, 1994; Clark et al., 2013; Szikra et al., 2014). In other words, light adaptation in cones translates into differential horizontal-cell-driven modulations in ganglion cells.

Here, we show that in a circuit consisting of parallel channels with different temporal properties and non-linearities, the effect of a given circuit element on another circuit element can take qualitatively different forms, depending on the properties of the pathway connecting the two. Thus, a given interneuron type can affect the output channels of a brain region in various ways. Furthermore, we show that the way in which an interneuron influences another neuron that is multiple synapses away can be different from its local influence on the neurons it directly forms synapses with (in the case of horizontal cells, the cones). The computational model helped us to understand the effects due to the perturbation of an interneuron type in the retina, however the employed processing principle—namely, the non-linear translation of a signal into parallel channels with different temporal properties—likely generalizes to other brain areas.

Conclusions

Neuronal circuits throughout the brain often contain a diverse set of local interneuron types. How local interneuron types contribute to the input-output transformations of a given brain region is not well understood. In my PhD, I focused on the computational roles of interneurons in the retina. I developed approaches to systematically and quantitatively investigate the function of retinal interneurons by combining precise circuit perturbations with a system-wide read-out of activity. I studied an example of a locally acting interneuron type, starburst amacrine cells, which specifically act on the direction-selective retinal output channels. Furthermore, I investigated the function an interneuron type that acts globally on many retinal output channels, horizontal cells, which modify the information flow at the first synapse of the retina.

My work on starburst amacrine cells is related to a frequent neurodevelopmental disease—congenital nystagmus. I showed that *FRMD7*, a gene that is defective in human congenital nystagmus, is required in the mouse retina to establish the spatially asymmetric inhibitory inputs from starburst cells to horizontal direction-selective ganglion cells (***Chapter 1***). Our work illustrates how a human disease can be instructive to decipher the molecular pathways underlying specific neuronal computations: The initial mapping of disease-associated genes to neuronal cell types, followed by analyzing the symptoms of human patients, provided the hint that FRMD7 is required to establish the asymmetric connectivity between starburst cells and ganglion cells.

Our findings provide a link between a specific neuronal computation and a human disease, and present an entry point for understanding the molecular pathways responsible for generating neuronal circuit asymmetries. In addition, due to the specificity of its retinal phenotype and the lack of *FRMD7* expression in higher visual areas, the *FRMD7*^{tm} mouse line constitutes a model system to obtain mechanistic insights into higher visual processing. *FRMD7*^{tm} mice were essential to identify two different forms of direction selectivity in primary visual cortex (***Chapter 2***) and are currently used to investigate the processing of visual signals in regions throughout the brain (Macé et al., in preparation; Chenglin et al., in preparation).

My work on horizontal cells shows how diverse retinal functions can arise at the first visual synapse. To study the function of horizontal cells, I targeted neuronal silencing tools to horizontal cells using viral vectors (***Chapter 3***). By combining the precise, yet retina-wide, perturbation of horizontal cells with a system-level readout of the retinal output, I uncovered that horizontal cells can differentially shape the response dynamics of individual retinal output channels (***Chapter 4***). Central to this work was the integration of experimental and

theoretical approaches: While the observed diversity of effects due to the perturbation of horizontal cells—a single, homogenous interneuron type—was surprising at first, our computational model captured the diverse effects and explained them by the dynamical, non-linear processing of the signal through parallel pathways. In addition, the model made predictions that were subsequently confirmed with additional experiments.

Our combined experimental and theoretical work constitutes a systematic and quantitative description of interneuron function, from which we obtained two conceptual insights: First, we show that a single, local interneuron type can have multiple functions, depending on which output channels of a brain region are monitored. Thus, the function of an interneuron depends on the input-output combinations of the brain region under study. Furthermore, our findings indicate that how a local interneuron type acts on the output neurons of a brain region can be fundamentally different from how it influences its direct synaptic partners. Thus, the function of an interneuron type should not only be interpreted in the context of its direct synaptic partners, but also in the context of the different output channels of the brain region under study.

Experimental procedures

Chapter 1

Animals. Wild type mice (C57BL/6) were obtained from Charles River. *FRMD7^{tm}* mice refer to the homozygous female or hemizygous male *FRMD7$^{tm1a(KOMP)Wtsi}$* mice, which were obtained from the Knockout Mouse Project (KOMP) Repository. A splicer acceptor-*IRES-lacZ* cassette is inserted into the intron between *FRMD7* exon 3 and exon 4, designed to result in the production of a truncated N-terminal part of the *FRMD7* protein (68 amino acids) and LacZ. The integrity of the targeted genomic region in the *FRMD7^{tm}* mouse was confirmed by PCR by the International Mouse Phenotyping Consortium (IMPC). Genotyping of *FRMD7^{tm}* mice was carried out according to KOMP instructions. Both male and female *FRMD7^{tm}* mice were used in this study. The mRNA variants expressed from the mutant *FRMD7* locus in *FRMD7^{tm}* mice are described below in the section "Mouse *FRMD7* mRNA analysis". *ChAT-Cre* mice (Ivanova et al., 2010) were obtained from Jackson Laboratory (strain: B6;129S6-*Chat$^{tm1(cre)Lowl}$*/J) and *Hoxd10-GFP* mice (Dhande et al., 2013) from Mutant Mouse Research and Resource Center (strain: STOCK Tg*(Hoxd10-EGFP)LT174Gsat/Mmucd*). Unless indicated, mice were between age P40 and P120. Mice were maintained in C57BL/6 background. A female cynomolgus monkey (Macaca fascicularis), was obtained from BioPRIM. Animals were housed in groups under maintained temperature (20-24°C), at least 40% humidity and a natural light cycle, and fed at least twice daily with a mixture of fruits and vegetables. Water and Kliba Nafag 3446 pellets (Kaiseraugst, Germany) were provided ad libitum. Euthanasia at age 19 was performed by intravenously applied 10 ml pentobarbital (Esconarkon, Streuli Pharma AG, Uznach, Switzerland). All animal procedures were performed in accordance with standard ethical guidelines (European Communities Guidelines on the Care and Use of Laboratory Animals, 86/609/EEC) and were approved by the Veterinary Department of the Canton of Basel-Stadt, Switzerland.

Human subjects. Eye movement was recorded from three human subjects with congenital nystagmus (ages 19, 22 and 41) as well as from four control subjects (ages 30, 30, 33, and 36). Human subjects with congenital nystagmus had a complete ophthalmologic examination, including slit-lamp examination, fundus examination and measurement of visual acuity. This prospective research was conducted in accordance with Good Clinical Practices. The research procedures followed the tenets of the Declaration of Helsinki, and all tests and examinations were performed after obtaining informed consent from all subjects. The study protocol was approved by the relevant Institutional Review Boards.

Eye movement detection. Eye tracking was performed using an ETL-200 eye tracking system (Iscan Inc., Woburn, Maine, USA). To visualize the pupil, eyes were illuminated with IR light and recorded with IR cameras, at 240 Hz in humans, and at 120 Hz in mice. The optokinetic reflex was quantified by counting the number of eye tracking movements (ETMs) as described previously (Cahill and Nathans, 2008). Briefly, the position of the pupil was plotted as a function of time, the derivative of this signal was calculated and a threshold was set. Events above threshold were counted as ETMs. The threshold was adjusted in wild type mice and in control human subjects so that all visually assessed ETMs were detected. This threshold was then applied to data from *FRMD7*^{tm} mice and human subjects with *FRMD7* mutation.

Visual stimulation, controlled by software written in Python (python.org), or PsychoPy (psychopy.org), was presented on a computer monitor. For humans, the monitor was placed 65 cm from the eye, which corresponded to 44° of visual angle horizontally and 28° vertically. The head was kept in place with a chin rest. For eye fixation, a spot of 0.25° diameter was presented for 15 s in the center of the monitor. For motion stimulation, black and white gratings (0.5 duty cycle) with 6° wide bars were moved at 15°/s. One degree corresponds to 300 μm retinal distance in humans (Oyster, 2006). For mice, visual stimulation was executed as described previously (Yonehara et al., 2009), except that here two monitors were placed in a 'V' position in front of the mouse for binocular stimulation. The head of the mouse was fixed with a head holder, and the body was restrained in a foam jacket. For motion stimulation black and white gratings (0.5 duty cycle) with 20°-wide bars were moved at 10°/s. One degree corresponds to 31 μm retinal distance in mice (Remtulla and Hallett, 1985).

AAV production. To obtain the production plasmid for serotype-7 AAV-EF1a-DIO-TVA66T-WPRE-hGHpA, we linearized pAAV-EF1a-double floxed-hChR2(H134R)-EYFP-WPRE-hGHpA (kindly provided by K. Deisseroth, Stanford University) using NheI/AscI sites. A TVA66T insert with NheI/AscI overhand sites was synthesized (GenScript) based on the CAG-Flex-TC66T sequence, which was obtained from Addgene (plasmid # 48331) and cut using NheI/AscI. To obtain the production plasmid for serotype-8 AAV-CMV-DIO-*FRMD7*-GFP-WPRE-hGHpA and AAV-CMV-DIO-GFP-*FRMD7*-WPRE-hGHpA, we linearized pAAV-EF1a-double-floxed-hChR2(H134R)-EYFP-WPRE-hGHpA using NheI/AscI sites. *FRMD7*-GFP and GFP-*FRMD7* fusion inserts, with NheI/AscI overhand sites, were synthesized (GenScript) and cut using NheI/AscI. The linearized vector and the inserts were ligated to yield pAAV-CMV-DIO-*FRMD7*-GFP-WPRE-hGHpA and pAAV-CMV-DIO-GFP-*FRMD7*-WPRE-hGHpA. We used the mouse *FRMD7* sequence (Genbank: NM_001190332.1) to produce the plasmids. AAVs were made according to standard

protocols. Genome copy (GC) number titration was performed using real-time PCR (Applied Biosystems, TaqMan reagents).

Rabies virus production. G-coated SADΔG-GFP rabies virus (Ian R. Wickersham et al., 2007)(provided by K.K. Conzelmann, Munich) was amplified by infecting B7GG cells. EnvA-coated SADΔG-GFP rabies virus was obtained by infecting BHK-EnvARGCD cells with the G-coated viruses (Ian R Wickersham et al., 2007). Viruses were concentrated by ultracentrifugation as described before (Ghanem et al., 2012). Titration using plaque-forming units (pfu) was performed by infecting BHK cells and HEK293T-TVA800 cells with G-coated virus and EnvA-coated virus, respectively.

Virus injections. Mice were anesthetized with an intraperitoneal injection of ketamine (108 mg/kg) and xylazine (14.4 mg/kg). To label starburst cells with GFP, serotype-7 AAV-EF1a-DIO-TVA66T-WPRE-hGHpA in PBS (1.8×10^{15} GC/ml) was loaded into pulled-glass pipettes (tip inner diameter 20-30 µm) and 2 µl was injected intravitreously into the eye of *ChAT-Cre* and *FRMD7^{tm}*;*ChAT-Cre* mice using a pneumatic microinjector (Narishige, IM-11-2). Two weeks later, EnvA-coated SADΔG-GFP rabies virus (2.8×10^{11} pfu/ml) was loaded into pulled-glass pipettes and 2 µl was injected intravitreously into the eye. One week later the retinas were isolated and fixed with 4% paraformaldehyde. To label starburst cells with GFP-tagged *FRMD7*, serotype-8 AAV-CMV-DIO-*FRMD7*-GFP-WPRE-hGHpA (1.2×10^{13} GC/ml) or AAV-CMV-DIO-GFP-*FRMD7*-WPRE-hGHpA in PBS (3.4×10^{13} GC/ml) was loaded into pulled-glass pipettes and 2 µl was injected intravitreously into the eye of *ChAT-Cre* mice. Three weeks later the retinas were isolated and fixed with 4% paraformaldehyde.

Fluorescent *in situ* hybridization. Double-label fluorescent *in situ* hybridization on retinal sections from mice and non-human primate, and brain sections from mice was carried out using the RNAscope Multiplex Fluorescent Assay (Advanced Cell Diagnostics) according to the manufacturer's instructions. Briefly, dissected retinas were fixed with 4% paraformaldehyde, cryoprotected with 30% sucrose in PBS, embedded in OCT compound, frozen on dry ice, and cryosectioned at 20 µm. To prepare embryonic retinal sections, embryos were fixed overnight in 4% paraformaldehyde in PBS and washed with PBS for at least 1 day at 4°C, cryoprotected with 30% sucrose in PBS, embedded in OCT compound, frozen on dry ice, and cryosectioned at 20 µm. To prepare brain sections, animals were transcardially perfused with 4% paraformaldehyde and the brains were post-fixed in 4% paraformaldehyde overnight at 4°C, cryoprotected with 30% sucrose in PBS, embedded in OCT compound, frozen on dry ice, and cryosectioned at 30 µm. Mouse retinal or brain sections were hybridized with probes for mouse *FRMD7* (Genbank: NM_001190332.1) and mouse *ChAT* (Genbank: NM_009891.2) mRNAs, as well as probes for positive and negative

controls, and signals were amplified. Non-human primate retinal sections were hybridized with probes for macaca fasicularis *FRMD7* (Genbank: XM_005594586.1) and macaca fasicularis *ChAT* (Genbank: XM_005565136.1) mRNAs as well as for positive and negative controls, and signals were amplified. Slides were stained with DAPI and mounted with Prolong Gold (Life Technologies). Positive staining was identified as punctate dots present within the cells.

Retrograde and anterograde tracer injections. To label ON DS cells projecting to the MTN, adult mice were anesthetized with an intraperitoneal injection of ketamine/xylazine and head-fixed with a stereotaxic instrument (Narishige, SR-5M). Cholera toxin subunit B Alexa Fluor 488 conjugate (Invitrogen, C34775) at 1 mg/µl in PBS was loaded into pulled-glass pipettes (tip inner diameter 20-30 µm), and 100 µl was injected into the MTN using a pneumatic microinjector (Narishige, IM-11-2).

To label retinal ganglion axons innervating retino-recipient nuclei, mice were anesthetized with an intraperitoneal injection of ketamine/xylazine. Cholera toxin subunit B Alexa Fluor 594 conjugate (Invitrogen, C34777) or 647 conjugate (C34778) at 1 mg/µl in PBS was loaded into pulled-glass pipettes (tip inner diameter 20-30 µm) and 2 µl was injected intravitreously into the eye. One week later brains were isolated and used for *in situ* hybridization or immunohistochemistry.

Preparation of retina for electrophysiology. Light-adapted mice were used for recordings. Retinas were isolated under dim red light (FGL610, Thorlabs) in Ringer's medium (in mM: 110 NaCl, 2.5 KCl, 1 $CaCl_2$, 1.6 $MgCl_2$, 10 d-glucose, 22 $NaHCO_3$) bubbled with 5% CO_2, 95% O_2. The dorsal side of the retina was marked with a small incision, which was later used to align the visual stimulation to the retinal axes. For multielectrode array recordings, a retinal patch was placed ganglion-cell-side-down on the multielectrode array. To secure the retina on the multielectrode array, a permeable membrane (polyester, 10 µm thickness, 0.4 µm pore size) was lightly pressed against the tissue. For patch-clamp recordings, the retina was mounted ganglion-cell-layer-up on a filter paper (Millipore) with a 2×2 mm aperture to allow visual stimulation of the photoreceptors. During multielectrode array and patch-clamp recordings, the retina was kept at 35°C and was continuously superfused with Ringer's medium bubbled with 5% CO_2, 95% O_2.

Multielectrode array recordings. Recordings and light stimulation were performed as described before (Fiscella et al., 2012). In most experiments, CMOS-based multielectrode arrays with 11,011 platinum electrodes with diameters of 7 µm and electrode center-to-center distances of 18 µm over an area of 2×1.75 mm were used (Fiscella et al., 2012; Frey et al., 2010, 2009). In some experiments CMOS-based multielectrode arrays with 26,400 platinum

electrodes over an area of 3.85×2.1 mm and 1,024 readout channels and a center-to-center electrode distance of 17.5 μm were used (Ballini et al., 2014; Muller et al., 2013) .

Visual stimuli. Flashed stimulus: this stimulus was used to determine if a cell was ON-OFF (responding to both light increments and decrements) or ON (responding to light increments only). A positive-contrast square stimulus (0.2×0.2 mm^2) was turned on for one second and turned off for one second in 5 repetitions. The stimulus moved sequentially in discrete non-overlapping steps over an area of ~1 mm^2 with a background irradiance of 0.2 $\mu W/cm^2$ and a square stimulus irradiance of 47 $\mu W/cm^2$. Motion stimulus: this stimulus was used to test direction selectivity. A 1 mm wide and 0.5 mm long (perpendicular to stimulus motion) white bar (background irradiance 0.2 $\mu W/cm^2$ and stimulus irradiance 47 $\mu W/cm^2$) moved across the retina at a velocity of 0.15 or 0.8 mm/s, along eight equidistant angular directions radially spaced at 45°. The large bar width (1 mm) was chosen to separate ON and OFF responses. Each motion stimulus was repeated five times.

Spike sorting and data analysis. For spike sorting we used a fully automatic two stage procedure that first identified spike templates for each neuron (Marre et al., 2012; Prentice et al., 2011) and then classified each spike using template matching (Franke et al., 2015). Spike data obtained from stimulus repetitions were averaged. The direction selectivity index (DSI) and preferred direction of a neuron were defined as described previously (Taylor and Vaney 2002). Briefly, eight vectors were formed, each associated with motion along a direction. The length of each vector was the mean number of spikes across stimulus repetitions along the relevant direction and the angle of the vector was the angle corresponding to the motion direction (0°, 45°, 90°, 135°, 180°, 225°, 270°, 315°). The DSI and preferred direction of the neuron were defined as the length and angle of the sum of the eight vectors divided by the sum of the lengths of the eight vectors (normalized vector sum), respectively. The horizontal and vertical DSIs were defined as the length of the horizontal and vertical components of the normalized vector sum. In the analysis of multielectrode electrode array data, we defined a neuron as direction selective if its DSI was higher than 0.5.

Slow- and fast-motion preferring DS cells were segregated using a velocity index (VI).

$$VI = (rF - rS)/(rS + rF)$$

rF is the maximum response of a cell across the eight stimulus directions using a motion velocity of 0.8 mm/s, and rS is the maximum response of the same cell across the eight stimulus directions using a motion velocity of 0.15 mm/s. VI ranges from −1 to 1. Cells with $VI > -0.5$ were categorized as fast DS cells and with $VI \leq -0.5$ as slow DS cells.

ON-OFF and ON DS cells were segregated using an ON-OFF index (OOI).

$$OOI = (rON - rOFF)/(rON + rOFF)$$

rON is the maximum response of a cell to a positive contrast, flashed stimulus stepped across its receptive field, and rOFF is the maximum response of a cell to a negative contrast, flashed stimulus stepped across its receptive field. The OOI ranges from −1 to 1. Cells with $|OOI| < 0.8$ were categorized as ON-OFF cells and cells with $OOI > 0.8$ as ON cells.

Two-photon targeted patch clamp recording. *Hoxd10-GFP* and *FRMD7^{tm}*;*Hoxd10-GFP* mice were used for targeted recordings of ON-OFF and ON ganglion cells with genetic identity of temporal motion preferring DS cells. Cells back-labeled from the MTN with cholera toxin subunit B Alexa Fluor 488 conjugate were targeted to record from vertically tuned ON DS cells in wild type and *FRMD7^{tm}* mice. The two-photon microscope system for targeted patch clamp recordings from GFP- or Alexa488-labeled cells, including the light pathways for visual stimulation of the retina, has been described before (Figure 5.1 and 5.2, Farrow et al., 2013). GFP- or Alexa488-labeled cells were targeted using a two-photon microscope equipped with a Mai Tai HP two-photon laser (Spectra Physics), set to 920 nm, which was integrated into the electrophysiological setup. The two-photon fluorescent image was overlaid on an IR image acquired with a CCD camera (SPOT Visitron Systems). The infrared light was produced with a digital light projector (V300X, NEC) and a 750 ± 25 nm filter. Spike recordings and whole-cell recordings were performed with borosilicate glass electrodes (BF100-50-10, Sutter Instruments), pulled to 5-7 MΩ, using an Axon Multiclamp 700B amplifier. Signals were digitized at 10 kHz and acquired using software written in LabVIEW (National Instruments). Spike recordings were made in loose cell-attached mode and electrodes were filled with Ringer's solution. Whole-cell recordings were made in voltage clamp mode and electrodes were filled with (in mM) 112.5 $CsCH_3SO_3$, 1 $MgSO_4$, 7.8×10^{-3} $CaCl_2$, 0.5 BAPTA, 10 HEPES, 4 ATP-Na_2, 0.5 GTP-Na_3, 5 lidocaine N-ethylbromide (Qx314-Br) and 7.75 neurobiotin chloride; pH adjusted to 7.2. Inhibitory and excitatory currents ('inhibition' and 'excitation') were separated by voltage clamping the cell to the equilibrium potential of unselective cation channels (0 mV) or the equilibrium potential of chloride (−60 mV), respectively (Roska and Werblin, 2001). The light for retinal stimulation was generated by a digital light projector (V300X, NEC) at a refresh rate of 75 Hz, and focused on the retinal photoreceptor layer after passing a neutral density filter (ND40). After targeting, the recorded cell was kept at a constant grey background level with light intensity of 60 μW/cm^2 on which the positive or negative contrast stimulus was displayed. The moving stimulus consisted of a 300 μm-diameter light spot with positive 50% contrast (122 μW/cm^2), which moved across the retina in eight directions at 300 μm/s. The

flashed stimulus consisted of a 300 µm-diameter light spot with positive or negative 50% contrast centered to the soma of the cell. All stimuli were repeated five times. The visual stimulation was controlled via custom-made software written in Python (Python Software Foundation).

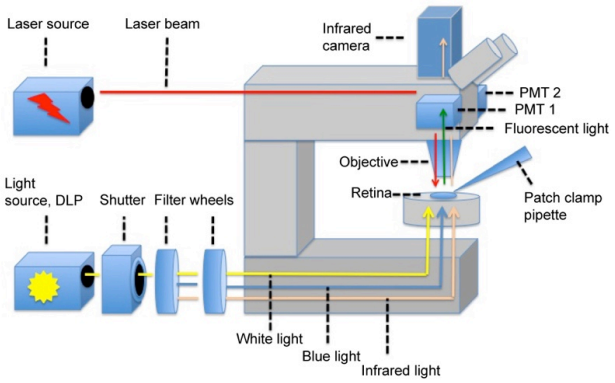

Figure 5.1 **Layout of the upright two-photon microscope.**

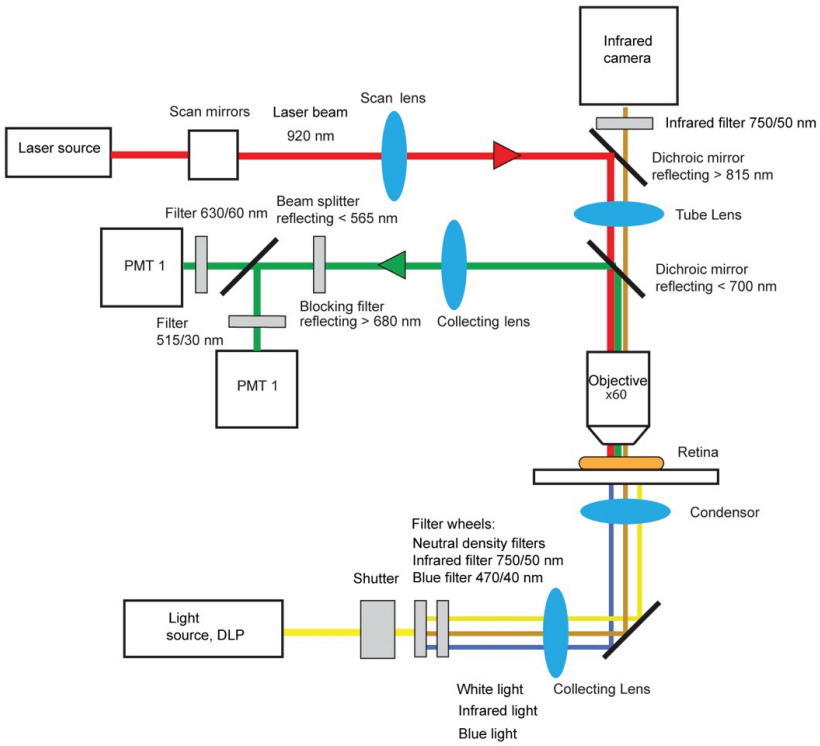

Figure 5.2 **Layout of the optical path**. A two-photon laser source provided a laser beam, which was attenuated by polarization optics and was scanned using mirrors mounted on an upright microscope.

The fluorescent signal from labeled cells was split and detected by two photomultipliers. An infrared camera was used to visualize the patch electrode and retinal cells. Infrared light, light for photoreceptor stimulation and light for bi-ChR2 stimulation were provided by a DLP projector. The light provided by the DLP projector was gated by a fast shutter and was modified by neutral density and band pass filters

Data were analyzed offline using MATLAB (Mathworks). Spikes were detected by thresholding. Spike data and inhibitory currents were averaged across stimulus repetitions. Responses were quantified by counting the spike events for the cell-attached data and measuring the amplitude of the inhibitory current for the whole-cell data for each motion direction. From these responses the DSI and the horizontal DSI were computed for both spike tuning and inhibitory tuning, as described in the multielectrode array section. Polar plots of the spike tuning and quantification of spiking DSI were only made for cells responding with at least 15 spikes in four stimulation trials. Spike rates were obtained by convolving the spike train with a Gaussian window (sigma = 35 ms). Inhibitory current traces were smoothed using the MATLAB smooth function with a span of 0.3 s for plotting the example cells (Figures 1.10 and 1.12) or a span of 0.01 s for plotting the time course of inhibition and excitation (Figure 1.11B-C). The duration of excitatory and inhibitory currents was quantified by the duration the current was higher than 75% of its maximal value. For normalization of motion-evoked magnitudes of inhibitory currents, values were divided by the magnitude of the inhibitory current evoked by the flashed spot stimulus for each cell.

Mouse *FRMD7* mRNA analysis. Total RNA was extracted from wild type and *FRMD7*^{tm} retinas using Trizol reagent (Invitrogen). To form cDNA, RNA was reverse transcribed using random hexamers and the Superscript III thermostable RT system (Invitrogen) according to the manufacturer's instructions. *FRMD7* splice variants were determined from wild type and *FRMD7*^{tm} cDNA by PCR amplification using the following primers: ex2F (5'-cgctcttcaacctgagctg), ex3R (5'-cttgcttcgttatgggcttc), ex3F (5'- tggaacttctgaagcccataa), ex4R (5'-agttcttcccgaagatgtcc), ex5R (5'-atgtgcgacaccattaaagc), En2R (5'-aactcagccttgagcctctg), lacZR1 (5'-caccacgctcatcgataattt), lacZF1 (5'-ttcaacatcagccgctacag), lacZR2 (5'-tttcaggttcaggggaggtgtg) (Figure 1.1A). PCR products were identified on agarose gel (Figure 1.1B), extracted, cloned using the TOPO Cloning Kit (Invitrogen) and sequenced, and the sequences were analyzed (Figures 1.1C-E). In wild type mice we identified a single transcript variant across exon 2 to exon 5 (*FRMD7*-WT, see below). In *FRMD7*^{tm} mice we found three major transcript variants (*FRMD7*-Mut, *FRMD7*-Mut-ex4-del and *FRMD7*-WT). *FRMD7*-Mut-ex4-del had two minor variants (*FRMD7*-Mut-ex4-del-v1 and *FRMD7*-Mut-ex4-del-v2). The *FRMD7*-Mut transcript contains the first three exons of *FRMD7* mRNA and the non-genomic En2-IRES-LacZ cassette. In *FRMD7*-Mut-ex4-del-transcripts exon 4 is deleted. Due to inserted, in-frame stop codons, both *FRMD7*-Mut and *FRMD7*-Mut-ex4-del transcripts are predicted to produce a truncated protein consisting of exons 1 to 3 in which the FERM-N

domain of *FRMD7* is disrupted and FERM-M and FERM-C domains omitted. The presence of (low levels of) wild type transcript is likely due to alternative splicing that skips the inserted LacZ cassette. The 5-prime region of the *FRMD7* transcript variants (Figure 1.1C) are shown below, the first in-frame stop codon is shown underlined and bold, the primer pair used to amplify the transcript fragment is shown in brackets.

FRMD7-Mut (ex3F/lacZR1):

tggaacttctgaagcccataacgaagcaagtcaaaaatcccaggtcccgaaaaccaaagaagaagaaccctaacaaagaggacaag
cggcctcgcacagccttcactgctgagcagctccagaggctcaaggctgagtttcagaccaacaggtacctgacagagcagcggcg
ccagagtctggcacaggagctcggtacccggaagatctggactctagagaattccgcccctctccctcccccccccctaacgttactg
gccgaagccgcttggaataaggccggtgtgcgtttgtctatatgttattttccaccatattgccgtcttttggcaatg**tga**gggcccggaa
acctggccctgtcttcttgacgagcattcctaggggtctttcccctctcgccaaaggaatgcaaggtctgttgaatgtcgtgaaggaagc
agttcctctggaagcttcttgaagacaaacaacgtctgtagcgacccctttgcaggcagcggaacccccccacctggcgacaggtgcctc
tgcggccaaaagccacgtgtataagatacacctgcaaaggcggcacaaccccagtgccacgttgtgagttggatagttgtggaaaga
gtcaaatggctctcctcaagcgtattcaacaaggggctgaaggatgcccagaaggtaccccattgtatgggatctgatctggggcctcg
gtgcacatgctttacatgtgtttagtcgaggttaaaaaacgtctaggccccccgaaccacggggacgtggttttcctttgaaaaacacgat
gataagcttgccacaaccatggaagatcccgtcgttttacaacgtcgtgactgggaaaaccctggcgttacccaacttaatcgccttgca
gcacatccccctttcgccagctggcgtaatagcgaagaggcccgcaccgatcgcccttcccaacagttgcgcagcctgaatggcgaa
tggcgctttgcctggtttccggcaccagaagcggtgccggaaagctggctggagtgcgatcttcctgaggccgatactgtcgtcgtccc
ctcaaactggcagatgcacggttacgatgcgcccatctacaccaacgtgacctatcccattacggtcaatccgccgtttgttcccacgga
gaatccgacgggttgttactcgctcacatttaatgttgatgaaagctggctacaggaaggccagacgcgaattatttttgatggcgttaact
cggcgtttcatctgtggtgcaacgggcgctgggtcggttacggccaggacagtcgtttgccgtctgaatttgacctgagcgcatttttac
gcgccggagaaaaccgcctcgcggtgatggtgctgcgctggagtgacggcagttatctggaagatcaggatatgtggcggatgagc
ggcattttccgtgacgtctcgttgctgcataaaccgactacacaaatcagcgatttccatgttgccactcgctttaatgatgatttcagccgc
gctgtactggaggctgaagttcagatgtgcggcgagttgcgtgactacctacgggtaacagtttctttatggcagggtgaaacgcaggt
cgccagcggcaccgcgcctttcggcggtgaaattatcgatgagcgtggtg

FRMD7-Mut-ex4-del-v1(ex3F/ex5R):
tggaacttctgaagcccataacgaagcaagtcaaaaaggtatctttttactcttcaaataaagaaggatttggctctgggaaggcttccat
gcag**tga**caactgcacagctttaatggtgtcgcacat

FRMD7-Mut-ex4-del-v2 (ex3F/ex5R):
tggaacttctgaagcccataacgaagcaagtcaaaaatccaggtatctttttactcttcaaa**taa**agaaggatttggctctgggaaggctt
ccatgcagtgacaactgcacagctttaatggtgtcgcacat

FRMD7-WT (ex3F/ex5R):

tggaacttctgaagcccataacgaagcaagtcaaaaatcctaaggaggttgttttcaaatttatggtgaaatttttcccagtggaccccgg
acatcttcgggaagaactcacaaggtatctttttactcttcaaataaagaaggatttggctctgggaaggcttccatgcagtgacaactgc
acagctttaatggtgtcgcacat

In RT-qPCR analysis the level of the three major transcript variants were determined relative to 18S rRNA (Figures S1D and S1E). The phenotype observed in *FRMD7*^{tm} mice likely results from the significant decrease in the level of the *FRMD7* protein. If, however, the truncated proteins made from the mutant transcripts are not degraded, it is possible that they act as dominant negative regulators of *FRMD7* function.

Immunohistochemistry. Mouse retinas were fixed for 30 min in 4% (wt/vol) paraformaldehyde in PBS (in mM: 137 NaCl, 2.7 KCl, 4.3 Na_2HPO_4, 1.47 KH_2PO_4; pH 7.4) and washed with PBS for at least 1 day at 4°C. Non-human primate retinas were fixed for one or two days in 4% paraformaldehyde in PBS and washed with PBS for at least 1 day at 4°C. To stain the mouse brains, animals were transcardially perfused with 4% paraformaldehyde. The brains were post-fixed in 4% paraformaldehyde overnight at 4°C and sectioned at 150 µm using a vibratome (Leica, VT1000S). To aid penetration of the antibodies, retinas were frozen and thawed three times after cryoprotection with 30% (wt/vol) sucrose in PBS. For staining with anti-β galactosidase, antigen retrieval was carried out by incubating retinas in Tris-EDTA buffer (10 mM Tris, 1 mM EDTA, 0.05% Tween20, pH 8.0) for 30 min at 80°C. All other procedures were carried out at room temperature, except for the secondary antibody reaction. After washing in PBS, retinas were blocked for 1 h in 10% (vol/vol) normal donkey serum (NDS; Chemicon), 1% (wt/vol) bovine serum albumin (BSA), and 0.5% (vol/vol) TritonX-100 in PBS. Primary antibodies were incubated for 6-7 days in 3% (vol/vol) NDS, 1% (wt/vol) BSA, 0.02% (wt/vol) sodium azide, and 0.5% (vol/vol) TritonX-100 in PBS. Secondary antibodies were incubated for one day at 4°C in 3% (vol/vol) NDS, 1% (wt/vol) BSA, and 0.5% (vol/vol) TritonX-100 in PBS together with streptavidin-Alexa Fluor 633 (Invitrogen, 1:200) and DAPI (4',6-diamidine-2-phenylindole dihydrochloride, Roche Diagnostics, 10 µg/ml) in some experiments. DAPI binds to DNA and, therefore, labels nuclei. After a final wash in PBS, retinas were embedded in Prolong Gold antifade (Life Technologies).

The following sets of primary and secondary antibody combinations were used for staining retinas: (i) Primary: goat anti-ChAT (1:200, AB144P, Chemicon). Secondary: donkey anti-goat IgG conjugated with Alexa Fluor 568 (1:200, Invitrogen). (ii) Primary: rabbit anti-GFP (1:200, A11122, Invitrogen). Secondary: donkey anti-rabbit IgG conjugated with Alexa Fluor 488 (1:200, Invitrogen). (iii) Primary: rat anti-GFP (1:500, 04404-84, Nacalai). Secondary: donkey anti-rat IgG conjugated with Alexa Fluor 488 (1:200, Invitrogen). (iv) Primary:

chick anti-β galactosidase (1:200, AB9361, abcam). Secondary: donkey anti-chicken IgY conjugated with Alexa Fluor 488 (1:200, Jackson ImmunoResearch).

Confocal analysis. Fluorescent *in situ* hybridization and immunohistochemistry signals in the retinas and brain sections were analyzed using a Zeiss LSM 700 confocal microscope. *In situ* hybridization signals were assessed from 1024×1024 pixel z-stack images at 0.35 µm z steps taken with a 63× oil immersion lens, numerical aperture (NA) 1.3. Immunohistrochemistry signals were assessed from 1024×1024 pixel z-stack images at 0.35 µm z steps taken with a 63× oil immersion lens, NA 1.3 or a 40× oil immersion lens, NA 1.0. Images were processed using Imaris (Bitplane), Fiji, or Mathematica (Wolfram). For quantification of fluorescent *in situ* hybridization, at each developmental time point (E12.5, E16.5, P1, P3, P5, P7, P9, P11, P13, and P30) we counted the number of punctuated dots for *ChAT* and *FRMD7* mRNAs present within the cell for five cells semi-automatically using the Imaris Spot function. To quantify the number of starburst cells in wild-type and *FRMD7^{tm}* retina, the ChAT-positive cells were counted manually from confocal images of anti-ChAT-stained retinas in Fiji. To quantify GFP-labeled starburst cell processes, we first drew a convex polygon by connecting the outer tips of the processes, and defined the area of the polygon as the dendritic field size in Fiji. For the dendritic asymmetry index, we determined the ratio between the widest and narrowest diameters of the polygon and expressed this as a percentage. The number of primary processes was counted in 3D-reconstructed confocal images in Imaris. To quantify the co-stratification of neurobiotin-filled DS cell dendrites and anti-ChAT-labeled starburst cell processes in retinas of *Hoxd10-GFP* and *FRMD7^{tm}*;*Hoxd10-GFP* mice, we first determined the fluorescence intensity profile for neurobiotin and ChAT signals along the depth of the retina on the side view of the confocal z-stack in Fiji. Next, Full Width at Half Maximum for neurobiotin and ChAT signals were determined and their overlap at each of the proximal and distal strata within the inner plexiform layer was determined. To quantify GFP-labeled cells in the retinas of *Hoxd10-GFP* and *FRMD7^{tm}*;*Hoxd10-GFP* mice, the GFP-expressing cells were counted manually from epi-fluorescent stereomicroscopic (Olympus SZX16) images of non-stained, freshly dissected retinas.

Statistical Analysis. We used the following statistical tests. Mann-Whitney-Wilcoxon test, Chi-square or Fisher exact test (if 'n' in a category ≤ 5), Kolmogorov-Smirnov test. Statistical significance is noted by * for $p < 0.05$, ** for $p < 0.01$, and *** for $p < 0.001$. Not significant is denoted as n.s. for $p \geq 0.05$

Chapter 2

Animals. *ChAT-Cre* (strain: B6;129S6-*ChAT*$^{tm1(cre)Lowl}$/J, stock number: 006410), *LSL-DTR* (strain: C57BL/6-*Gt(ROSA)26Sor*$^{tm1(HBEGF)Awai}$/J, stock number: 007900), *LSL-tdTomato* (strain: B6;129S6-*Gt(ROSA)26Sor*$^{tm9(CAG-tdTomato)Hze}$/J, stock number: 007905), *Hb9-GFP* (strain: Tg(Hlxb9-GFP)1Tmj, stock number: 005029), and *Bl6* ('wild type', strain: C57BL/6J, stock number: 000664) were purchased from Jackson laboratories. *Drd4-GFP* (strain: Tg(Drd4-EGFP)W18Gsat/Mmnc, stock number: 000231-UNC) was obtained from MMRRC. *FRMD7*^{tm} mice refer to the homozygous female or hemizygous male *FRMD7*$^{tm1a(KOMP)Wtsi}$ mice, which were obtained from the Knockout Mouse Project (KOMP) Repository. Wild type mice in which DT was injected into both eyes served as control in experiments performed with DT. Animals were between two and eight months old. Both males and females were used. All animal experiments and procedures were performed in accordance with standard ethical guidelines (European Communities Guidelines on the Care and Use of Laboratory Animals, 86/609/EEC) and were approved by the Veterinary Department of the Canton of Basel-Stadt.

Two-photon targeted patch clamp recordings in retina. For targeted recordings of GFP-labeled single types of retinal ON-OFF DS cells, retinas were isolated under dim red light in oxygenated Ringer's medium. Retinas were mounted ganglion-cell-layer-up on a filter paper (Millipore) in which a 2 mm × 2 mm window was cut to enable visual stimulation of the retina. During recording, the retina was continuously superfused with oxygenated Ringer's medium and the temperature was kept at 35-36°C. The two-photon microscope system for targeted patch-clamp recordings from GFP-expressing cells, including the light pathways for visual stimulation of the retina, has been described before (Farrow et al., 2013). Fluorescent cells were targeted using a two-photon microscope equipped with a Mai Tai HP two-photon laser (Spectra Physics), set to 920 nm, integrated into the electrophysiological setup. The two-photon fluorescent image was overlaid on an IR image acquired using a CCD camera (SPOT Visitron Systems). The infrared light was produced with a digital light projector (PLUS) and a 750±25 nm filter. Spike recordings were performed in loose cell-attached mode with 5-7 MΩ glass electrodes (BF100-50-10, Sutter Instruments) filled with Ringer's solution with a Multiclamp 700B amplifier (Molecular Devices). Signals were digitized at 10 kHz (National Instruments A/D board) and acquired using software written in LabVIEW (National Instruments). The light patterns for retinal stimulation were generated using a DLP projector (PLUS; refresh rate of 75 Hz) and focused on the retina, after passing a neutral density filter (ND30). The stimuli were controlled via software written in Python. Direction selectivity was tested by moving a 300 μm diameter white light spot (1000 R*/s light intensity) on black

background across the retina in eight different directions at 1200 μm/s. All stimuli were repeated six times, the first repetition was excluded from analysis. Data was analyzed in Matlab and Python. Spikes were detected via thresholding.

Diphtheria toxin injection. Diphtheria toxin (DT) stock solution was made from diphtheria toxin (Sigma, D0564) dissolved in PBS (Phosphate Buffered Saline) at 2 μg/μl concentration and was stored at −80°C. Before eye injection, the stock was diluted with PBS to a final concentration of 1.76 ng/μl. Mice were anesthetized with fentanyl-medetomidine-midazolam (fentanyl 0.05 mg/kg, medetomidine 0.5 mg/kg, midazolam 5.0 mg/kg). A hole was made close to the border between sclera and cornea using a 30G needle. 2 μl toxin solution was loaded into a pulled borosilicate glass pipette (1.5 mm outer diameter, tip diameter 100 μm). The pipette was guided through the hole and the solution was injected into the vitreous. Both eyes were injected. After the eye injection, anesthesia was antagonized with a mix of naloxone 1.2 mg/kg, atipamezol 2.5 mg/kg, and flumazenil 0.5 mg/kg. Each eye was re-injected two days after the initial injection. Starburst-ablated recordings were performed seven days after the initial injection.

Antibody staining and confocal imaging. Retina: Antibody staining and confocal imaging was performed in whole-mount retinas as described before (Siegert et al., 2009). In all staining procedures four labels were used. Hoechst-labeling of the cell nuclei and ChAT-antibody-labeling of the starburst cells were included in all stainings. At the end of all physiological and imaging experiments involving DT injection, the presence of starburst cells was detected with immunostaining and the results were only analyzed if starburst cells were not detectable in the retina. The primary antibodies used were goat anti-ChAT (Chemicon, AB144P-200UL, 1:200), rabbit anti-GABA (Sigma, A2052, 1:2000), rabbit anti-calbindin D-28k (Swant, CB38, 1:1000), and rat anti-glycine (Immunosolution, IG1002, 1:7500). The secondary antibodies used were Alexa 555 anti-goat (Invitrogen, A21432), Alexa 488 anti-goat (Invitrogen, A11055), Alexa 488 anti-rabbit (Invitrogen, A21206), Cy3 anti-rabbit (Jackson ImmunoResearch, 711-165-152) and Cy5 anti-rat (Jackson ImmunoResearch, 711-175-153) all at a concentration of 1:200. Nuclei were stained with Hoechst (1:1000). Lectin peanut agglutinin (PNA) coupled to Alexa 568 (Invitrogen, L32458, 1:500) was used to label cones. Stained retinas were imaged using a Zeiss LSM 720 confocal microscope.

Brain slice: To quantify the number of ChAT positive cells per unit volume of V1 in DT-injected and uninjected *ChAT-Cre* × *LSL-DTR* × *LSL-tdTomato* mice, brains were isolated and fixed for two hours in 4% paraformaldehyde (PFA) and were then cut to 150 μm thick slices using a vibratome. Slices were washed with PBS three times for ten minutes then mounted and imaged under a 10× air objective in a Zeiss LSM 720 confocal microscope.

tdTomato-expressing cells were counted manually. To quantify the proportion of cortical cells labeled by GCaMP6s and the proportion of cells colabeled with parvalbumin (PV) after intravenous delivery of serotype PHP.B AAV, mice were perfused for seven minutes with cold PBS containing 10 units/ml heparin, then for seven minutes with cold 4% PFA. Brains were dissected after perfusion and incubated in 4% PFA for two hours then sectioned at 150 µm thickness. Slices were washed with PBS three times for ten minutes then incubated with blocking solution (3% NDS, 1% BSA, 0.1% tritonX, 0.01% sodium azide) for two hours, incubated with primary antibodies for 48 hours, washed three times for ten minutes with PBS, incubated with secondary antibodies for two hours, washed three times for ten minutes with PBS, and mounted on glass slides with ProLong Gold (Thermo Fisher Scientific). Slices were imaged under a 20× air objective in a Zeiss 720 LSM confocal microscope. Cells were counted manually on a maximum intensity projection of the top 20 µm of a slice. The primary antibodies used were: guinea pig anti-PV (Synaptic Systems, 195 004, 1:500), rabbit anti-GFP (Millipore, AB3080, 1:500). Secondary antibodies used were: goat anti-guinea pig Alexa 647 (Thermo Fisher Scientific, A-21450, 1:500), donkey anti-rabbit Alexa 568 (Life technologies, A10042, 1:750).

Microelectrode array recordings. A CMOS-based microelectrode array was used for extracellular recordings from mouse retinal ganglion cells as described before (Fiscella et al., 2012; Frey et al., 2009). The array has 26,400 platinum electrodes at a density of 3265 electrodes/mm2 and extracellular signals can be recorded simultaneously from an arbitrarily selectable and reconfigurable subset of maximum 1024 electrodes (Müller et al., 2015a). Spike sorting and light stimulation has been described before (Fiscella et al., 2012; Franke et al., 2015). Two light stimuli were used. First, a flashed square stimulus was used to determine if a cell was ON-OFF type (responding to both light increments and decrements). A positive-contrast square (0.2 mm × 0.2 mm) was turned on for one second and turned off for one second in five repetitions. The stimulus moved sequentially in discrete non-overlapping steps over an area of ≈1mm^2 with a background irradiance of 0.2 µW/cm^2 and a square stimulus irradiance of 47 µW/cm^2 (Michelson contrast = 0.99). Second, a grating with white and black bars, 300 and 900 µm wide, was moved at 1200 µm/s in eight directions (Michelson contrast = 0.99). This stimulus was the same as the stimulus used in cortical experiments. The preferred direction was defined as the direction of motion of the grating stimulus that elicited the highest spike rate. The null direction was the 180° rotated direction with respect to the preferred direction.

Retinal response quantification. The direction selectivity index (DSI) and orientation selectivity index (OSI) were defined as described before (Mazurek et al., 2014):

$$\mathrm{DSI} = \left| \frac{\sum_{j=1}^{8} R_j e^{i\theta_j}}{\sum_{j=1}^{8} R_j} \right|$$

$$\mathrm{OSI} = \left| \frac{\sum_{j=1}^{8} R_j e^{2i\theta_j}}{\sum_{j=1}^{8} R_j} \right|$$

where R_j denotes the peak firing rate in each of the eight directions of stimulus movement ordered in ascending directions 0-360° in 45° steps. The following thresholds were used to define selective and non-selective cells. Direction-selective cell: DSI > 0.5, orientation-selective cell: OSI > 0.2 and DSI < 0.2, non-selective cell: OSI < 0.2 and DSI < 0.2.

ON-OFF versus not-ON-OFF cells were classified based on the responses to the flashed-square stimulus using an ON-OFF index (OOI).

$$\mathrm{OOI} = \frac{R_{\mathrm{ON}} - R_{\mathrm{OFF}}}{R_{\mathrm{ON}} + R_{\mathrm{OFF}}}$$

where R_{ON} and R_{OFF} refer to the peak firing rates to the onset and offset of the positive-contrast square, respectively. A cell was defined as ON-OFF if |OOI| < 0.3.

The "peak firing rates" of a ganglion cell, in response to motion stimulation, were determined as follows. Spiking responses to five repetitions of stimuli moving in eight different directions were recorded. Each spiking response was binned (bin width=10 ms) and convolved with a Gaussian kernel (σ=100ms), resulting in five response curves. The maxima of the five response curves were averaged. The resulting single value was defined as the peak firing rate. Using this algorithm, the peak firing rate for each stimulus direction was computed. Therefore, the peak firing rates of a single ganglion cell, in response to motion stimulation, were described with eight numbers, one for each direction. These eight numbers were normalized to their maximum (therefore scale from 0 to 1), yielding "normalized peak firing rates" which were plotted on polar plots in Figures 2.1C-D and 2.5B-C. "peak firing rates" for flashed-square stimulus were defined similarly.

The "mean of the peak firing rates" of a group of ganglion cells, in response to motion stimulation, was determined as follows. The peak firing rate (defined above) in each stimulus direction was determined for each retinal ganglion cell of the group. This resulted in eight numbers for each recorded cell. These eight numbers were averaged across the group, resulting again in eight numbers, the mean of the peak firing rates of the group. "Normalized mean of the peak firing rates" was defined for two groups of retinal ganglion cells, the control and mutant groups, by taking the mean of the peak firing rates of both groups (2 x 8 numbers)

and normalizing these 16 numbers to their maximum (scale from 0 to 1). Normalized means of the peak firing rates were plotted on polar plots in Figures 2.1E, 2.5D and 2.7D.

The "complementary cumulative distribution of DSI values" of a group of retinal ganglion cells was determined as follows. The peak firing rate (defined above) for each of the eight stimulus directions was determined for each retinal ganglion cell of the group. This resulted in eight numbers for each recorded cell. Based on the eight numbers, a DSI value was calculated for each cell, resulting in "n" DSI values for the group of ganglion cells, where n is the number of cells in the group. The complementary cumulative distribution of these DSI values shows the proportion of cells with DSI larger than the value indicated on the x-axis and is equivalent to 1 minus the cumulative distribution. Complementary cumulative distributions of DSI values are shown in Figures 2.1F, 2.5E and 2.7E.

The "complementary cumulative distribution of peak firing rates across all stimulus directions" of a group of retinal ganglion cells was determined as follows. The peak firing rate (defined above) for each of the eight stimulus directions was determined for each retinal ganglion cell of the group. This resulted in eight numbers for each recorded cell. These eight numbers were collected for all ganglion cells in the group resulting in n x 8 numbers (n=number of ganglion cells in the group). The complementary cumulative distribution (defined above) of the n x 8 numbers was called the complementary cumulative distribution of peak firing rates across all stimulus directions of the group, and was plotted in Figures 2.1G, 2.5F and 2.7F-G.

Adeno-associated viruses (AAV). AAVs were made as described previously (Grieger et al., 2006). Genome copy (GC) number titration was performed using real-time PCR (Applied Biosystems, TaqMan reagents). Two different AAVs were used. The first AAV, AAV-EF1a-GCaMP6s-WPRE, was obtained by cutting commercially synthesized GCaMP6s with BamHI/EcoRI overhang sites (Genewiz Inc.) with BamHI/EcoRI. This was then inserted into pAAV-EF1a-DIO-hChR2(H134R)-EYFP-WPRE (kindly provided by K. Deisseroth) using BamHI/EcoRI sites. The serotype of this AAV was 1, PHP.B or 7. Serotype 1 (6.6×10^{12} GC/ml) was used in experiments in the cortex of *FRMD7^{tm}* and corresponding control mice (Figure 2.11) except for analyzing the influence of the number of stimulus repetitions and for determining the speed tuning of cortical cells. Serotype PHP.B (1.7×10^{14} GC/ml) was used in experiments in the cortex of *FRMD7^{tm}* and corresponding control mice for analyzing the influence of the number of stimulus repetitions and for determining the speed tuning of cortical cells (Figure 2.16). Serotype 7 (3.5×10^{12} GC/ml) was used in experiments in the LGN of starburst-ablated and corresponding control mice (Figure 2.8). The second AAV, AAV-hSyn-GCaMP6f-WPRE was generated by PCR amplifying the hSyn promoter from

pAAV.hSyn.GCaMP3.3 (kindly provided by J.M. Wilson) flanked with MluI and BamHI restriction sites, and replacing the EF1a promoter in pAAV-EF1a-GCaMP6f-WPRE using MluI/BamHI digest. The serotype of this AAV was 1 (1.4×10^{12} GC/ml). This AAV was used in experiments in the cortex of starburst-ablated and corresponding control mice (Figure 2.12).

Viral injection to the eye. The procedure followed the diphteriatoxin injection protocol described above. 2 µl serotype 7 AAV-EF1a-GCaMP6s-WPRE was loaded into a pulled borosilicate glass pipette and was injected into the vitreous. Only the eye contralateral to the imaged LGN was injected. LGN recordings were performed three weeks after the virus injection.

Two-photon imaging of ganglion cell axon terminals in the LGN. Mice were anesthetized as described for toxin injection and placed in a stereotaxic frame (Narishige, SR-5M). Coliquifilm (Allergan) was applied to the eyes to prevent dehydration during surgery. A metal bar for head fixation during imaging was glued to the skull[38]. An 8 mm diameter craniotomy was made above the LGN. The exposed cortex and the underlying hippocampus were aspirated, exposing the LGN. The tissue was kept moist with a buffer (135 mM NaCl, 5.4 mM KCl, 5 mM HEPES, 1.8 mM $CaCl_2$, pH 7.2). A 2 mm diameter glass coverslip was slightly pushed against the LGN, while the tissue between the edges of the coverslip and the skull was covered with superglue and dental cement. After surgery, anesthesia was antagonized as described above for eye injections, and mice were left to recover on a heating pad for one hour. Before imaging, mice were anesthetized with 0.25% isoflurane and 2.5 mg/kg chlorprothixene. Retinal ganglion cell axons terminals in the LGN were imaged through a 16× objective (Nikon, 0.8 numerical aperture (NA)) down to 200 µm depth. The rest of the imaging and stimulation procedure was the same as described below for cortical two-photon imaging and visual stimulation.

Optokinetic reflex and pupil reflex measurement. Eye tracking was performed using an ETL-200 eye tracking system (Iscan Inc., Woburn, Maine, USA). To visualize the pupil, eyes were illuminated with IR light and recorded with IR cameras at 120 Hz. The optokinetic response was quantified by counting the number of eye tracking movements (ETMs) as described previously[39]. Briefly, the position of the pupil was plotted as a function of time, the derivative of this signal was calculated, and a threshold was set. Events above threshold were counted as ETMs. The threshold was adjusted in control mice so that all visually assessed ETMs were detected. This threshold was then applied to starburst-ablated mice. Visual stimulation was performed as described previously (Yonehara et al., 2016), except that here two monitors were placed in a 'V' position in front of the mouse for binocular stimulation.

The head of the mouse was fixed with a head holder, and the body was restrained in a foam jacket. For motion stimulation, black and white gratings (0.5 duty cycle) with 10°-wide bars were moved at 10°/s. 1° corresponds to 31 μm retinal distance in mice[41]. To test the pupil reflex of the mouse, the pupil diameter was measured first under dark conditions and then while a full-field white flash was shown to the mouse. White flash intensity was 40 $\mu W/cm^2$ measured at the screen surface.

Cranial-window implantation and virus injection to cortex. Mice were anesthetized as described above for toxin injections and placed in a stereotaxic frame (Narishige, SR-5M). Coliquifilm (Allergan) was applied to the eyes to prevent dehydration during surgery. A thin iron ring and a metal bar for head fixation during imaging were glued to the skull (Holtmaat et al., 2009). A 3 mm diameter craniotomy was made above the primary visual cortex, 2.5 mm lateral from the medial blood vessel and 1.0 mm frontal from the coronal blood vessel. The cortical surface was kept moist with a buffer (135 mM NaCl, 5.4 mM KCl, 5 mM HEPES, 1.8 mM $CaCl_2$, pH 7.2). 100 nl AAV was slowly injected into the visual cortex at a depth of 100–400 μm using a borosilicate glass micropipette (tip diameter 30 μm) at multiple (3–5) sites. After viral injection, the cortex was covered with a 3 mm diameter glass coverslip and sealed with dental acrylic cement (Paladur, Heraeus Kulzer). Dental acrylic cement was also used to mount a head bar on the skull to immobilize the mouse during imaging (Holtmaat et al., 2009).

Viral labeling of cortex by intravenous injection. Intravenous injection was used for analyzing the influence of the number of stimulus repetitions and for determining the speed tuning of cortical cells. The advantage of intravenously delivered serotype PHP.B (Deverman et al., 2016) AAV was that it led to widespread labeling of cortical cells and yielded no nuclear expression of GCaMP6 for at least 10 weeks, the longest time tested (Figure 5.3). Mice were anesthetized with 5% isoflurane and received a single retro-orbital injection of 10 μl serotype PHP.B (Deverman et al., 2016) AAV-EF1a-GCaMP6s-WPRE. Cortical recordings were performed from three weeks after injection. The proportion of visually responsive cells in layer 2/3 of the V1 infected by intravenous injection of serotype PHP.B AAV was slightly lower than the proportion of visually responsive cells infected by direct cortical injection of serotype 1 AAV (Mann-Whitney U test, $p = 0.03$, intravenous injection, 9.21% ± 1.65% s.e.m, n = 16 mice, direct injection, 12.1 % ± 1.58 % s.e.m, n = 18 mice). The proportion of visually responsive cells was quantified as follows. We stimulated and extracted responding cells as described below in "Cortical two-photon imaging and visual stimulation" and "Online response detection". We included calcium traces recorded during both the static and the moving part of the stimulus. Visually responsive cells were defined using ANOVA ($p < 0.01$) and a threshold $\Delta F/F$ (> 0.05) in the direction with largest amplitude. After

intravenously delivery of AAV-Ef1a-GCaMP6s-WPRE, 22.2% of the cells in V1 were labeled with GCaMP6. The proportion of PV-and-GCaMP6 colabeled cells among GCaMP6-labeled cells was 8.4%, similar to the proportion of PV-labeled cells among all V1 cells (7.4%) (Figure 5.3).

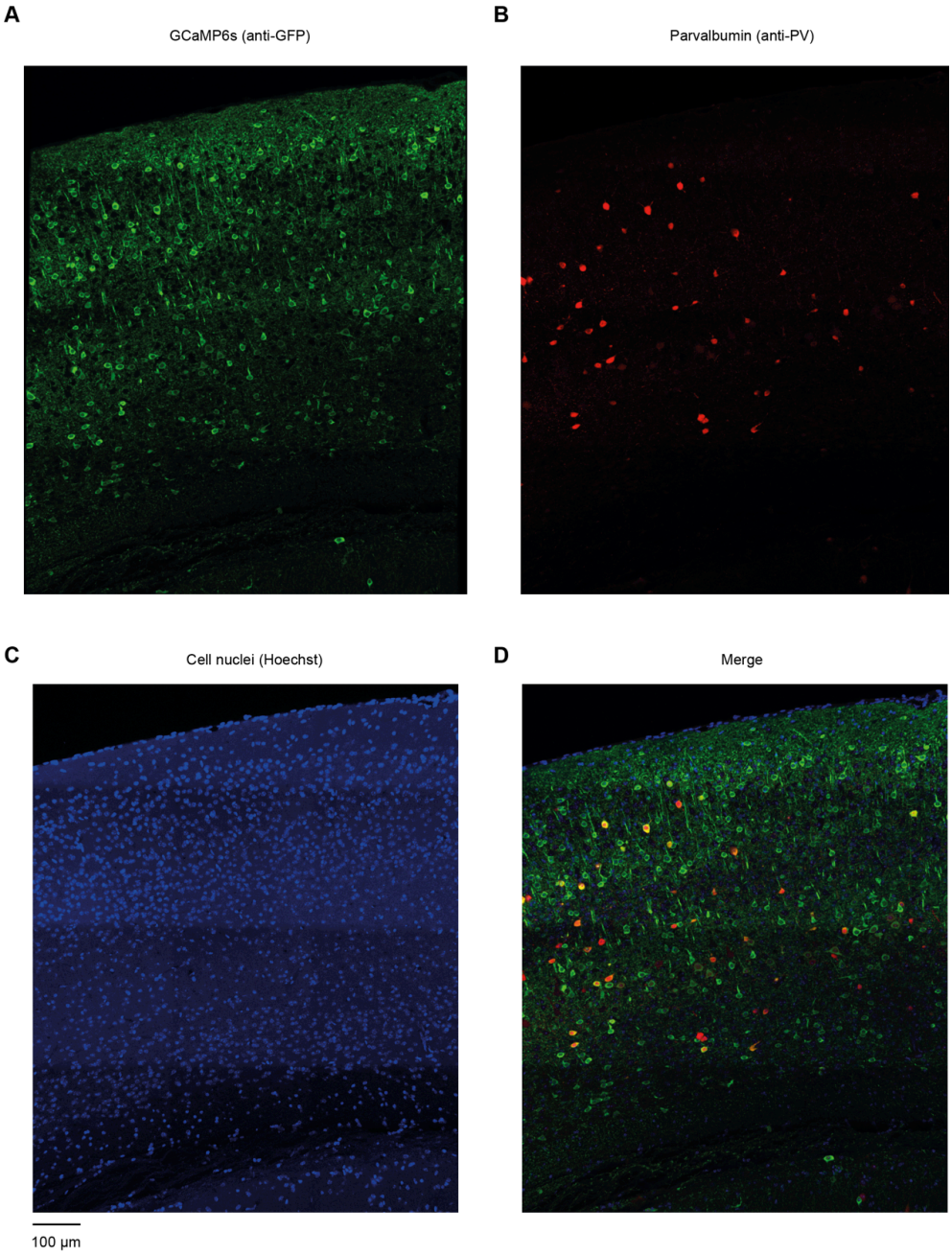

Figure 5.3 **Intravenous injection of AAV serotype PHP.B yields widespread expression of GCaMP6s in the cortex without nuclear expression.** Sagittal view of V1. (**A**) Staining with anti-GFP antibody shows cells expressing GCaMP6s. (**B**) PV-expressing cells stained with anti-PV antibody. (**C**)

Nuclei of cortical cells stained with Hoechst. (**D**) Merge of (A-C) shows cells coexpressing GCaMP6s and PV.

Cortical two-photon imaging and visual stimulation. The activity of neurons in V1 was recorded by imaging fluorescence using a two-photon microscope (Femtonics, Femto3D-RC) and a mode-locked Ti:Sapphire laser (Newport, Mai Tai DeepSee) at 920 nm through either a 20× (Olympus, 0.95 NA) or a 16× (Nikon, 0.8 NA) water-immersion objective. During imaging, mice were anesthetized with 0.25% isoflurane and 2.5 mg/kg chlorprothixene and vital signs such as heart rate, breathing rate, and oxygen saturation were monitored (Starr Life Sciences, Mouse Ox). To shield light coming from the stimulation screen, a metal cone with a magnetic base ring was mounted on the head by attaching it to the iron ring. 1% low melting point agar solution with a black pigment (Lukas) was used to fill in the gaps between the cone and the metal ring on the head of the mouse.

A Python-based user interface controlled visual stimulation, data recording, and alignment. Scanning was performed in a horizontal plane at 6-8 Hz between 100 and 250 μm below the surface of the cortex in 10 μm steps. Visual stimulation was performed with an LED projector (Acer, K10), projecting images onto a 40 cm × 29 cm (width × height) screen positioned 28 cm from the right eye. We presented moving gratings in eight directions. The widths of the white and black bars of the grating were 10 and 30 visual degrees respectively (10 visual degrees translate to about 300 μm on the retina). The speed of the grating was 40 visual degrees/s (°/s, 1200 μm/s on the retina) for most cortical experiments, except for the experiments performed to estimate the speed tuning. Here mice were stimulated with the same grating moving at four distinct speeds: 10, 16.6, 26.6 and 40 °/s (300 μm/s, 500 μm/s, 800 μm/s, and 1200 μm/s on the retina). The average stimulus intensity at the animal's eye was 2.2 $\mu W/cm^2$, Michelson contrast was 0.99. The grating, with an orientation orthogonal to the future motion direction, was first presented on the screen for 3.8 s. It then moved in one of eight directions (0, 45, 90, 135, 180, 225, 270, 315 degrees) for 3.8 s, and finally remained motionless on the screen for 4 s. With the exception of the experiments testing the effect of stimulus repetitions, every image plane was acquired 2-4 times. Since the same cells were imaged in 2-3 planes, the stimulus was presented to, and responses were measured from, each cell 4-12 times. In the experiments testing the effect of stimulus repetitions, the stimulus was repeated and the images were acquired six times in each image plane.

Online response detection. The sequence of images acquired in an experiment was stored in a 3D data cube in which the first two dimensions correspond to the rows and columns of one two-photon image, and the third dimension corresponded to the time the image was acquired. In the data cube, calcium transients were treated as 3D objects. To detect the 3D location of

the calcium transients, the data cube was first filtered using the Wiener filter, the result was thresholded at 2 × the standard deviation (s.d.), and shot noise was reduced by applying a binary opening operator followed by a closing operator. In the resulting binary 3D data cube, 3D-continuous objects were detected using a connected-feature detection algorithm. To remove small transients, the object set was further filtered by setting a threshold on the spatial projections of the objects (> 3.6 μm or 3 pixels) and on the temporal projection (decay time > 1 s). Next, all objects were projected onto the 2D spatial plane, resulting in a connected pixel set for each object. Independent component analysis was then performed on the original time series of measured fluorescence at these pixel sets for each object. This step connected together those pixels where responses were correlated in time. We kept those independent components as response transients where the amplitude distribution was skewed towards high amplitudes. This was done by setting a threshold for the skew and kurtosis of the distribution. The 2D spatial pixel sets belonging to the independent component responses were defined as 'responding cells'. The response of a responding cell was expressed as ΔF/F, where F was defined as either the location of the peak on the histogram of recorded fluorescence values from the responding cell, or the mean of the fluorescence values acquired before the beginning of the stimulation: the smaller of the two quantities was used. The activity traces of responding objects were determined online during recording using Python. Finding all responding objects and displaying the responses took less than half the data collection time. Based on the two-photon images, the responding objects were manually classified as cell bodies or dendrites. Apart from LGN data, all analyses and data presented in the paper are based on responses from cell bodies.

Cortical response quantification. For each response belonging to a cell body, motion-response amplitudes were assigned for each motion direction. The motion-response amplitude value for each direction of motion was determined by sorting all the recorded data points during image motion in a particular direction, and taking the mean of the larger half. For each cell in a recording, a response threshold was defined as the average of the response values recorded before the start of visual stimulation + 4 × s.d. The cell was classified as 'responding' if its response to the stimulus moving in any of the directions was above the response threshold for a contiguous block of at least 1 s for at least two repetitions of the stimulus.

The direction selectivity index (DSI) and orientation selectivity index (OSI) were defined as described for retinal cells.

The “peak response” of a cortical cell in a given stimulus direction was defined similarly to the “peak firing rate” of a ganglion cell recorded *ex vivo*, except that here the maxima of the ΔF/F response curves obtained during repeated stimulus presentations were averaged.

The “mean of the peak response” and the “normalized mean of the peak response” of a group of cortical cells were determined similarly to the “mean of the peak firing rate” and “normalized mean of the peak firing rate” for retinal ganglion cells. Normalized means of the peak responses were plotted on polar plots in Figure 2.14A and 2.14D.

The horizontal versus vertical direction selectivity index was defined as:

$$\mathrm{HVI} = \frac{N_H - N_V}{N_H + N_V}$$

Where N_H and N_V denote the number of cells preferring horizontal or vertical directions respectively (Figures 2.11F, 2.12F, 2.14C, 2.14F, 2.15C, 2.15F, 2.15I, 2.15L and 2.15O). Alternatively, the horizontal versus vertical direction selectivity index was defined for the mean of the peak responses using the same equations but N_H and N_V were used to denote the mean of the peak responses in horizontal or vertical directions respectively (Figures 2.14C and 2.14F).

The “complementary cumulative distribution of DSI values” of a group of cortical cells was determined as described for retinal ganglion cells *ex vivo* but here, instead of the peak firing rates, the peak responses were used. Complementary cumulative distributions of DSI values are shown in Figures 2.11A and 2.12G.

The posterior component of the responses of cortical DS cells was computed by taking posterior ±45° direction preferring cortical DS cells and summing the projection of their response amplitudes on the posterior axis. This sum was normalized by the number of cells in each condition. The posterior component of the responses of cortical DS cells is shown in Figure 2.16.

LGN response quantification. We used the same procedure as described for cortical cells to obtain responding objects. Based on the two-photon images, the responding objects were manually classified as axon terminals. ΔF/F response curves and response amplitudes of axon terminals were defined as described for cortical cells.

The “peak response” of a ganglion cell axon terminal within the LGN in a given stimulus direction was defined similarly to the “peak firing rate” of a ganglion cell recorded *ex vivo*, except here the maxima of the ΔF/F response curves obtained during repeated stimulus presentations were averaged.

The “complementary cumulative distribution of DSI values” of a group of retinal ganglion cell axon terminals in the LGN was determined as described for retinal ganglion cells *ex vivo* but here, instead of the peak firing rates, the peak responses were used. Complementary cumulative distributions of DSI values are shown in Figure 2.8D.

The “complementary cumulative distribution of peak responses across all stimulus directions” of a group of retinal ganglion cell axon terminals in the LGN was determined as described for retinal ganglion cells *ex vivo* but here, instead of the peak firing rates, the peak responses were used. These distributions are plotted in Figure 2.8E.

Statistics. We used the following notations. n.s.: $p >= 0.05$; *: $0.05 > p >= 0.01$, **: $0.01 > p >= 0.001$, ***: $p < 0.001$. s.e.m: standard error of the mean, s.d.: standard deviation. In boxplots, bottom and top whiskers: minimum and maximum; bottom and top of the rectangle: first and third quartiles; central line: median. We used the following statistical statistical tests: Kolmogorov-Smirnov test, Mann-Whitney U test (one-tailed), Hodges-Ajne test, Fisher's exact test, Kruskal-Wallis H test. No statistical methods were used to pre-determine sample sizes. We did not use randomization; data collection and analysis were not performed blind to the conditions of the experiments. Data was not excluded from analysis.

Chapter 3

Animals. All animal experiments and procedures were performed in accordance with standard ethical guidelines (European Communities Guidelines on the Care and Use of Laboratory Animals, 86/609/EEC) and were approved by the Veterinary Department of the Canton of Basel-Stadt. Three mice were housed in a cage and animals were maintained under a 12-hour light-dark cycle. The age of the animals varied between postnatal day 30 and 90. C57BL/6 mice, which served as 'wild type', were obtained from RCC Ltd. *Cnga3*$^{-/-}$ mice were provided by M. Biel (Biel et al., 1999), *Gnat2*^{cpfl3} mice were obtained from Jackson Laboratory (B6.Cg-Gnat2cpfl3/Boc, #006795). *Chrnb4*-GFP mice, in which cones are selectively labeled with GFP (Siegert et al., 2009), were obtained from MMRRC (Tg(Chrnb4-EGFP)1Gsat). *Gja10*-Cre mice, in which Cre is only expressed in horizontal cells (Siegert et al., 2012), were developed in house. The *Pcp2*-GFP mice, in which rod bipolar cells are labeled with GFP (Tomomura et al., 2001), were obtained from Jackson Laboratory (B6:FVB-Tg(Pcp2-EGFP)2Yuza, #004690). *Chrnb4*-GFP and *Pcp2*-GFP mice were backcrossed at least five times with C57BL/6 mice. *Pvalb*^{Cre}×*Thy*$^{Stp\text{-}EYFP}$×*Cx36*$^{-/-}$ mice (Münch et al., 2009) were made by crossing mice provided by S. Arber (*Pvalb*^{Cre}), J. Sanes (*Thy*$^{Stp\text{-}EYFP}$) and D. Paul (*Cx36*$^{-/-}$).

AAV plasmids. We refer to the C128S ChR2 mutant (Berndt et al., 2009) as bi-ChR2. To obtain pAAV-EF1a-double floxed-bi-ChR2-2A-EGFP-WPRE-hGHpA we linearized pAAV-EF1a-double floxed-hChR2(H134R)-EYFP-WPRE-hGHpA (provided by K. Deisseroth, Stanford University) using NheI/AscI. Bi-ChR2-2A-EGFP was modified 5' with an NheI site followed by an optimized Kozak sequence (GCCACC) and 3' with an AscI site. The DNA fragment was synthesized by DNA2.0 Inc. and digested using NheI and AscI, and a ligation was performed.

AAV production. Serotype 8 recombinant AAVs were made as previously described (Grieger et al., 2006) by triple-transfection of HEK 293T cells using branched polyethylenimine (Polysciences, no.23966) with a plasmid containing the transgene between the internal terminal repeats of AAV2, the AAV-helper plasmid encoding Rep2 and Cap for serotype 8, and the pHGTI-Adeno1 plasmid harboring helper adenoviral genes (both provided by C. Cepko, Harvard Medical School). Vectors were purified using a discontinuous iodixanol gradient (Sigma, Optiprep). Encapsidated DNA was quantified using TaqMan© RT-PCR (forward primer: GGCTGTTGGGCACTGACAA; reverse primer: CCAAGGAAAGGACGATGATTTC; probe: TCCGTGGTGTTGTCG) following denaturation of the AAV particles using proteinase K, and titers were calculated as genome copies (GC) per ml (titer: 1.84×10^{12} GC/ml).

Subretinal AAV administration. The animals were anaesthetized with 2.5% Attane™ Isoflurane. A small incision was made with a sharp 27-gauge needle in the sclera near the lens. Through this hole, 2 µl of AAV particles were injected slowly into the subretinal space using a blunt 5 µl Hamilton syringe that was held by a micromanipulator (World Precision Instruments). Mice older than P30 were used for injections. There was a minimum incubation time of 14 days before performing experiments with injected animals.

Immunohistochemistry. Retinas were fixed for 30 min in 4% paraformaldehyde in phosphate-buffered saline (PBS) (in mM: 137 NaCl, 2.7 KCl, 4.3 Na_2HPO_4, 1.47 KH_2PO_4, pH 7.4) at room temperature and washed with PBS for at least one day at 4°C. The retinas were treated with three freeze-thaw cycles after cryoprotection with 30% sucrose. All of the following procedures were performed at room temperature. After washing in PBS, retinas were incubated for 30–60 min in a blocking solution (10% normal donkey serum (NDS; Chemicon), 1% bovine serum albumin (BSA), 0.5 % Triton X-100 in PBS, pH 7.4). Primary and secondary antibodies were applied in 3% NDS, 1% BSA, 0.02% sodium azide and 0.5% Triton X-100 in PBS. Primary antibodies were incubated for 5-7 days. Secondary antibodies were incubated for 2 hours together with DAPI (4',6-diamidine-2-phenylindole dihydrochloride, Roche Diagnostics, 10 µg ml^{-1}), which was used to visualize cell nuclei. After three final washing steps in PBS, the retinas were mounted using Prolong Gold antifade (Invitrogen). To quantify the number of infected horizontal cells, the following antibodies were used: primary: rabbit anti-GFP (1:200, Invitrogen, A11122), mouse anti-calbindin (1:1000, Swant, Code 300); secondary: donkey anti-rabbit IgG conjugated with Alexa Fluor 488 (1:200, Invitrogen, A21206), donkey anti-mouse IgG conjugated with Alexa Fluor 647 (1:200, Invitrogen, A31571).

Confocal microscopy. A Zeiss LSM 700 laser-scanning confocal microscope with a plan-apochromat ×40 oil immersion objective lens (NA 1.2) was used.

Quantification of infected horizontal cells. The entire depth of the inner nuclear layer and outer plexiform layer of at least three highly infected retinal regions per animal was scanned with the confocal microscope. Cells were counted automatically using the spot function of Imaris (Bitplane). After automatic cell counting, stacks were manually inspected to correct false automatic counts. Calbindin was used to mark horizontal cells. The total number of horizontal cells was determined by counting the calbindin-positive cells in highly infected retinal regions of AAV-transduced *Gja10*-Cre mice. In the same retinal regions, the number of infected horizontal cells was determined by counting calbindin-positive cells expressing the virus-driven EGFP. The infection rate was calculated by dividing the number of cells positive for both calbindin and EGFP by the total number of calbindin-positive cells.

Two-photon targeted patch clamp recordings. Recordings from different retinal cell types were taken from wholemount retinas and from retina slices. Animals were dark-adapted for two hours prior to recording. Retinas were isolated in Ringer's medium (in mM: 110 NaCl, 2.5 KCl, 1 $CaCl_2$, 1.6 $MgCl_2$, 10 D-glucose, 22 $NaHCO_3$, bubbled with 5% CO_2/95% O_2) using infrared illumination and infrared goggles. Wholemount retinas were mounted ganglion cell side up on filter paper (MF-membrane, Millipore) with a ~2×2 mm window in the middle. For retinal slice preparations retinas were mounted ganglion cell side down on the same type of filter paper but without a window. 200 μm-thick slices were prepared using a tissue chopper (Stoelting CO) under infrared illumination. Wholemount and slice tissues were superfused in Ringer's medium at 36°C, bubbled with 5% CO_2/95% O_2. Pharmacological agents were delivered using a valve system (VC-6, Warner Instruments) in the following concentrations: 10 μM NBQX (6-nitro-2,3-dioxo-1,4-dihydrobenzo[f]quinoxaline-7-sulfonamide, blocking AMPA and kainate receptors), 10 μM APB (L-(+)-2-amino-4-phosphonobutyric acid, blocking metabotropic glutamate receptors), 100 μM picrotoxin (blocking GABA A and C receptors), and 10 μM strychnine (blocking glycine receptors), 20 mM HEPES (4-(2-hydroxyethyl)-1-piperazineethanesulfonic acid). APB was obtained from Calbiochem, NBQX, CPP, picrotoxin, strychnine, and HEPES from Sigma-Aldrich.

Fluorescent cells were targeted for recording (see also 'Targeting cells in wholemount' below) using a two-photon microscope equipped with a Mai Tai HP two-photon laser (Spectra Physics) tuned to 920 nm (Farrow et al., 2013). Infrared illumination and a CCD camera (Diagnostic Instruments) were used to visualize the retina and the recording electrode during two-photon scanning. A fused infrared-two photon image was used to target labeled cells in the retina. The infrared image was digitally filtered to enable better visualization of cells deep in the retina.

Whole-cell recordings were made using an Axon Multiclamp 700B amplifier (Molecular Devices). Signals were digitized at 1 kHz and low-pass filtered at 50 Hz. Patch electrodes were made from borosilicate glass (BF100-50-10, Sutter Instruments) pulled to 8 – 11 MΩ resistance. For voltage recording, the pipettes were filled with (in mM): 115 K gluconate, 10 KCl, 1 $MgCl_2$, 0.5 $CaCl_2$, 1.5 EGTA, 10 HEPES, 4 ATP-Na_2 at pH 7.2. Horizontal cells and rod bipolar cells were recorded in whole-cell current-clamp mode. Photoreceptors were recorded using perforated patch clamp in current-clamp mode (Rae et al., 1991). For perforated patch-clamp recordings the intracellular solution was supplemented with amphotericin B (70 μg/ml, Sigma). Since amphotericin B is permeable for chloride, the reversal potential of chloride (–60 mV) was set by the concentration of chloride in the pipette and in the Ringer's medium. We did not find a difference in the magnitude of rod

depolarization in experiments in which we measured it directly after getting a seal and in others where we measured it at the end of the experimental series (Figure 3.1A). It is therefore unlikely that a potential change in chloride concentration within the cell increased rod depolarization during the experiments. Furthermore, since rod bipolar cells displayed hyperpolarization when stimulated with large spots at high background light levels, it is not possible that the chloride concentration in the pipette changed the polarity of the responses in rods. The recordings were made at 0.5–1 mm distance from the optic disc, unless indicated in the text, at random positions relative to the dorsal-ventral axis of the retina. Current recordings were made in whole-cell voltage-clamp mode, with electrodes pulled to 5–8 MΩ resistance and filled with 112.5 mM $CsCH_3SO_3$, 1 mM $MgSO_4$, 7.8×10^{-3} mM $CaCl_2$, 0.5 mM BAPTA, 10 mM HEPES, 4 mM ATP-Na_2, 0.5 mM GTP-Na_3, 5 mM lidocaine N-ethyl bromide (QX314-Br), 7.5 mM neurobiotin chloride at pH 7.2. To measure inhibitory input currents we clamped the cells at 0 mV. The liquid junction potential was measured and used for voltage correction. Recordings were made using software based on Labview (National Instruments) and analyzed in Matlab (Mathworks Inc.). The presented response traces from rods are averages from 50–100 individual recordings; in other cells we averaged 3–20 individual recordings.

Targeting cells in wholemount. A small area above the ganglion cells was cleaned (i.e. the inner limiting membrane was removed) under infrared light with a patch pipette filled with mouse Ringer's solution. After cleaning, a new pipette was filled with intracellular solution and lowered towards the clean area with positive pressure inside the pipette. For patching cells in the outer retina, the patch pipette was penetrated through the inner plexiform layer and was moved diagonally towards the photoreceptor layer. The transition from the inner plexiform layer to the inner nuclear layer was detectable due to the emerging cell bodies in the inner nuclear layer. Similarly, the transition from the inner nuclear layer to the photoreceptor layer was detectable due to the change in appearance of the cell bodies (rod cell bodies are smaller and more regularly shaped and give high infrared contrast). Rod targeting was performed using infrared light by lowering the pipette into the photoreceptor layer, and patching rods in the second photoreceptor layer (measured from the outer plexiform layer). Note that there are no cones in this layer. Cone, rod bipolar, horizontal cell, and ganglion cell targeting was performed using combined two-photon and infrared imaging in mice that expressed GFP or EYFP in the respective cell type. PV5 ganglion cells were identified in the $Pvalb^{Cre}\times Thy^{Stp\text{-}EYFP}\times Cx36^{-/-}$ retina by the stratification of the ganglion cell dendrites and by the shape and size of the cell body (Münch et al., 2009).

Light stimulation. Photoreceptors and bi-ChR2 expressing horizontal cells were stimulated with light patterns generated by a projector equipped with a digital light processor (DLP) at

75 Hz (V-339, PLUS Vision Corp.). The maximum power produced by the projector was 229 ± 35 mW/cm^2 (mean ± s.e.m.). The intensity and spectrum of the projected light were measured at the focal plane, at the position of the retina on the stage, with a power meter (S130VC; Thorlabs) and a spectrometer (USB4000-UV-VIS; Ocean Optics). The photoisomerization rate (photoisomerizations per rod per second, R*/s) was computed based on the spectral sensitivity of the photoreceptors using a collecting area of 0.5 μm^2 for rods and 0.2 μm2 for cones (Lyubarsky et al., 1999). Light intensity covered 10 log units, ranging from 0.006 to 1.03×10^7 R*/s. The light path was intersected with a shutter (SC10, Thorlabs) and was modulated by neutral density and band pass filters, which were built into two filter wheels (FW102, Thorlabs).

For most experiments, the contrast (intensity of foreground / intensity of background) of the light stimulation was 1000, and this was kept constant across all light levels. The contrast was varied (30, 50, 100, 200) for the experiment shown on Figure 3.1. To record light responses in photoreceptors, spots of different diameters were presented (25, 50, 100, 200, 400, 800, 1600 μm). For bi-ChR2 stimulation we used two types of stimuli. The test flash came from the DLP projector as white light without spectral filtering. The switch flash was a 50 ms, full-field, blue flash. Here the light from the DLP projector was filtered with a band pass filter (470/40 nm, Chroma Technology Corp.). A fast shutter was used to gate the light path. The DLP projector in combination with an infrared filter (750/50 nm, Chroma Technology Corp.) served as an infrared source. For recording the spectrum of rod and cone responses in the ventral part of the retina we used a Polychrome V (Till Photonics) light source combined with a computer-controlled shutter (SC10, Thorlabs). The optic fiber of the Polychrome V was plugged into the epifluorescent part of the microscope and provided full-field illumination. The stimulus sequences were generated using software written in Matlab (Mathworks Inc.), Labview (National Instruments), or Python.

Model. We model the outer retina response in an extension of the phenomenological description of cones (Clark et al., 2013). There, the photoreceptor response is calculated as

$$(1) \qquad \tau_r \frac{dr}{dt} = \alpha y(t) - [1 + \beta z(t)]r,$$

where $r = V(t) - V_{\text{rest}}$, $V(t)$ and V_{rest} are the instantaneous and resting membrane potentials respectively, and α and β are numerical factors. The time-varying functions, $y(t)$ and $z(t)$, are related to the light input through linear convolutions, as

(2) $y(t) = \int_{-\infty}^{t} dt' K_y(t-t') I(t')$,

(3) $z(t) = \int_{-\infty}^{t} dt' K_z(t-t') I(t')$,

where $I(t)$ is the light intensity. It was found that a filter with the simple form

$$(4) \quad K_y(t) = \frac{t}{\tau_y} \frac{e^{-t/\tau_y}}{\tau_y}$$

yields good fits; the second filter has a similar form but contains a delayed component, as

(5) $K_z(t) = \gamma \frac{t}{\tau_y} \frac{e^{-t/\tau_y}}{\tau_y} + (1-\gamma) \frac{t}{\tau_z} \frac{e^{-t/\tau_z}}{\tau_z}$,

where $0 \leq \gamma \leq 1$ ensures proper normalization. Throughout, we shall adopt these forms for all our filters.

Here, we also describe the cone response, r_C, according to this model:

(6) $\tau_r^C \frac{dr_C}{dt} = \alpha_C y_C(t) - [1 + \beta_C z_C(t)] r_C$,

where $y_C(t)$ and $z_C(t)$ are calculated with two filters $K_y^C(t)$ and $K_z^C(t)$.

In order to describe rod responses in slice accurately, we introduce an additional time scale to allow for the slower tapering of the response after turning off the stimulus. The model of rod response in slice reads

(7) $\tau_r^R \frac{dr_R}{dt} = \frac{\alpha_R y_R(t) - [1+\beta_R z_R(t)] r_R}{1+\delta_R w_R(t)}$,

where

$$(8) \quad w_R(t) = \int_{-\infty}^{t} dt' K_w^R(t-t') I(t')$$

and the filter $K_w^R(t)$ has the same form as the filter $K_y(t)$ above. In the case of the rod, we find that data is well fit in the absence of any delayed non-linearity, so that we set $\gamma = 1$ in $K_Z^R(t)$.

For the response of both cone in slice and rod in slice, the model parameters were fit by hand to the five experimental traces shown in Figure 3.11. They took the values $\alpha_C = -8.8 \cdot 10^{-6}$

s/R*, $\beta_C = 1.2 \cdot 10^{-5}$ s/R*, $\tau_r^C = 24$ ms, $\tau_y^C = 43$ ms, $\tau_z^C = 450$ ms, $\gamma = 0.64$, $\alpha_R = -3.9 \cdot 10^{-3}$ s/R*, $\beta_R = 3.9 \cdot 10^{-3}$ s/R*, $\tau_r^R = 600$ ms, $\tau_y^R = 17$ ms, $\tau_w^R = 260$ ms, $\delta_R = 2.9 \cdot 10^{-5}$ s/R*.

Finally, we model the response of the rod in the wholemount preparation, r_{RH} (where the "*H*" in the subscript is a reminder of the cone feedback through the horizontal cell). It is computed simply by supplementing the rod model in slice by an interaction term, r_H, which provides inhibitory feedback:

$$(9) \qquad \tau_r^R \frac{dr_{RH}}{dt} = \frac{\alpha_R y_R(t) - [1+\beta_R z_R(t)](r_{RH}+r_H)}{1+\delta_R w_R(t)}.$$

The horizontal cell feedback, r_H is calculated in the same formalism, with the cone output serving as input:

$$(10) \qquad \tau_r^H \frac{dr_H}{dt} = \alpha_H r_C - (1+\beta_H r_C) r_H.$$

In Eq. 9, r_H enters in such a way as to be modulated by the gain control and temporal adaptation properties of r_{RH}; this ensures that the cone output, which has a narrow dynamic range, can be effective over several decades of light intensity and, furthermore, that it affects the slow rod dynamics appropriately. Note that the subscript "*H*" appears in the newly added term only, in Eq. 9: all other parameters in the model are the ones extracted from slice data. Thus, only the three horizontal cell parameters were allowed to vary in the fit to wholemount data. They took the values $\alpha_H = 80$ per unit of cone response, $\beta_H = -2.8$ per unit of cone response, $\tau_r^H = 300$ ms.

Statistical analysis. Bar graphs indicate mean and standard error of mean (s.e.m.). Significance is indicated by * for $P < 0.05$, ** for $P < 0.01$ and *** for P<0.001. "n" shown on figures refers to the number of recorded cells. No samples or animals were excluded from the study and no data randomization was performed. The experiments were not blinded for animal group allocation (knockout versus wild type).

Chapter 4

Animals. All animal procedures were approved by the Veterinary Department of the Canton of Basel-Stadt, following the standard ethical guidelines as stated in the European Communities Guidelines on the Care and Use of Laboratory Animals, 86/609/EEC. Adult mice (4-16 weeks old) of both sexes were used. Mice were housed in groups (max. five animals per cage) and maintained on a 12-hour light/dark cycle. Mice were kept in Individually Ventilated Cages (Blue Line IVCs cages, Tecniplast) with nesting material (Plexx) and bedding (Lignocel BK8-15, Rettenmaier & Söhne GmbH & Co KG). Water and food pellets (KLIBA NAFAG irradiated rodent breeding diet 3302.PM.V20, Provimi Kliba AG) were provided ad libitum.

Gja10Cre (strain: TGN-B6CF1 BAC-Gja10-Cre-F14) is a BAC transgenic line developed in-house (Siegert et al., 2012; Szikra et al., 2014). *PVCre* mice (Hippenmeyer et al., 2005) (strain: B6.129P2-Pvalbtm1Arbr/J, stock number: 017320) were kindly provided by S. Arber, FMI Basel, and crossed with *Bl6* mice (strain: C57BL/6J, stock number: 000664). *PV-FlpO* mice (strain: B6.Cg-Pvalbtm2.1(FLPo)Hze/J, stock number: 022730) were purchased from Jackson laboratories. *Flp-GFP*-reporter mice, which were obtained by crossing the $R26^{NZG}$ mouse strain (FVB.Cg-Gt(Rosa)26SorTm1(CAG-lacZ-EFGP)Glh, Jackson stock number: 012429) with *CMV-Cre* deleter mice (Dupe et al., 1997) to remove Cre-dependence, were kindly provided by F. Rijli, FMI Basel. *Flp-GFP*-reporter mice were crossed with *PV-FlpO* and *Gja10Cre* mice to obtain triple transgenic *Gja10Cre*×*PV-Flp*×*Flp-GFP*-reporter mice.

Adeno-associated viruses (AAV). AAV production was carried out according to standard protocols (Grieger et al., 2006). Genome copy number titration was performed using real-time PCR (Applied Biosystems, TaqMan reagents). pAAV-Ef1a-DIO-PSAM was used to express PSAM (pharmacologically selective actuator module, $PSAM^{L141F\ Y115F}$-GlyR (Magnus et al., 2011)) in Cre-expressing horizontal cells. To obtain pAAV-Ef1a-DIO-PSAM, PSAM was PCR-amplified from pCAG-PSAM-IRES-GFP (kindly provided by S. Sternson, Janelia Research Campus) and sub-cloned into pAAV-ef1a-DIO-ChR2-EYFP (kindly provided by K. Deisseroth, Stanford University) using AscI/NheI sites. pAAV-ProA1-GCaMP6s was used to target the calcium indicator GCaMP6s to cones. ProA1 is a cone-specific promoter, which is part of a large-scale AAV promoter screen that will be published in Juettner, J. *et al.* (in preparation). pAAV-ProA1-GCaMP6s-WPRE was produced by replacing the promoter in pAAV-EF1a-GCaMP6s-WPRE (Wertz et al., 2015). pAAV-ProA5-DIO-PSAM was used to target PSAM to Cre-expressing ganglion cells. ProA5 expresses in ganglion cells. pAAV-ProA5-DIO-PSAM was produced by replacing the promoter in pAAV-Ef1a-DIO-PSAM.

AAV injections. Injections were performed in mice anesthetized with 2.5% Attane Isoflurane. To infect horizontal cells, AAVs (viral titer between 1×10^{14} and 9×10^{14} GC/ml) coated with the PHP.B capsid (Deverman et al., 2016) were administered systemically by injecting AAV intravenously via retro-orbital injections (Yardeni et al., 2011). A syringe (BD Micro-Fine insulin syringe 0.5 ml, 30G) was front-loaded with 30 µl AAV solution in PBS (phosphate buffered saline). The AAV solution was prepared such that at least 3.3×10^{11} viral particles were injected per gram of mouse. The injection needle was positioned behind the globe of the eye, in the retro-orbital sinus coming from the nasal side. Retinas were collected 4-5 weeks after injection. Before the systemic AAV administration was established, horizontal cells were infected by injecting serotype-BP2 (Cronin et al., 2014) AAV (viral titer 2×10^{14} GC/ml) into the subretinal space as described previously (Szikra et al., 2014). Since systemic administration using the PHP.B capsid is not efficient to infect cones (Deverman et al., 2016), subretinal injections of serotype-BP2 AAV (viral titer 7×10^{12} GC/ml) were carried out to infect cones. Retinas were collected 3-5 weeks after injection. To infect ganglion cells, intravitreal injections of serotype-7m8 (Dalkara et al., 2013) AAV were performed. 2 µl of serotype-7m8 AAV solution (viral titer 7×10^{13} GC/ml) was front-loaded into a blunt 5 µl Hamilton syringe and injected into the vitreous. To maximize infection of ganglion cells, a second injection was performed after 2-7 days. Retinas were collected 10-12 weeks after injection.

Optimizing PSAM expression in horizontal cells. We tested eight AAVs with different serotypes, promoters and coding sequences to optimize PSAM expression in the retinas of *Gja10Cre* mice. PSAM expression was visualized by staining the fixed retina with α-bungarotoxin conjugated to Alexa-555 (Thermo Fischer, B35451, 2 mg/ml). Only weak expression was obtained after subretinal injections of pAAV-EF1a-DIO-EGFP-T2A-PSAM coated with serotype 2/8, pAAV-EF1a-DIO-PSAM-IRES-EGFP coated with serotype 2/8, pAAV-EF1a-DIO-EGFP-T2A-PSAM coated with serotype 2/8 or serotype BP2, and pAAV-EF1a-DIO-PSAM coated with serotype 2/8. Subretinal injections of pAAV-CBA-FLEX-GFP-T2A-PSAM coated with serotype 2/8 led to degeneration of photoreceptor outer segments. Intravenous injection of pAAV-Ef1a-DIO-PSAM coated with the PHP.B capsid and subretinal injection of pAAV-Ef1a-DIO-PSAM coated with serotype BP2 led to retina-wide, strong PSAM expression in horizontal cells (Figures 4.1 and 4.2).

Preparation of retina for physiology. Light-adapted mice were deeply anesthetized with Attane Isoflurane and killed by decapitation. Retinas were isolated under dim red-light illumination in oxygenated Ringer's medium. For imaging experiments and targeted single-cell recordings, retinas were mounted ganglion-cell-layer-up on filter paper (MF-membrane 0.45 µm pore size, Millipore) with a 3×2 mm^2 aperture to allow for light stimulation of the

photoreceptors. The ventral part of the retina was placed over the aperture. For microelectrode array recordings, a 3×3 mm^2 patch was cut from the ventral part of the retina and placed ganglion-cell-layer-down on the array. To secure the retina, a polyamid mesh (opening size 200 µm, thickness 100 µm) was lightly pressed against the tissue. During all physiological experiments, the retina was kept at 35°C and continuously superfused with oxygenated Ringer's medium bubbled for the duration of the experiment (max. 6 hours).

Administration of the chemogenetic ligand PSEM. The pharmacologically selective effector molecule (PSEM) was bath-applied during physiological experiments. In pilot experiments, application of an initial version of PSEM ($PSEM^{89S}$, kindly provided by S. Sternson, Janelia Research Campus) at a concentration of 30 µM led to increased spiking activity of ganglion cells in control retinas. We therefore used a different version of PSEM, $PSEM^{308}$ (Apex Scientifica), bath-applied at 3 µM (as in Basu et al., 2013) throughout the study. 3 µM $PSEM^{308}$ did not show any significant off-target effects in control retinas, neither on GCaMP6s signals in cone axon terminals (Figure 4.3C-F), nor on the spiking responses of ganglion cells (Figure 4.5). PSEM was applied and washed out for 12 minutes at a perfusion rate of 1.8 ml/min, which was monitored using a liquid flow meter (SLJ-2000, Sensirion). Switching between Ringer's solution and $PSEM^{308}$ solution was controlled by a switched valve controller (VC-6, Warner Instruments).

Calcium imaging of cone axon terminals. GCaMP6s-expressing cone axon terminals were imaged in a whole-mount preparation of the retina. The two-photon imaging system used has been described previously (Yonehara et al., 2013). Briefly, the system was equipped with a Mai Tai HP two-photon laser (Spectra Physics) tuned to 920 nm, a 60× water-immersion objective (Fluor, 1.0 NA, Nikon), and a 510/20 nm band pass emission filter. For light stimulation of the retina, a custom-built UV LED projector (Acer, LED 405 nm) was triggered by a TTL (transistor-transistor logic) signal synchronized with the end of each horizontal line scan. Light stimuli were exclusively presented during the fly-back period of the horizontal scanning mirror. Image acquisition was performed using custom-made software written in LabVIEW (National Instruments), acquiring images of 3 µm/pixel at a rate of 10 Hz. Light stimulation was controlled via custom-made software written in Python and consisted of three repetitions of a small (120 µm diameter) or large (3900 µm diameter) flashed, circular light spot (duration 2 s). The light intensity of the spot stimulus was 41.9 mW/cm^2, corresponding to 7.23×10^7 photoisomerizations per rod per second (R*/s, measured and computed as described previously (Farrow et al., 2013)). The background light intensity was 0.079 mW/cm^2, corresponding to 1.37×10^5 R*/s. The same cone axon terminals were imaged before, during, and after PSEM application and during subsequent application of NBQX (Tocris Bioscience, bath-applied at 10 µM).

Microelectrode array recordings. Electrical activity of ganglion cells was recorded by using CMOS-based microelectrode arrays as described before (Fiscella et al., 2012). In initial experiments, arrays with 11,011 electrodes were used (Fiscella et al., 2012). In most experiments, arrays had 26,400 platinum electrodes over an area of 3.85×2.1 mm^2, and a center-to-center electrode distance of 17.5 µm (Ballini et al., 2013; Müller et al., 2015b) (Figure 4.4B). Electrical activity was simultaneously recorded from an arbitrarily selectable and reconfigurable subset of 1,024 electrodes. High-density electrode configurations, which allowed for simultaneous recording of cells in two 400×400 $µm^2$ retinal areas at maximal electrode density, were selected. By monitoring the online spiking responses to a 75 µm diameter circular light spot, the stimulation area was centered on each electrode configuration by moving the stage via a joystick-controlled system (Scientifica).

For light stimulation of the retina, a custom-built projector (Acer K10, LEDs 395 and 505 nm) was used to generate stimuli at a refresh rate of 60 Hz. The light was focused on the microelectrode array by a camera lens (Nikon) and a 5× objective lens (LMPlanFLN Olympus, NA 0.13) after passing a neutral density filter (ND20, Thorlabs) (Figure 4.4A). The size of the stimulation area was 2.5×1.9 mm^2. The retina was adapted to grey background light (0.0217 mW/cm2, corresponding to $8.8×10^4$ R*/s) for >30 minutes before recording started.

Visual stimulation during microelectrode array experiments. Light stimuli were controlled via custom-made software written in Python. The sequence of spatially uniform light steps of increasing and decreasing contrasts started with grey background light and consisted of the eight light steps (duration 1.86 s, Figure 4.4C). The stimulus was repeated five times. Using

$$\text{Michelson contrast} = \frac{\text{Intensity}_{\text{after step}} - \text{Intensity}_{\text{before step}}}{\text{Intensity}_{\text{after step}} + \text{Intensity}_{\text{before step}}}$$

the stimulus consisted of the following contrast values: 11%, −25%, 33%, −50%, 55%, −75%, 77%, −99%.

The barcode stimulus (Figures 4.10 and 4.11) was composed of a pattern of greyscale, vertical bars moving horizontally across the screen. The intensity profile of the bar pattern mimicked the 1/f distribution (f: spatial frequency) of light intensities of natural scenes, in which lower spatial frequencies have larger amplitudes and higher spatial frequencies have smaller amplitudes. The bar pattern was generated by superimposing sine waves (spatial frequency: between 1/9600 - 1/120 1/µm in 1/9600 1/µm steps; amplitude: 1/spatial frequency; phase: pseudo-random value between -180 and 180 degrees). The background

light intensity was 8.8×10^4 R*/s, the intensity ranged from 5.9×10^2 R*/s ('black') to 1.76×10^5 R*/s ('white'). The bar pattern moved horizontally across the screen at a constant speed of 864 µm/s. The length of the pattern (duration × speed) was 9600 µm. The bar pattern initially appeared at one side of the screen ('flying in'), then moved across the screen, and left the screen at the other side of the screen ('flying out'): this ensured that each cell was exposed to each horizontal pixel of the pattern at some point in time. The stimulus was repeated six times.

The stimulus to detect PSEM-silenced ganglion cells (Figure 4.11G) consisted of seven repetitions of a short (6 s duration) natural movie. Spatially uniform light steps were used to further classify PSEM-identified ganglion cells into PV1, PV5, and PV6 cells (Figure 4.12B), ranging from 5.9×10^2 R*/s ('black') to 1.76×10^5 R*/s ('white').

The stimulus to measure lateral inhibition in ganglion cells (Figure 4.16H) consisted of small (200 µm diameter) and large (2000 µm diameter) flashed, circular light spots of increasing contrasts (1.76×10^5 R*/s, 33% Michelson contrast) and decreasing contrasts (5.9×10^2 R*/s, −99% Michelson contrast). Stimuli were presented for 0.5 s, interleaved with 1 s grey background stimulation (8.8×10^4 R*/s). The position of the small spots alternated pseudo-randomly among 100 positions rasterizing an area of 0.5×0.5 mm^2 large area with a distance of 50 µm. Small spots of both contrasts were presented pseudo-randomly five times at each position. Large spots of both contrasts were presented ten times, pseudo-randomly interleaved among the small spot presentations.

Two-photon laser-targeted patch-clamp recordings. The recording setup for targeted single-cell recordings, which includes a Mai Tai HP two-photon laser (Spectra Physics), has been described before (Farrow et al., 2013; Yonehara et al., 2016). To target GFP-labeled cells in retinas of *Gja10Cre* × *PV-Flp* × *Flp-GFP*-reporter mice, the two-photon fluorescence image was overlaid on an infrared image acquired using a CCD camera. PV1, PV5, and PV6 cells were targeted by selecting GFP-labeled cells with large somata, and further recognized based on their previously described physiological properties (Farrow et al., 2013; Viney, 2010). Light stimulation was controlled via custom-made software written in Python. A digital light projector (V300X, NEC) generated light stimuli at a refresh rate of 75 Hz. The light was focused on the photoreceptor layer after passing a neutral density filter (Thorlabs, ND40). The background light intensity was set to 6.4×10^4 R*/s ('grey'), the intensity of the stimuli ranged from 9.1×10^2 R*/s ('black') to 1.3×10^5 R*/s ('white'). Spiking activity and inhibitory currents were recorded as described before (Farrow et al., 2013; Yonehara et al., 2016). Briefly, spike recordings were made in cell-attached mode with electrodes pulled to 3–5 MΩ resistance and filled with Ringer's solution. Whole-cell recordings were made in

voltage-clamp mode with electrodes pulled to 5-7 MΩ resistance and filled with caesium-based intracellular solution (Farrow et al., 2013; Yonehara et al., 2016). Inhibitory currents ('inhibition') were recorded by voltage clamping the cell to 0 mV, the equilibrium potential of unselective cation channels (Roska and Werblin, 2001).

Immunohistochemistry. Whole-mount retinas and retinal sections were stained as described previously (Szikra et al., 2014; Yonehara et al., 2016). The 150 µm thick retinal sections were cut using a vibratome, after embedding the fixed retina in 3% agarose in PBS. The following sets of primary and secondary antibodies were used: (i) Primary: mouse anti-calbindin (Swant, Code 300, 1:1000); secondary: donkey anti-mouse IgG conjugated with Alexa-647 (Thermo Fischer, A31571) (Figure 4.1F). (ii) Primary: rabbit anti-cone arrestin (Millipore, AB15282, 1:200); secondary: donkey anti-rabbit IgG conjugated with Alexa-633 (Invitrogen, A31573) (Figure 4.1H). (iii) Primary: rat anti-GFP (Nacalai Tesque, 04404-84, 1:200); secondary: donkey anti-rabbit IgG conjugated with Alexa-488 (Life technologies, A21206) (Figure 4.1G). (iv) Primary: rabbit anti-GFP (Life Tech, A11122); secondary: donkey anti-rat IgG conjugated with Alexa-488 (Life technologies, A21208) (Figure 4.13C). The secondary antibodies were applied at a concentration of 1:200. PSAM was stained with α-Bungarotoxin conjugated to Alexa-555 (Thermo Fischer, B35451, 2 mg/ml), and nuclei were stained with Hoechst 33342 (Thermo Fischer, H1399, 1:200), together with the secondary antibodies.

Confocal microscopy. Confocal images were acquired using a Zeiss LSM 700 laser-scanning confocal microscope equipped with a Fluar 5×/0.25 M27 objective (Figure 4.1E), a Plan-Apochromat 10×/0.45 objective (Figure 4.2), an EC Plan-Neofluar 40×/1.30 Oil M27 objective (Figures 4.1C-D, 4.1F, 4.11F, and 4.13C), and a Plan-Apochromat 63×/1.40 Oil DIC M27 objective (Figure 4.1B, G-H). The overview image of the retina (Figure 4.1E) was acquired performing a 4×4 tile scan with the 5× objective and online-stitched using the ZEN Black 2012 software (Zeiss). Confocal image stacks were processed using Imaris (Bitplane).

Circuit model. We modeled the cone response in an extension of the phenomenological models presented in Clark et al., 2013; Szikra et al., 2014, in which we added inhibitory horizontal cell feedback. The cone response was calculated as

$$\tau_c \frac{dr}{dt} = \alpha_c y(t) - [1 + \beta_c z(t)]\big(r(t) + \varphi h(t)\big) \quad (1)$$

where

$$r(t) = V(t) - V_{dark}, \quad (2)$$

$V(t)$ and V_{dark} were the instantaneous and dark membrane potentials of the cone, respectively, $h(t)$ was the feedback signal from the horizontal cell, and α_c, β_c, and φ were numerical factors. The time-varying functions, $y(t)$ and $z(t)$, were related to the light input through linear convolutions, as

$$y(t) = \int_{-\infty}^{t} dt' K_y(t-t') I(t'), \qquad (3)$$

$$z(t) = \int_{-\infty}^{t} dt' K_z(t-t') I(t'), \qquad (4)$$

where $I(t)$ was the incident light intensity (or, more precisely, R*/s). A simple filter of the form

$$K_y(t) = \frac{t}{\tau_y} \frac{e^{-\frac{t}{\tau_y}}}{\tau_y} \qquad (5)$$

yielded faithful fits to experimentally measured cone responses (Clark et al., 2013; Szikra et al., 2014). The second filter had a similar form but also contained a delayed component, as

$$K_z(t) = \gamma K_y(t) + (1-\gamma) \frac{t}{\tau_z} \frac{e^{-t/\tau_z}}{\tau_z}, \qquad (6)$$

where τ_z was larger than τ_y, and $0 \leq \gamma \leq 1$ ensured proper normalization. Note that $\int_0^\infty dt' K_y(t-t') = 1$ for all filters. The horizontal cell response was modeled analogously to the cone response, as

$$\tau_h \frac{dh}{dt} = \alpha_h y_h(t) - [1 + \beta_h z_h(t)] h(t), \qquad (7)$$

$$h(t) = V_h(t) - V_{h,dark}\,, \qquad (8)$$

where $V_h(t)$ and $V_{h,dark}$ were the instantaneous and dark membrane potentials of the horizontal cells, respectively, $y_h(t)$ and $z_h(t)$ were the quantities analogous to $y(t)$ and $z(t)$ but received the cone potential, instead of the light intensity, as input. Equations (1) and (7) are coupled differential equations. The solution to the approximated system of equations, in which the parameters τ_c and τ_h have been set to 0, i.e.,

$$\alpha_c y(t) - [1 + \beta_c z(t)]\big(r(t) + \varphi h(t)\big) = 0, \qquad (9)$$

$$\alpha_h y_h(t) - [1 + \beta_h z_h(t)]h(t) = 0, \qquad (10)$$

yielded good fits to the cone response. Furthermore, for the stimuli considered in this study, the parameter β_h could be set to zero without appreciable degradation of the fits; for all simulations shown here, we set $\beta_h = 0$. Without loss of generality, we can then set $\varphi = 1$, and the simplified, coupled system now reads

$$r(t) = \frac{\alpha_c y(t)}{[1 + \beta_c z(t)]} - h(t), \qquad (11)$$

$$h(t) = \alpha_h \int_{-\infty}^{t} dt' K_h(t - t') r(t'), \qquad (12)$$

where

$$K_h(t) = \frac{t}{\tau_h} \frac{e^{-t/\tau_h}}{\tau_h}. \qquad (13)$$

All the parameters of the outer retina component (equations (11) and (12)) of our circuit model were fit once to cone responses (Figure 3.2E), and then kept unchanged for all simulations reported here. The fitted values were $\alpha_c = -2.400 * 10^{-4}, \beta_c = -1.148 * 10^{-5}, \gamma = 0.764, \alpha_h = 0.176, \tau_y = 50.6\, ms, \tau_z = 576.9\, ms, \tau_h = 371.0\, ms$. The data used to fit the model were recordings in retinal slices (Szikra et al., 2014), where we expected that an appreciable part of the horizontal cell feedback to cones was absent, as compared to a whole-mount retina. As such, we expected that our fits underestimated the value of the parameter α_h for whole-mount retinas. Indeed, the larger value we used in our simulations, $\alpha_h = 0.792$, yielded good qualitative agreement with the ganglion cell recordings presented in this study. To model the effect of PSEM, we set $\alpha_h = 0$ which removed the horizontal cell feedback from the cone.

The activity in the inner retina pathways, $b_{p,k}(t)$, was modeled as a threshold-linear functional of the cone potential,

$$b_{p,k}(t) = \left\lfloor -1^k \left(\int_{-\infty}^{t} dt' K_p(t - t') V(t') - \theta_{p,k} \right) \right\rfloor, \qquad (14)$$

where $p = 1,2,3$ labeled the pathway (fast, intermediate, slow), $k = 0$ for OFF pathways and $k = 1$ for ON pathways,

$$\lfloor x \rfloor = \begin{cases} 0, x < 0 \\ x, x \geq 0 \end{cases} \quad (15)$$

was a thresholding non-linearity, and $\theta_{p,k}$ acted as threshold. The details of the form of the filters, $K_p(t)$, did not influence the results qualitatively; K_1 represented a high-pass filter which took the derivative of the cone potential on the order of 1 ms; K_2 was a high-pass filter with a very low cut-off frequency, in effect removing the DC-component of the cone potential; K_3 passed on the cone potential, including its DC-component, downstream. We chose the forms

$$K_1(t) = \sin\left(\frac{\pi t}{\mu}\right) \frac{1}{\sqrt{2\pi}\sigma} e^{-\frac{1}{2}\left(\frac{t-\mu}{\sigma}\right)^2}, with\ \mu = 3ms, \sigma = 1ms, \quad (15)$$

$$K_2(t) = \frac{1}{\tau_2} e^{-\frac{t}{\tau_2}} - \frac{1}{c_2 \tau_2} e^{-t/(c_2 \tau_2)}, with\ \tau_2 = 50ms, \quad (16)$$

$$K_3(t) = \frac{1}{\tau_3} e^{-t/\tau_3}, with\ \tau_3 = 100ms, \quad (17)$$

where c_2 was a large positive numerical factor. The threshold $\theta_{p,k}$ was non-zero in two cases: In the fast pathways $\theta_{1,k} = -1^k \cdot 0.1$ and in the slow pathways $\theta_{3,k} = -23.5$, where -23.5 was the cone potential (with horizontal cell feedback) in response to a constant grey stimulus with the same light intensity as the first contrast value of our stimulus. We note that this choice of parameters worked for the stimulus used in this study but may not work for other stimuli.

Finally, the input $I_g(t)$ to a model ganglion cell was computed as a weighted sum of the activity in the inner retina pathways,

$$I_g(t) = \sum_{p=1}^{3} \sum_{k=0}^{1} w_{g,p,k} b_{p,k}(t). \quad (18)$$

Here, $g = 1, \ldots, 7$ labeled the seven different simulated ganglion cells ((i-vii) in Figure 4.15E); for each of these, at most two of the 3×2 prefactors, $w_{g,p,k}$, were non-vanishing. The spiking rate of a model ganglion cell was obtained as the thresholded, weighted sum of the input and a temporally coarse version of its derivative (Figure 4.15B),

$$R_g(t) = \left\lfloor (1-\alpha) I_g(t) + \alpha \left(\int_{-\infty}^{t} dt' K_g(t-t') I_g(t') \right) - \theta_g \right\rfloor, \quad (19)$$

where $K_g(t)$ was a biphasic filter similar in its form to $K_1(t)$. Hereafter, we provide the parameters for the seven simulated ganglion cells (*i*-*vii*); the threshold, θ_g, was given as a multiple of the peak response to the largest contrast step, all $w_{g,p,k} = 0$ except when indicated otherwise, and $ON = 1, OFF = 0$. For the sake of readability, we omit the subscript g.

(*i*) $w_{2,ON} = 1, \alpha = 1, \theta_g = .3$;

(*ii*) $w_{2,ON} = 1, \alpha = 0, \theta_g = .1$;

(*iii*) $w_{2,ON} = 2, w_{3,ON} = 1, \alpha = 0, \theta_g = 0$;

(*iv*) + (*v*) $w_{1,OFF} = 3, w_{2,ON} = -1, \alpha = 1, \theta_g = 0$;

(*vi*) $w_{2,OFF} = 1, w_{3,OFF} = 10, \alpha = 0, \theta_g = -.1$;

(*vii*) $w_{1,ON} = 1, \alpha = 0, \theta_g = 0$.

The parameters of the inner retina component and ganglion cell component were chosen by hand, without systematic fitting to the data, with the aim of capturing the observed effects qualitatively. All simulations were computed with a 1 ms sampling interval.

Quantification of retinal infection. To quantify PSAM expression in retinas of *Gja10-Cre* mice injected with AAV Ef1a-DIO-PSAM, confocal stacks were acquired from stained whole-mount retinas using an EC Plan-Neofluar 40×/1.30 Oil M27 objective. No PSAM-positive cells were observed outside the inner nuclear layer and outer plexiform layer (Figure 4.1B). Cells were counted manually on a maximum-intensity projection of the inner nuclear layer and the outer plexiform layer. Calbindin was used to mark horizontal cells. To quantify GCaMP6s expression in retinas of mice injected with AAV-ProA1-GCaMP6s (Figure 4.1H), confocal stacks were acquired from stained retinal slices using a Plan-Apochromat 63×/1.40 Oil DIC M27 objective. Cells were counted manually across all retinal layers. Cone arrestin was used to mark cones.

Automated segmentation of cone axon terminals. Cone axon terminals were automatically detected semi-online via custom-made software written in Python. The temporal sequence of two-photon images was averaged in time to yield a 2D image, which was subsequently smoothed by a Gaussian filter (sigma = 1 µm). The putative centers of the terminals were located by finding the local maxima on the smoothed image. Starting from each of these local

maxima, the radius of a terminal was estimated by first growing a circular mask (starting radius 2 µm, limit radius 3 µm) and an annulus surrounding the circular mask with an area larger or equal to the area of the growing circular mask. The proportion of the average pixel intensities under the circular and annulus masks was calculated in each step. The radius of the terminal was defined as the radius of the circular mask at which the proportion of the circular/annulus average pixel intensities was maximal. Pixels under this circular region were thresholded using Otsu's method, and the contiguous set of pixel coordinates overlapping with the center of the circular region was used to extract the time series of the two-photon signal. Automatic detection of cone terminals was manually corrected if the detection of single terminals failed for two closely positioned terminals.

Analysis of cone imaging data. Data analysis was performed offline using MATLAB (MathWorks). For each terminal, fluorescence values were computed as the mean of all pixels belonging to the terminal. The background fluorescence (mean of the 10% dimmest pixels of each image frame) was subtracted. The activity was expressed as ΔF/F, where F represents the baseline fluorescence (mean fluorescence of 1 s time window before stimulus onset). ΔF/F values of three stimulus repetitions were averaged. Terminals with low signal-to-noise ratio (difference of maximal and minimal baseline fluorescence <2 ΔF/F) were excluded from the analysis.

The response amplitude (Figure 4.3D, J) was defined as the mean of the absolute ΔF/F values during the second half of the stimulation period.

The lateral inhibition index (LII) of cone terminals (Figure 4.3F, L) was defined as

$$\mathrm{LII} = \frac{R_\mathrm{S} - R_\mathrm{L}}{R_\mathrm{S} + R_\mathrm{L}}$$

where R_S and R_L denote the responses (mean of ΔF/F values in second half of stimulation period) to small and large spot stimuli. The LII in the non-PSEM condition was computed by averaging the LII before PSEM application and after PSEM washout.

The substance-induced change in LII (ΔLII, Figure 4.3M, N) was defined as

$$\Delta\mathrm{LII} = \mathrm{LII}_{\text{substance}} - \mathrm{LII}_{\text{non-substance}}$$

where, to quantify NBQX-induced effects, $\mathrm{LII}_{\text{substance}}$ denotes the LII during NBQX application and $\mathrm{LII}_{\text{non-substance}}$ denotes the LII before NBQX application (same as washout of PSEM); and, to quantify PSEM-induced effects, $\mathrm{LII}_{\text{substance}}$ denotes the LII during PSEM application and $\mathrm{LII}_{\text{non-substance}}$ denotes the LII in the non-PSEM condition. The fraction of

cones with decreased lateral inhibition was defined as the fraction of cones with substance-induced difference of LII < 0.

Analysis of microelectrode array data. Data were analyzed offline using MATLAB (MathWorks). Spikes were sorted automatically using a two-stage procedure that first identified spike templates for each neuron via mean-shift clustering (Marre et al., 2012; Prentice et al., 2011) and then classified each spike using template matching (Franke, 2011; Franke et al., 2015). We excluded cells using a two-step procedure. First, cells with a template waveform amplitude below $6*\sigma_N$ on all electrodes, where σ_N is the noise standard deviation, were excluded from the analysis. For each remaining cell, the number of electrodes on which the template amplitude surpassed the spike detection threshold ('active electrodes') was computed. Cells with a template amplitude below $8*\sigma_N$ and with fewer than 15 active electrodes were also excluded from the analysis. The spatial location of a ganglion cell on the microelectrode array (Figure 4.8) was approximated to the spatial location of the electrode that recorded the largest signal from the cell.

To analyze the response to the sequence of spatially uniform light steps of increasing and decreasing contrast (Figures 4.6, 4.13, 4.14, and 4.16E-F), data were averaged across stimulus repetitions; the first of the five stimulus repetitions was excluded from the analysis. The transient part of the on-response, the sustained part of the on-response, the rebound on-response, and the entire on-response ('all-on') were computed as the mean spike rate during the respective time window, averaged over the four positive contrast steps; for the transient part of the off-responses and the entire off-response ('all-off') the procedure was identical, except that the data were averaged over the four negative contrast steps. Only visually responsive and stable cells were included in the analysis: a cell was classified as visually responsive if its transient response to the maximal contrast was larger than 10 Hz; a cell was classified as stable if the transient part of the response after washout of PSEM was not smaller than 50% and not larger than 150% of the transient part of the response before PSEM application. Moreover, for each combination of the response polarity and the response time window, cells were excluded from the analysis if their mean spike rate during the respective time window before PSEM application was smaller than 2 Hz.

Cells were classified as ON cells (on off index > 0.5) or OFF cells (on off index < −0.5) based on their responses before PSEM application using

$$\text{on off index} = \frac{R_{\text{ON}} - R_{\text{OFF}}}{R_{\text{ON}} + R_{\text{OFF}}}$$

where R_{ON} denotes the transient part of the on-response and R_{OFF} denotes the transient part of the off-response. A transient OFF cell was classified as a cell with rebound on-response if its rebound on-response (spike rate during 0.5-1.5 s time window after light increments) before PSEM application was larger than 2 Hz.

The relative change of the response (ΔR) in PSEM versus non-PSEM conditions (Figures 4.6, 4.13, 4.14 and 4.16E-F) was defined as

$$\Delta R = \frac{R_{\text{PSEM}} - R_{\text{Non-PSEM}}}{R_{\text{Non-PSEM}} + 1}$$

where R_{PSEM} denotes the mean spike rate during PSEM application and $R_{Non\text{-}PSEM}$ denotes the mean spike rate in the non-PSEM condition (mean value of before PSEM application and after PSEM washout).

The fraction of cells with PSEM-affected responses in PSAM retinas and control retinas was computed using two thresholds

$$t_- = mean(\Delta R_{\text{Control}}) - 2 * s.d.(\Delta R_{\text{Control}})$$

$$t_+ = mean(\Delta R_{\text{Control}}) + 2 * s.d.(\Delta R_{\text{Control}})$$

where $\Delta R_{Control}$ was measured in control retinas. Responses were classified as 'PSEM-suppressed' if $\Delta R < t_-$; responses were classified as 'PSEM-enhanced' if $\Delta R > t_+$.

The response range of a cell (Figures 4.9C-D and 4.16A) was computed by normalizing the responses evoked by the four stimulus contrasts to the maximal response in the non-PSEM condition. The response range was then defined as the difference between the maximal and minimal normalized responses.

To classify cells in slow-responding and fast-responding cells (Figure 4.16E) the first time point at which the spike rate reached 50% of the maximal spike rate of the response ('time to half peak response') was computed. Cells were classified as fast-responding if the time to half peak response to the step of maximal contrast was less than 0.65 s.

The LII of ganglion cells (Figure 4.16H) was computed analogously to that of cones. Among the 100 different locations of the small spot, the location that elicited the largest response was chosen to compute the response to the small (200 µm) spot for each ganglion cell. Positive contrast stimuli were evaluated for ON cells, negative contrast stimuli were evaluated for OFF cells.

Clustering of responses to barcode stimulus. To cluster ganglion cells according to their responses to the barcode stimulus, each cell's spike trains were converted into spike rate profiles using a 50 ms bin length, and averaging the responses of all six trials. The spike rate profiles were smoothed by convolution with a kernel of length 5 bins (250 ms), before computing the pairwise distances between all pairs of cells. The cells responded to the barcode stimulus with different temporal lags, depending on their receptive field locations. Therefore, the distance between each pair of cells was computed as one minus the peak of the normalized cross-correlation function between the spike rate profiles of the two cells. The distances were used to construct a pairwise distance matrix from which a hierarchical cluster tree was computed with MATLAB's 'linkage' function and the group average as a measure for cluster distance. The hierarchical cluster tree represented the data as an ordered sequence of merging steps between cells or clusters of cells with increasing distance between the merged clusters. This sequence starts with as many clusters as there are cells in the data (each cell is in its own cluster) and successively merges pairs of clusters until all cells are within a single cluster. To decide upon the numbers of clusters and when to stop the merging within this sequence, the number of clusters with at least 30 members, and the distance between the merged clusters were plotted versus the ordered sequence of merging steps. The merging was stopped at the point in the sequence where the distance between successive merging steps started to grow exponentially, and the number of clusters with at least 30 members showed a plateau. As the precise position of this point did not qualitatively influence the results, we selected a point where 30 clusters remained, following Baden et al., 2016.

The 30 clusters were ordered according to the polarity of the cells that they contained (clusters 1-12: dominated by ON cells, clusters 13-24: dominated by OFF cells, clusters 25-30: both ON and OFF cells) and by the number of cells per cluster. To plot the responses within each cluster (Figures 4.11B-C), responses were aligned with respect to the cross-correlation with a randomly chosen cell in each cluster, and ordered with respect to the correlation to the mean response across all cells of the cluster.

To test if the responses of the PSEM-identified PV1, PV5 and PV6 cells to the barcode stimulus (Figure 4.11H) were significantly different, we first computed the mean firing rate profile for each cell over all six trials (spike count histogram with 50 ms bin width, smoothed with a Gaussian kernel of 100 ms width). The dimensionality of all averaged firing rate profiles was reduced to k by principal-component analysis. One-way multivariate analysis of variance (MANOVA) was then performed in the reduced subspace. We performed the MANOVA on a range of different values for k: independent of the number of dimensions used, the *P*-value was always smaller than 10^{-6}.

Identification of ganglion cell types on microelectrode arrays. The identification of PV1, PV5, and PV6 cells on the microelectrode arrays in retinas of *PV-Cre* mice, injected with AAVs conditionally expressing PSAM (Figure 4.11D-G), was performed in two steps (Figure 4.12). In a first step, chemogenetically labeled PV ganglion cells were identified by analyzing the spiking responses to short natural movies (seven repetitions), recorded before ('before'), during ('PSEM'), and after ('wash') PSEM application. The mean spike count across stimulus repetitions was computed for each of the three conditions. Additionally, the standard deviation of the mean of the spike count was estimated as the standard deviation over the mean spike counts of randomly chosen sets of five of the seven repetitions. Cells were classified as PSEM-silenced if two conditions were met: (1) the mean of the 'PSEM' distribution was smaller than the mean of the 'before' distribution minus four times the standard deviation of the mean in the 'before' distribution, and (2) the mean of the 'PSEM' distribution was smaller than the mean of the 'wash' distribution minus four times the standard deviation of the mean in the 'wash' distribution.

In a second step, PV1, PV5, and PV6 cells were further categorized based on their previously described light responses (Farrow et al., 2013; Viney, 2010). PV1, PV5, and PV6 cells are the only PV ganglion cell types that respond strongly and reliably to large (2.5×1.9 mm^2), spatially uniform stimuli (Farrow et al., 2013; Viney, 2010). We focused on PV1, PV5, and PV6 cells by selecting PSEM-silenced cells with strong and reliable responses to large, spatially uniform stimuli and discarding PSEM-silenced cells in which large stimuli evoked only weak responses (corresponding to the other PV-expressing ganglion cell types (Farrow et al., 2013; Viney, 2010)). The three types were further differentiated based on the polarity of their responses (PV1 cells are ON cells, PV5 and PV6 cells are OFF cells) and the temporal modulation of their spiking activity (PV5 cells have low background firing and transient off-responses, PV6 cells have high background firing and sustained off-responses) (Figure 4.12).

Analysis of targeted single-cell recordings. Data were analyzed offline using MATLAB (Mathworks). Spikes were detected by thresholding. The spiking responses to the sequence of spatially uniform light steps of increasing and decreasing contrast (Figure 4.13) were analyzed as described for the data obtained with microelectrode arrays. Inhibitory currents ('Inhibition', Figure 4.16C-D) were normalized to pre-stimulus levels (mean inhibition in 1 s time window before stimulus onset) for each trial. Data were averaged across stimulus repetitions. To quantify inhibition during the time window of the rebound on-response (0.5-0.8 s after stimulus onset), inhibition was normalized to the 'before' condition (Figure 4.16D).

Statistical analysis. The following statistical tests were used: two-sided sign-test, Mann-Whitney U test, Fisher's exact test, one-way multivariate analysis of variance (MANOVA), two-sided paired ***t***-test, Kolmogorov-Smirnoff test. The following notations were used: n.s.: $P >= 0.05$; *: $0.05 > P >= 0.01$, **: $0.01 > P >= 0.001$, ***: $P < 0.001$. s.e.m.: standard error of the mean; s.d.: standard deviation. Sample sizes were not pre-determined using statistical methods. We did not use randomization. Data collection and analysis were not performed blindly to the experimental conditions.

References

Altimus, C.M., Güler, A.D., Alam, N.M., Arman, A.C., Prusky, G.T., Sampath, A.P., Hattar, S., 2010. Rod photoreceptors drive circadian photoentrainment across a wide range of light intensities. Nat. Neurosci. 13, 1107–1112. doi:10.1038/nn.2617

Applebury, M.L., Antoch, M.P., Baxter, L.C., Chun, L.L., Falk, J.D., Farhangfar, F., Kage, K., Krzystolik, M.G., Lyass, L. a, Robbins, J.T., 2000. The murine cone photoreceptor: a single cone type expresses both S and M opsins with retinal spatial patterning. Neuron 27, 513–523. doi:10.1016/S0896-6273(00)00062-3

Asteriti, S., Gargini, C., Cangiano, L., 2014. Mouse rods signal through gap junctions with cones. Elife 3, e01386. doi:10.7554/eLife.01386

Azeredo da Silveira, R., Roska, B., 2011. Cell Types, Circuits, Computation. Curr. Opin. Neurobiol. doi:10.1016/j.conb.2011.05.007

Babai, N., Thoreson, W.B., 2009. Horizontal cell feedback regulates calcium currents and intracellular calcium levels in rod photoreceptors of salamander and mouse retina. J. Physiol. 587, 2353–2364. doi:10.1113/jphysiol.2009.169656

Baden, T., Berens, P., Franke, K., Román Rosón, M., Bethge, M., Euler, T., 2016. The functional diversity of retinal ganglion cells in the mouse. Nature 529, 345–50. doi:10.1038/nature16468

Baden, T., Schubert, T., Chang, L., Wei, T., Zaichuk, M., Wissinger, B., Euler, T., 2013. A tale of two retinal domains: Near-Optimal sampling of achromatic contrasts in natural scenes through asymmetric photoreceptor distribution. Neuron 80, 1206–1217. doi:10.1016/j.neuron.2013.09.030

Ballini, M., Muller, J., Livi, P., Chen, Y., Frey, U., Shadmani, a, Jones, I.L., Gong, W., Fiscella, M., Radivojevic, M., Bakkum, D., Stettler, a, Heer, F., Hierlemann, a, 2013. A 1024-channel CMOS microelectrode-array system with 26'400 electrodes for recording and stimulation of electro-active cells in-vitro. VLSI Circuits (VLSIC), 2013 Symp. 54–55.

Ballini, M., Muller, J., Livi, P., Yihui Chen, Frey, U., Stettler, A., Shadmani, A., Viswam, V., Lloyd Jones, I., Jackel, D., Radivojevic, M., Lewandowska, M.K., Wei Gong, Fiscella, M., Bakkum, D.J., Heer, F., Hierlemann, A., 2014. A 1024-Channel CMOS Microelectrode Array With 26,400 Electrodes for Recording and Stimulation of Electrogenic Cells In Vitro. IEEE J. Solid-State Circuits 49, 2705–2719. doi:10.1109/JSSC.2014.2359219

Basu, J., Srinivas, K., Cheung, S., Taniguchi, H., Huang, Z.J., Siegelbaum, S., 2013. A Cortico-Hippocampal Learning Rule Shapes Inhibitory Microcircuit Activity to Enhance Hippocampal Information Flow. Neuron 79, 1208–1221. doi:10.1016/j.neuron.2013.07.001

Baylor, D.A., Fuortes, M.G., O'Bryan, P.M., 1971. Receptive fields of cones in the retina of the turtle. J. Physiol. 214, 265–294. doi:10.1113/jphysiol.1971.sp009432

Berndt, A., Yizhar, O., Gunaydin, L.A., Hegemann, P., Deisseroth, K., 2009. Bi-stable neural state switches. Nat. Neurosci. 12, 229–234. doi:10.1038/nn.2247

Biel, M., Seeliger, M., Pfeifer, A., Kohler, K., Gerstner, A., Ludwig, A., Jaissle, G., Fauser, S., Zrenner, E., Hofmann, F., 1999. Selective loss of cone function in mice lacking the cyclic nucleotide-gated channel CNG3. Proc. Natl. Acad. Sci. U. S. A. 96, 7553–7557.

Bloomfield, S.A., Volgyi, B., 2009. The diverse functional roles and regulation of neuronal gap junctions in the retina. Nat Rev Neurosci 10, 495–506. doi:nrn2636 [pii]\r10.1038/nrn2636

Borst, A., Euler, T., 2011. Seeing Things in Motion: Models, Circuits, and Mechanisms. Neuron. doi:10.1016/j.neuron.2011.08.031

Borst, A., Helmstaedter, M., 2015. Common circuit design in fly and mammalian motion vision. Nat. Neurosci. 18, 1067–1076. doi:10.1038/nn.4050

Briggman, K.L., Helmstaedter, M., Denk, W., 2011. Wiring specificity in the direction-selectivity circuit of the retina. Nature 471, 183–188. doi:10.1038/nature09818

Bryan, A.S., Angelaki, D.E., 2009. Optokinetic and vestibular responsiveness in the macaque rostral vestibular and fastigial nuclei. J. Neurophysiol. 101, 714–720. doi:10.1152/jn.90612.2008

Buch, T., Heppner, F.L., Tertilt, C., Heinen, T.J.A.J., Kremer, M., Wunderlich, F.T., Jung, S., Waisman, A., 2005. A Cre-inducible diphtheria toxin receptor mediates cell lineage ablation after toxin administration. Nat. Methods 2, 419–426. doi:10.1038/nmeth762

Burkhardt, D. a, 1994. Light adaptation and photopigment bleaching in cone photoreceptors in situ in the retina of the turtle. J. Neurosci. 14, 1091–1105.

Burton, G.J., Moorhead, I.R., 1987. Color and spatial structure in natural scenes. Appl. Opt. 26, 157. doi:10.1364/AO.26.000157

Cahill, H., Nathans, J., 2008. The optokinetic reflex as a tool for quantitative analyses of nervous system function in mice: application to genetic and drug-induced variation. PLoS One 3, e2055. doi:10.1371/journal.pone.0002055

Chang, B., Dacey, M.S., Hawes, N.L., Hitchcock, P.F., Milam, A.H., Atmaca-Sonmez, P., Nusinowitz, S., Heckenlively, J.R., 2006. Cone photoreceptor function loss-3, a novel mouse model of achromatopsia due to a mutation in Gnat2. Invest. Ophthalmol. Vis. Sci. 47, 5017–5021. doi:10.1167/iovs.05-1468

Chaya, T., Matsumoto, A., Sugita, Y., Watanabe, S., Kuwahara, R., Tachibana, M., Furukawa, T., 2017. Versatile functional roles of horizontal cells in the retinal circuit. Sci. Rep. 7, 5540. doi:10.1038/s41598-017-05543-2

Chen, M., Lee, S., Park, S.J.H., Looger, L.L., Zhou, Z.J., 2014. Receptive field properties of bipolar cell axon terminals in direction-

selective sublaminas of the mouse retina. J. Neurophysiol. 112, 1950–1962. doi:10.1152/jn.00283.2014

Chen, T.-W., Wardill, T.J., Sun, Y., Pulver, S.R., Renninger, S.L., Baohan, A., Schreiter, E.R., Kerr, R.A., Orger, M.B., Jayaraman, V., Looger, L.L., Svoboda, K., Kim, D.S., 2013. Ultrasensitive fluorescent proteins for imaging neuronal activity. Nature 499, 295–300. doi:10.1038/nature12354

Clark, D.A., Benichou, R., Meister, M., Azeredo da Silveira, R., 2013. Dynamical Adaptation in Photoreceptors. PLoS Comput. Biol. 9. doi:10.1371/journal.pcbi.1003289

Cook, P.B., McReynolds, J.S., 1998. Lateral inhibition in the inner retina is important for spatial tuning of ganglion cells. Nat. Neurosci. 1, 714–719. doi:10.1038/3714

Cronin, T., Vandenberghe, L.H., Hantz, P., Juttner, J., Reimann, A., Kacsó, A.-E., Huckfeldt, R.M., Busskamp, V., Kohler, H., Lagali, P.S., Roska, B., Bennett, J., 2014. Efficient transduction and optogenetic stimulation of retinal bipolar cells by a synthetic adeno-associated virus capsid and promoter. EMBO Mol. Med. 6, 1175–90. doi:10.15252/emmm.201404077

Cruz-Martín, A., El-Danaf, R.N., Osakada, F., Sriram, B., Dhande, O.S., Nguyen, P.L., Callaway, E.M., Ghosh, A., Huberman, A.D., 2014. A dedicated circuit links direction-selective retinal ganglion cells to the primary visual cortex. Nature 507, 358–361. doi:10.1038/nature12989

Dalkara, D., Byrne, L.C., Klimczak, R.R., Visel, M., Yin, L., Merigan, W.H., Flannery, J.G., Schaffer, D. V, 2013. In vivo-directed evolution of a new adeno-associated virus for therapeutic outer retinal gene delivery from the vitreous. Sci. Transl. Med. 5, 189ra76. doi:10.1126/scitranslmed.3005708

Davenport, C.M., Detwiler, P.B., Dacey, D.M., 2008. Effects of pH buffering on horizontal and ganglion cell light responses in primate retina: evidence for the proton hypothesis of surround formation. J. Neurosci. 28, 456–464. doi:10.1523/JNEUROSCI.2735-07.2008

Deans, M.R., Volgyi, B., Goodenough, D.A., Bloomfield, S.A., Paul, D.L., 2002. Connexin36 is essential for transmission of rod-mediated visual signals in the mammalian retina. Neuron 36, 703–712.

Dedek, K., Pandarinath, C., Alam, N.M., Wellershaus, K., Schubert, T., Willecke, K., Prusky, G.T., Weiler, R., Nirenberg, S., 2008. Ganglion cell adaptability: Does the coupling of horizontal cells play a role? PLoS One 3. doi:10.1371/journal.pone.0001714

Deverman, B.E., Pravdo, P.L., Simpson, B.P., Kumar, S.R., Chan, K.Y., Banerjee, A., Wu, W.-L., Yang, B., Huber, N., Pasca, S.P., Gradinaru, V., 2016. Cre-dependent selection yields AAV variants for widespread gene transfer to the adult brain. Nat. Biotechnol. advance on, 1–7. doi:10.1038/nbt.3440

Dhande, O.S., Estevez, M.E., Quattrochi, L.E., El-Danaf, R.N., Nguyen, P.L., Berson, D.M., Huberman, A.D., 2013. Genetic dissection of retinal inputs to brainstem nuclei controlling image stabilization. J. Neurosci. Off. J. Soc. Neurosci. 33, 17797–17813. doi:10.1523/JNEUROSCI.2778-13.2013

Distler, C., Hoffmann, K.-P., 2011. Visual pathway for the optokinetic reflex in infant macaque monkeys. J. Neurosci. Off. J. Soc. Neurosci. 31, 17659–17668. doi:10.1523/JNEUROSCI.4302-11.2011

Duan, X., Krishnaswamy, A., De la Huerta, I., Sanes, J.R., 2014. Type II cadherins guide assembly of a direction-selective retinal circuit. Cell 158, 793–807. doi:10.1016/j.cell.2014.06.047

Dupe, V., Davenne, M., Brocard, J., Dolle, P., Mark, M., Dierich, A., Chambon, P., Rijli, F.M., 1997. In vivo functional analysis of the Hoxa-1 3′ retinoic acid response element (3′RARE). Development. 124, 399–410.

Elstrott, J., Anishchenko, A., Greschner, M., Sher, A., Litke, A.M., Chichilnisky, E.J., Feller, M.B., 2008. Direction selectivity in the retina is established independent of visual experience and cholinergic retinal waves. Neuron 58, 499–506. doi:10.1016/j.neuron.2008.03.013

Euler, T., Detwiler, P.B., Denk, W., 2002. Directionally selective calcium signals in dendrites of starburst amacrine cells. Nature 418, 845–852. doi:10.1038/nature00931

Famiglietti, E. V., 1991. Synaptic organization of starburst amacrine cells in rabbit retina: analysis of serial thin sections by electron microscopy and graphic reconstruction. J. Comp. Neurol. 309, 40–70. doi:10.1002/cne.903090105

Farrow, K., Teixeira, M., Szikra, T., Viney, T.J., Balint, K., Yonehara, K., Roska, B., 2013. Ambient illumination toggles a neuronal circuit switch in the retina and visual perception at cone threshold. Neuron 78, 325–338. doi:10.1016/j.neuron.2013.02.014

Faulstich, B.M., Onori, K.A., du Lac, S., 2004. Comparison of plasticity and development of mouse optokinetic and vestibulo-ocular reflexes suggests differential gain control mechanisms. Vision Res. 44, 3419–3427. doi:10.1016/j.visres.2004.09.006

Field, D., 1987. Relations between the statistics of natural images and the response properties of cortical cells. Josa a 4.

Fiscella, M., Farrow, K., Jones, I.L., Jäckel, D., Müller, J., Frey, U., Bakkum, D.J., Hantz, P., Roska, B., Hierlemann, A., 2012. Recording from defined populations of retinal ganglion cells using a high-density CMOS-integrated microelectrode array with real-time switchable electrode selection. J. Neurosci. Methods 211, 103–113. doi:10.1016/j.jneumeth.2012.08.017

Franke, F., 2011. Real-Time Analysis of Extracellular Multielectrode Recordings. PhD Thesis, Technische Universität Berlin, Berlin. doi:10.13140/RG.2.1.2899.8885

Franke, F., Quian Quiroga, R., Hierlemann, A., Obermayer, K., 2015. Bayes optimal template matching for spike sorting combining fisher discriminant analysis with optimal filtering. J. Comput. Neurosci. 38, 439–459. doi:10.1007/s10827-015-0547-7

Frey, U., Egert, U., Heer, F., Hafizovic, S., Hierlemann, A., 2009. Microelectronic system for high-resolution mapping of extracellular electric fields applied to brain slices. Biosens. Bioelectron. 24, 2191–2198. doi:10.1016/j.bios.2008.11.028

Frey, U., Sedivy, J., Heer, F., Pedron, R., Ballini, M., Mueller, J., Bakkum, D., Hafizovic, S., Faraci, F.D., Greve, F., Kirstein, K.-U., Hierlemann, A., 2010. Switch-Matrix-Based High-Density Microelectrode Array in CMOS Technology. IEEE J. Solid-State Circuits 45, 467–482. doi:10.1109/JSSC.2009.2035196

Fried, S.I., Münch, T.A., Werblin, F.S., 2002. Mechanisms and circuitry underlying directional selectivity in the retina. Nature 420, 411–414. doi:10.1038/nature01179

Gauvain, G., Murphy, G.J., 2015. Projection-specific characteristics of retinal input to the brain. J. Neurosci. Off. J. Soc. Neurosci. 35, 6575–6583. doi:10.1523/JNEUROSCI.4298-14.2015

Gavrikov, K.E., Dmitriev, A. V., Keyser, K.T., Mangel, S.C., 2003. Cation--chloride cotransporters mediate neural computation in the retina. Proc. Natl. Acad. Sci. U. S. A. 100, 16047–16052. doi:10.1073/pnas.2637041100

Gavrikov, K.E., Nilson, J.E., Dmitriev, A. V., Zucker, C.L., Mangel, S.C., 2006. Dendritic compartmentalization of chloride cotransporters underlies directional responses of starburst amacrine cells in retina. Proc. Natl. Acad. Sci. U. S. A. 103, 18793–18798. doi:10.1073/pnas.0604551103

Ghanem, A., Kern, A., Conzelmann, K.-K., 2012. Significantly improved rescue of rabies virus from cDNA plasmids. Eur. J. Cell Biol. 91, 10–16. doi:10.1016/j.ejcb.2011.01.008

Giolli, R.A., Blanks, R.H.I., Lui, F., 2006. The accessory optic system: basic organization with an update on connectivity, neurochemistry, and function. Prog. Brain Res. 151, 407–440. doi:10.1016/S0079-6123(05)51013-6

Gollisch, T., Meister, M., 2010. Eye Smarter than Scientists Believed: Neural Computations in Circuits of the Retina. Neuron. doi:10.1016/j.neuron.2009.12.009

Gottlob, I., Proudlock, F.A., 2014. Aetiology of infantile nystagmus. Curr. Opin. Neurol. 27, 83–91. doi:10.1097/WCO.0000000000000058

Grieger, J.C., Choi, V.W., Samulski, R.J., 2006. Production and characterization of adeno-associated viral vectors. Nat Protoc 1, 1412–1428. doi:10.1038/nprot.2006.207

Grimes, W.N., Schwartz, G.W., Rieke, F., 2014. The synaptic and circuit mechanisms underlying a change in spatial encoding in the retina. Neuron 82, 460–473. doi:10.1016/j.neuron.2014.02.037

Güler, A.D., Ecker, J.L., Lall, G.S., Haq, S., Altimus, C.M., Liao, H.-W., Barnard, A.R., Cahill, H., Badea, T.C., Zhao, H., Hankins, M.W., Berson, D.M., Lucas, R.J., Yau, K.-W., Hattar, S., 2008. Melanopsin cells are the principal conduits for rod–cone input to non-image-forming vision. Nature 453, 102–105. doi:10.1038/nature06829

Guo, C., Hirano, A.A., Stella, S.L.J., Bitzer, M., Brecha, N.C., 2010. Guinea pig horizontal cells express GABA, the GABA-synthesizing enzyme GAD 65, and the GABA vesicular transporter. J. Comp. Neurol. 518, 1647–1669. doi:10.1002/cne.22294

Hagihara, K.M., Murakami, T., Yoshida, T., Tagawa, Y., Ohki, K., 2015. Neuronal activity is not required for the initial formation and maturation of visual selectivity. Nat. Neurosci. 18, 1780–1788. doi:10.1038/nn.4155

Hausselt, S.E., Euler, T., Detwiler, P.B., Denk, W., 2007. A dendrite-autonomous mechanism for direction selectivity in retinal starburst amacrine cells. PLoS Biol. 5, e185. doi:10.1371/journal.pbio.0050185

Hengen, K.B., Torrado Pacheco, A., McGregor, J.N., Van Hooser, S.D., Turrigiano, G.G., 2016. Neuronal Firing Rate Homeostasis Is Inhibited by Sleep and Promoted by Wake. Cell 165, 180–191. doi:10.1016/j.cell.2016.01.046

Hillier, D., Fiscella, M., Drinnenberg, A., Trenholm, S., Rompani, S.B., Raics, Z., Katona, G., Juettner, J., Hierlemann, A., Rozsa, B., Roska, B., 2017. Causal evidence for retina-dependent and -independent visual motion computations in mouse cortex. Nat. Neurosci. 20, 960–968. doi:10.1038/nn.4566

Hippenmeyer, S., Vrieseling, E., Sigrist, M., Portmann, T., Laengle, C., Ladle, D.R., Arber, S., 2005. A developmental switch in the response of DRG neurons to ETS transcription factor signaling. PLoS Biol. 3, 0878–0890. doi:10.1371/journal.pbio.0030159

Hirasawa, H., Kaneko, A., 2003. pH changes in the invaginating synaptic cleft mediate feedback from horizontal cells to cone photoreceptors by modulating Ca2+ channels. J. Gen. Physiol. 122, 657–671. doi:10.1085/jgp.200308863

Hoffmann, K.P., 1989. Control of the optokinetic reflex by the nucleus of the optic tract in primates. Prog. Brain Res. 80, 173-182–172.

Hoffmann, K.P., Fischer, W.H., 2001. Directional effect of inactivation of the nucleus of the optic tract on optokinetic nystagmus in the cat. Vision Res. 41, 3389–3398.

Hoggarth, A., McLaughlin, A.J., Ronellenfitch, K., Trenholm, S., Vasandani, R., Sethuramanujam, S., Schwab, D., Briggman, K.L., Awatramani, G.B., 2015. Specific wiring of distinct amacrine cells in the directionally selective retinal circuit permits independent coding of direction and size. Neuron 86, 276–291. doi:10.1016/j.neuron.2015.02.035

Holtmaat, A., Bonhoeffer, T., Chow, D.K., Chuckowree, J., De Paola, V., Hofer, S.B., Hübener, M., Keck, T., Knott, G., Lee, W.-C.A., Mostany, R., Mrsic-Flogel, T.D., Nedivi, E., Portera-Cailliau, C., Svoboda, K., Trachtenberg, J.T., Wilbrecht, L., 2009. Long-term, high-resolution imaging in the mouse neocortex through a chronic cranial window. Nat. Protoc. 4, 1128–1144. doi:10.1038/nprot.2009.89

Hubel, D.H., Wiesel, T.N., 1962. Receptive fields, binocular interaction and functional architecture in the cat's visual cortex. J. Physiol. 160, 106.

Hubel, D.H., Wiesel, T.N., 1959. Receptive fields of single neurones in the cat's striate cortex. J. Physiol. 148, 574–591.

Huberman, A.D., Wei, W., Elstrott, J., Stafford, B.K., Feller, M.B., Barres, B.A., 2009. Genetic Identification of an On-Off Direction-Selective Retinal Ganglion Cell Subtype Reveals a Layer-Specific Subcortical Map of Posterior Motion. Neuron 62, 327–334. doi:10.1016/j.neuron.2009.04.014

Ichinose, T., Lukasiewicz, P.D., 2005. Inner and outer retinal pathways both contribute to surround inhibition of salamander ganglion cells. J Physiol 565, 517–535. doi:10.1113/jphysiol.2005.083436

Ivanova, E., Hwang, G.S., Pan, Z.H., 2010. Characterization of transgenic mouse lines expressing Cre recombinase in the retina. Neuroscience 165, 233–243. doi:10.1016/j.neuroscience.2009.10.021

Iwashita, M., Kanai, R., Funabiki, K., Matsuda, K., Hirano, T., 2001. Dynamic properties, interactions and adaptive modifications of vestibulo-ocular reflex and optokinetic response in mice. Neurosci. Res. 39, 299–311.

Jackman, S.L., Babai, N., Chambers, J.J., Thoreson, W.B., Kramer, R.H., 2011. A positive feedback synapse from retinal horizontal cells to cone photoreceptors. PLoS Biol. 9. doi:10.1371/journal.pbio.1001057

Joesch, M., Meister, M., 2016. A neuronal circuit for colour vision based on rod–cone opponency. Nature 532, 236–239. doi:10.1038/nature17158

Kamermans, M., Fahrenfort, I., Schultz, K., Janssen-Bienhold, U., Sjoerdsma, T., Weiler, R., 2001. Hemichannel-mediated inhibition in the outer retina. Science (80-.). 292, 1178–1180. doi:10.1126/science.1060101

Kay, J.N., De la Huerta, I., Kim, I.-J., Zhang, Y., Yamagata, M., Chu, M.W., Meister, M., Sanes, J.R., 2011. Retinal ganglion cells with distinct directional preferences differ in molecular identity, structure, and central projections. J. Neurosci. Off. J. Soc. Neurosci. 31, 7753–7762. doi:10.1523/JNEUROSCI.0907-11.2011

Ke, J.-B., Wang, Y. V, Borghuis, B.G., Cembrowski, M.S., Riecke, H., Kath, W.L., Demb, J.B., Singer, J.H., 2014. Adaptation to background light enables contrast coding at rod bipolar cell synapses. Neuron 81, 388–401. doi:10.1016/j.neuron.2013.10.054

Keck, T., Keller, G.B., Jacobsen, R.I., Eysel, U.T., Bonhoeffer, T., Hübener, M., 2013. Synaptic Scaling and Homeostatic Plasticity in the Mouse Visual Cortex In Vivo. Neuron 80, 327–334. doi:10.1016/j.neuron.2013.08.018

Kemmler, R., Schultz, K., Dedek, K., Euler, T., Schubert, T., 2014. Differential regulation of cone calcium signals by different horizontal cell feedback mechanisms in the mouse retina. J. Neurosci. 34, 11826–43. doi:10.1523/JNEUROSCI.0272-14.2014

Kim, J.S., Greene, M.J., Zlateski, A., Lee, K., Richardson, M., Turaga, S.C., Purcaro, M., Balkam, M., Robinson, A., Behabadi, B.F., Campos, M., Denk, W., Seung, H.S., EyeWirers, 2014. Space-time wiring specificity supports direction selectivity in the retina. Nature 509, 331–336. doi:10.1038/nature13240

Klaassen, L.J., Sun, Z., Steijaert, M.N., Bolte, P., Fahrenfort, I., Sjoerdsma, T., Klooster, J., Claassen, Y., Shields, C.R., Ten Eikelder, H.M.M., Janssen-Bienhold, U., Zoidl, G., McMahon, D.G., Kamermans, M., 2011. Synaptic transmission from horizontal cells to cones is impaired by loss of connexin hemichannels. PLoS Biol. 9. doi:10.1371/journal.pbio.1001107

Kolb, H., 1974. The connections between horizontal cells and photoreceptors in the retina of the cat: electron microscopy of Golgi preparations. J. Comp. Neurol. 155, 1–14. doi:10.1002/cne.901550102

Kolb, H., 1970. Organization of the outer plexiform layer of the primate retina: electron microscopy of Golgi-impregnated cells. Philos. Trans. R. Soc. Lond. B. Biol. Sci. 258, 261–283.

Kramer, R.H., Davenport, C.M., 2015. Lateral Inhibition in the Vertebrate Retina: The Case of the Missing Neurotransmitter. PLoS Biol. 13. doi:10.1371/journal.pbio.1002322

Lee, S., Kim, K., Zhou, Z.J., 2010. Role of ACh-GABA cotransmission in detecting image motion and motion direction. Neuron 68, 1159–1172. doi:10.1016/j.neuron.2010.11.031

Lee, S., Zhou, Z.J., 2006. The synaptic mechanism of direction selectivity in distal processes of starburst amacrine cells. Neuron 51, 787–799. doi:10.1016/j.neuron.2006.08.007

Li, P.H., Verweij, J., Long, J.H., Schnapf, J.L., 2012. Gap-junctional coupling of mammalian rod photoreceptors and its effect on visual detection. J. Neurosci. Off. J. Soc. Neurosci. 32, 3552–3562. doi:10.1523/JNEUROSCI.2144-11.2012

Liu, X., Hirano, A. a, Sun, X., Brecha, N.C., Barnes, S., 2013. Calcium channels in rat horizontal cells regulate feedback inhibition of photoreceptors through an unconventional GABA- and pH-sensitive mechanism. J. Physiol. 591, 3309–24. doi:10.1113/jphysiol.2012.248179

Lyubarsky, A.L., Falsini, B., Pennesi, M.E., Valentini, P., Pugh, E.N.J., 1999. UV- and midwave-sensitive cone-driven retinal responses of the mouse: a possible phenotype for coexpression of cone photopigments. J. Neurosci. Off. J. Soc. Neurosci. 19, 442–455.

Magnus, C.J., Lee, P.H., Atasoy, D., Su, H.H., Looger, L.L., Sternson, S.M., 2011. Chemical and genetic engineering of selective ion channel-ligand interactions. Science 333, 1292–6. doi:10.1126/science.1206606

Mangel, S.C., 1991. Analysis of the horizontal cell contribution to the receptive field surround of ganglion cells in the rabbit retina. J. Physiol. 442, 211–34. doi:10.1113/jphysiol.1991.sp018790

Marre, O., Amodei, D., Deshmukh, N., Sadeghi, K., Soo, F., Holy, T.E., Berry, M.J., 2012. Mapping a Complete Neural Population in the Retina. J. Neurosci. 32, 14859–14873. doi:10.1523/JNEUROSCI.0723-12.2012

Marshel, J.H., Kaye, A.P., Nauhaus, I., Callaway, E.M., 2012. Anterior-posterior direction opponency in the superficial mouse lateral geniculate nucleus. Neuron 76, 713–720. doi:10.1016/j.neuron.2012.09.021

Masland, R.H., 2012. The Neuronal Organization of the Retina. Neuron. doi:10.1016/j.neuron.2012.10.002

Maybodi, M., 2003. Infantile-onset nystagmus. Curr. Opin. Ophthalmol. 14, 276–285.

Mazurek, M., Kager, M., Van Hooser, S.D., 2014. Robust quantification of orientation selectivity and direction selectivity. Front. Neural Circuits 8. doi:10.3389/fncir.2014.00092

McLaughlin, T., Hindges, R., O'Leary, D.D.M., 2003. Regulation of axial patterning of the retina and its topographic mapping in

the brain. Curr. Opin. Neurobiol. 13, 57–69.

McMahon, M.J., Packer, O.S., Dacey, D.M., 2004. The classical receptive field surround of primate parasol ganglion cells is mediated primarily by a non-GABAergic pathway. J. Neurosci. 24, 3736–3745. doi:10.1523/JNEUROSCI.5252-03.2004

Miyamichi, K., Shlomai-Fuchs, Y., Shu, M., Weissbourd, B.C., Luo, L., Mizrahi, A., 2013. Dissecting local circuits: parvalbumin interneurons underlie broad feedback control of olfactory bulb output. Neuron 80, 1232–1245. doi:10.1016/j.neuron.2013.08.027

Moleirinho, S., Tilston-Lunel, A., Angus, L., Gunn-Moore, F., Reynolds, P.A., 2013. The expanding family of FERM proteins. Biochem. J. 452, 183–193. doi:10.1042/BJ20121642

Müller, J., Ballini, M., Livi, P., Chen, Y., Radivojevic, M., Shadmani, A., Viswam, V., Jones, I.L., Fiscella, M., Diggelmann, R., Stettler, A., Frey, U., Bakkum, D.J., Hierlemann, A., 2015a. High-resolution CMOS MEA platform to study neurons at subcellular, cellular, and network levels. Lab Chip 15, 2767–2780. doi:10.1039/C5LC00133A

Müller, J., Ballini, M., Livi, P., Chen, Y., Radivojevic, M., Shadmani, A., Viswam, V., Jones, I.L., Fiscella, M., Diggelmann, R., Stettler, A., Frey, U., Bakkum, D.J., Hierlemann, A., Muller, J., Ballini, M., Livi, P., Chen, Y., Radivojevic, M., Shadmani, A., Viswam, V., Jones, I.L., Fiscella, M., Diggelmann, R., Stettler, A., Frey, U., Bakkum, D.J., Hierlemann, A., 2015b. High-resolution CMOS MEA platform to study neurons at subcellular, cellular, and network levels. Lab Chip 15, 2767–2780. doi:10.1039/C5LC00133A

Muller, J., Ballini, M., Livi, P., Chen, Y., Shadmani, A., Frey, U., Jones, I.L., Fiscella, M., Radivojevic, M., Bakkum, D.J., Stettler, A., Heer, F., Hierlemann, A., 2013. Conferring flexibility and reconfigurability to a 26,400 microelectrode CMOS array for high throughput neural recordings. IEEE, pp. 744–747. doi:10.1109/Transducers.2013.6626873

Münch, T. a, da Silveira, R.A., Siegert, S., Viney, T.J., Awatramani, G.B., Roska, B., 2009. Approach sensitivity in the retina processed by a multifunctional neural circuit. Nat. Neurosci. 12, 1308–1316. doi:10.1038/nn.2389

Naarendorp, F., Esdaille, T.M., Banden, S.M., Andrews-Labenski, J., Gross, O.P., Pugh, E.N.J., 2010. Dark light, rod saturation, and the absolute and incremental sensitivity of mouse cone vision. J. Neurosci. Off. J. Soc. Neurosci. 30, 12495–12507. doi:10.1523/JNEUROSCI.2186-10.2010

Naka, K.I., 1971. Receptive field mechanism in the vertebrate retina. Sci. (New York, NY) 171, 691–693. doi:10.2307/1731472

Nath, A., Schwartz, G.W., 2016. Cardinal Orientation Selectivity Is Represented by Two Distinct Ganglion Cell Types in Mouse Retina. J. Neurosci. 36, 3208–3221. doi:10.1523/JNEUROSCI.4554-15.2016

Nelson, R., von Litzow, A., Kolb, H., Gouras, P., 1975. Horizontal cells in cat retina with independent dendritic systems. Science 189, 137–139.

Oesch, N., Euler, T., Taylor, W.R., 2005. Direction-selective dendritic action potentials in rabbit retina. Neuron 47, 739–750. doi:10.1016/j.neuron.2005.06.036

Osterhout, J.A., Stafford, B.K., Nguyen, P.L., Yoshihara, Y., Huberman, A.D., 2015. Contactin-4 mediates axon-target specificity and functional development of the accessory optic system. Neuron 86, 985–999. doi:10.1016/j.neuron.2015.04.005

Otero-Millan, J., Macknik, S.L., Serra, A., Leigh, R.J., Martinez-Conde, S., 2011. Triggering mechanisms in microsaccade and saccade generation: a novel proposal. Ann. N. Y. Acad. Sci. 1233, 107–116. doi:10.1111/j.1749-6632.2011.06177.x

Oyster, C.W., 2006. The human eye: structure and function. Sinauer Associates ; Macmillan [distributor], Sunderland, Mass.; Basingstoke.

Oyster, C.W., Takahashi, E., Collewijn, H., 1972. Direction-selective retinal ganglion cells and control of optokinetic nystagmus in the rabbit. Vision Res. 12, 183–193.

Pan, F., Massey, S.C., 2007. Rod and cone input to horizontal cells in the rabbit retina. J. Comp. Neurol. 500, 815–831. doi:10.1002/cne.21127

Pandarinath, C., Bomash, I., Victor, J.D., Prusky, G.T., Tschetter, W.W., Nirenberg, S., 2010. A novel mechanism for switching a neural system from one state to another. Front. Comput. Neurosci. 4, 2. doi:10.3389/fncom.2010.00002

Park, S.J.H., Kim, I.-J., Looger, L.L., Demb, J.B., Borghuis, B.G., 2014. Excitatory synaptic inputs to mouse on-off direction-selective retinal ganglion cells lack direction tuning. J. Neurosci. Off. J. Soc. Neurosci. 34, 3976–3981. doi:10.1523/JNEUROSCI.5017-13.2014

Peichl, L., González-Soriano, J., 1994. Morphological types of horizontal cell in rodent retinae: a comparison of rat, mouse, gerbil, and guinea pig. Vis. Neurosci. 11, 501–517. doi:10.1017/S095252380000242X

Piscopo, D.M., El-Danaf, R.N., Huberman, A.D., Niell, C.M., 2013. Diverse visual features encoded in mouse lateral geniculate nucleus. J. Neurosci. Off. J. Soc. Neurosci. 33, 4642–4656. doi:10.1523/JNEUROSCI.5187-12.2013

Prentice, J.S., Homann, J., Simmons, K.D., Tkačik, G., Balasubramanian, V., Nelson, P.C., 2011. Fast, scalable, bayesian spike identification for Multi-Electrode arrays. PLoS One 6. doi:10.1371/journal.pone.0019884

Priebe, N.J., Ferster, D., 2005. Direction selectivity of excitation and inhibition in simple cells of the cat primary visual cortex. Neuron 45, 133–145. doi:10.1016/j.neuron.2004.12.024

Pu, J., Mao, Y., Lei, X., Yan, Y., Lu, X., Tian, J., Yin, X., Zhao, G., Zhang, B., 2013. FERM domain containing protein 7 interacts with the Rho GDP dissociation inhibitor and specifically activates Rac1 signaling. PLoS One 8, e73108. doi:10.1371/journal.pone.0073108

Rae, J., Cooper, K., Gates, P., Watsky, M., 1991. Low access resistance perforated patch recordings using amphotericin B. J. Neurosci. Methods 37, 15–26.

Remtulla, S., Hallett, P.E., 1985. A schematic eye for the mouse, and comparisons with the rat. Vision Res. 25, 21–31.

Ribelayga, C., Cao, Y., Mangel, S.C., 2008. The circadian clock in the retina controls rod-cone coupling. Neuron 59, 790–801. doi:10.1016/j.neuron.2008.07.017

Rivlin-Etzion, M., Zhou, K., Wei, W., Elstrott, J., Nguyen, P.L., Barres, B.A., Huberman, A.D., Feller, M.B., 2011. Transgenic mice reveal unexpected diversity of on-off direction-selective retinal ganglion cell subtypes and brain structures involved in motion processing. J. Neurosci. Off. J. Soc. Neurosci. 31, 8760–8769. doi:10.1523/JNEUROSCI.0564-11.2011

Roska, B., Werblin, F.S., 2001. Vertical interactions across ten parallel, stacked representations in the mammalian retina. Nature 410, 583–587. doi:10.1038/35069068\r35069068 [pii]

Sakuta, H., Takahashi, H., Shintani, T., Etani, K., Aoshima, A., Noda, M., 2006. Role of bone morphogenic protein 2 in retinal patterning and retinotectal projection. J. Neurosci. Off. J. Soc. Neurosci. 26, 10868–10878. doi:10.1523/JNEUROSCI.3027-06.2006

Sanes, J.R., Masland, R.H., 2015. The types of retinal ganglion cells: current status and implications for neuronal classification. Annu. Rev. Neurosci. 38, 221–46. doi:10.1146/annurev-neuro-071714-034120

Schmidt, M., van der Togt, C., Wahle, P., Hoffmann, K.P., 1998. Characterization of a directional selective inhibitory input from the medial terminal nucleus to the pretectal nuclear complex in the rat. Eur. J. Neurosci. 10, 1533–1543.

Schweigart, G., Mergner, T., Evdokimidis, I., Morand, S., Becker, W., 1997. Gaze stabilization by optokinetic reflex (OKR) and vestibulo-ocular reflex (VOR) during active head rotation in man. Vision Res. 37, 1643–1652.

Seung, H.S., 2002. Amplification , Attenuation , and Integration. Handb. Comput. Neurosci. 6–10.

Shelley, J., Dedek, K., Schubert, T., Feigenspan, A., Schultz, K., Hombach, S., Willecke, K., Weiler, R., 2006. Horizontal cell receptive fields are reduced in connexin57-deficient mice. Eur. J. Neurosci. 23, 3176–3186. doi:10.1111/j.1460-9568.2006.04848.x

Shintani, T., Kato, A., Yuasa-Kawada, J., Sakuta, H., Takahashi, M., Suzuki, R., Ohkawara, T., Takahashi, H., Noda, M., 2004. Large-scale identification and characterization of genes with asymmetric expression patterns in the developing chick retina. J. Neurobiol. 59, 34–47. doi:10.1002/neu.10338

Siegert, S., Cabuy, E., Scherf, B.G., Kohler, H., Panda, S., Le, Y.Z., Fehling, H.J., Gaidatzis, D., Stadler, M.B., Roska, B., 2012. Transcriptional code and disease map for adult retinal cell types. Nat Neurosci 15, 487–95, S1-2. doi:10.1038/nn.3032

Siegert, S., Scherf, B.G., Del Punta, K., Didkovsky, N., Heintz, N., Roska, B., 2009. Genetic address book for retinal cell types. Nat. Neurosci. 12, 1197–1204. doi:10.1038/nn.2370

Simpson, J.I., 1984. The accessory optic system. Annu. Rev. Neurosci. 7, 13–41. doi:10.1146/annurev.ne.07.030184.000305

Sivyer, B., van Wyk, M., Vaney, D.I., Taylor, W.R., 2010. Synaptic inputs and timing underlying the velocity tuning of direction-selective ganglion cells in rabbit retina. J. Physiol. 588, 3243–3253. doi:10.1113/jphysiol.2010.192716

Sivyer, B., Williams, S.R., 2013. Direction selectivity is computed by active dendritic integration in retinal ganglion cells. Nat. Neurosci. 16, 1848–1856. doi:10.1038/nn.3565

Sonntag, S., Dedek, K., Dorgau, B., Schultz, K., Schmidt, K.F., Cimiotti, K., Weiler, R., Lowel, S., Willecke, K., Janssen-Bienhold, U., 2012. Ablation of retinal horizontal cells from adult mice leads to rod degeneration and remodeling in the outer retina. J Neurosci 32, 10713–10724. doi:10.1523/JNEUROSCI.0442-12.2012

Soodak, R.E., Simpson, J.I., 1988. The accessory optic system of rabbit. I. Basic visual response properties. J. Neurophysiol. 60, 2037–2054.

Stanley, G.B., Jin, J., Wang, Y., Desbordes, G., Wang, Q., Black, M.J., Alonso, J.-M., 2012. Visual Orientation and Directional Selectivity through Thalamic Synchrony. J. Neurosci. 32, 9073–9088. doi:10.1523/JNEUROSCI.4968-11.2012

Ströh, S., Sonntag, S., Janssen-Bienhold, U., Schultz, K., Cimiotti, K., Weiler, R., Willecke, K., Dedek, K., 2013. Cell-specific cre recombinase expression allows selective ablation of glutamate receptors from mouse horizontal cells. PLoS One 8. doi:10.1371/journal.pone.0083076

Sugita, Y., Miura, K., Araki, F., Furukawa, T., Kawano, K., 2013. Contributions of retinal direction-selective ganglion cells to optokinetic responses in mice. Eur. J. Neurosci. 38, 2823–2831. doi:10.1111/ejn.12284

Sun, L.O., Brady, C.M., Cahill, H., Al-Khindi, T., Sakuta, H., Dhande, O.S., Noda, M., Huberman, A.D., Nathans, J., Kolodkin, A.L., 2015. Functional assembly of accessory optic system circuitry critical for compensatory eye movements. Neuron 86, 971–984. doi:10.1016/j.neuron.2015.03.064

Sun, L.O., Jiang, Z., Rivlin-Etzion, M., Hand, R., Brady, C.M., Matsuoka, R.L., Yau, K.-W., Feller, M.B., Kolodkin, A.L., 2013. On and off retinal circuit assembly by divergent molecular mechanisms. Science 342, 1241974. doi:10.1126/science.1241974

Sun, W., Tan, Z., Mensh, B.D., Ji, N., 2016. Thalamus provides layer 4 of primary visual cortex with orientation- and direction-tuned inputs. Nat. Neurosci. 19, 308–315. doi:10.1038/nn.4196

Szikra, T., Trenholm, S., Drinnenberg, A., Jüttner, J., Raics, Z., Farrow, K., Biel, M., Awatramani, G., Clark, D.A., Sahel, J.-A., da Silveira, R.A., Roska, B., 2014. Rods in daylight act as relay cells for cone-driven horizontal cell–mediated surround inhibition. Nat. Neurosci. doi:10.1038/nn.3852

Tarpey, P., Thomas, S., Sarvananthan, N., Mallya, U., Lisgo, S., Talbot, C.J., Roberts, E.O., Awan, M., Surendran, M., McLean, R.J., Reinecke, R.D., Langmann, A., Lindner, S., Koch, M., Jain, S., Woodruff, G., Gale, R.P., Bastawrous, A., Degg, C., Droutsas, K., Asproudis, I., Zubcov, A.A., Pieh, C., Veal, C.D., Machado, R.D., Backhouse, O.C., Baumber, L., Constantinescu, C.S., Brodsky, M.C., Hunter, D.G., Hertle, R.W., Read, R.J., Edkins, S., O'Meara, S., Parker, A., Stevens, C., Teague, J., Wooster, R., Futreal, P.A., Trembath, R.C., Stratton, M.R., Raymond, F.L., Gottlob, I., 2006. Mutations in FRMD7, a newly identified member of the FERM family, cause X-linked idiopathic congenital nystagmus. Nat. Genet. 38, 1242–1244. doi:10.1038/ng1893

Thomas, M.G., Crosier, M., Lindsay, S., Kumar, A., Araki, M., Leroy, B.P., McLean, R.J., Sheth, V., Maconachie, G., Thomas, S., Moore, A.T., Gottlob, I., 2014. Abnormal retinal development associated with FRMD7 mutations. Hum. Mol. Genet. 23, 4086–4093. doi:10.1093/hmg/ddu122

Thomas, M.G., Crosier, M., Lindsay, S., Kumar, A., Thomas, S., Araki, M., Talbot, C.J., McLean, R.J., Surendran, M., Taylor, K., Leroy, B.P., Moore, A.T., Hunter, D.G., Hertle, R.W., Tarpey, P., Langmann, A., Lindner, S., Brandner, M., Gottlob, I., 2011. The clinical and molecular genetic features of idiopathic infantile periodic alternating nystagmus. Brain A J. Neurol. 134, 892–902. doi:10.1093/brain/awq373

Thomas, S., Proudlock, F.A., Sarvananthan, N., Roberts, E.O., Awan, M., McLean, R., Surendran, M., Kumar, A.S.A., Farooq, S.J., Degg, C., Gale, R.P., Reinecke, R.D., Woodruff, G., Langmann, A., Lindner, S., Jain, S., Tarpey, P., Raymond, F.L., Gottlob, I., 2008. Phenotypical characteristics of idiopathic infantile nystagmus with and without mutations in FRMD7. Brain A J. Neurol. 131, 1259–1267. doi:10.1093/brain/awn046

Thoreson, W.B., Babai, N., Bartoletti, T.M., 2008. Feedback from horizontal cells to rod photoreceptors in vertebrate retina. J. Neurosci. Off. J. Soc. Neurosci. 28, 5691–5695. doi:10.1523/JNEUROSCI.0403-08.2008

Thoreson, W.B., Mangel, S.C., 2012. Lateral interactions in the outer retina. Prog. Retin. Eye Res. doi:10.1016/j.preteyeres.2012.04.003

Tikidji-Hamburyan, A., Reinhard, K., Seitter, H., Hovhannisyan, A., Procyk, C.A., Allen, A.E., Schenk, M., Lucas, R.J., Munch, T.A., 2015. Retinal output changes qualitatively with every change in ambient illuminance. Nat Neurosci 18, 66–74. doi:10.1038/nn.3891

Tomomura, M., Rice, D.S., Morgan, J.I., Yuzaki, M., 2001. Purification of Purkinje cells by fluorescence-activated cell sorting from transgenic mice that express green fluorescent protein. Eur. J. Neurosci. 14, 57–63.

Trenholm, S., Johnson, K., Li, X., Smith, R.G., Awatramani, G.B., 2011. Parallel mechanisms encode direction in the retina. Neuron 71, 683–694. doi:10.1016/j.neuron.2011.06.020

Trenholm, S., McLaughlin, A.J., Schwab, D.J., Turner, M.H., Smith, R.G., Rieke, F., Awatramani, G.B., 2014. Nonlinear dendritic integration of electrical and chemical synaptic inputs drives fine-scale correlations. Nat. Neurosci. 17, 1759–1766. doi:10.1038/nn.3851

Trümpler, J., Dedek, K., Schubert, T., de Sevilla Müller, L.P., Seeliger, M., Humphries, P., Biel, M., Weiler, R., 2008. Rod and cone contributions to horizontal cell light responses in the mouse retina. J. Neurosci. Off. J. Soc. Neurosci. 28, 6818–6825. doi:10.1523/JNEUROSCI.1564-08.2008

Tsukamoto, Y., Morigiwa, K., Ueda, M., Sterling, P., 2001. Microcircuits for night vision in mouse retina. J. Neurosci. Off. J. Soc. Neurosci. 21, 8616–8623.

Van Alphen, A.M., Stahl, J.S., De Zeeuw, C.I., 2001. The dynamic characteristics of the mouse horizontal vestibulo-ocular and optokinetic response. Brain Res. 890, 296–305. doi:10.1016/S0006-8993(00)03180-2

van der Togt, C., van der Want, J., Schmidt, M., 1993. Segregation of direction selective neurons and synaptic organization of inhibitory intranuclear connections in the medial terminal nucleus of the rat: an electrophysiological and immunoelectron microscopical study. J. Comp. Neurol. 338, 175–192. doi:10.1002/cne.903380204

Vaney, D.I., Sivyer, B., Taylor, W.R., 2012. Direction selectivity in the retina: symmetry and asymmetry in structure and function. Nat. Rev. Neurosci. 13, 194–208. doi:10.1038/nrn3165

VanLeeuwen, M., Fahrenfort, I., Sjoerdsma, T., Numan, R., Kamermans, M., 2009. Lateral gain control in the outer retina leads to potentiation of center responses of retinal neurons. J. Neurosci. 29, 6358–6366. doi:10.1523/JNEUROSCI.5834-08.2009

Venkataramani, S., Taylor, W.R., 2010. Orientation Selectivity in Rabbit Retinal Ganglion Cells Is Mediated by Presynaptic Inhibition. J. Neurosci. 30, 15664–15676. doi:10.1523/JNEUROSCI.2081-10.2010

Vessey, J.P., Stratis, A.K., Daniels, B.A., Da Silva, N., Jonz, M.G., Lalonde, M.R., Baldridge, W.H., Barnes, S., 2005. Proton-mediated feedback inhibition of presynaptic calcium channels at the cone photoreceptor synapse. J. Neurosci. Off. J. Soc. Neurosci. 25, 4108–4117. doi:10.1523/JNEUROSCI.5253-04.2005

Vigh, J., Witkovsky, P., 1999. Sub-millimolar cobalt selectively inhibits the receptive field surround of retinal neurons. Vis. Neurosci. 16, 159–68. doi:10.1017/S095252389916111X

Viney, T.J., 2010. The diverse roles of inhibition in identified neural circuits. PhD Thesis, University of Basel, Faculty of Science. doi:10.5451/unibas-005285488

Vroman, R., Klaassen, L.J., Kamermans, M., 2013. Ephaptic communication in the vertebrate retina. Front. Hum. Neurosci. 7, 612. doi:10.3389/fnhum.2013.00612

Vroman, R., Klaassen, L.J., Kamermans, M., 2013. Ephaptic communication in the vertebrate retina. Front Hum Neurosci 7, 612. doi:10.3389/fnhum.2013.00612

Wang, T.-M., Holzhausen, L.C., Kramer, R.H., 2014. Imaging an optogenetic pH sensor reveals that protons mediate lateral inhibition in the retina. Nat. Neurosci. 17, 262–8. doi:10.1038/nn.3627

Wässle, H., 2004. Parallel processing in the mammalian retina. Nat. Rev. Neurosci. 5, 747–757. doi:10.1038/nrn1497

Wei, W., Feller, M.B., 2011. Organization and development of direction-selective circuits in the retina. Trends Neurosci. 34, 638–645. doi:10.1016/j.tins.2011.08.002

Weiler, R., Pottek, M., He, S., Vaney, D.I., 2000. Modulation of coupling between retinal horizontal cells by retinoic acid and endogenous dopamine. Brain Res. Rev. doi:10.1016/S0165-0173(99)00071-5

Weng, S., Sun, W., He, S., 2005. Identification of ON-OFF direction-selective ganglion cells in the mouse retina. J. Physiol. 562,